TECHNISCHE UNIVERSITÄT MÜNCHEN
TUM School of Natural Sciences

Neutrinos in cosmology

Precision modeling of the large-scale structure of the Universe

Petter Taule

Vollständiger Abdruck der von der TUM School of Natural Sciences der Technischen Universität München zur Erlangung des akademischen Grades eines

Doktors der Naturwissenschaften (Dr. rer. nat.)

genehmigten Dissertation.

Vorsitzender:		Prof. Dr. Susanne Mertens
Prüfer der Dissertation:	1.	Priv.-Doz. Dr. Mathias Garny
	2.	Prof. Dr. Björn Garbrecht

Die Dissertation wurde am 22.08.2022 bei der Technischen Universität München eingereicht und durch die TUM School of Natural Sciences am 27.9.2022 angenommen.

Abstract

In this thesis, we perform precision studies of cosmological observables in several setups. We develop a formalism within cosmological perturbation theory that can take into account the full time- and scale-dependence of the dynamics. The formalism is applied to the case of massive neutrinos in structure formation, which features scale-dependent dynamics due to the freestreaming of the neutrinos. Our results show that the impact of exact time- and scale-dependence in that case exceeds a percent at $k = 0.17h$ Mpc^{-1} for the power spectrum at NNLO. When embedding the theory in an EFT framework however, we find that this change is largely degenerate with counterterms. Next, we compute the NNLO correction to the bispectrum of large-scale structure, showing that it extends the reach of the theoretical prediction from $k \simeq 0.08$ to $0.15h$ Mpc^{-1}. We show that the double-hard region of the two-loop correction can be renormalized by the EFT operators already introduced at one-loop, and we renormalize the single-hard contribution with a simplified treatment adding one extra parameter. The impact of the departure from EdS at late times is analyzed for the one-loop correction to the bispectrum. Finally, we analyze non-standard neutrino interactions with Planck CMB data. Using a generic set of interaction rates modeling neutrino interactions that halt freestreaming, we establish a *freestreaming window* $2000 \lesssim z \lesssim 10^5$ in which neutrinos are not allowed to interact significantly. Furthermore, we derive an upper bound for the interaction rate $\Gamma_{\rm nfs}/H \lesssim 1$–$10$ within the freestreaming window. We investigate the potential of future CMB Stage IV experiments, finding that they can improve the bound on $\Gamma_{\rm nfs}/H$ by an order of magnitude.

Zusammenfassung

In dieser Arbeit führen wir Präzisionsstudien für kosmologische Observablen in mehreren Szenarien durch. Wir entwickeln einen Formalismus innerhalb der kosmologischen Störungstheorie, der die volle Zeit- und Skalenabhängigkeit der Dynamik berücksichtigt. Der Formalismus wird auf den Fall massiver Neutrinos bei der Strukturbildung angewendet, die aufgrund der freien Bewegung der Neutrinos eine skalenabhängige Dynamik aufweisen. Unsere Ergebnisse bei zweiter nicht-trivialer Ordnung in der Störungstheorie zeigen, dass der Einfluss der exakten Zeit- und Skalenabhängigkeit in diesem Fall bei $k = 0{,}17h$ Mpc^{-1} ein Prozent der spektralen Leistungsdichte übersteigt. Bei der Einbettung der Theorie im Rahmen einer Effektiven Feldtheorie (EFT) stellen wir jedoch fest, dass diese Änderung weitgehend mit EFT Korrekturen entartet ist. Als nächstes berechnen wir das Bispektrum der großräumigen Struktur in zweiter nicht-trivialer Ordnung und zeigen, dass die Reichweite der theoretischen Vorhersage von $k \simeq 0{,}08$ auf $0{,}15h$ Mpc^{-1} erweitert wird. Wir zeigen, dass die doppelt-harte-Region der zweiten nicht-trivialen Korrektur durch die bereits bei der ersten nicht-trivialen Korrektur eingeführten EFT-Operatoren renormiert werden kann, und wir renormieren den einzel-harten-Beitrag mit einer vereinfachten Behandlung, die einen zusätzlichen Parameter hinzufügt. Der Einfluss der Abweichung von der EdS Näherung zu späten Zeiten wird für die erste nicht-triviale Korrektur des Bispektrums quantifiziert. Schließlich analysieren wir exotische Neutrinowechselwirkungen mit Messungen der kosmischen Mikrowellenhintergrundstrahlung (CMB) des Planck Satelliten. Unter

Verwendung eines generischen Ansatzes für die Wechselwirkungsraten des Neutrinos finden wir einen Rotverschiebungsbereich $2000 \lesssim z \lesssim 10^5$, in dem Neutrinos nicht signifikant interagieren dürfen. Darüber hinaus leiten wir eine Obergrenze für die Wechselwirkungsrate $\Gamma_{\rm nfs}/H \lesssim 1$–$10$ innerhalb dieses Bereichs ab. Wir untersuchen das Potenzial der nächsten Generation von CMB Experimenten und stellen fest, dass sie die Grenze von $\Gamma_{\rm nfs}/H$ um eine Größenordnung verbessern können.

Preface

This thesis deals with the precise modeling of cosmological observables. It is based on the four papers listed below, which are the product of research concucted during my period as a Ph.D. candidate at the Physics Department at the Technical University of Munich from 2018 to 2022. The aim of the text is to put the results of the papers in a broader context for non-experts, therefore the first three chapters provide an introductionary review (with certain exceptions) of physical cosmology and in particular modeling of the large-scale structure of the Universe. The remaining chapters present the main results of the papers; more details can be found in the articles themselves, referenced below.

Acknowledgements

First and foremost I would like to thank my supervisor Mathias Garny, for the support and guidance in my research work. Thank you for taking me into the group having worked on a significantly different topic for my Master degree, as well as for the passion, expertise and patience you have exerted in training me as a scientist. A great thanks also goes to Miguel Escudero, for excellent collaboration and indispensable help and guidance both with physics but also with the practical sides of working as a physicist. Furthermore, I am grateful to my collaborators Tobias Baldauf and Theo Steele, in particular for your efforts finalizing our project also after having left physics.

I would like to thank the other cosmology members of the T31 group: Henrique Rubira, Dominik Laxhuber, Asmaa Mazoun and Lea Fuß for instructive discussions and great company. A particular thanks goes to Henrique and Dominik for proofreading this thesis. Moreover, many thanks go to the other members of the T31 group for a good atmosphere and great company at lunch, and especially Prof. Martin Beneke for agreeing to temporarily being my official supervisor as well as Elke Hutsteiner for helping with administrative struggles.

Thanks also to my officemates in 1141 and 3239 for a friendly environment and sporadic distractions; in particular thanks to Sebastian for great discussions and help with technical and administrative issues. I am very greatful to Peter, Kåre, Sebastian, Soobeen, Amy and Félix for great friendship and for contributing to a superb few years in Munich. Last but not least, thanks to my father, mother and brother for love, unconditional support and encouragement, without which this would not have been possible.

This work was supported by the Deutsche Forschungsgemeinschaft (SFB1258).

List of papers

The papers included in this thesis are the following, referred to with roman numerals in the text:

I M. Garny and **P. Taule**, *Loop corrections to the power spectrum for massive neutrino cosmologies with full time- and scale-dependence*, *JCAP* **01** (2021) 020 [2008.00013].

II T. Baldauf, M. Garny, **P. Taule** and T. Steele, *Two-loop bispectrum of large-scale structure*, *Phys. Rev. D* **104** (2021) 123551 [2110.13930].

III M. Garny and **P. Taule**, *Two-loop power spectrum with full time- and scale-dependence and EFT corrections: impact of massive neutrinos and going beyond EdS*, *JCAP* **09** (2022) 054 [2205.11533].

IV **P. Taule**, M. Escudero and M. Garny, *Global view of neutrino interactions in cosmology: The freestreaming window as seen by Planck*, *Phys. Rev. D* **106** (2022) 063539 [2207.04062].

Contents

List of Figures

Abbreviations

2dFGRS 2-degree Field Galaxy Redshift Survey.

6dFGRS 6-degree Field Galaxy Redshift Survey.

BAO baryon acoustic oscillations.

BBN Big Bang nucleosynthesis.

BOSS Baryon Oscillation Spectroscopic Survey.

CνB cosmic neutrino background.

CDM cold dark matter.

CMB Cosmic Microwave Background.

DES Dark Energy Survey.

DESI Dark Energy Spectroscopic Instrument.

eBOSS enhanced Baryon Oscillation Spectroscopic Survey.

EdS Einstein–de-Sitter.

EFT effective field theory.

EFTofLSS effective field theory of large-scale structure.

FLRW Friedmann-Lemaître-Robertson-Walker.

GR General Relativity.

ISW integrated Sachs-Wolfe.

KFT Kinetic Field Theory.

LPT Lagrangian Perturbation Theory.

LSS large-scale structure.

MCMC Markov Chain Monte Carlo.

NLO next-to-leading order.

NNLO next-to-next-to-leading order.

PDF probability density function.

QED quantum electrodynamics.

QFT quantum field theory.

RGE renormalization group equation.

RPT renormalized perturbation theory.

RSD redshift space distortions.

SDSS Sloan Digital Sky Survey.

SM Standard Model.

SPT Standard Perturbation Theory.

TRG time-renormalization group.

1 Introduction

Cosmology deals with the some of the most fundamental questions of existence. What is the composition and evolution of the Universe? What is its future? As a scientific disipline, the study of cosmology is a relatively new one, arguably emerging just a century ago with the introduction of General Relativity (GR) by Einstein [1] and the contemporary advancements in telescopes allowing for explorations beyond the Milky Way [2–4]. Over the last several decades, cosmology has gone from a field short of experimental data, with order-of-magnitude estimates, to a precision science with formidable amounts of data [3]. Remarkably, these advancements have allowed us to provide informed answers to the above questions, although several substantial conundrums remain to be explained.

The observational progress of cosmology includes several complementary probes of the cosmos. The anisotropies in the Cosmic Microwave Background (CMB) was measured first by the COBE satellite [5], and afterwards with high precision by the WMAP and Planck satellites [6–8]. Together with the measurements of the abundance of light elements in the Universe, the CMB yields firm evidence for the hot Big Bang model of cosmology [9]. Distance measurements of Type Ia Supernovae have revealed that the Universe is expanding faster and faster, necessitating the existence of some form of dark energy [10, 11]. Redshift surveys seek to map out the structure of the Universe on large scales by measuring the angular position of and distance to galaxies. An important step in this pursuit was the detection of the baryon acoustic oscillations (BAO) feature in the large-scale structure (LSS) of the Universe by the Sloan Digital Sky Survey (SDSS) project [12]. In addition, the recent detection of gravitational waves offers a new window into the cosmos, allowing for advanced tests of GR as well as providing a means to see past the last scattering surface of the CMB to the very early Universe [13, 14]. Even more recently, the James Webb Space Telescope has observed the earliest galaxies ever seen, reportedly at about 250 million years after the Big Bang [15].

The current standard model of cosmology, the ΛCDM model describes the Universe from a fraction of a second after the beginning to the present (and future), 13 billion years later [2, 16–18]. The model is supported by an abundance of experimental data, with different probes yielding consistent values of cosmological parameters, resulting in the model being referred to as *concordant* [4]. Nevertheless, there are many big open questions: What is the nature of the dark components of the Universe? What is the physics underlying cosmic inflation? How was the matter-anti matter asymmetry of the Universe generated? Ongoing and future cosmological probes can offer new insights into these issues by scrutinizing the impacts of dark matter, testing gravity on large scales and determining the initial conditions for structure formation set by inflation [19–25]. Moreover, they are expected to determine the absolute neutrino mass scale [20].

Naturally, obtaining valueable information from cosmological probes requires robust theoretical predictions. While LSS observables potentially contain considerably more

information than the CMB, it is much harder to extract: gravitational collapse is difficult to model and we cannot observe the structure of the Universe directly as it is mostly comprised of dark matter. On large enough scales however, where the fluctuations are small and can be treated as close to linear, perturbative approaches have been developed over the last couple of decades [26]. Recently, such models have been successfully been applied to the Baryon Oscillation Spectroscopic Survey (BOSS) galaxy clustering data [27–29]. As the modeling is very complex, several approximations are utilized. In particular, only the first order correction to the linear theory is taken into account; adding the two-loop allows for accurate predictions to even smaller scales. The deviation from an Einstein–de-Sitter (EdS) universe at very late times in the ΛCDM model is only taken into account at the linear level. Similarly, the impact of the neutrino component is only accounted for in linear theory. Moreover, relativistic effects are neglected and baryons are treated as dark matter. While these approximations are expected to be accurate at the few percent level or better, they need to be scrutinized and/or corrected for to achieve (sub-)percent accuracy in accordance with expected sensitivity of future LSS surveys.

Neutrinos are ubiquitous in cosmology and play an important role in the evolution of the Universe throughout its history [30]. Consequently, cosmological probes are potent in shedding light on neutrino properties, most notably their energy density in the early Universe as well as the sum of their masses. We know that neutrinos are massive from neutrino oscillation experiments, finding mass splittings that translate to a lower bound $\sum m_\nu > 0.06$ eV$/c^2$ for the sum of neutrino masses [31]. On the other hand, current cosmological observations set upper bounds: CMB measurements constrain the sum of neutrino masses to $\sum m_\nu < 0.26$ eV$/c^2$ at 95 % C.L. [8]. In addition, the presence of neutrinos imprint a characteristic scale on the LSS of the Universe: due to their substantial velocities, neutrinos slow down structure growth on scales smaller than their *freestreaming* length, the distance neutrinos typically travel in a Hubble time. This distinguishing feature is expected to be detectable by the Euclid survey, with which a neutrino mass measurement with $\sigma(\sum m_\nu) \simeq 0.02$–$0.03$ eV$/c^2$ is forecasted [20, 32–41]. The presence of the neutrino freestreaming scale makes however the modeling of dark matter gravitational clustering more complicated beyond linear theory, as the dynamics of structure growth becomes scale-dependent.

Cosmological probes can also constrain properties of beyond-Standard Model (SM) neutrinos. Although three SM neutrinos are consistent with current observations, there are many viable scenarios with exotic neutrino interactions. Freestreaming, i.e. non-interacting neutrinos in the early Universe leave a distinctive signal in the CMB that cannot be mimicked by other cosmological parameters [30, 42, 43]. Consequently, measurements of the CMB anisotropies serve as a laboratory to test and constrain scenarios with non-standard neutrino interactions.

Hence, current and future cosmological probes can yield major insights into the evolution of the Universe and the fundamental laws of physics that govern it. To achieve this, accurate theoretical modeling is required. In this thesis, we discuss recent advancements hereof put forward in Papers I–IV [44–47]. We seek to answer the following questions:

i) *What is the impact of exact time- and scale-dependent structure growth in the presence of massive neutrinos on LSS observables?* The scale-dependent dynamics of structure

formation due to freestreaming neutrinos is not typically taken into account beyond linear theory in LSS analyses. Moreover, EdS dynamics is often assumed since it simplifies the calculations. We develop a framework within cosmological perturbation theory that can capture general scale- and time-dependent dynamics in structure formation. This framework is rather versatile and can capture a wide range of extended cosmolocial models. Applying this framework to cosmologies with massive neutrinos, we can relax both abovementioned approximations and assess their impact on the next-to-next-to-leading order (NNLO) power spectrum of matter fluctuations.

ii) *How can the bispectrum be modeled at NNLO in an effective field theory (EFT) framework, and to what scale can the perturbative description be trusted?* The bispectrum was for the first time modeled at NNLO order in an EFT framework in Paper II. We compare the perturbative result at one- and two-loop to N-body simulations, and determine to what degree adding the two-loop term extends the reach of the theory.

iii) *In models with non-standard neutrino interactions, what is the window of redshifts in which neutrinos are not allowed to interact significantly given cosmological observations? And how will these constraints improve with future experiments?* Cosmological probes can put stringent constraints on exotic neutrino interactions. We determine the window of redshifts in which neutrinos cannot interact efficiently given Planck CMB data. Moreover, we forecast how much next generation CMB experiments can extend this window assuming that the true cosmology is ΛCDM.

Outline of the thesis

The rest of the thesis is structured as follows: First, the stage is set with a brief introduction and overview of the basics of physical cosmology in Chapter 2. We present the description of the Universe as a homogeneous and isotropic FLRW background with density fluctuations on top. Furthermore, we outline the use of Bayesian statistical inference in cosmology, which will be later applied in Chapter 6. As a major focus of the thesis will be on large-scale structure formation to address questions i) and ii), we devote Chapter 3 to a description of cosmological perturbation theory in the Eulerian picture. In particular, after defining Standard Perturbation Theory (SPT), we describe in Section 3.4 an extension that can capture scale- and time-dependent dynamics that was introduced and developed in Papers I and III. We moreover discuss an EFT framework for cosmological perturbation theory as well the effect of large bulk flows on mildly non-linear scales.

In Chapter 4, we present the results of Papers I and III, undertaking item i) above. After reviewing the cosmic neutrino background (CνB), we introduce a fluid model for structure formation in the presence of massive neutrinos. We embed the model in an EFT framework, and compare it to commonly adopted simplified treatments. Next, question ii) is addressed in Chapter 5, presenting the results of Paper II. We compute the NNLO correction to the bispectrum in an EFT setup, showing that it significantly extends the reach of the perturbation theory. Furthermore, we assess the impact of using exact ΛCDM time-dependent dynamics on the one-loop correction to the bispectrum.

In Chapter 6, we change gears a bit and consider beyond-SM scenarios featuring non-standard neutrino interactions as relevant for question iii). Such models can be tested with

CMB experiments. We present the analysis of Paper IV, where a redshift window in which neutrinos are not allowed to significantly interact given current cosmological observations was determined. In addition, we make a forecast of how these constraints will improve with future CMB experiments.

Finally, in Chapter 7 we summarize the main conclusions of the thesis and provide an outlook for future work. In Appendix A, we give explicit expressions and diagrams for the two-loop correction to the bispectrum, relevant for the discussion in Chapter 5.

Notations and conventions

We work in natural units where the speed of light c, the Planck constant $\hbar$ as well as the Boltzmann constant $k_{\rm B}$ is set to unity. Distances and inverse distances are measured in Mpc/h and h/Mpc, respectively, where $1\,\mathrm{pc} = 3.086 \times 10^{16}\,\mathrm{m} = 3.262\,\mathrm{ly}$ and h is the *reduced Hubble constant*:

$$h = \frac{H_0}{100\,\mathrm{km\,s^{-1}Mpc^{-1}}}\,. \tag{1.1}$$

The expansion rate today H_0 will be defined precisely in Chapter 2. Measuring distances in Mpc/h thus effectively corresponds to quantifying them in terms of the Hubble radius $1/H_0$, which is useful since the dynamics of a mode depends on the relative size of the mode compared to the Hubble radius.

We use metric signature $(-,+,+,+)$. Spacetime indices are denoted by Greek letters, e.g. $\mu = \{0,1,2,3\}$, while latin indices denote conventional summations starting at 1. Einstein's summation convention is used. Three-dimensional vectors are written in bold, e.g. $\mathbf{q}$, and their absolute values in italics, $|\mathbf{q}| = q$. We denote the Dirac delta function by $\delta_{\rm D}$ and the Kronecker delta function by $\delta^{(\rm K)}$.

Finally, we adopt the following convention for the three-dimensional Fourier transform:

$$\tilde{f}(\mathbf{k}) = \int \frac{\mathrm{d}^3\mathbf{x}}{(2\pi)^3}\,\mathrm{e}^{-\mathrm{i}k\mathbf{x}} f(\mathbf{x})\,, \qquad \tilde{f}(\mathbf{x}) = \int \mathrm{d}^3\mathbf{k}\,\mathrm{e}^{\mathrm{i}k\mathbf{x}} f(\mathbf{k}) = \int_{\mathbf{k}} \mathrm{e}^{\mathrm{i}k\mathbf{x}} f(\mathbf{k})\,, \tag{1.2}$$

where we in the last equation also introduced the shorthand notation $\int_{\mathbf{k}} \equiv \int \mathrm{d}^3\mathbf{k}$.

2 Fundamentals of physical cosmology

Physical cosmology deals with the origin and evolution of the Universe as well as the observed structures and dynamics on large scales. Starting with Einstein's postulation of GR in 1915 [1] and the observation that the Universe is expanding by Edwin Hubble in 1929 [48], theories of cosmology emerged, with the *Big Bang model* eventually established as the leading theory. Its predictions of the abundance of light elements as well as the existence of the CMB, was later experimentally confirmed, providing firm evidence for the model [49, 50]. In this chapter, we give a brief overview of the standard model of cosmology, with a focus on parts relevant for this thesis. The review is in no way complete; more comprehensive and pedagogical material on cosmology can be found in e.g. Refs [2, 16–18, 30, 51, 52]. In Section 2.1, we introduce the Friedmann-Lemaître-Robertson-Walker (FLRW) metric and the Friedmann equations. Section 2.2 provides a brief list of main events in the course of the Universe, and we discuss the inhomogeneous Universe in more detail in Section 2.3, including observables such as the power spectrum and the CMB temperature anisotropies. We end the chapter by briefly describing the use of Bayesian inference in cosmology.

2.1 Friedmann-Lemaître-Robertson-Walker universe

Two fundamental cornerstones lie at the base of the standard model of cosmology: General Relativity and the *cosmological principle*. GR is the description of gravity as a geometric property of four-dimensional spacetime. The central equation is the Einstein field equation [1],

$$G_{\mu\nu} = 8\pi G\, T_{\mu\nu}\,, \tag{2.1}$$

with G being Newtons gravitational constant. This equation expresses how the geometrical properties of spacetime, described by the Einstein tensor $G_{\mu\nu}$, is influenced by the *stress-energy* tensor $T_{\mu\nu}$. The stress-energy tensor represents the density and flux of energy and momentum at each point in spacetime, with contributions from all sources of matter, radiation and energy that populate spacetime. The Einstein tensor can be written in terms of the spacetime *metric* $g_{\mu\nu}$, relating observer-dependent coordinates X^μ to the invariant line element via $\mathrm{d}s^2 = g_{\mu\nu}\,\mathrm{d}X^\mu\,\mathrm{d}X^\nu$.

The cosmological principle is the assumption that on large scales, the Universe is homogeneous and isotropic. The most general metric describing a spacetime compatible with the cosmological principle is the Friedmann-Lemaître-Robertson-Walker metric, given by the following line element [53–56]:

$$\mathrm{d}s^2 = -\,\mathrm{d}t^2 + a^2(t)\left[\frac{\mathrm{d}r^2}{1-kr^2} + r^2\left(\mathrm{d}\theta^2 + \sin^2\theta\;\mathrm{d}\phi^2\right)\right], \tag{2.2}$$

where t is the time coordinate and r, θ and ϕ are *comoving* spherical coordinates. The parameter k describes the curvature of a three-dimensional spatial slice of the Universe. Furthermore, the *scale-factor* a is a function of time, describing the expansion (or contraction) of space. Note that if we simultaneously rescale $a \to a\lambda$, $r \to r/\lambda$ and $k \to \lambda^2 k$, the line element remains invariant. Therefore we can rescale a so that $a_0 = 1$ today, following common conventions. We define the *Hubble* rate as the relative rate of change of the scale factor with respect to time,

$$H = \frac{1}{a}\frac{\mathrm{d}a}{\mathrm{d}t}\,. \tag{2.3}$$

The expansion rate today is named the *Hubble constant*: $H_0 = (67.4 \pm 0.5)\,\mathrm{km\,s^{-1}Mpc^{-1}}$, with the quoted value being the measurement (68 % C.L.) from the Planck CMB experiment [8].

Our inferences of the evolution of the Universe is based on measuring the light (and recently gravitational waves) that we receive from distant objects. Due to the expansion of the Universe, the wavelength of photons is stretched as they propagate, and hence an observer measures wavelengths that are *redshifted* compared the emitted wavelengths. More precisely, given emitted and observed frequencies ν_e and ν_o, respectively, we define the *redshift* z as the relative change

$$z = \frac{\nu_\mathrm{e} - \nu_\mathrm{o}}{\nu_\mathrm{o}} = \frac{a_\mathrm{o}}{a_\mathrm{e}} - 1\,, \tag{2.4}$$

which we in the second equation related to the scale factors at the time of emission and observation. For observers today, $a_0 = 1$, such that light emitted when the scale factor equaled a has a redshift z given by $1 + z = 1/a$.

The stress-energy tensor compatible with homogeneity and isotropy on large scales is that of a *perfect fluid*, given in the rest frame as

$$T^\mu{}_\nu = \mathrm{diag}\left[-\rho, P, P, P\right]\,, \tag{2.5}$$

where ρ is the energy density and P is the pressure of the fluid. Both depend only on time to respect homogeneity. The generalization of energy and momentum conservation in GR is the conservation equation $\nabla_\nu T^\mu{}_\nu = 0$. For the perfect fluid, the zeroth component of this equation yields an equation for the conservation of energy density,

$$\frac{\mathrm{d}\rho}{\mathrm{d}t} + 3H(\rho + P) = 0\,. \tag{2.6}$$

The evolution of the scale factor can be derived for the homogeneous and isotropic FLRW universe by inserting the metric (2.2) and the stress-energy tensor (2.5) into Einstein's equation (2.1). After a straightforward, but lengthy derivation (see e.g. Ref. [2]) one obtains the *Friedmann equations*:

$$H^2 = \frac{8\pi G}{3}\rho - \frac{k}{a^2}\,, \tag{2.7a}$$

$$\frac{1}{a}\frac{\mathrm{d}^2 a}{\mathrm{d}t^2} = -\frac{4\pi G}{3}(\rho + 3P)\,. \tag{2.7b}$$

Cosmic inventory

To be able to make further progress, we need to specify the contents of the Universe. We will assume that the density and pressure of each component i can be related by an (in general time-dependent) *equation of state* w_i, i.e. $p_i = w_i \rho_i$. Inserting the relation into the conservation equation (2.6) yields the dependence of the energy density on the scale factor

$$\rho_i \propto a^{-3(1+w_i)} \,. \tag{2.8}$$

Hence, it is useful to classify the different components in the Universe by the equation of state. We distinguish between the following:

- **Matter.** Components whose pressure is much less than the energy density is referred to as matter, $w \to 0$. From Eq. (2.8), we see that $\rho \propto a^{-3}$: matter dilutes with the volume expansion. The main matter components in our Universe are dark matter, baryons and neutrinos at late times. The former is an unknown type of weakly interacting matter hypothesized as an explanation of various gravitational phenomena in the Universe; see Refs. [57–60] for reviews on dark matter. In cosmology, "baryons" refer to nuclei and electrons (even though the latter are leptons).

- **Radiation.** For a gas of relativistic particles, the equation of state is $w = 1/3$. We refer to components with this pressure-energy ratio as *radiation*. From the equations above it follows that radiation redshifts as a^{-4}. Photons and neutrinos (at early times) are important radiation components in our Universe.

- **Dark energy.** Einstein's equations allow for an additional term referred to as the *cosmological constant* term. We can however equivalently describe this constant as an additional component with $w = -1$ and hence $\rho \propto a^0$ constant. Just before the turn of the century, measurements of Type Ia Supernovae demonstrated that the expansion of the Universe is accelerating [10, 11]. A species can drive accelerated expansion if its equation of state satisfies $w < -1/3$. Thus, a cosmological constant could be driving the acceleration. However, it is many orders of magnitude smaller than what is expected from the ground state energy in quantum field theory (QFT) [61]. Therefore, other models of dark energy or modified gravity have been proposed to explain the accelerated expansion. We refer to Refs. [62–65] for discussions of dark energy and modified gravity in the context of cosmology.

Given these scalings, it is clear that the different components dominate the energy content of the Universe at different points in time. At early times, during the *radiation domination* era, the scale factor is small and radiation comprises the dominant energy density of the Universe. Since radiation dilutes faster than matter when the Universe expands, there is a point at which the radiation and matter energy densities are equal. This is known as *matter-radiation equality*. After a subsequent era of *matter domination*, dark energy takes over at some point and becomes the dominant component. This crossover can be referred to as *matter-dark energy equality*. Depending on which component dominates the total energy of the Universe, we can derive the following time-dependence of the scale factor from the

Friedmann equations (2.7),

$$a(t) \propto \begin{cases} t^{2/(3(1+w))}\,, & w \neq -1\,, \\ \mathrm{e}^{Ht}\,, & w = -1\,. \end{cases} \tag{2.9}$$

While this result only exactly applies for a single-component universe, it can be used to very good approximation deep in the various eras of the Universe at which either radiation, matter or dark energy dominates.

It is convenient define a *critical density* $\rho^0_{\mathrm{crit}} = 3H_0^2/8\pi G$, such that we can quantify the contribution of each component to the energy density today in terms of dimensionless density parameters,

$$\Omega_i^0 = \frac{\rho_i(t_0)}{\rho^0_{\mathrm{crit}}} \qquad \text{and} \qquad \omega_i \equiv \Omega_i^0 h^2\,, \tag{2.10}$$

where the sub-/superscript 0 indicates today (we will generalize the definition below). The second set of equivalent parameters ω_i is useful since it is *independent* of h (Ω_i^0 depends on h through ρ^0_{crit}). Using Eq. (2.8), we can rewrite the first Friedmann equation as

$$H(z) = H_0\sqrt{\Omega_{\mathrm{r}}^0(1+z)^4 + \Omega_{\mathrm{m}}^0(1+z)^3 + \Omega_\Lambda^0(1+z)^{3(1+w)} + \Omega_K^0(1+z)^2 + \frac{\rho_\nu}{\rho^0_{\mathrm{crit}}}}\,, \tag{2.11}$$

where Ω_{r}^0, Ω_{m}^0 and Ω_Λ^0 are the radiation, matter and dark energy density parameters, respectively. In addition, we defined $\Omega_K = -k/H_0^2$, treating curvature as an effective additional component of the Universe. CMB measurements indicate that curvature makes up a permille of the total energy density of the Universe today [8]. We will therefore neglect curvature from now on. As we will see more in detail in Chapter 4, neutrinos behave as radiation in the early Universe and as matter at very late times, hence their energy density ρ_ν does not scale with the same power throughout the history of the Universe.

Finally, we introduce some notation that in particular will be useful for the description of structure formation in Chapter 3. First, we define *conformal time* τ via $\mathrm{d}\tau \equiv \mathrm{d}t/a$. Then, the FLRW metric can be written as (assuming no curvature)

$$\mathrm{d}s^2 = a^2(\tau)\left[-\mathrm{d}\tau^2 + \mathrm{d}r^2 + r^2\left(\mathrm{d}\theta^2 + \sin^2\theta\ \mathrm{d}\phi^2\right)\right]\,, \tag{2.12}$$

and radial, light-like geodesics are simply given by $\Delta\tau = \Delta r$. Starting at $\tau = 0$ at the Big Bang, τ is hence the maximum distance information can have propagated since, and therefore referred to as the *comoving horizon*. Furthermore, we generalize the density parameters defined above: let $\rho_{\mathrm{crit}}(\tau) = 3H(\tau)^2/8\pi G$ be the *time-dependent* critical density, then we define density parameters $\Omega_i(\tau) = \rho_i(\tau)/\rho_{\mathrm{crit}}(\tau)$. We can write down the Friedmann equations one more time in terms of these density parameters:[1]

$$1 = \Omega_{\mathrm{r}}(\tau) + \Omega_{\mathrm{m}}(\tau) + \Omega_\Lambda(\tau)\,, \tag{2.13a}$$

$$\frac{\mathrm{d}\mathcal{H}}{\mathrm{d}\tau} = \left(\Omega_\Lambda(\tau) - \frac{\Omega_{\mathrm{m}}(\tau)}{2} - \Omega_{\mathrm{r}}\right)\,, \tag{2.13b}$$

where $\mathcal{H}$ is the conformal Hubble rate,

$$\mathcal{H} = \frac{1}{a}\frac{\mathrm{d}a}{\mathrm{d}\tau} = aH\,. \tag{2.14}$$

[1] Written in this form, we can include neutrinos in the radiation or matter contributions as appropriate.

The ΛCDM model

The currently most accepted model of cosmology is the ΛCDM model. Described by six parameters, it agrees well with observations, and moreover different probes find consistent values for the parameters.[2] In ΛCDM, spacetime is described by a spatially flat FLRW metric, and the ingredients in the Universe are baryons, cold dark matter, photons[3], neutrinos (with $\sum m_\nu = 0.06$ eV fixed) and a homogeneous dark energy component with $w = -1$ (e.g. a cosmological constant). The best constraints on the ΛCDM model are provided by the Planck CMB measurements, yielding the following density parameters [8]:

$$\Omega^0_{\rm cdm} = (0.2660 \pm 0.0074)\,, \quad \Omega^0_{\rm b} = (0.0493 \pm 0.0009)\,, \quad \Omega^0_\Lambda = (0.6847 \pm 0.0073)\,. \quad (2.15)$$

Hence, the dark components dominate the cosmic energy budget today: almost 70 % of the energy density is composed by dark energy and dark matter contributes 27 %. The remaining parameters of the model control the amplitude and tilt of the primordial power spectrum, as will be discussed below, and a parameter describing the amount of reionization of the Universe at late times during the formation of stars [69].

2.2 A brief history of the Universe

In the standard picture of an expanding Universe that was initially in a hot, dense Big Bang state, the main events of the thermal history are the following:

- **Inflation.** The theory of inflation is a hypothesized period in the very early Universe in which the scale factor increased exponentially [70–73]. While not confirmed experimentally, this hypothesis explains certain puzzles in the hot Big Bang model, for example why the CMB is remarkably uniform across (presumably disconnected causal regions of) the sky, and why the curvature of the Universe is so small. Moreover, inflation can explain the initial, seed density fluctuations in the early Universe. We do not discuss the inflationary hypothesis in detail in this thesis, but refer to comprehensive reviews in e.g. Refs. [74–78].

- **Baryogenesis.** We observe an overabundance of matter over antimatter today, in particular a baryon-to-photon ratio $n_{\rm b}/n_\gamma \sim 10^{-9}$. If the amount of matter and anti-matter was equal in the early Universe, particles and anti-particles would have annihilated and left a Universe with only radiation. Therefore, models of baryogenesis attempt to construct a mechanism from which a matter-anti-matter asymmetry could have arisen. In-depth discussions of baryogenesis can be found in Refs. [79–82].

- **Electroweak phase transition.** When the Universe has cooled to $T \sim 100$ GeV, corresponding to about $z \sim 10^{15}$, the Higgs field acquired a non-zero vacuum expectation value, breaking electroweak symmetry, generating masses to fermions via the Higgs-mechanism.

[2] There are a few mild tensions that somewhat break the concordance of the ΛCDM model, e.g. the H_0 and S_8 tensions [66, 67]. Nevertheless, they do not (yet) rule out the model.

[3] The photon energy density today is taken as fixed since it has been measured directly by the COBE satellite [68].

- **QCD phase transition.** At $T \sim 100$ MeV, strong interactions between quarks and gluons become important, and they confine to mesons and baryons. This corresponds to a redshift $z \sim 10^{12}$.
- **Neutrino decoupling.** After the temperature has dropped to $T \approx 1$ MeV, or $z \sim 10^9$, weak interactions between electrons and neutrinos become inefficient and neutrinos decouple from the thermal plasma.
- **Big Bang nucleosynthesis.** At temperatures of $T \approx 100$ keV, the formation of light nuclei starts, a process known as Big Bang nucleosynthesis (BBN). The Universe is about three minutes old at this point, corresponding to a redshift $z \sim 10^8$.
- **Matter-radiation equality.** At $z_{\rm eq} \approx 3400$, the radiation and matter contributions to the total energy density of the Universe are equal.
- **Recombination.** The production of neutral Hydrogen becomes favored compared to the reverse ionization process at $z \approx 1100$. Hence the free electron fraction of the Universe becomes suppressed and the Universe ceases to be opaque to radiation. Shortly after recombination, photon scattering with free electrons becomes inefficient (because most have recombined with protons in Hydrogen) and photons decouple. They freestream ever since, and are observed today as the Cosmic Microwave Background.
- **Matter-vacuum energy equality.** At this point, vacuum energy starts to become the dominant contributor to the cosmic energy budget. For a model with $\Omega_{\rm m} = 0.3$ and $\Omega_\Lambda = 0.7$ today, matter-vacuum energy equality happens at $z_\Lambda \approx 0.3$.

Today ($z = 0$), the Universe is about 13.8×10^9 years old with a temperature $T \approx 0.24$ meV.

2.3 Density fluctuations

While the overall properties of the Universe appear to be homogeneous, we see inhomogeneous structure from small scales up to hundreds of Mpc [83, 84]. These structures presumably contain rich amount of information about the initial conditions of the Big Bang as well as the subsequent evolution of the Universe. Therefore, the study of these inhomogeneities is the main focus of precision cosmology today [8, 20, 21, 85, 86]. A natural observable is the *density contrast* δ: the fluctuations of energy densities $\rho(\mathbf{x})$ around the mean $\bar{\rho}$,

$$\delta(\mathbf{x}) = \frac{\rho(\mathbf{x}) - \bar{\rho}}{\bar{\rho}} \,. \tag{2.16}$$

We will discuss in great detail how this quantity can be modeled theoretically in the next chapter.

The density fluctuations of the Universe are believed to have arisen from tiny, primordial seed perturbations in the early Universe that over cosmological time-scales were amplified by gravitational instability [26]. We have no direct measurements of the primordial fluctuations, but the most appealing explanation for their physical origin is the inflationary paradigm [70–73]. In models of inflation, the seed perturbations typically arise from quantum fluctuations

in the dynamical field driving inflation, often called the inflaton. Under this assumption, the primordial fluctuations therefore arose from stochastic processes, i.e. they are realizations of an ensemble of possibilities with statistical properties depending on the inflationary model.

This statistical nature of the initial seed perturbations predicted by inflation implies that cosmological observables are in general *statistic* rather than deterministic. In addition, cosmological evolution has a time-scale much longer than the one over which we can observe: in our past light-cone we can observe different objects which are in different stages of their evolution, but we cannot follow the evolution of a single system. Hence, we model the Universe as a realization of an ensemble of universes with certain statistical properties. To measure these properties, one makes use of the *ergodic theorem* to replace ensemble averages by spatial averages (we have only one realization, one universe that we can measure). This replacement is only valid if fields are uncorrelated in the large-scale limit and separate regions can be considered independent realizations.

The statistical properties of fields can be characterized by moments of the probability density function (PDF), i.e. ensemble averages of $\mathcal{N}$ fields referred to as correlation functions or $\mathcal{N}$-point functions. For Gaussian random variables, all information is encoded in the two-point correlation function. Random fields are *statistically homogeneous* and *statistically isotropic* if the PDF or its moments are invariant under spatial translations and rotations. We will assume that cosmic fields are drawn from statistically homogeneous and isotropic distributions, in accordance with the cosmological principle on large scales.

Power spectrum

Since the density perturbations in the Universe grow from tiny initial conditions, it is useful to define observables as fluctuations around the background value, as we did for the energy density in Eq. (2.16). Then, applying the ergodic theorem, the first moment or the average of fluctuation fields vanishes exactly. Hence, the first non-trivial moment is therefore the two-point correlation function, $\xi(|\mathbf{r}|) \equiv \langle \delta(\mathbf{x})\delta(\mathbf{x}+\mathbf{r})\rangle$ for the density contrast. Due to the assumption of statistical homogeneity and isotropy, it can only depend on the *distance* $|\mathbf{r}|$ between the two positions $\mathbf{x}$ and $\mathbf{x}+\mathbf{r}$.

As we will see in the next chapter, it is useful to model the density perturbations in Fourier space. Given the density contrast in Fourier space $\tilde{\delta}(\mathbf{k})$, we define the *power spectrum* $P(k)$ via[4]

$$\left\langle \tilde{\delta}(\mathbf{k})\tilde{\delta}(\mathbf{k}')\right\rangle = \delta_{\mathrm{D}}(\mathbf{k}+\mathbf{k}')P(k)\,, \tag{2.17}$$

where δ_{D} is the Dirac delta function. Due to statistical homogeneity and isotropy, the power spectrum only depends on the norm of the wavenumber k [26]. The power spectrum of density fluctuations will be one of the main observables modeled and discussed in this thesis.

The simplest, single-field inflationary models predict initial conditions that are generally almost scale-invariant, adiabatic[5] and that are very close to Gaussian [76]. This is in good

[4] Note that there are two conventions for the definition of the power spectrum in the literature, depending on the placement of (2π) factors in the Fourier transform. In contrast to the definition (2.17), the power spectrum is defined as $\langle\delta(\mathbf{k})\delta(\mathbf{k}')\rangle \equiv (2\pi)^3\delta_{\mathrm{D}}(\mathbf{k}+\mathbf{k}')P(k)$ when adopting the Fourier convention with a factor $(2\pi)^3$ in the transform *to* real space.

[5] For *adiabatic* perturbations all perturbations of individual species are related to each other (as well as to the *curvature perturbation* [76]) by a rescaling. The opposite case, *isocurvature* fluctuations, has

agreement with measurements of the CMB as measured by Planck [8, 87], in particular measurements of the three-point function, the bispectrum, puts constraints on the primordial non-Gaussianity to be about four orders of magnitude smaller than the Gaussian part [88]. Throughout this thesis we will therefore assume Gaussian initial conditions. In total, the initial density fluctuations can be parametrized by the following *primordial* power spectrum:

$$P_{\text{prim}}(k) = A \left(\frac{k}{k_\star} \right)^{n_s} \tag{2.18}$$

where A is the amplitude, $k_\star$ is a reference scale (typically $k_\star = 0.05$ Mpc^{-1}) and the spectral index n_s quantifies the tilt. Nearly scale-invariant initial conditions implies $n_s \simeq 1$; many inflation models predict a value slightly lower than unity [76]. Current CMB data measures $n_s = (0.9645 \pm 0.0004)$ at 68 % C.L. [8], but is however not yet sensitive enough to detect deviations from power-law initial conditions (a scale-dependence or "running" of the spectral index) [87].

The various events and evolution between inflation and present times shape the power spectrum, hence we measure a "processed" version of the primordial power spectrum. We can parametrize this processing as $P(k, \tau) = D^2(\tau) T^2(k) P_{\text{prim}}(k)$, where D is a time-dependent *growth factor* and T is the *transfer function*. As the Universe evolves after inflation, larger and larger comoving regions come in causal contact as they enter the comoving horizon. A mode with wavenumber k enters the horizon when $k\tau = 1$. It is useful to distinguish between modes that enter the horizon during radiation domination, and modes that enter during matter domination, $k > k_{\text{eq}}$ and $k < k_{\text{eq}}$, respectively, where k_{eq} is the mode that enters exactly at matter-radiation equality. The reason for this is that during radiation domination, radiation pressure prevents growth of structure, and the density contrast grows like $\delta \propto \ln a$, while during matter domination it grows as $\delta \propto a$. [2, 18, 30]. Therefore, we expect a different power shape for scales that enter the horizon before and after equality, with a turnover at k_{eq}. Indeed, proper analytic (linear) treatments find [2, 17, 18, 30, 89]

$$T(k) \propto \begin{cases} 1 & k < k_{\text{eq}} \,, \\ \frac{1}{k^2} \ln\left(\frac{k}{k_{\text{eq}}} \right) & k > k_{\text{eq}} \,. \end{cases} \tag{2.19}$$

During radiation domination, the perturbations in the photon fluid oscillate due to the gravitational attraction and radiation pressure. Before recombination, baryons and photons are coupled together via efficient Compton scatterings, and thus baryons partake in these oscillations before they decouple, leading to the so-called BAO imprint on the matter power spectrum. The BAO feature is a series of wiggles on the power spectrum around $k \sim 0.1h$ Mpc^{-1}.

The power spectrum of matter fluctuations can be obtained by Boltzmann solvers such as `CLASS` [90, 91] and `CAMB` [92]. They solve numerically the linearized system of equations to high accuracy [93]. As we will see in the next chapters, linear theory is only valid up to $k \sim 0.1h$ Mpc^{-1} (depending on redshift and required accuracy). A major focus of this thesis will be to describe structure formation beyond linear theory, in particular in Chapters 3, 4 and 5. We show the linear power spectrum computed by `CLASS` in Fig. 2.1 for $z = 0$ in a

perturbations of each species that adds to a vanishing total fluctuation.

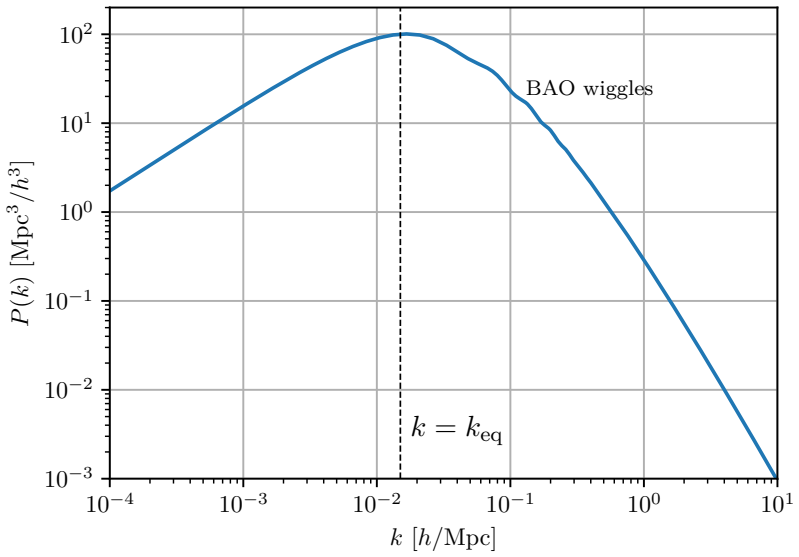

Figure 2.1: Linear matter power spectrum at $z = 0$, computed in `CLASS`. The vertical dashed line correspond to $k_{\rm eq}$, the mode that enters the horizon at matter-radiation equality. The BAO feature can be seen around $k \approx 0.1h$ Mpc^{-1}.

ΛCDM model. We can appreciate the turnover at $k_{\rm eq}$, as well as the BAO feature around $k \approx 0.1\ h$ Mpc^{-1} (somewhat invisible on the log-log plot).

The matter power spectrum (as well as higher order $\mathcal{N}$-point correlation functions) contains rich amounts of information on the cosmological initial conditions and evolution, and thus also on fundamental physics. As we discuss in detail in the next chapter, there is consequently a significant effort to theoretically model and measure the structure of the Universe on large scales.

Cosmic Microwave Background

Shortly after recombination, when electrons and protons form natural hydrogen, photons decouple from electrons due to the greatly reduced number of free electrons. Subsequently, photons freestream, forming the CMB today. At the time of photon decoupling, the Universe was exceedingly homogeneous and isotropic, with inhomogeneities of amplitudes 10^{-5}. Nevertheless, those fluctuations result in temperature anisotropies in the CMB that have been observed, first in the 1990s by COBE [5] and subsequently with high precision by WMAP [6] and Planck [8].

Consider the temperature of CMB photons reaching us from a direction $\hat{\mathbf{n}}$: $T(\hat{\mathbf{n}})$. We can define the temperature fluctuation

$$\Theta(\hat{\mathbf{n}}) = \frac{T(\hat{\mathbf{n}}) - T_0}{T_0}\,, \tag{2.20}$$

where $T_0 = (2.7255 \pm 0.0006)\,\mathrm{K}$ is the mean CMB temperature [68]. Including anisotropies in all directions $\hat{\mathbf{n}}$ yields a two-dimensional map defined on the surface of a sphere, hence it

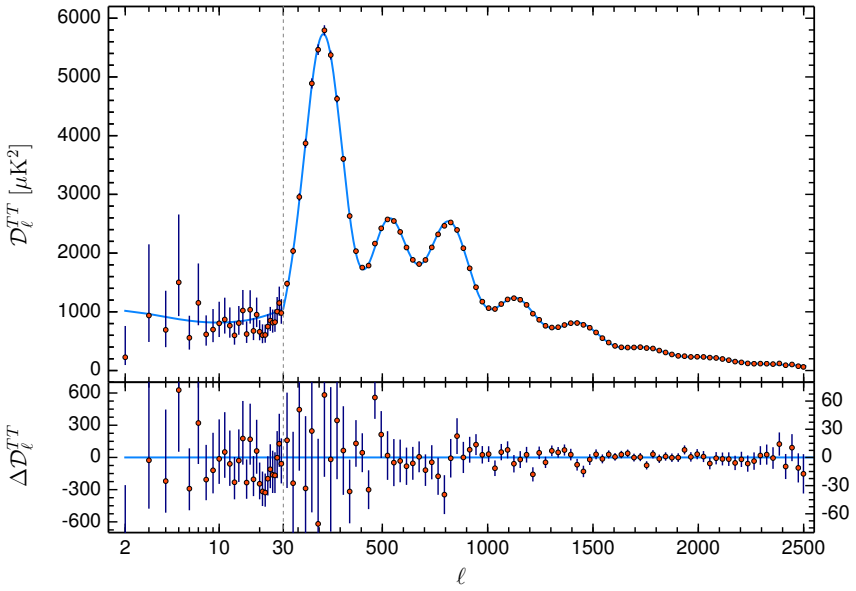

Figure 2.2: Angular power spectrum of the CMB temperature anisotropies as measured by Planck. Figure reprinted from Ref. [8]. The measurement is fitted to a ΛCDM model, shown in blue, and the lower panel shows residuals with respect to this model.

is useful to expand in spherical harmonics:

$$\Theta(\hat{\mathbf{n}}) = \sum_{l,m} a_{lm} Y_{lm}(\hat{\mathbf{n}}) \,, \tag{2.21}$$

with expansion coefficients a_{lm}. As reviewed above, we can only describe the statistical properties of the fluctuations a_{lm}. Statistical isotropy implies that different m's are equivalent, i.e. there is no preferred direction. Thus, assuming Gaussian initial conditions, we can describe the statistical properties as

$$\langle a_{lm} \rangle = 0 \,, \qquad \langle a_{lm} a^*_{l'm'} \rangle = \delta^{(\mathrm{K})}_{ll'} \delta^{(\mathrm{K})}_{mm'} C_l \,, \tag{2.22}$$

where $\delta^{(\mathrm{K})}$ is the Kronecker delta function. The variance C_l for the two-dimensional distribution is analogous to the three-dimensional power spectrum.

The temperature anisotropies of the CMB are sensitive to the entire cosmological evolution: in particular to the fluctuations of the photon fluid in the early Universe and until recombination, but they are also influenced by various effects between recombination and today. We will not discuss the origin and evolution of the CMB anisotropies in detail in this thesis, and refer the reader to Refs. [2, 8, 17, 30] for reviews. The exception is neutrinos: we will describe the effects of cosmic neutrinos on the CMB in Chapter 4, and furthermore examine the CMB impact of beyond-SM neutrinos in Chapter 6.

The angular spectrum of temperature anisotropies C_l, as measured by the Planck experiment, is shown in Fig. 2.2 (more precisely, the equivalent quantity $\mathcal{D}_l = T_0^2 \, l(l+1) C_l$ is

plotted). The spectrum is fitted to a ΛCDM model, the blue line, and the residuals are shown in the lower panel. Thus, the Planck measurements of the CMB provides currently the tightest constraints on the ΛCDM cosmological model [8]. Moreover, future CMB Stage IV experiments such as Simons Observatory [94], LiteBIRD [95] and CMB-S4 [86] (as well as the proposed CORE-M5 [96] and PICO [97] satellite projects) are expected to yield significant improvements by measuring the small scale anisotropies in greater detail and the *polarization* of the CMB photons with improved precision compared to Planck.

2.4 Bayesian statistics

We have seen that statistics plays an important role in the study of physical cosmology. The last part of this chapter will therefore be devoted to a brief introduction to the Bayesian school of statistics. More in-depth material can e.g. be found in the comprehensive reference for Bayesian probability [98], or in Refs. [99–101] for reviews of Bayesian statistics in cosmology.

Bayesian probability is a view of probability in which probabilities are quantified in the degree of belief or knowledge given partial information. To determine the probability of a hypothesis, the Bayesian statistician specifies a *prior* probability, related to their knowledge or belief in the hypothesis before new evidence is presented. Subsequently, this prior probability is updated to the *posterior* probability by taking into account new evidence via Bayes' theorem [98–101]. It is opposed to the *frequentist* view of probability, where the probability of an event is defined as the relative frequency in the limit of an infinite number of trials with equal probability. This definition is however somewhat unsatisfactory [99, 100]: it is strictly speaking circular, assuming that trials have equal *probability*. Moreover, it only applies to repeatable events, and only exactly in the infinite limit. The Bayesian definition of probability can on the other hand be applied to any event (even unrepeatable). Nevertheless, critics argue that while the frequentist definition is objective, the Bayesian one is not: the probability depends on the subjective selection of the prior.

The use of Bayesian statistics in cosmology has had an upturn in the last decades [100, 101]. The Bayesian point of view is useful since we only have one Universe on which we can measure and it is difficult to replicate surveys as they are exceedingly expensive. Nevertheless, one can use the ergodic theorem to produce frequentist trials; see e.g. Ref. [102] for cosmological inference performed in both a Bayesian and frequentist way. There are furthermore good tools for Bayesian parameter inference in cosmology, such as `CosmoMC` [103] and `MontePython` [104, 105], that are easily linked to Boltzmann solvers such as `CAMB` and `CLASS`.

At the heart of Bayesian inference is Bayes' theorem. As a simple consequence of basic axioms of probability, the theorem itself is not controversial, only its use in Bayesian inference is [100]. Let $p(A|B)$ be the conditional probability of A given B and let $p(A, B)$ be the joint probability of A and B. Furthermore, let I represent information that is assumed to be true. Bayes' theorem states that

$$p(B|A, I) = \frac{p(A|B, I)p(B|I)}{p(A|I)} \,. \tag{2.23}$$

For our purposes, it is more illuminating to replace A with experimental data $\mathbf{d}$, and B with the parameters $\boldsymbol{\alpha}$ of a model $I = M$. Then, Bayes theorem reads

$$p(\boldsymbol{\alpha}|\mathbf{d}, M) = \frac{p(\mathbf{d}|\boldsymbol{\alpha}, M)p(\boldsymbol{\alpha}|M)}{p(\mathbf{d}|M)} \,. \tag{2.24}$$

The conditional probability on the LHS, $p(\boldsymbol{\alpha}|\mathbf{d}, M)$ is the posterior probability, i.e. the updated probability of the parameters $\boldsymbol{\alpha}$ after taking the new evidence, the data $\mathbf{d}$, into account. It is proportional to the prior probability $p(\boldsymbol{\alpha}|M)$ times the *likelihood* $\mathcal{L}(\boldsymbol{\alpha}) = p(\mathbf{d}|\boldsymbol{\alpha}, M)$. The prior probability expresses the degree of knowledge on $\boldsymbol{\alpha}$ before confronted with data. Prior information can for example incorporate that a mass parameter must be positive. The likelihood is a function of the model parameters $\boldsymbol{\alpha}$, and represents the plausibility of the measurement given those parameters. Furthermore, as a function of the $\boldsymbol{\alpha}$'s, it is not a PDF and not normalized. The denominator in Eq. (2.24), $p(\mathbf{d}|M)$, is known as the *Bayesian evidence* or the *marginal likelihood*. It is the normalization of the posterior PDF. If one is only interested in parameter inference, rather than e.g. model comparison, the normalization is irrelevant since only ratios of the posterior at different points in parameter space are of interest. Then it is sufficient to apply Bayes' theorem as $p(\boldsymbol{\alpha}|\mathbf{d}, M) \propto \mathcal{L}(\boldsymbol{\alpha})p(\boldsymbol{\alpha}|M)$.

Hence, to perform Bayesian inference on cosmological parameters, we need to specify a prior on those parameters as well as compute the likelihood given the observed data. A typical analysis involves $\mathcal{O}(10)$ free parameters, therefore a naive grid exploration of parameter space is unfeasible. Moreover, most of parameter space is typically ruled out with a very low posterior, and therefore worthless to explore. A better approach is to sample parameter space in a clever way. One such method is the Markov Chain Monte Carlo (MCMC) technique [106]. The aim of the MCMC method is to constructs a sequence of points in parameter space, where the density of each point in the chain is proportional to the posterior PDF. The sequence is defined as a Markov chain, with the property that it converges to a steady state in which the points are sampled from the posterior distribution. The elements of the chain are sampled in a random manner; various MCMC algorithms have different prescriptions for picking and accepting/rejecting points in parameter space. One example is the Metropolis-Hastings algorithm, defined as follows [107, 108]: let the current element of the chain be the point $\boldsymbol{\alpha}$, and draw a new point $\boldsymbol{\alpha}'$ from a proposal distribution $q(\boldsymbol{\alpha}'|\boldsymbol{\alpha})$. Calculate the *Hastings ratio*:

$$r(\boldsymbol{\alpha}, \boldsymbol{\alpha}') = \frac{p(\boldsymbol{\alpha}')}{p(\boldsymbol{\alpha})} \frac{q(\boldsymbol{\alpha}'|\boldsymbol{\alpha})}{q(\boldsymbol{\alpha}|\boldsymbol{\alpha}')} \,. \tag{2.25}$$

The proposed new step is accepted with probability $\beta = \min(1, r(\boldsymbol{\alpha}, \boldsymbol{\alpha}'))$. To save the calculation of the ratio of proposal distributions above, one often chooses a symmetric distribution $q(\boldsymbol{\alpha}'|\boldsymbol{\alpha}) = q(\boldsymbol{\alpha}|\boldsymbol{\alpha}')$, for example by letting the proposal distribution only depend on the distance between the points, $q(\boldsymbol{\alpha}'|\boldsymbol{\alpha}) = f(|\boldsymbol{\alpha}' - \boldsymbol{\alpha}|)$. We will use the Metropolis-Hastings algorithm for parameter inference when we consider non-standard neutrino interactions in a cosmological context in Chapter 6.

For a MCMC chain with N steps, one can estimate the mean of a parameter as

$$\langle \alpha \rangle = \frac{1}{N} \sum_{i=1}^{N} \alpha^{(i)} \,. \tag{2.26}$$

3 Eulerian perturbation theory

In this chapter we discuss LSS as a probe of cosmology and fundamental physics, and how structure formation can be modeled in the Eulerian fluid picture using perturbation theory. The text serve as a review, introducing the SPT description in the Eulerian setup and its embedding in an EFT framework (the effective field theory of large-scale structure (EFTofLSS)), with one important exception: in Section 3.4 we describe an extension of the standard formalism, introduced in Paper I [44] and further developed in Paper III [46], that can capture non-trivial time- and scale-dependence in the dynamics. This extension is applied to the case of massive neutrinos in structure formation in Chapter 4. In addition, we will adopt the EFT framework described here to model the bispectrum in Chapter 5.

3.1 Large-scale structure as a probe of fundamental physics

Probing the structure of the Universe on large scales is one of the efforts that drives precision cosmology today [19–21, 26, 109]. Starting from tiny fluctuations in the early Universe, structures have formed over billions of years under gravitational collapse. This process depends strongly on the cosmological model, and thus the observed over- and under-densities contain a lot of information on fundamental physics. In particular, observations of the LSS of the Universe can shed light on the properties of the dark components of the Universe, deviations from general relativity on large scales, the initial conditions of the early Universe as well as yield a measurement of the absolute neutrino mass scale [19, 20].

One way to probe the structure of the Universe is by redshift surveys, where the angular position and redshift of astronomical objects such as galaxies and clusters of galaxies are measured. The first redshift surveys were initiated in the 1970's with a few thousand galaxies [110]; by the turn of the century a few hundred thousand redshifts could be measured by the 2-degree Field Galaxy Redshift Survey (2dFGRS) [111, 112]. The observations established the rich variety of structure on large scales, in accordance with expectations based on theory and computer simulations of gravitational collapse [113]. In the last decade, survey volumes allowing for precision cosmology was attained, starting with the 6dFGRS [114, 115] and the WiggleZ Dark Energy Survey [116, 117], followed by the BOSS [118], one of the four surveys of the SDSS-III [119] project, which measured the BAO scale at the percent level [85, 120, 121]. Within the last generation of the SDSS [122], the enhanced Baryon Oscillation Spectroscopic Survey (eBOSS) significantly increased the number of objects and redshifts at which BAO and redshift space distortions (RSD) was measured [123]. (We describe RSD shortly.) Building on this legacy, the ongoing Dark Energy Spectroscopic Instrument (DESI) [21, 124] and near-future surveys Euclid [19, 20], the Vera C. Rubin Observatory [22], the Prime Focus Spectrograph (PFS) [23], Spectro-Photometer for the History of the Universe, Epoch of Reionization and Ices Explorer

(SPHEREx) [24] and the Nancy Grace Roman Space Telescope [25] are expected to map out the structure of the Universe at unprecedented precision.

Complementary to galaxy surveys, photometric surveys such as the Kilo-Degree Survey (KiDS) [125, 126], Dark Energy Survey (DES) [127, 128] and the Hyper Suprime Cam (HSC) [129] are other leading probes of cosmology. They measure galaxy shear, i.e. the distortions of images of distant sources due to gravitational lensing by large structures between source and observer. Thus, they are sensitive to the dark matter structures of the Universe as well as relative distances between objects and hence the expansion history of the Universe [128]. Another probe of the LSS of the Universe is the Lyman α forest, a series of absorption lines in the light from distant quasars due to the Lyman α transition in natural hydrogen [130]. The position and depth of the absorption feature informs about the position (redshift) and amount of hydrogen, which traces the underlying dark matter distribution. By measurements of a few hundred thousands quasars, BOSS and eBOSS have observed the BAO feature in the Lyman α forest [131–133].

A natural question to ask is why one would devote such an amount of resources to probe the LSS when the measurements of the CMB has already constrained the parameters of the ΛCDM model to an excellent degree of precision [8, 134], with significant improvements expected from the next generation CMB Stage IV experiments. The answer is that the constraints are limited by the number of available modes $l_{\max} \sim 10^6$, and LSS can provide plenty additional independent modes by utilizing the three-dimensional distribution of galaxies in the Universe. If survey volumes increase, and the maximum wavenumber up to which data can be reliably analyzed is $k_{\max} \approx 0.3$, the number of LSS modes scales as $(k_{\max}/k_{\min})^3 \sim 10^8$, i.e. a few orders of magnitude more than the CMB. Moreover, LSS surveys can be done tomographically in the sense that the structure can be observed at several redshifts, while the CMB is seen at a fixed redshift. The LSS is also probed in the era of the Universe when vacuum energy dominates, and further sensitive to the properties of dark energy.

On the other hand, extracting information from the LSS is a challenging task due to the non-linear nature of gravitational collapse as well as the fact that one cannot observe directly the structure itself, but rather *tracers* of the underlying dark matter distribution. In the currently accepted picture of structure formation, small, initial inhomogeneities in the energy density grew over cosmic times due to gravitational collapse and became the rich structures of galaxies and clusters we see today [2, 26, 89]. The evolution is assumed to be dominated by a cold dark matter (CDM) component, and one assumes that the only relevant force on large distances is gravity. These assumptions will be discussed more in detail below. Combined with the assumption of an initial power spectrum $P \propto k^{n_s}$ with $n_s > -3$[1], they yield a *hierarchical* model of structure formation, where small scales collapse first and subsequently larger and larger scales collapse over time [26]. Therefore, a linear description of the fluctuations, warranted at early times when the inhomogeneities are small, is only applicable on larger and larger scales as time goes on. We can define a characteristic wavelength λ_{NL} with corresponding wavenumber k_{NL}, which defines the scale below which structure has become non-linear and objects have collapsed and become gravitationally bound. In our Universe we have $k_{\mathrm{NL}} \approx 0.3h$ Mpc^{-1} today, and a slightly

[1] As quoted in Chapter 2, the Planck CMB measurement yields $n_s = (0.965 \pm 0.004)$ at 68 % C.L.

larger value at typical redshifts at which the LSS is observed, e.g. $k_{\rm NL} \approx 0.4h$ Mpc^{-1} at $z = 0.5$. Hence on scales $k \ll k_{\rm NL}$, corresponding to distances $\lambda > \lambda_{\rm NL}$, linear theory can be reliably applied, while on highly non-linear scales $k > k_{\rm NL}$ the dynamics is exceedingly complicated to solve from first principles and one can only resort to computer simulations or empiric models. Our focus in this thesis will be the intermediate region, *mildly non-linear scales* $k \simeq 0.1$–$0.3h$ Mpc^{-1}, in which the fluctuations are small enough to be treated in a perturbative expansion.

Given the coverage of mildly non-linear scales of the abovementioned ongoing and upcoming galaxy surveys, there has been in the previous decades a vast interest in obtaining an accurate perturbation theory for the present day matter density fluctuations [26, 135–137]. On very large, linear scales, observations are limited by cosmic variance, while on small scales the theoretical modeling becomes unworkable due to non-linear collapse. Hence, it is of great interest to model the intermediate scales as accurate as possible, and preferably in an efficient manner for fast scans of parameter space (MCMC). As noted above, increasing the maximum $k_{\rm max}$ at which the theory can be trusted greatly increases the number of available modes. At the time of writing, the dark matter power spectrum has been computed up to three-loop corrections [138, 139] and the bispectrum up to two-loop [45, 140]. Nevertheless, additional ingredients are required for constraining the theory with galaxy clustering data. Firstly, galaxies are *biased tracers* of the underlying matter density field, i.e. their fluctuations do not faithfully follow the matter counterparts. The topic of biased tracers is vast and beyond the scope of this thesis; we refer the reader to the extensive review [137]. Secondly, galaxy surveys do not measure three comoving coordinates but rather two angles and a redshift for each galaxy. The conversion to distance needs to take into account Hubble flow as well as peculiar motions. The former can be accounted for by assuming a fiducial cosmology, while the latter requires a modeling of the peculiar velocities, known as redshift space distortions [26, 141–143]. RSD can be accounted for by a (non-trivial) change of coordinates, with the new coordinate system referred to as *redshift space*. In this thesis we do not consider RSD, and compute statistics in real space. Thirdly, to account for the effect on non-linear scales $k > k_{\rm NL}$ on mildly non-linear scales, an EFT approach (the EFTofLSS) has been successfully developed for structure formation [144, 145]. We describe the EFT framework in detail in Sec 3.6. In the opposite limit, very long wavelength modes correspond to large bulk flows, the effect of which on intermediate scales can be resummed to all orders [146–149]. This is known as IR resummation and will be discussed in Section 3.7. Including all these ingredients, as well as employing tools for fast evaluation of the theory [150–152], the BOSS *full shape* power spectrum has been successfully analyzed at one-loop order [27–29, 153–156] (see also [157]) as well as the bispectrum at tree- and one-loop level [158–161] (see also [162, 163]), yielding in particular constraints on H_0 and $\Omega_{\rm m}$ comparable with Planck CMB measurements [8, 27].

Hence, several elements enter a rigorous theory for LSS. In this chapter, we will describe the fundamental components in the Eulerian picture, focusing on those relevant for this thesis. After ending this section with an overview of the overall assumptions, we will in the next section derive the central equation describing structure formation: the *Vlasov-Poisson system*. Moreover, we map the system onto a fluid with Eulerian coordinates and discuss the linear solutions. In Section 3.3, we tackle the non-linear problem and introduce SPT. Subsequently, Section 3.4 is a good point to discuss the extension of SPT described in

Papers I and III. LSS is ultimately described statistically, and the perturbative solutions are related to statistical observables in Section 3.5. Finally, the effective theory for LSS and IR resummation are discussed in Section 3.6 and Section 3.7, respectively.

General assumptions

The following overall assumptions are standard for descriptions of LSS, and will also be used in this work:

- *We assume that dark matter is cold and collisionless on large scales, and comprises the dominant actor in structure formation.* Even though there is no direct detection of dark matter yet, there are vast amounts of indirect evidence [164]. For reviews on dark matter, see e.g. Refs. [57–60]. An important piece of this evidence is in fact the observed large-scale structure of the Universe, which depends on the amount and nature of dark matter. Warm or hot dark matter cannot cluster on small scales, and the measured substantial power on scales $k \sim 10h$ Mpc^{-1} yields a lower keV bound on dark matter [165–167]. A small fraction of dark matter could nevertheless have a significant velocity. Observations of merging clusters constrain self-interactions of dark matter [168]; a certain degree of such interactions could on the other hand explain various small-scale problems [169]. On very large scales however, we can assume that dark matter is collisionless. Finally, measurements of the CMB yield a dark matter fraction of the total matter that is approximately 85 % [8].
- *We will describe dark matter (and baryons) collectively as a fluid on large scales.* Assuming that the only agent responsible for structure formation on large scales is gravity, and that the Universe was almost homogeneous with tiny fluctuations at early times, matter flows coherently into gravitational wells. Hence, we can assume a *single-stream* flow with no crossing streams on very large scales, i.e. a pressureless fluid. The validity of this assumption will be discussed in detail below.
- *On subhorizon scales, general relativity can be described by Newtonian gravity.* Starting from general relativity, it can be shown that on scales much smaller than Hubble, $k \gg \mathcal{H}$, a Newtonian treatment is justified [89]. Nevertheless, relativistic corrections scale as $(\mathcal{H}/k)^2$ and if future surveys access volumes close to Hubble they need to be taken into account [74, 170, 171].

3.2 Vlasov-Poisson system

In this section, we derive the Vlasov-Poisson system in an expanding universe, which is the fundamental equation in the study of LSS. We map the system onto a fluid description, using Eulerian coordinates, and consider the solutions of the linearized equations. Similar discussions can be found in e.g. Refs. [26, 89, 135, 136].

Particle dynamics in the Newtonian limit

A natural starting point is to establish the motion of a particle in an expanding Universe. We consider small distances compared to the Hubble scale, $r \ll H$, where Newtonian

dynamics is applicable. Hence, the equation of motion for a particle at position $\mathbf{r}$ is

$$\frac{\mathrm{d}^2\mathbf{r}}{\mathrm{d}t^2} = -\nabla_{\mathbf{r}}\Phi(\mathbf{r},t)\,, \tag{3.1}$$

where Φ is the smooth gravitational potential sourced by the mass density $\rho(\mathbf{x},t)$ as given by the Poisson equation

$$\nabla^2_{\mathbf{r}}\Phi(\mathbf{r},t) = 4\pi G\rho(\mathbf{r},t)\,. \tag{3.2}$$

We work in comoving coordinates $\mathbf{x}$ defined by $\mathbf{r} = a\mathbf{x}$; in the following all gradients will be taken with respect to $\mathbf{x}$, i.e. $\nabla \equiv \nabla_{\mathbf{x}} = a\nabla_{\mathbf{r}}$. The physical velocity can be written in terms of comoving coordinates as

$$\frac{\mathrm{d}\mathbf{r}}{\mathrm{d}t} = \mathcal{H}\mathbf{x} + \mathbf{v}\,, \tag{3.3}$$

where the first term accounts for the background expansion and $\mathbf{v} = a\,\mathrm{d}\mathbf{x}/\mathrm{d}t = \mathrm{d}\mathbf{x}/\mathrm{d}\tau$ is the peculiar velocity, i.e. the deviation from the Hubble flow. We defined the latter in terms of conformal time, $\mathrm{d}\tau = a\,\mathrm{d}t$.

The Lagrangian describing a particle with mass m subject to the gravitational potential Φ is therefore [89, 172]

$$\mathcal{L} = \frac{1}{2}m\left(\mathcal{H}\mathbf{x} + \mathbf{v}\right)^2 - m\Phi(\mathbf{x},t)\,. \tag{3.4}$$

By introducing the generating function $\Lambda = ma\mathcal{H}x^2/2$, we can perform a canonical transformation $\mathcal{L} \to \mathcal{L} - \mathrm{d}\Lambda/\mathrm{d}t$ and obtain

$$\mathcal{L} = \frac{1}{2}m\mathbf{v}^2 - m\phi(\mathbf{x},t)\,, \tag{3.5}$$

where we defined the *peculiar* potential ϕ via

$$\Phi = -\frac{1}{2}\frac{\mathrm{d}\mathcal{H}}{\mathrm{d}\tau}x^2 + \phi\,. \tag{3.6}$$

Using Eq. (3.2) we obtain its field equation,

$$\nabla^2\phi = 4\pi G a^2\rho + 3\frac{\mathrm{d}\mathcal{H}}{\mathrm{d}\tau} = 4\pi G a^2(\rho - \bar{\rho})\,, \tag{3.7}$$

where we used the second Friedmann equation in the second equality. It is clear that the potential ϕ is only sourced by the energy density *fluctuations* of the Universe. From the Lagrangian (3.5), the canonical momentum $\mathbf{p}$ is given by

$$\mathbf{p} = \frac{\partial\mathcal{L}}{\partial\left(\mathrm{d}\mathbf{x}/\mathrm{d}t\right)} = a\frac{\partial\mathcal{L}}{\partial\mathbf{v}} = am\mathbf{v}\,. \tag{3.8}$$

Therefore, in comoving coordinates, the Newtonian equation of motion follows as

$$\frac{\mathrm{d}\mathbf{p}}{\mathrm{d}\tau} = -ma\nabla\phi\,. \tag{3.9}$$

This equation can equivalently be derived from the geodesic equation assuming small distances compared to the Hubble scale and small metric perturbations [89].

Vlasov equation

To describe N_p collisionless particles in an expanding universe, we introduce the distribution function $f(\mathbf{x}, \mathbf{p}, \tau)$, i.e. the probability of finding a particle in a phase space volume $\mathrm{d}^3\mathbf{x}\,\mathrm{d}^3\mathbf{p}$ at conformal time τ. In the microscopic picture we have

$$f(\mathbf{x}, \mathbf{p}, \tau) = \sum_{i=1}^{N_p} \delta_{\mathrm{D}}(\mathbf{x} - \mathbf{x}_i)\delta_{\mathrm{D}}(\mathbf{p} - \mathbf{p}_i) \ , \tag{3.10}$$

with each particle following the trajectory $\{\mathbf{x}_i, \mathbf{p}_i\}$. By the Liouville theorem the distribution function is conserved along system trajectories, $\mathrm{d}f/\mathrm{d}t = 0$, yielding the *Klimontovich equation* for the microscopic distribution function [135]. For cosmological structure formation, we consider the limit of large number of particles $N_p \to \infty$ (with the density kept constant) so that the microscopic description can be replaced by a continuum one. This corresponds to coarse-graining the distribution function, such that the individual information of each particle is lost. In this smoothed-out limit, the Klimontovich equation becomes the *Vlasov equation* [26]:

$$\frac{\mathrm{d}f}{\mathrm{d}\tau} = \frac{\partial f}{\partial \tau} + \frac{\mathrm{d}\mathbf{x}}{\mathrm{d}\tau} \cdot \nabla f + \frac{\mathrm{d}\mathbf{p}}{\mathrm{d}\tau}\frac{\partial f}{\partial \mathbf{p}} = \frac{\partial f}{\partial \tau} + \frac{\mathbf{p}}{ma} \cdot \nabla f - am\nabla\phi \frac{\partial f}{\partial \mathbf{p}} = 0 \, , \tag{3.11}$$

where we in the second equation used Eqs. (3.8) and (3.9). This equation is also referred to as the collisionless Boltzmann equation. It expresses conservation of particle number in phase space. Coupling this equation to the Poisson equation for the potential (3.7), we obtain the *Vlasov-Poisson system*, which is the fundamental system of equations for describing structure formation in the Universe.

The Vlasov-Poisson system is a seven-dimensional non-linear differential set of equations, and therefore notoriously difficult to solve. We will use perturbation theory in the Eulerian fluid picture to solve it, however it is informative to pause here and briefly mention other approaches: One can simulate the system on a computer by initializing particles on a grid and evolve them according to Eqs. (3.11) and (3.7). This is known as *N-body simulations*, and the state-of-the-art collisionless simulations involve about 10^{10} particles [173, 174] with boxes of typical size 100–1000 Mpc. On non-linear scales they are essentially the only tool available, since analytic approaches break down. Nevertheless, a major challenge is to accurately simulate complicated baryonic processes on very small scales [175] and even on scales $k \simeq 1$–$10h$ Mpc^{-1} different N-body codes produce power spectra with percent differences [176]. N-body simulations are very computationally expensive, and can therefore hardly be used in parameter scans such as MCMC analyses. In this thesis, we will use N-body simulations as benchmark results for the power- and bispectrum on mildly non-linear scales, to which we can compare our perturbative results.

Another approach that follows the microscopic system by considering the individual N_p particles is the recently introduced Kinetic Field Theory (KFT) [177–179]. Inspired by QFT, a path integral approach is used to keep track of phase space trajectories over time, and macroscopic quantities can be extracted from the corresponding generating functional. This task is formidable, and has only been performed in relatively simplified setups so far [180, 181].

Alternatively, one can use the *Schrödinger-Poisson* method. This framework is typically applied to "fuzzy" dark matter which has a macroscopic de Broglie wavelength of $\hbar/p \sim 1$ kpc [182]. If there are no other relevant interactions than gravity, fuzzy dark matter can be described as a condensate with the Schrödinger equation coupled to the Poisson equation for the gravitational potential. On the other hand, this system can be viewed as describing clustering of *cold* dark matter with a coarse-graining scale $\hbar/m$ in phase space [183]. By taking the limit $\hbar/m \to 0$, one expects to recover the solution of the Vlasov-Poisson system, however this limit is non-trivial and needs to be taken with care. We refer to Refs. [183–190] for more in-depth discussions on the Schrödinger-Poisson method.

Finally, complementary to the perturbative method in the Eulerian picture, one can solve the Vlasov-Poisson system in Lagrangian Perturbation Theory (LPT). Starting from an initial (Lagrangian) position $\mathbf{q}$, Lagrangian theory follows the particle trajectory to the final position $\mathbf{x}(\mathbf{q},\tau) = \mathbf{q} + \mathbf{\Psi}(\mathbf{q},\tau)$. The dynamical quantity $\mathbf{\Psi}$ can be expanded perturbatively, and solutions for macroscopic fluid quantities can be obtained order by order. See Refs. [26, 135, 136] for reviews on LPT, and Ref. [157] for a recent application to galaxy clustering data.

In this thesis, we will employ Eulerian perturbation theory to solve the Vlasov-Poisson system. In the Eulerian picture, instead of following individual trajectories, one describes the fluid quantities at each spatial (comoving) coordinate over time. The fluid quantities can be obtained by taking velocity moments of the distribution function, i.e. integrating over the distribution function and multiplying by products of velocity components. Written in terms of these moments, the Vlasov equation becomes an infinite hierarchy which needs to be truncated in an approximate way. The first moments correspond to the density ρ, velocity flow $\mathbf{v}$ and velocity dispersion σ_{ij} (also referred to as anisotropic stress), and are given by

$$\rho(\mathbf{x},\tau) = \frac{m}{a^3}\int \mathrm{d}^3p\, f(\mathbf{x},\mathbf{p},\tau)\,, \tag{3.12a}$$

$$v_i(\mathbf{x},\tau) = \frac{1}{\int \mathrm{d}^3p\, f(\mathbf{x},\mathbf{p},\tau)}\int \mathrm{d}^3p\, \frac{p_i}{am} f(\mathbf{x},\mathbf{p},\tau)\,, \tag{3.12b}$$

$$v_i(\mathbf{x},\tau)v_j(\mathbf{x},\tau) + \sigma_{ij}(\mathbf{x},\tau) = \frac{1}{\int \mathrm{d}^3p\, f(\mathbf{x},\mathbf{p},\tau)}\int \mathrm{d}^3p\, \frac{p_ip_j}{a^2m^2} f(\mathbf{x},\mathbf{p},\tau)\,. \tag{3.12c}$$

As we saw in the previous chapter, it is useful to decompose the density in a homogeneous and an inhomogeneous part:

$$\rho(\mathbf{x},\tau) = \bar{\rho}(\tau)\left(1+\delta(\mathbf{x},\tau)\right)\,, \tag{3.13}$$

where $\delta(\mathbf{x},\tau)$ is the density contrast and $\bar{\rho}(\tau)$ is the mean mass density, scaling like a^{-3} for non-relativistic species in the matter-dominated era. We recall that the potential ϕ was only sourced by fluctuations of the energy density (Eq. (3.7)), and we can write the Poisson equation again in terms of the density contrast,

$$\nabla^2\phi = \frac{3}{2}\mathcal{H}^2\Omega_\mathrm{m}\delta\,. \tag{3.14}$$

In the periods relevant for structure formation, i.e. deep in the matter era as well as during vacuum-energy domination, the radiation contribution to the Poisson equation and Hubble rate is completely negligible, hence we do not include it.

To obtain fluid equations for the density contrast, velocity flow and velocity dispersion we take moments of the Vlasov equation (3.11). We get the following zeroth-order moment by integrating over momentum, using integration by parts and that the potential is independent of momentum,

$$\frac{\partial \rho(\mathbf{x},\tau)}{\partial \tau} + 3\mathcal{H}\rho(\mathbf{x},\tau) + \nabla\cdot[\rho(\mathbf{x},\tau)\mathbf{v}(\mathbf{x},\tau)] = 0\,. \tag{3.15}$$

This equation is referred to as the *continuity equation*. Since the Vlasov equation expresses conservation of particle number in phase space, the continuity equation formulate the corresponding conservation in real space. The second term arises due to the overall a^{-3} dilution, and inserting the decomposition (3.13), we obtain the equation in terms of the density contrast,

$$\frac{\partial \delta}{\partial \tau} + \nabla\cdot[(1+\delta)\mathbf{v}] = 0\,. \tag{3.16}$$

The next moment of the Vlasov equation yields an equation of motion for the velocity flow $\mathbf{v}$. Using also the continuity equation, this can be reduced to

$$\frac{\partial \mathbf{v}}{\partial \tau} + \mathcal{H}\mathbf{v} + (\mathbf{v}\cdot\nabla)\mathbf{v} = -\nabla\phi - \frac{1}{\rho}\mathbf{e}_i\nabla_j\left[\rho\sigma^{ij}\right]\,, \tag{3.17}$$

where $\mathbf{e}$ is the unit vector, referred to as the *Euler equation*. This equation expresses conservation of momentum, and the right hand side terms are the gravitational force and a (anisotropic) pressure term, respectively. We see that the equation of motion for the n-th moment of the Vlasov equation couples to the $(n+1)$-moment, leading to a hierarchy of equations. To get a closed system of equations, we need a way of truncating the hierarchy.

Closing the Vlasov-Poisson hierarchy

In order to close the continuity and Euler system of equations (3.16) and (3.17), one can postulate an ansatz for the velocity dispersion. In standard fluid dynamics [191], the velocity dispersion can be split into isotropic and anisotropic parts

$$\sigma_{ij} = -p\delta^{(\mathrm{K})}_{ij} + \zeta\delta^{(\mathrm{K})}_{ij}\nabla\cdot\mathbf{v} + \eta\left(\nabla_i v_j + \nabla_j v_i - \frac{2}{3}\delta^{(\mathrm{K})}_{ij}\nabla\cdot\mathbf{v}\right)\,, \tag{3.18}$$

where p is the pressure and ζ and η are viscosity coefficients.

We are interested in clustering of CDM, which in the initial phase of gravitational collapse has a negligible velocity dispersion compared to the velocity flow, because of the almost homogeneous initial condition. The velocity dispersion denotes the deviation from single coherent flow, therefore it vanishes before shell-crossing, i.e. before multiple streams pulled by gravity cross each other. The assumption that $\sigma_{ij} = 0$ is known as the *single-stream* approximation, which is equivalent to

$$f(\mathbf{x},\mathbf{p},\tau) = \frac{a^3\rho(\mathbf{x},\tau)}{m}\delta_{\mathrm{D}}\left[\mathbf{p} - ma\mathbf{v}(\mathbf{x},\tau)\right]\,, \tag{3.19}$$

hence demanding that all particles at a given point move with the same velocity. The Euler equation (3.17) in the single-stream approximation describes a perfect, pressureless fluid, and therefore the clustering of matter can be modeled as such as long as the single-stream

approximation is valid. As time goes on, larger and larger scales collapse under gravity yielding multiple flows, the dynamics of which is hard to describe analytically and one mostly has to rely on N-body simulations. On sufficiently large scales however, the single-stream approximation can be used to analyze a large number of effects in LSS. We will initially employ this approximation when we set up the perturbative solution of the non-linear equations below. However, in Section 3.6, we will see that the single-stream approximation is not completely consistent on scales relevant for perturbative corrections in the mildly non-linear regime, leading to a breakdown of perturbation theory in the perfect, pressureless fluid picture. As described in detail in that section, the predictive power of the perturbative theory can be restored by including a non-zero anisotropic stress tensor, written down in an effective theory framework.

Vorticity

The gravitational term in the Euler equation (the only source term in the single-stream regime) can not source a curl mode in the velocity field, and it is therefore useful to follow the divergence and curl components of the velocity separately. From Helmholtz theorem we can uniquely (assuming that $\mathbf{v}$ vanishes at the boundary) decompose the velocity into a velocity divergence part θ and a divergenceless vorticity part, thus [192]

$$\theta(\mathbf{x},\tau) = \nabla\cdot\mathbf{v}(\mathbf{x},\tau)\,, \qquad \mathbf{w}(\mathbf{x},\tau) = \nabla\times\mathbf{v}(\mathbf{x},\tau)\,. \tag{3.20}$$

The equation for the vorticity is obtained by taking the curl of the Euler equation,

$$\frac{\partial\mathbf{w}(\mathbf{x},\tau)}{\partial\tau} + \mathcal{H}\mathbf{w}(\mathbf{x},\tau) - \nabla\times[\mathbf{v}(\mathbf{x},\tau)\times\mathbf{w}(\mathbf{x},\tau)] = \nabla\times\left[\frac{1}{\rho}\mathbf{e}_i\nabla_j\sigma^{ij}\right]\,. \tag{3.21}$$

In the single-stream regime, the RHS vanishes, and if the vorticity is zero initially it remains zero at all times. Moreover, in the linear theory only the first two terms above are present and any initial vorticity decays as $\mathbf{w}\propto a^{-1}$. Nevertheless, an initial vorticity can be amplified non-linearly by the third term in Eq. (3.21), and once the single-stream approximation breaks down vorticity can be created by multi-streams and shocks [193]. In this work we neglect the effect of vorticity. Based on mass and momentum conservation arguments, the vorticity-vorticity power spectrum sourced by contributions to the anisotropic stress tensor in the EFT (see Section 3.6 below) is suppressed by $k^4/k^4_{\rm NL}$ [194], and moreover N-body simulations reveal that it is suppressed by 3–4 orders of magnitude compared to the density power spectrum on mildly non-linear scales [193, 195, 196]. Hence, we expect this approximation to have negligible impact on the results.

Linear solutions

We proceed to discuss the solutions of the continuity and Euler equations (3.16) and (3.17) in the linear regime, where the fluctuation fields δ and θ and are small compared to the mean density and homogeneous Hubble flow, respectively. This regime is relevant on large scales or early times, where the Universe is smooth. In addition, understanding the linear solutions is central in constructing a perturbative description of the mildly non-linear regime.

In the single-stream approximation, the linearized equations read

$$\frac{\partial \delta(\mathbf{x},\tau)}{\partial \tau} + \theta(\mathbf{x},\tau) = 0\,, \tag{3.22a}$$

$$\frac{\partial \theta(\mathbf{x},\tau)}{\partial \tau} + \mathcal{H}(\tau)\theta(\mathbf{x},\tau) + \frac{3}{2}\Omega_{\mathrm{m}}(\tau)\mathcal{H}^2(\tau)\delta(\mathbf{x},\tau) = 0\,, \tag{3.22b}$$

where we used the Poisson equation (3.14) as well as the definition of the velocity divergence (3.20). The velocity divergence can be eliminated from the second equation by using the first equation, yielding a second order differential equation for the density contrast:

$$\frac{\partial^2 \delta(\mathbf{x},\tau)}{\partial \tau^2} + \mathcal{H}(\tau)\frac{\partial \delta(\mathbf{x},\tau)}{\partial \tau} - \frac{3}{2}\Omega_{\mathrm{m}}(\tau)\mathcal{H}^2(\tau)\delta(\mathbf{x},\tau) = 0\,. \tag{3.23}$$

We note that no operator acting on spatial coordinates appear in the above solution, implying that fluctuations will evolve independent of scale. This would not be the case in general for $\sigma^{ij} \neq 0$ and is a particular feature of the perfect pressureless fluid. Due to the scale-independence it is useful to factorize $\delta(\mathbf{x},\tau) = D(\tau)\delta_0(\mathbf{x})$ where D is named the *linear growth factor* and $\delta_0(\mathbf{x})$ is the initial density contrast. From Eq. (3.23) we obtain the differential equation for the linear growth factor

$$\frac{\mathrm{d}^2 D(\tau)}{\mathrm{d}\tau^2} + \mathcal{H}(\tau)\frac{\mathrm{d}D(\tau)}{\mathrm{d}\tau} - \frac{3}{2}\Omega_{\mathrm{m}}(\tau)\mathcal{H}^2(\tau)D(\tau) = 0\,. \tag{3.24}$$

The two independent solutions of this second order differential equation are denoted $D^+(\tau)$ and $D^-(\tau)$, where the former is the faster growing mode of the two. For general $\mathcal{H}$ there is a simple analytic solution for D^- [197]

$$D^-(\tau) = \frac{1}{a}\frac{\mathcal{H}}{\mathcal{H}_0}\,, \tag{3.25}$$

where $\mathcal{H}_0$ is the conformal Hubble rate today, and we normalized the solution such that at present time, $D^-(z=0) = 1$. This solution decays with time and is labeled the *decaying mode*. The other mode has no analytic solution in general, but can be expressed in an integral representation as [197]

$$D^+(\tau) = \frac{5}{2}\Omega_{\mathrm{m}}\mathcal{H}_0^2\frac{\mathcal{H}}{a}\int_0^a \frac{\mathrm{d}a'}{\mathcal{H}^3(a')}\,, \tag{3.26}$$

known as the *growing mode* since it increases with time.

In total, the linearized solution is given by a linear combination of the growing and decaying modes,

$$\delta_0 = D^+(\tau)\delta_0^+(\mathbf{x}) + D^-(\tau)\delta_0^-(\mathbf{x})\,, \tag{3.27}$$

where $\delta_0^\pm(\mathbf{x})$ are the initial field configurations. Using Eq. (3.22a), we can obtain the corresponding linear solution for the velocity divergence,

$$\theta = -\mathcal{H}(\tau)\left[f(\tau)D^+(\tau)\delta_0^+(\mathbf{x}) + g(\tau)D^-(\tau)\delta_0^-(\mathbf{x})\right]\,, \tag{3.28}$$

with the *growth rates* defined as

$$f(\tau) \equiv \frac{\mathrm{d}\ln D^+}{\mathrm{d}\ln a} = \frac{1}{\mathcal{H}(\tau)}\frac{\mathrm{d}\ln D^+}{\mathrm{d}\tau} \qquad \text{and} \qquad g(\tau) \equiv \frac{\mathrm{d}\ln D^-}{\mathrm{d}\ln a}\,. \tag{3.29}$$

We can immediately obtain the growth rate $g(\tau)$ from the simple decaying mode solution (3.25),

$$g(\tau) = \frac{1}{\mathcal{H}^2}\frac{\mathrm{d}\mathcal{H}}{\tau} - 1 = \Omega_\Lambda - \frac{\Omega_\mathrm{m}}{2} - 1\,, \tag{3.30}$$

where in the second equality we used the second Friedmann equation (2.13b).

In general, the growth factors $D^\pm(\tau)$ and corresponding growth rates $f(\tau)$ and $g(\tau)$ depend on the background cosmology, in particular the matter density Ω_m and the vacuum energy density Ω_Λ via the Hubble rate. One can obtain closed-form expressions for these solutions in certain cosmologies; an overview can be found in e.g. Ref. [26]. Here we mention one important case: the linear growth solutions in an EdS Universe.

The Einstein–de-Sitter Universe contains only matter ($\Omega_\mathrm{m} = 1$, $\Omega_\Lambda = 0$) and no curvature ($\Omega_K = 0$). This model is a very good approximation of our Universe sufficiently after matter-radiation equality as well as before vacuum energy domination, and is therefore particularly interesting. The Friedmann Eqs. (2.13) yields $a \propto \tau^2$ and $\mathcal{H} = 2/\tau$ for EdS. The general solutions (3.27) and (3.28) as well as Eq. (3.29) reduce to

$$D^+(\tau) = a\,, \qquad D^-(\tau) = a^{-3/2}\,, \qquad f(\tau) = 1\,, \qquad g(\tau) = -\frac{3}{2}\,. \tag{3.31}$$

Thus, deep in the matter dominated era, where the EdS approximation is applicable, the density contrast (3.27) growths with the scale factor a and the growth rates are constant. Hence, a sets the typical time-scale for growth of structure on large scales. Moreover, inserting the growing mode solution into the Poisson equation (3.14) reveals that the gravitational potential in the linear regime is constant during matter domination. In a model with dark energy, the Hubble rate deviates from the EdS case at late times when the dark component gives a sizable contribution to the cosmic energy budget, $z \lesssim 5$ in our universe. The relatively larger Hubble rate leads to a suppression of the growth of fluctuations (cf. Eq. (3.26)), i.e. a slower growth than $D^+ \propto a$ and hence $f(\tau) < 1$. In particular, in a ΛCDM Universe, the growth factor D^+ is reduced by 20 % and $f \approx 0.5$ today. This can be appreciated from Fig. 3.1, where we show the growth functions as a function of redshift in an EdS and ΛCDM cosmology. At $z = 10$, when the ΛCDM universe is matter dominated, the growth functions agree (we normalized the growth factors D in EdS and ΛCDM such that they agree deep in the matter era), but approaching today the vacuum energy in the ΛCDM universe becomes significant, suppressing the growth.

3.3 Perturbation theory in the mildly non-linear regime

We go on to the full non-linear equations of motion. In this section, we discuss their perturbative solutions when expanding in the fluctuation fields. We work in the single-stream approximation and neglect vorticity. The single-stream approximation will be relaxed

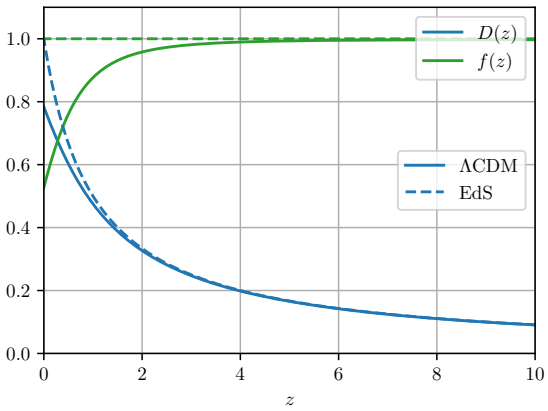

Figure 3.1: Growth functions in a ΛCDM and EdS Universe. We show the growth factor D (blue) and growth rate f (green) as a function of redshift in ΛCDM (solid lines) and EdS (dashed lines). The ΛCDM growth factor is normalized such that it agrees with the EdS one deep in the matter dominated era $z \gg 1$. The matter content is set to $\Omega_\mathrm{m} = 0.3175$ in the ΛCDM model.

when discussing EFT corrections in Section 3.6. Under these assumptions and using the Poisson equation (3.14), the non-linear continuity and Euler equations read

$$\frac{\partial \delta(\mathbf{x},\tau)}{\partial \tau} + \theta(\mathbf{x},\tau) = -\nabla\cdot\left[\delta(\mathbf{x},\tau)\mathbf{v}(\mathbf{x},\tau)\right] , \tag{3.32a}$$

$$\frac{\partial \theta(\mathbf{x},\tau)}{\partial \tau} + \mathcal{H}(\tau)\theta(\mathbf{x},\tau) + \frac{3}{2}\Omega_\mathrm{m}(\tau)\mathcal{H}^2(\tau)\delta(\mathbf{x},\tau) = -\nabla\cdot\left\{\left[\mathbf{v}(\mathbf{x},\tau)\cdot\nabla\right]\mathbf{v}(\mathbf{x},\tau)\right\} . \tag{3.32b}$$

It is convenient to go to Fourier space to study these equations. The reason is that in Fourier space, linear modes evolve independently and the statistical properties of each mode is conserved. While this is valid in the linear regime on very large scales, on smaller scales different wavenumber modes are coupled via the non-linear terms. The LHS of the above set of equations can immediately be written down in Fourier space; for the RHS we use that for vanishing vorticity, the Fourier transforms of the velocity and its divergence are related by $\tilde{\mathbf{v}}(\mathbf{k}) = -\mathrm{i}\mathbf{k}\,\tilde{\theta}(\mathbf{k})/k^2$ to obtain

$$\nabla\cdot\left[\delta(\mathbf{x},\tau)\mathbf{v}(\mathbf{x},\tau)\right] = \int_{\mathbf{k}_1,\mathbf{k}_2} \mathrm{e}^{\mathrm{i}\mathbf{x}\cdot(\mathbf{k}_1+\mathbf{k}_2)}\tilde{\delta}(\mathbf{k}_1,\tau)\tilde{\theta}(\mathbf{k}_2,\tau)\frac{(\mathbf{k}_1+\mathbf{k}_2)\cdot\mathbf{k}_2}{k_2^2} ,$$

$$\nabla\cdot\left\{\left[\mathbf{v}(\mathbf{x},\tau)\cdot\nabla\right]\mathbf{v}(\mathbf{x},\tau)\right\} = \int_{\mathbf{k}_1,\mathbf{k}_2} \mathrm{e}^{\mathrm{i}\mathbf{x}\cdot(\mathbf{k}_1+\mathbf{k}_2)}\tilde{\theta}(\mathbf{k}_1,\tau)\tilde{\theta}(\mathbf{k}_2,\tau)\frac{\mathbf{k}_1\cdot\mathbf{k}_2(\mathbf{k}_1+\mathbf{k}_2)^2}{2k_1^2k_2^2} .$$

where we use the notation $\int_\mathbf{k} \equiv \int \mathrm{d}^3\mathbf{k}$. The last factors in the integrals above are conventionally compiled in two *mode coupling functions*,

$$\alpha(\mathbf{k}_1,\mathbf{k}_2) = \frac{(\mathbf{k}_1+\mathbf{k}_2)\cdot\mathbf{k}_2}{k_2^2} \qquad \text{and} \qquad \beta(\mathbf{k}_1,\mathbf{k}_2) = \frac{\mathbf{k}_1\cdot\mathbf{k}_2(\mathbf{k}_1+\mathbf{k}_2)^2}{2k_1^2k_2^2} , \tag{3.33}$$

which specify the coupling of different modes with wavenumbers $\mathbf{k}_1$ and $\mathbf{k}_2$. Note that β is symmetric in its arguments while α is not, because α couples different fields. Thus, the equations of motion in Fourier space become

$$\frac{\partial\tilde{\delta}(\mathbf{k},\tau)}{\partial\tau} + \tilde{\theta}(\mathbf{k},\tau) = -\int_{\mathbf{k}_1,\mathbf{k}_2} \delta_{\mathrm{D}}(\mathbf{k}-\mathbf{k}_{12})\alpha(\mathbf{k}_1,\mathbf{k}_2)\tilde{\delta}(\mathbf{k}_1,\tau)\tilde{\theta}(\mathbf{k}_2,\tau)\,, \tag{3.34a}$$

$$\frac{\partial\tilde{\theta}(\mathbf{k},\tau)}{\partial\tau} + \mathcal{H}(\tau)\tilde{\theta}(\mathbf{k},\tau) + \frac{3}{2}\Omega_{\mathrm{m}}(\tau)\mathcal{H}^2(\tau)\tilde{\delta}(\mathbf{k},\tau) = -\int_{\mathbf{k}_1,\mathbf{k}_2} \delta_{\mathrm{D}}(\mathbf{k}-\mathbf{k}_{12})\beta(\mathbf{k}_1,\mathbf{k}_2)\tilde{\theta}(\mathbf{k}_1,\tau)\tilde{\theta}(\mathbf{k}_2,\tau)\,, \tag{3.34b}$$

where we introduced the notation $\mathbf{k}_{12} \equiv \mathbf{k}_1+\mathbf{k}_2$. The Dirac delta function ensures momentum conservation required by translation invariance in a spatially homogeneous universe, i.e. the evolution of the $\tilde{\delta}$ and $\tilde{\theta}$ fluctuations are determined by the coupling of all pairs of wavenumbers $\mathbf{k}_1$ and $\mathbf{k}_2$ whose sum is $\mathbf{k}$. Importantly, one recovers the linear theory (3.22) from Eq. (3.34) by taking the large scale limit $\mathbf{k} \to 0$ because the mode-coupling functions α and β vanishes in the limit where the sum of their arguments go to zero. There are in general no closed-form solution of these equations, and one has to employ perturbative techniques, simulate the system on a computer or make certain assumptions to make progress.

As we will mostly work in Fourier space, we drop the tilde notation to denote fields in Fourier space from now on, and make it clear from the context whenever we consider the fields in real space.

Before we pursue a perturbative solution of the non-linear Vlasov-Poisson system (3.34), we introduce a compact notation which treats the fields in a symmetric manner and will be crucial when we extend the formalism to cosmologies with non-trivial scale-dependence in Section 3.4. Since the typical time scale for structure formation is set by the growth factor $D^+(\tau)$ (growing mode), we may choose a time variable defined by the relative change in it, i.e. use $\eta(\tau) \equiv \ln D^+(\tau)$. From Eq. (3.29) we can immediately relate $\partial/\partial\tau = \mathcal{H}f\partial/\partial\eta$. Furthermore, in the linear regime we have $\theta = -\mathcal{H}f\delta$ (growing mode, cf. (3.28)), so it is convenient to collect the fields into a tuple [198]

$$\psi_a(\mathbf{k},\eta) \equiv \left(\delta(\mathbf{k},\eta),\, -\frac{\theta(\mathbf{k},\eta)}{\mathcal{H}f}\right)\,. \tag{3.35}$$

In order to write down the equations of motion in the new set of variables, we use that the growth factor per definition satisfies the linear equation (3.24), here repeated in terms of $\ln a$ for convenience:

$$\left[\frac{\mathrm{d}^2}{\mathrm{d}(\ln a)^2} + \left(1 + \frac{\mathrm{d}\ln\mathcal{H}}{\mathrm{d}\ln a}\right)\frac{\mathrm{d}}{\mathrm{d}\ln a} - \frac{3}{2}\Omega_{\mathrm{m}}\right] D^+(a) = 0\,.$$

Furthermore, $\partial_\eta\mathcal{H} = f\partial_{\ln a}\mathcal{H} = f\mathcal{H}(1 - 3\Omega_{\mathrm{m}}/2 - 2\Omega_{\mathrm{r}})$ (using Eq. (2.13b) and including in principle a non-zero radiation content for completeness), from which one can obtain

$$\frac{\partial\theta}{\partial\tau} = \mathcal{H}^2 f^2\left[-\frac{\partial}{\partial\eta} + \frac{1}{f} - \frac{3}{2}\frac{\Omega_{\mathrm{m}}}{f^2} + 1\right]\psi_2\,.$$

All together, the equations of motion become

$$\frac{\partial}{\partial\eta}\psi_a(\mathbf{k},\eta)+\Omega_{ab}(\eta)\psi_b(\mathbf{k},\eta)=\int_{\mathbf{k}_1,\mathbf{k}_2}\delta_{\mathrm{D}}(\mathbf{k}-\mathbf{k}_{12})\gamma_{abc}(\mathbf{k},\mathbf{k}_1,\mathbf{k}_2)\psi_b(\mathbf{k}_1,\eta)\psi_c(\mathbf{k}_2,\eta)\,, \tag{3.36}$$

where it is understood that repeated indices are summed over and the linear evolution is encoded in

$$\Omega_{ab}(\eta)=\begin{pmatrix}0 & -1\\ -\frac{3}{2}\frac{\Omega_{\mathrm{m}}}{f^2} & \frac{3}{2}\frac{\Omega_{\mathrm{m}}}{f^2}-1\end{pmatrix}. \tag{3.37}$$

The only non-zero elements of γ_{abc} are

$$\gamma_{121}(\mathbf{k},\mathbf{k}_1,\mathbf{k}_2)=\alpha(\mathbf{k}_1,\mathbf{k}_2)\qquad\text{and}\qquad\gamma_{222}(\mathbf{k},\mathbf{k}_1,\mathbf{k}_2)=\beta(\mathbf{k}_1,\mathbf{k}_2)\,. \tag{3.38}$$

In this notation, the linear growing and decaying modes of the equations of motion are

$$u_a^{(+)}=\mathrm{e}^{\eta}\begin{pmatrix}1\\1\end{pmatrix}\qquad\text{and}\qquad u_a^{(-)}=\mathrm{e}^{-\frac{3}{2}\frac{\Omega_{\mathrm{m}}}{f^2}\eta}\begin{pmatrix}1\\-\frac{3}{2}\frac{\Omega_{\mathrm{m}}}{f^2}\end{pmatrix}. \tag{3.39}$$

This result is completely equivalent to the linear solutions (3.27) and (3.28), and the simple form of the growing eigenmode simply reflects the suitable rescaling of the velocity divergence in the new dynamical variables. Remarkably, the growing mode is independent of the in general time-dependent ratio Ω_{m}/f^2. This fact will be important when we discuss the EdS approximation below. Note also that if we specialize to an EdS universe, $\mathrm{e}^{\eta}=a$ and $\Omega_{\mathrm{m}}/f^2=1$ so that we recover Eq. (3.31).

We proceed in the following to solve Eq. (3.36) in perturbation theory. In SPT [26, 89, 136, 198–207], one assumes that the density and velocity fields can be expanded about the linear solutions, which amounts to the assumption that the variance of linear fluctuations can be treated as a small expansion parameter (we return to this assumption and discuss it in Section 3.6). We can write

$$\psi_a(\mathbf{k},\eta)=\sum_{n=1}^{\infty}\psi_a^{(n)}(\mathbf{k},\eta)\,, \tag{3.40}$$

where $\psi_a^{(1)}$, $\psi_a^{(2)}$, … are linear, quadratic, etc. in the growing mode linear solution and therefore also in the initial fields, since the growing mode is a simple (time-dependent) scaling of the initial condition.

Perturbative solution in an Einstein–de-Sitter cosmology

As the perturbative approach simplifies quite a bit in an EdS universe, we study this case as a first example. The growth factor equals the scale factor, as derived in Eq. (3.31), so that $\mathrm{e}^{\eta}=a$ and furthermore the growth rate is $f=1$, hence the evolution matrix reduces to

$$\Omega_{ab}|_{\mathrm{EdS}}=\begin{pmatrix}0 & -1\\ -\frac{3}{2} & \frac{1}{2}\end{pmatrix}. \tag{3.41}$$

We assume initial conditions in the infinite past $\eta_{\rm ini} \to -\infty$, so that the decaying modes have had time to die out and the system completely resides in the growing mode. In other words, we assume that the time-dependence can be factorized out thus[2]

$$\psi_a(\mathbf{k}, a) = \sum_{n=1}^{\infty} a^n \zeta_a^{(n)}(\mathbf{k}) \equiv \sum_{n=1}^{\infty} a^n \begin{pmatrix} \delta^{(n)}(\mathbf{k}) \\ -\theta^{(n)}(\mathbf{k})/\mathcal{H} \end{pmatrix} . \tag{3.42}$$

This is a perturbative expansion in the linear growing mode solution proportional to a with time-independent coefficients $\zeta_a^{(n)}(\mathbf{k})$ or equivalently $\delta^{(n)}(\mathbf{k})$ and $\theta^{(n)}(\mathbf{k})$ on the fluid level (recall the definition of ψ in Eq. (3.35) with $f = 1$ in EdS). The solution is therefore separable in time and momentum, which will allow us to obtain analytic expressions for the coefficients $\zeta_a^{(n)}(\mathbf{k})$. Inserting the expansion (3.42) into the equation of motion (3.36) yields

$$\left(n\delta_{ab}^{(\mathrm{K})} + \Omega_{ab}\big|_{\mathrm{EdS}}\right) \zeta_b^{(n)}(\mathbf{k}) = \sum_{m=1}^{n-1} \int_{\mathbf{k}_1,\mathbf{k}_2} \delta_{\mathrm{D}}(\mathbf{k} - \mathbf{k}_{12}) \gamma_{abc}(\mathbf{k}, \mathbf{k}_1, \mathbf{k}_2) \zeta_b^{(m)}(\mathbf{k}_1) \zeta_c^{(n-m)}(\mathbf{k}_2) \,, \tag{3.43}$$

at n-th order in perturbation theory. At first order the solution is simply the initial condition, $\zeta_a^{(1)}(\mathbf{k}) = \delta^{(1)}(\mathbf{k}, \eta_{\rm ini}) = -\theta^{(1)}(\mathbf{k}, \eta_{\rm ini})/\mathcal{H}$, and repeated application of (3.43) yields $\zeta_a^{(n)} = \mathcal{O}([\delta^{(1)}]^n)$, consistent with the overall perturbative ansatz (3.40). We can therefore write $\zeta_a^{(n)}$ as convolutions of linear density fields

$$\zeta_a^{(n)}(\mathbf{k}) = \int_{\mathbf{q}_1,\ldots,\mathbf{q}_n} \delta_{\mathrm{D}}(\mathbf{k} - \mathbf{q}_{1\cdots n})\, F_a^{(n)}(\mathbf{q}_1, \ldots, \mathbf{q}_n) \prod_{i=1}^{n} \delta_0(\mathbf{q}_i) \,, \tag{3.44}$$

where the perturbative expansion is furnished by the *kernels* $F_a^{(n)}$ that are dimensionless, scalar functions of the set of wavevectors $\mathbf{q}_1, \ldots, \mathbf{q}_n$. A diagrammatic representation of this series expansion is shown in Fig. 3.2. In Eq. (3.44), $\delta_0(\mathbf{q}_i)$ is the initial linear density field for the mode $\mathbf{q}_i$ and the Dirac delta function enforces momentum conservation for the coupling of different modes, i.e. demanding $\mathbf{k} = \mathbf{q}_{1\cdots n} \equiv \sum_{i=1}^{n} \mathbf{q}_i$. Note that we use a slightly different notation for the kernels than what is typically found in the literature, anticipating their generalization in Section 3.4, in particular the usual F_n and G_n kernels correspond in our notation to $F_n = F_1^{(n)}$ and $G_n = F_2^{(n)}$. Furthermore, without loss of generality, we use *symmetrized* kernels, in other words we will demand that they are symmetric under exchange of the momentum arguments, i.e. under permutations of the set $\{\mathbf{q}_1, \ldots, \mathbf{q}_n\}$. This property is useful for example when manipulating momentum integrals over combinations of the kernels.

At $n = 1$, we recover the linear solution by $F_a^{(1)} = 1$. We obtain solutions for the higher order kernels $n > 2$ by inserting the expansion (3.44) in Eq. (3.43):

$$\left(n\delta_{ab}^{(\mathrm{K})} + \Omega_{ab}\big|_{\mathrm{EdS}}\right) F_b^{(n)}(\mathbf{q}_1, \ldots, \mathbf{q}_n) = \sum_{m=1}^{n-1} \Big[\gamma_{abc}(\mathbf{k}, \mathbf{q}_{1\cdots m}, \mathbf{q}_{m+1\cdots n}) F_b^{(m)}(\mathbf{q}_1, \ldots, \mathbf{q}_m) F_c^{(n-m)}(\mathbf{q}_{m+1}, \ldots, \mathbf{q}_n)\Big]_{\mathrm{sym}} \,, \tag{3.45}$$

[2]The subscript index a is unrelated to the scale factor.

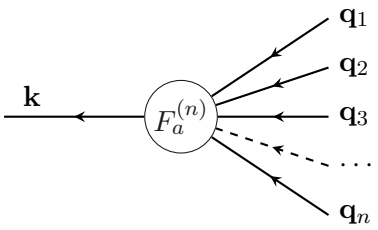

Figure 3.2: Diagrammatic representation of the expansion in Eq. (3.44). The lines on the right side represent initial fluctuation fields with momentum $\mathbf{q}_j$ and the line left of the kernel F_n represent an n-th order field with momentum $\mathbf{k} = \mathbf{q}_{1\cdots n}$.

where the RHS is understood to be symmetrized with respect to permutations exchanging momenta in the $\{\mathbf{q}_1, \ldots, \mathbf{q}_m\}$ set with momenta in the $\{\mathbf{q}_{m+1}, \ldots, \mathbf{q}_n\}$ set, i.e. summing over all permuted expressions and dividing by the total number of permutations $N_m = \frac{n!}{m!(n-m)!}$. This way, the n-th order kernel will be symmetric under exchange of momentum arguments provided that all lower order kernels are.

Defining

$$\Upsilon(n) = \left(n\delta_{ab}^{(\mathrm{K})} + \Omega_{ab}\big|_{\mathrm{EdS}}\right)^{-1} = \frac{1}{(2n+3)(n-1)} \begin{pmatrix} 2n+1 & 2 \\ 3 & 2n \end{pmatrix}, \tag{3.46}$$

the solution of Eq. (3.45) is given by the recursive relation

$$F_a^{(n)}(\mathbf{k}) = \Upsilon_{ab}(n) \sum_{m=1}^{n-1} \gamma_{bcd}(\mathbf{k}, \mathbf{q}_{1\cdots m}, \mathbf{q}_{m+1\cdots n}) F_c^{(m)}(\mathbf{q}_1, \ldots, \mathbf{q}_m) F_d^{(n-m)}(\mathbf{q}_{m+1}, \ldots, \mathbf{q}_n) \tag{3.47}$$

or more explicitly in terms of the mode-coupling functions α and β (see also derivations in e.g. Refs. [203, 204])

$$F_1^{(n)}(\mathbf{q}_1, \ldots, \mathbf{q}_n) = \sum_{m=1}^{n-1} \frac{F_2^{(m)}(\mathbf{q}_1, \ldots, \mathbf{q}_m)}{(2n+3)(n-1)} \Big[(2n+1)\alpha(\mathbf{q}_{1\cdots m}, \mathbf{q}_{m+1\cdots n}) F_1^{(n-m)}(\mathbf{q}_{m+1}, \ldots, \mathbf{q}_n)$$
$$+ 2\beta(\mathbf{q}_{1\cdots m}, \mathbf{q}_{m+1\cdots n}) F_2^{(n-m)}(\mathbf{q}_{m+1}, \ldots, \mathbf{q}_n) \Big], \tag{3.48a}$$

$$F_2^{(n)}(\mathbf{q}_1, \ldots, \mathbf{q}_n) = \sum_{m=1}^{n-1} \frac{F_2^{(m)}(\mathbf{q}_1, \ldots, \mathbf{q}_m)}{(2n+3)(n-1)} \Big[3\alpha(\mathbf{q}_{1\cdots m}, \mathbf{q}_{m+1\cdots n}) F_1^{(n-m)}(\mathbf{q}_{m+1}, \ldots, \mathbf{q}_n)$$
$$+ 2n\beta(\mathbf{q}_{1\cdots m}, \mathbf{q}_{m+1\cdots n}) F_2^{(n-m)}(\mathbf{q}_{m+1}, \ldots, \mathbf{q}_n) \Big]. \tag{3.48b}$$

Starting from $n = 1$, with $F_a^{(1)} = 1$, one can use these recursive relations to obtain higher order kernels; explicit expressions for kernels up to $n = 4$ are given in Ref. [202]. At second

order, the kernels are given by the simple form

$$F_1^{(2)}(\mathbf{q}_1, \mathbf{q}_2) = \frac{5}{7} + \frac{1}{2}\mu\left(\frac{q_2}{q_1} + \frac{q_1}{q_2}\right) + \frac{2}{7}\mu^2\,, \tag{3.49a}$$

$$F_2^{(2)}(\mathbf{q}_1, \mathbf{q}_2) = \frac{3}{7} + \frac{1}{2}\mu\left(\frac{q_2}{q_1} + \frac{q_1}{q_2}\right) + \frac{4}{7}\mu^2\,, \tag{3.49b}$$

where $q_i = |\mathbf{q}_i|$ and μ is the cosine of the angle between $\mathbf{q}_1$ and $\mathbf{q}_2$, i.e. $\mathbf{q}_1 \cdot \mathbf{q}_2 = \mu q_1 q_2$.

The kernels $F_a^{(n)}$ satisfy certain properties that follow from underlying symmetries of the system [26, 194, 202, 208, 209]:

- Due to momentum conservation, as $\mathbf{k} = \sum_{i=1}^n \mathbf{q}_i$ goes to zero, but the individual $\mathbf{q}_i$ does not, the kernels scale like $F^{(n)} \propto k^2$.
- As one argument $\mathbf{p}$ becomes large while the argument sum $\mathbf{k}$ stays fixed, the kernel vanishes like the second power of the large argument, i.e. for $p \gg q_i$

$$F^{(n)}(\mathbf{q}_1, \ldots, \mathbf{q}_{n-2}, \mathbf{p}, -\mathbf{p}) \propto 1/p^2\,. \tag{3.50}$$

- In the limit where a subset $\{q_1, \ldots, q_m\}$ of the arguments is much smaller than the remaining arguments $\{q_{m+1}, \ldots, q_n\}$, the kernels can be factorized as

$$F^{(n)}(\mathbf{q}_1, \ldots, \mathbf{q}_n) \to \frac{m!}{n!} F^{(m)}(\mathbf{q}_1, \ldots, \mathbf{q}_m) \frac{\mathbf{k}\cdot\mathbf{q}_{m+1}}{q_{m+1}^2} \cdots \frac{\mathbf{k}\cdot\mathbf{q}_n}{q_n^2}\,, \tag{3.51}$$

  where again $\mathbf{k} = \sum_{i=1}^n \mathbf{q}_i$. This result follows from Galilean invariance. In the special case where one argument q_i becomes soft, there is an infrared divergence $\mathbf{q}_i/q_i^2$. On the other hand, there is no infrared divergence if partial sums of momenta go to zero.

These properties hold also for the generalized kernels we define below in Section 3.4, as long as momentum conservation and Galilean invariance are satisfied by the underlying dynamics.

In total, the perturbative solution for the density contrast and velocity divergence in the EdS universe is

$$\psi_a(\mathbf{k}, a) = \begin{pmatrix} \delta(\mathbf{k}, a) \\ -\theta(\mathbf{k}, a)/\mathcal{H} \end{pmatrix} = \sum_{n=1}^{\infty} a^n \int_{\mathbf{q}_1,\ldots,\mathbf{q}_n} \delta_{\mathrm{D}}(\mathbf{k} - \mathbf{q}_{1\cdots n})\, F_a^{(n)}(\mathbf{q}_1, \ldots, \mathbf{q}_n) \prod_{i=1}^n \delta_0(\mathbf{q}_i)\,, \tag{3.52}$$

where the kernels are given by the recursive relation (3.48). From here on we refer to the kernels in the EdS model as *EdS-SPT* kernels, since we will generalize the perturbative expansion and derive kernels for cosmologies beyond EdS in Section 3.4 below.

Einstein–de-Sitter-approximation

Specializing to an EdS universe and neglecting the decaying mode allowed us in the previous paragraphs to obtain analytic solutions for the fluctuation fields where the time- and space-dependence separated completely. This is not the case for a general cosmology. Even though our Universe today does not resemble an EdS one, it turns out that the EdS-SPT kernels

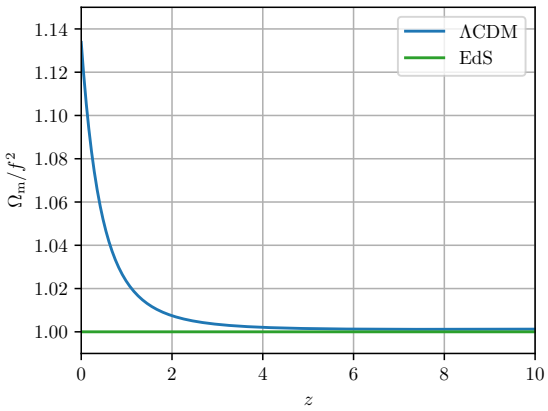

Figure 3.3: Ratio Ω_m/f^2 as a function of redshift in ΛCDM and EdS. The matter content is set to $\Omega_\mathrm{m} = 0.3175$ in the ΛCDM model.

can be applied to good approximation nevertheless. This is the *EdS-approximation*, and the logic proceeds as follows: Consider a cosmology in which the dynamics have non-trivial time-dependence, such as ΛCDM, meaning that the evolution matrix $\Omega_{ab}(\eta)$ is not constant in time as in the EdS case. Assume that the decaying modes have vanished and write down the fluctuation field as an expansion in the linear growing mode solution:

$$\psi_a(\mathbf{k},\eta) = \sum_{n=1}^{\infty} \mathrm{e}^{n\eta}\psi_a^{(n)}(\mathbf{k})\,, \tag{3.53}$$

with $\eta = \ln D^+$. If the evolution matrix (Eq. (3.37)) can be approximated by the EdS one,

$$\Omega_{ab}(\eta) = \begin{pmatrix} 0 & -1 \\ -\frac{3}{2}\frac{\Omega_\mathrm{m}}{f^2} & \frac{3}{2}\frac{\Omega_\mathrm{m}}{f^2} - 1 \end{pmatrix} \xrightarrow[\text{EdS}]{} \begin{pmatrix} 0 & -1 \\ -\frac{3}{2} & \frac{1}{2} \end{pmatrix}\,, \tag{3.54}$$

the momentum structure of the solution (3.53) is given by the EdS-SPT solution, i.e. $\psi_a^{(n)}(\mathbf{k}) = \zeta_a^{(n)}(\mathbf{k})$. There are two reasons why one expects this replacement to be a good approximation. Firstly, in a model with both matter and vacuum energy (no curvature), the growth rate can to good approximation be given by $f(\Omega_\mathrm{m}, 1-\Omega_\mathrm{m}) \approx \Omega_\mathrm{m}^{5/9}$ [26], therefore the ratio $\Omega_\mathrm{m}/f^2 \approx \Omega_\mathrm{m}^{-1/9}$ is very insensitive to the matter content. In Fig. 3.3 we show this ratio for a model with $\Omega_\mathrm{m} \simeq 0.32$. The ratio deviates less than 1 % from unity all the way down to $z \simeq 1.5$, and differs by $\mathcal{O}(10\,\%)$ today. Secondly, the linear growing mode solution (3.39) in the general time-dependent case is independent of Ω_m/f^2, and therefore equal in the EdS-approximation and the exact time-dependent case.

In summary, in the EdS-approximation the evolution matrix is approximated by the EdS one, so that the solution to the equations of motion (3.36) is

$$\psi_a(\mathbf{k},\eta) = \sum_{n=1}^{\infty} \mathrm{e}^{n\eta} \int_{\mathbf{q}_1,\ldots,\mathbf{q}_n} \delta_\mathrm{D}(\mathbf{k}-\mathbf{q}_{1\cdots n})\, F_a^{(n)}(\mathbf{q}_1,\ldots,\mathbf{q}_n) \prod_{i=1}^{n} \delta_0(\mathbf{q}_i)\,, \tag{3.55}$$

with $F_a^{(n)}$ being the analytic EdS-SPT kernels and the time-dependent prefactor $\mathrm{e}^{n\eta} = (D^+)^n$ computed exactly in ΛCDM. The approximation has been shown to work at the percent level for the power spectrum [44, 46, 210–212] and similarly for the bispectrum [213] in the mildly non-linear regime for ΛCDM models. We discuss explicitly the impact of the EdS-approximation on the one-loop bispectrum in Chapter 5, presenting results from Paper II. The inaccuracy could potentially increase in cosmological models in which the background evolution is altered significantly at late times, see e.g. Ref. [214].

Since the perturbative solution is a momentum integral over the kernels, having analytic expressions for them is very useful and allows for simplifications and fast evaluation. In particular, techniques for rapid computation of integrals over kernels have been developed, as we will discuss briefly in Section 3.5 below. Therefore the EdS-approximation in widely used in the literature, and is in particular used in the pipelines that analyze and constrain cosmological parameters from the BOSS galaxy clustering data [27–29]. Recently, Ref. [215] analyzed that data set with exact time-dependence, finding no significant shift in the posteriors of the cosmological parameters. Nevertheless, with enhanced precision of future surveys, the EdS approximation may be insufficient.

3.4 Extension of standard perturbation theory

In this section we discuss an extension of SPT introduced in Paper I [44] and further developed in an EFT framework in Paper III [46]. Inspired by Ref. [216], the idea is to be able to apply perturbation theory also in models where the dynamics have non-trivial scale- and time-dependence, as well as in fluids with more than one component. This extended framework will be applied in Chapter 4 to model structure formation in the presence of massive neutrinos. Due to the increased complexity of the dynamics, the solutions will in general not factorize in separate time- and space-dependence, so that one needs to resort to numerical methods. This is made possible by the algorithm for computing loop corrections developed in Refs. [44, 138, 216, 217].

We assume that structure formation can be described by a fluid comprising N species, following the density contrast and velocity divergence of each species. The fluid perturbations are described by

$$\psi_a(\mathbf{k},\eta) = \left(\ldots, \delta_i(\mathbf{k},\eta), -\frac{\theta_i(\mathbf{k},\eta)}{\mathcal{H}f}, \ldots\right) , \tag{3.56}$$

where the index a runs from 1 to $2N$, and the index i labels the i-th species. Moreover, we assume that the non-linear equations of motion of ψ_a can be written in analogous form as Eq. (3.36),

$$\frac{\partial}{\partial\eta}\psi_a(\mathbf{k},\eta) + \Omega_{ab}(k,\eta)\psi_b(\mathbf{k},\eta) = \int_{\mathbf{k}_1,\mathbf{k}_2} \delta_{\mathrm{D}}(\mathbf{k}-\mathbf{k}_{12})\gamma_{abc}(\mathbf{k},\mathbf{k}_1,\mathbf{k}_2)\psi_b(\mathbf{k}_1,\eta)\psi_c(\mathbf{k}_2,\eta) , \tag{3.57}$$

where we allowed for both a time- and scale-dependence in the (now $2N \times 2N$) evolution matrix $\Omega_{ab} = \Omega_{ab}(|\mathbf{k}|,\eta)$. We allow in general for non-linear terms in the vertex γ_{abc} in addition to the standard ones in Eq. (3.38).

As in SPT, we look for a perturbative solution as an expansion around the linear density contrast:

$$\begin{aligned}\psi_a(\mathbf{k},\eta) &= \sum_{n=1}^{\infty} \psi_a^{(n)}(\mathbf{k},\eta) \\ &= \sum_{n=1}^{\infty} \int_{\mathbf{q}_1,\ldots,\mathbf{q}_n} \delta_{\mathrm{D}}(\mathbf{k}-\mathbf{q}_{1\cdots n})\, \mathrm{e}^{n\Delta\eta} F_a^{(n)}(\mathbf{q}_1,\ldots,\mathbf{q}_n;\eta) \prod_{i=1}^{n} \delta_0(\mathbf{q}_i)\,, \end{aligned} \tag{3.58}$$

where $\Delta\eta \equiv \eta - \eta_{\mathrm{ini}}$ and δ_0 is an initial condition that will be discussed shortly. Notice that contrary to the expansions in the EdS Universe (3.42) or in the EdS-approximation for ΛCDM (3.53), we have not factorized the time- and wavenumber-dependence in the ansatz above. The kernels here have a dependence on time in addition to the wavenumbers. Therefore, the solution (3.58) accounts for the full time- and scale-dependence of the dynamics. Finally, we extracted the factor $\mathrm{e}^{n\Delta\eta}$ from the time-dependent kernels at each order in perturbation theory above for convenience, expecting that it captures the predominant time-dependence of the solution. Thus, the kernels exhibit smaller variation which improves the numerical stability when we integrate their time-dependence.

Inserting the perturbative solution (3.58) into the equation of motion (3.57) yields the following recursive equation for the kernels:

$$\begin{aligned}&(\partial_\eta + n)\, F_a^{(n)}(\mathbf{q}_1,\ldots,\mathbf{q}_n;\eta) + \Omega_{ab}(k,\eta) F_b^{(n)}(\mathbf{q}_1,\ldots,\mathbf{q}_n;\eta) = \\ &\quad \sum_{m=1}^{n-1} \Big[\gamma_{abc}(\mathbf{k},\mathbf{q}_{1\cdots m},\mathbf{q}_{m+1\cdots n}) F_b^{(m)}(\mathbf{q}_1,\ldots,\mathbf{q}_m;\eta) F_c^{(n-m)}(\mathbf{q}_{m+1},\ldots,\mathbf{q}_n;\eta)\Big]_{\mathrm{sym}}\,, \end{aligned} \tag{3.59}$$

where the RHS is symmetrized in the same way as described below Eq. (3.45) and $\mathbf{k} = \mathbf{q}_{1\cdots n}$.

Applications

The extended formalism with N species and time- and scale-dependent evolution matrix defined above allows us to model structure formation in many scenarios beyond the standard case, including the following:

i) ΛCDM universe where the EdS-approximation is relaxed. This is perhaps the simplest application, with only one species (cold dark matter) and no scale-dependence. However the solution (3.58) captures the exact, time-dependent growth also beyond the linear solution, and can therefore be used to test the accuracy of the EdS-approximation.

ii) Furthermore, cosmologies with altered recent expansion history, such as for example ones including a dynamical dark energy component, e.g. [214], can be treated with exact time-dependence.

iii) A dark matter fluid with effective sound velocity and viscosity descriptions that can be captured by additional linear terms in the equations of motion, yielding a scale-dependent Ω_{ab}-matrix as described in Refs. [216, 218, 219].

iv) Structure formation with massive neutrinos coupled via gravity to dark matter (or a joint fluid of baryons and dark matter). As we will describe in detail in Chapter 4, neutrinos freestream over long distances in a Hubble time. This freestreaming scale adds a scale-dependence to the dynamics which can precisely be described by a scale- and time-dependent evolution matrix with $N = 2$. This application is discussed in detail in that chapter.

v) Baryons and dark matter are normally treated as a single component in LSS. This assumption could be scrutinized with the formalism above.[3]

vi) In effective large-scale structure models of modified gravity or dark energy, the Poisson equation gets additional terms which are second and third order in the fields [222]. While the extension of SPT defined above could not capture the third-order terms, the second order terms could be incorporated by promoting γ_{abc} to a time-dependent function.

Combinations of these scenarios could also be captured by the formalism defined above, nevertheless with potential increased complexity. We will for example relax the EdS-approximation (item i)) *and* incorporate freestreaming neutrinos (item iv)) in the composite fluid model treated in Chapter 4.

Strategies for numerical solutions

Since there is in general no analytic solution of Eq. (3.59), we will integrate it numerically using the Runge-Kutta-Fehlberg method of the GSL library.[4] For a given set of wavenumbers $\{\mathbf{q}_1, \ldots, \mathbf{q}_n\}$, our routine for solving $F_a^{(n)}$ as a function of time will recursively call itself to compute the RHS of the ODE (3.59), until it reaches $F_a^{(1)}$. For the linear case the RHS is zero, and the equation of motion can immediately be integrated numerically. We store the result on a grid with N_η points between the initial time and the final time. Now the $F_a^{(2)}$ kernels can be computed by interpolating the linear result, and this procedure can be repeated up until we reach the n-th order kernels.

This procedure is considerably more computationally expensive compared to calculations of EdS-SPT kernels. To obtain non-linear corrections to e.g. the power spectrum we will need to integrate over certain combinations and configurations of the kernels, as we will see in the next section. For the EdS-SPT kernels, analytic expressions are known, and the integrals can be manipulated in such a way that they can be evaluated very efficiently. We briefly describe one such technique, the *FFTLog*-method below. For our generalized setup, we do not have analytic solutions, and hence the integrations entail $\mathcal{O}(10^6)$ executions of the above algorithm that solves the hierarchy of ODEs. In total, our extension is therefore not suited for MCMC analysis of galaxy clustering data (at least presently, it could see

[3] Even on large scales, due to the small, lingering coupling to the photons, baryons do not behave entirely as dark matter until very late times, leading to slightly different initial conditions for structure formation at $z = \mathcal{O}(10)$. On small scales, baryons obviously behave very differently than dark matter, which in the EFT description leads to additional counterterms, see e.g. Ref. [220, 221].

[4] https://www.gnu.org/software/gsl/

significant speed-up in the future), but rather useful to scrutinize common approximations and model extended cosmological setups.

To solve the equation of motion for the kernels (3.57), we need to specify suitable initial conditions. The formalism is tailored for late time structure formation, and the entire prior evolution will be left to a linear Boltzmann solver (`CLASS`). Therefore, $\eta_{\rm ini}$ needs to be chosen well after recombination, deep in the matter era and when the baryon drag can be completely neglected, but also sufficiently prior to the point at which non-linearities become important on mildly non-linear scales. We assume adiabatic initial conditions so that all initial fields are correlated, i.e.

$$\psi_a(\mathbf{k}, \eta_{\rm ini}) = F_a^{(1)}(k, \eta_{\rm ini})\delta_0(\mathbf{k})\,, \tag{3.60}$$

where $\delta_0(\mathbf{k})$ is the initial fluctuation at $\eta_{\rm ini}$ (which can be treated as fully linear since $\eta_{\rm ini}$ was chosen when non-linear corrections are negligible). Furthermore, we will assume that $\delta_0(\mathbf{k})$ is drawn from a Gaussian distribution, so that we will only need to specify the initial linear power spectrum $\langle\delta_0(\mathbf{k})\delta_0(\mathbf{k}')\rangle = \delta_{\rm D}(\mathbf{k}+\mathbf{k}')P_0(k)$. We discuss the statistical observables in more detail in the next section.

In practice, since we cannot take the initial time in the infinite past, we find that one needs to be careful in setting the initial conditions for the kernels $F_a^{(n)}(k, \eta_{\rm ini})$. By $\eta_{\rm ini}$ the decaying modes of the matter fluid in the Universe have had ample time to die out, and therefore we need to make sure that we initialize the kernel hierarchy in the growing mode solution at $\eta_{\rm ini}$, lest transient modes that do not entirely decay by the present time might be excited. In the EdS case, this was not an issue since the dynamics was time independent and the $\eta_{\rm ini} \to -\infty$ limit could trivially be taken, hence the perturbative solution could be written analytically entirely in terms of the growing mode.

For some generalized setups, if the system can be mapped onto an EdS one at the initial time, the EdS-SPT kernels can be used as initial conditions. This is for example the case for the ΛCDM application i) above, testing the impact of exact time-dependent growth at late times due to vacuum energy domination. Since $\Omega_{\rm m}/f^2$ is very close to unity at $z \gtrsim 10$ (see Fig. 3.3), EdS-SPT initial conditions can be used. In general however, the system cannot be mapped exactly enough onto the analytic EdS solution at the initial time; if the EdS kernels differs only slightly from the actual growing mode, transient modes that traverse the hierarchy are excited. Hence we need a different strategy. We opt for obtaining the growing mode initial condition numerically in the following way: Fixing the dynamics to be the initial time one, $\Omega_{ab} = \Omega_{ab}(k, \eta_{\rm ini})$, we can evolve the system from the infinite past, $\eta_{\rm asymp} \to -\infty$, up to $\eta_{\rm ini}$. This way, the transient modes have died out and the kernel hierarchy completely resides in the growing mode by $\eta = \eta_{\rm ini}$. As long as $\eta_{\rm asymp}$ is sufficiently early, we can then in principle use any initial value for the kernels, because only the growing mode will remain at $\eta_{\rm ini}$, which then can serve as the initial condition when dynamics is "turned on" for $\eta > \eta_{\rm ini}$. Nevertheless, since the linear growing mode can easily be obtained by computing the eigenvectors $u_a(k)$ of $\Omega_{ab}(k, \eta_{\rm ini})$, it is advantageous to set

$$F_a^{(n)}(k, \eta_{\rm asymp}) = \begin{cases} u_a(k)\exp\left[(1-\lambda_1)(\eta_{\rm asymp}-\eta_{\rm ini})\right]\,, & n=1\,, \\ 0\,, & n>1\,, \end{cases} \tag{3.61}$$

as asymptotic initial condition, where $1-\lambda_1$ is the growing mode eigenvalue of $n\delta_{ab}^{(\rm K)} +$

$\Omega_{ab}(k, \eta_{\rm ini})$ for $n = 1$ (cf. Eq. (3.58)). Hence, starting at $\eta_{\rm asymp}$ and evolving the kernels to $\eta_{\rm ini}$ using $\Omega(k, \eta_{\rm ini})$, the linear kernels remain in the growing mode by construction, and higher order transient modes have sufficient time to die out before $\eta_{\rm ini}$. We will use this method for the initialization of the kernels when we model structure formation in the presence of massive neutrinos in Chapter 4.

3.5 Statistical quantities

The description of LSS is ultimately a statistical one. As discussed in Chapter 2, the rich structure of the Universe today arose from small seed perturbations in the early Universe. In typical models of inflation, the perturbations materialize due to quantum fluctuations in the dynamical field driving the exponential expansion. As we have no direct measurement of these primordial initial conditions and furthermore since we can not observe the cosmic evolution of a single system, cosmological observables are statistic rather than deterministic. In this section, we implement the perturbative solutions described above in statistical observables of LSS.

We want to describe the statistical properties of cosmic fields such as the density fluctuation, the velocity divergence or the gravitational potential on large scales. The stochastic fields can be characterized by their $\mathcal{N}$-point functions. Since the first moment, i.e. the average of the fluctuation fields ψ_a vanishes, the first non-trivial moment is the power spectrum P_{ab}[5], defined analogously to Eq. (2.17),

$$\langle \psi_a(\mathbf{k}) \psi_b(\mathbf{k}') \rangle \equiv \delta_{\rm D}(\mathbf{k} + \mathbf{k}') P_{ab}(k) \,. \tag{3.62}$$

Here, we assume statistical homogeneity and isotropy in accordance with the cosmological principle, such that the power spectrum only depends on the norm of the wavenumber k [26].

Since we adopt Gaussian primordial initial conditions, the statistical properties of the fluctuations ψ_a are completely determined by the initial power spectrum $P_{ab}(k, \eta_{\rm ini})$ at $\eta = \eta_{\rm ini}$.[6] Furthermore, for adiabatic initial perturbations, we can use Eq. (3.60) to relate correlations of any fields to a single initial power spectrum $P_0(k)$,

$$\begin{aligned} \langle \psi_a(\mathbf{k}, \eta_{\rm ini}) \psi_b(\mathbf{k}', \eta_{\rm ini}) \rangle &= F_a^{(1)}(k, \eta_{\rm ini}) F_b^{(1)}(k, \eta_{\rm ini}) \langle \delta_0(\mathbf{k}) \delta_0(\mathbf{k}') \rangle \\ &\equiv F_a^{(1)}(k, \eta_{\rm ini}) F_b^{(1)}(k, \eta_{\rm ini}) \, \delta_{\rm D}(\mathbf{k} + \mathbf{k}') P_0(k) \,. \end{aligned} \tag{3.63}$$

We will typically choose P_0 to be the initial power spectrum of the ψ_1 field, $P_0(k) = P_{11}(k, \eta_{\rm ini})$, which fixes $F_1^{(1)}(k, \eta_{\rm ini}) = 1$. The initial, linear spectrum P_0 can be computed by a Boltzmann solver such as `CLASS`, which incorporates the primordial spectrum as well as the entire linear evolution up to $\eta_{\rm ini}$ (by computing accurately the growth and transfer functions discussed in Section 2.3).

[5] We use the subscript ab to indicate which field components of the vector ψ_a that are correlated. This should not be confused with the conventional labels of the various diagrams entering loop corrections to the power spectrum, which we will denote with a superscript, e.g. $P^{(22)}$.

[6] As discussed in the previous section, we take $\eta_{\rm ini}$ long after recombination but before structure formation starts. Since non-linear corrections are completely negligible between inflation and $\eta_{\rm ini}$, the primordial statistics are conserved until $\eta_{\rm ini}$.

Due to the non-linear evolution of clustering matter under gravity, non-Gaussian features are generated on larger and larger scales, even under the assumption of purely Gaussian initial conditions. The leading non-Gaussian statistic is the *bispectrum* B_{abc}, defined via

$$\langle \psi_a(\mathbf{k}_a,\eta)\psi_b(\mathbf{k}_b,\eta)\psi_c(\mathbf{k}_c,\eta)\rangle = \delta_{\mathrm{D}}(\mathbf{k}_a+\mathbf{k}_b+\mathbf{k}_c)B_{abc}(\mathbf{k}_a,\mathbf{k}_b,\mathbf{k}_c;\eta)\,, \tag{3.64}$$

where the Dirac delta function ensures momentum conservation which is demanded by statistical homogeneity and isotropy. The bispectrum is an important observable because it can be used to constrain primordial non-Gaussianity and in addition it is instrumental in disentangling bias from cosmological parameters [223]. We discuss the bispectrum in more detail when we describe the NNLO bispectrum in an EFT framework in Chapter 5.

Diagrams and Feynman rules

We want to obtain the $\mathcal{N}$-point function at some time η using perturbation theory as described in Secs. 3.3 and 3.4 above. Consider first the two-point function, by inserting the perturbative expansion (3.58) we obtain

$$\begin{aligned}\langle \psi_a(\mathbf{k},\eta)\psi_b(\mathbf{k}',\eta)\rangle = \sum_{n=1}^{\infty}\sum_{n'=1}^{\infty} \mathrm{e}^{(n+n')\Delta\eta} \int_{\mathbf{p}_1,\ldots,\mathbf{p}_n}\int_{\mathbf{p}'_1,\ldots,\mathbf{p}'_{n'}} \delta_{\mathrm{D}}(\mathbf{k}-\mathbf{p}_{1\cdots n})\delta_{\mathrm{D}}(\mathbf{k}'-\mathbf{p}'_{1\cdots n'}) \\ \times F_a^{(n)}(\mathbf{p}_1,\ldots,\mathbf{p}_n;\eta)\,F_b^{(n')}(\mathbf{p}'_1,\ldots,\mathbf{p}'_{n'};\eta)\left\langle \prod_{i=1}^{n}\delta_0(\mathbf{p}_i)\prod_{i'=1}^{n'}\delta_0(\mathbf{p}'_i)\right\rangle .\end{aligned} \tag{3.65}$$

Note that all the statistical information is contained in the expectation value of the initial fluctuation δ_0. We can reorder the sum and collect terms with equal powers of the δ_0 fields, thus

$$\begin{aligned}\langle \psi_a(\mathbf{k},\eta)\psi_b(\mathbf{k}',\eta)\rangle = \sum_{L=0}^{\infty}\sum_{m=1}^{2(L+1)} \mathrm{e}^{2(L+1)\Delta\eta} \int_{\mathbf{q}_1,\ldots,\mathbf{q}_{2(L+1)}} \delta_{\mathrm{D}}\left(\mathbf{k}-\mathbf{q}_{1\cdots m}\right)\delta_{\mathrm{D}}\left(\mathbf{k}'-\mathbf{q}_{m+1\cdots 2(L+1)}\right) \\ \times F_a^{(m)}\left(\mathbf{q}_1,\ldots,\mathbf{q}_m;\eta\right)F_b^{(2(L+1)-m)}\left(\mathbf{q}_{m+1},\ldots,\mathbf{q}_{2(L+1)};\eta\right) \\ \times\left\langle\prod_{i=1}^{2(L+1)}\delta_0(\mathbf{q}_i)\right\rangle .\end{aligned} \tag{3.66}$$

Here, each term in the sum over L contains $2(L+1)$ factors of δ_0; we will see shortly that L will correspond to the number of loops in the diagrammatic representation of the perturbation expansion of the power spectrum. Since the initial perturbation δ_0 is assumed to be Gaussian, we can use the *Wick theorem* to relate $\mathcal{N}$-point functions to products of two-point functions. The Wick theorem is a cornerstone in both classical and quantum field theories, relating ensemble averages of any products of stochastic variables to products of ensemble averages of pairs [224]. Explicitly, for the Gaussian random field δ_0 in Fourier

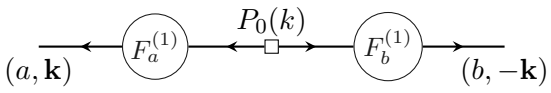

Figure 3.4: Diagrammatic representation of the tree-level power spectrum. The box represents the initial spectrum P_0, and blobs represent kernels F.

space we have

$$\left\langle \prod_i^{2p+1} \delta_0(\mathbf{q}_i) \right\rangle = 0\,, \tag{3.67a}$$

$$\left\langle \prod_i^{2p} \delta_0(\mathbf{q}_i) \right\rangle = \sum_{\substack{\text{all pair} \\ \text{associations}}} \prod_{p \text{ pairs } (i,j)} \langle \delta_0(\mathbf{q}_i)\delta_0(\mathbf{q}_j)\rangle\,, \tag{3.67b}$$

where p is an integer. Hence, expectation values of an odd number of Gaussian fields vanish, while expectation values of an even number $2p$ of fields can be decomposed into $(2p)!/(2^p p!) = (2p-1)!!$ terms corresponding to all pairs p of the fields. The expectation value of pairs of initial fields δ_0 can be related to the power spectrum P_0 via Eq. (3.63). In consequence, higher order $\mathcal{N}$-point correlation functions of Gaussian random fields can be constructed completely from the power spectrum, and moreover for cosmic fields with Gaussian initial conditions the statistical properties are entirely determined by the initial, linear power spectrum.

The application of the Wick theorem to Eq. (3.66) can be nicely represented diagrammatically by *Feynman diagrams* in a similar spirit to loop diagrams in QFTs. Representing each kernel F_a and F_b by the diagram Fig. 3.2, where each incoming line illustrates an initial fluctuation δ_0, the sum in Wick's theorem corresponds to pairing incoming lines between the diagrams. Each pairing corresponds to a two-point function which can be related to the initial power spectrum: $\langle \delta_0(\mathbf{q}_i)\delta_0(\mathbf{q}_j)\rangle = \delta_\mathrm{D}(\mathbf{q}_i + \mathbf{q}_j)P_0(q_i)$. The linear or tree-level diagram is shown in Fig. 3.4. Each kernel has only one incoming line, which are connected together, accompanied by an initial power spectrum. We depict P_0 by square boxes, kernels by blobs, and the endpoint labels indicate which fields (labeled by their indices a, b) we compute the correlation of, as well as their wavenumbers, which must sum to zero due to translation invariance (cf. Eq. (3.62)). The corresponding mathematical expression is simply

$$P_{ab}^\mathrm{tree}(\mathbf{k}, \eta) = \mathrm{e}^{2\Delta\eta} F_a^{(1)}(\mathbf{k}, \eta) F_b^{(1)}(\mathbf{k}, \eta) P_0(k)\,. \tag{3.68}$$

At one-loop, three separate diagrams contribute, named $P^{(31)}$, $P^{(22)}$ and $P^{(13)}$. The superscript corresponds to the order of the kernels that appear in the diagram, e.g. $P^{(31)}$ contains a third order kernel and a first order kernel. In Fig. 3.5 we display $P^{(31)}$, $P^{(22)}$; the diagram $P^{(13)}$ is completely equivalent to $P^{(31)}$ with a and b exchanged. In Fig. 3.5 we also label the momentum flowing in each internal line; the kernels conserve momentum, hence the total momentum of each incoming line to a kernel equals the outgoing momentum. Note that all pairs in the Wick theorem (3.67) sum do not contribute: disconnected diagrams would

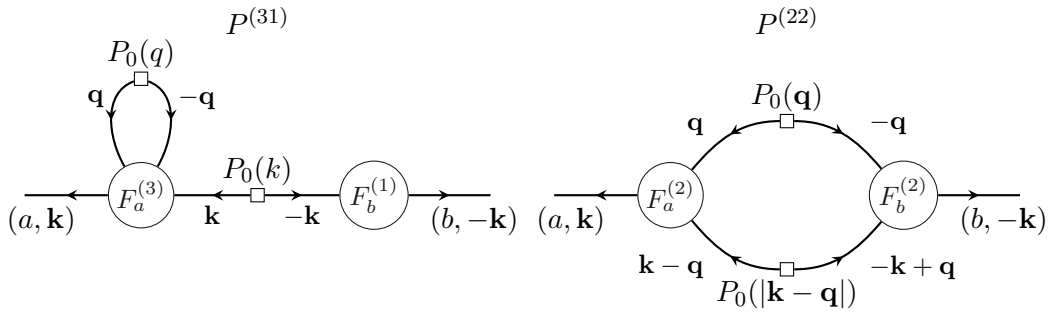

Figure 3.5: Diagrammatic representation of the contributions $P^{(31)}$ and $P^{(22)}$ to the one-loop power spectrum correction. We do not show the one-loop diagram $P^{(31)}$ which is equivalent to $P^{(31)}$ when exchanging $a \leftrightarrow b$.

correspond to ensemble averages over the fields, $\langle \psi_a(\mathbf{k}, \eta) \rangle$, which vanish [225]. Another way to see that disconnected diagrams do not contribute is to note that they would involve kernels whose sum of arguments is zero, yielding zero. Furthermore, multiple Wick theorem pairs yield equivalent diagrammatic contributions. At one-loop, there are three distinct ways to pair incoming lines between kernels $F^{(3)}$ and $F^{(1)}$ to obtain the $P^{(31)}$ diagram (and equivalently for $P^{(13)}$), and similarly two ways to obtain the $P^{(22)}$ diagram. In general, each diagram has an associated symmetry factor that counts equivalent contributions.

A general diagram at L-loop can be characterized by the number of lines connecting the F_a and F_b kernels as well as the number of "daisy" loops attached to each kernel [138]. We show this classification in Fig. 3.6, where m counts the number of lines connecting the kernels (there has to be at least one, $m \geq 1$, otherwise the diagram is disconnected), and l and r corresponds to the number of daisy loops attached to F_a and F_b, respectively. The total number of loops in the diagram is $L = l + r + m - 1$. Since there are two incoming lines from each daisy loop, the order of the kernels are $2l + m$ and $2r + m$, respectively.

Relating a diagram at L-loop to the corresponding mathematical expression is relatively straightforward, and can be summarized concisely by the following *Feynman rules* [206]:

1) Draw all distinct diagrams, corresponding to all combinations of integers (l, m, r) that satisfy $m \geq 1$, $l \geq 0$, $r \geq 0$ and $l + r + m = L + 1$.
   i) Assign an initial linear power spectrum $\delta_{\mathrm{D}}(\mathbf{q} + \mathbf{q}')P_0(q)$ to each of the $l + r + m$ square boxes.
   ii) For each kernel blob with incoming momenta $\mathbf{q}_i$ and outgoing momenta $\mathbf{p}$, write down the kernel $F(\dots, \mathbf{q}_i, \dots)$ as well as a Dirac delta function for momentum conservation $\delta_{\mathrm{D}}(\mathbf{p} - \sum_i \mathbf{q}_i)$.
   iii) Integrate over all inner momenta $\mathbf{q}_i$.
   iv) Multiply by the symmetry factor

$$S(l, m, r) = \frac{(2l + m)!(2r + m)!}{2^{l+r} l! r! m!} \,. \tag{3.69}$$

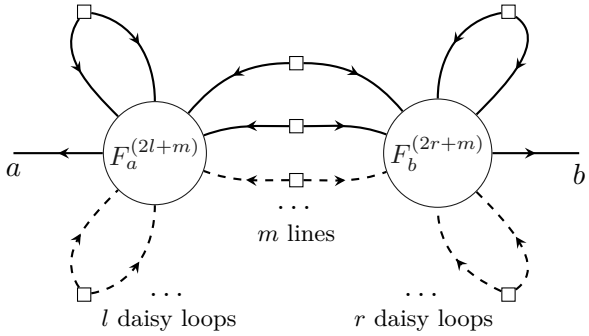

Figure 3.6: General diagram for loop contributions to the power spectrum. The kernels $F_a^{(2l+m)}$ and $F_b^{(2r+m)}$ are connected by m lines. Moreover, they have l and r daisy loops connected to them, respectively. The loop order of the diagram is $L = l + r + m - 1$.

2) Add the expressions from each diagram, and multiply the result with the overall time-dependent factor $\mathrm{e}^{2(L+1)\Delta\eta}$.

Applying these rules we obtain the following expression for the one-loop correction to the power spectrum:

$$\begin{aligned} P_{ab}^{1L}(k,\eta) &= P_{ab}^{(13)} + P_{ab}^{(31)} + P_{ab}^{(22)} \\ &= \mathrm{e}^{4\Delta\eta} \int_{\mathbf{q}} P_0(q) \Big[3F_a^{(1)}(k;\eta) P_0(k) F_b^{(3)}(\mathbf{k},\mathbf{q},-\mathbf{q};\eta) \\ &\quad + 3F_a^{(3)}(\mathbf{k},\mathbf{q},-\mathbf{q};\eta) P_0(k) F_b^{(1)}(k;\eta) \\ &\quad + 2F_a^{(2)}(\mathbf{k}-\mathbf{q},\mathbf{q};\eta) P_0(|\mathbf{k}-\mathbf{q}|) F_b^{(2)}(\mathbf{k}-\mathbf{q},\mathbf{q};\eta) \Big] . \end{aligned} \tag{3.70}$$

Similarly, by drawing all diagrams contributing to the two-loop correction, see Fig. 3.7, the two-loop expression can be obtained as follows

$$\begin{aligned} P_{ab}^{2L}(k,\eta) &= P_{ab}^{(15)} + P_{ab}^{(51)} + P_{ab}^{(24)} + P_{ab}^{(42)} + P_{ab}^{(33-I)} + P_{ab}^{(33-II)} \\ &= \mathrm{e}^{6\Delta\eta} \int_{\mathbf{q},\mathbf{p}} P_0(q) P_0(p) \Big[15F_a^{(1)}(k;\eta) P_0(k) F_b^{(5)}(\mathbf{k},\mathbf{p},-\mathbf{p},\mathbf{q},-\mathbf{q};\eta) \\ &\quad + 15F_a^{(5)}(\mathbf{k},\mathbf{p},-\mathbf{p},\mathbf{q},-\mathbf{q};\eta) P_0(k) F_b^{(1)}(k;\eta) \\ &\quad + 12F_a^{(2)}(\mathbf{k}-\mathbf{q},\mathbf{q};\eta) P_0(|\mathbf{k}-\mathbf{q}|) F_b^{(4)}(\mathbf{k}-\mathbf{q},\mathbf{q},\mathbf{p},-\mathbf{p};\eta) \\ &\quad + 12F_a^{(4)}(\mathbf{k}-\mathbf{q},\mathbf{q},\mathbf{p},-\mathbf{p};\eta) P_0(|\mathbf{k}-\mathbf{q}|) F_b^{(2)}(\mathbf{k}-\mathbf{q},\mathbf{q};\eta) \\ &\quad + 9F_a^{(3)}(\mathbf{k},\mathbf{q},-\mathbf{q};\eta) P_0(k) F_b^{(3)}(\mathbf{k},\mathbf{p},-\mathbf{p};\eta) \\ &\quad + 6F_a^{(3)}(\mathbf{k}-\mathbf{p}-\mathbf{q},\mathbf{p},\mathbf{q};\eta) P_0(|\mathbf{k}-\mathbf{p}-\mathbf{q}|) F_b^{(3)}(\mathbf{k}-\mathbf{p}-\mathbf{q},\mathbf{p},\mathbf{q};\eta) \Big] . \end{aligned} \tag{3.71}$$

Note that the highest order kernel entering in the one- and two-loop expressions are of order $n = 3$ and $n = 5$, respectively (in general the highest order kernel at L-loop has

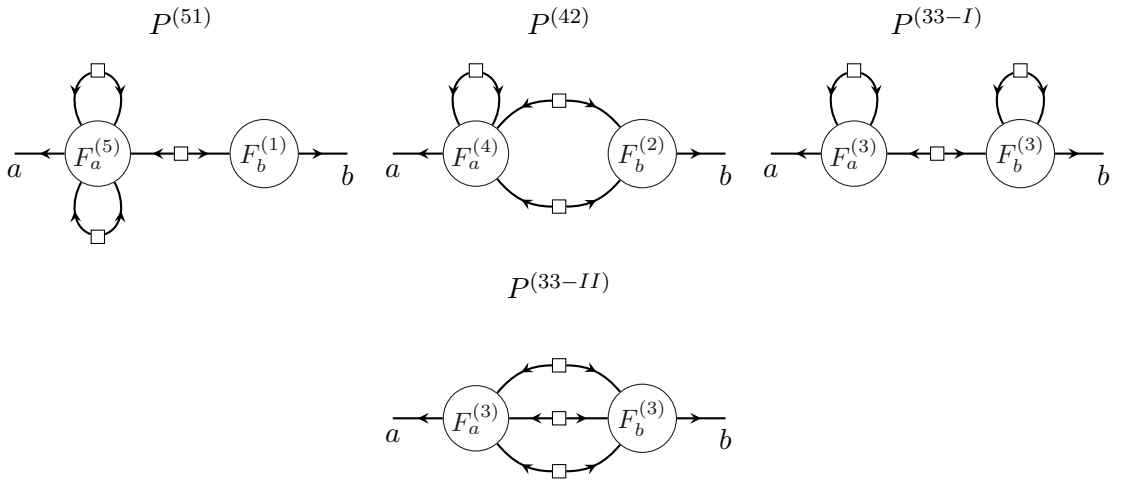

Figure 3.7: Diagrams contributing to the two-loop power spectrum correction. There are two separate diagrams with two third-order kernels $P^{(33-I)}$ and $P^{(33-II)}$, distinguished by roman numerals. The equivalent contributions $P^{(15)}$ and $P^{(24)}$ with a and b exchanged are not shown.

$n = 2L - 1$). Due to the recursive structure of the equations of motion of the kernels, they become progressively harder to compute at higher order, making the integrals above increasingly complicated to evaluate at higher loop order. In the rest of this section, we discuss the calculation of loop integrals.

Loop integrals in EdS

Having derived general expressions for loop corrections to the power spectrum, we now specialize to the EdS case, where the analytic solutions allows us to examine the loop integrals in more detail. The one-loop correction to the matter power spectrum using EdS-SPT kernels has been widely studied in the literature, see e.g. Refs. [26, 138, 206, 207, 217, 225, 226]. By inserting the EdS-SPT recursion relation (3.48), we obtain the $P^{(22)}$ diagram contribution to the one-loop power spectrum for the density contrast $P_{\delta\delta} = P_{11}$ as

$$\begin{aligned} P_{11}^{(22)}(k,\eta) &= 2\mathrm{e}^{4\Delta\eta} \int_{\mathbf{q}} P_0(q) P_0(|\mathbf{k}-\mathbf{q}|) \left[F_1^{(2)}(\mathbf{k}-\mathbf{q},\mathbf{q})\right]^2 \\ &= 4\pi\, \mathrm{e}^{4\Delta\eta} \int^{\Lambda} \mathrm{d}q\, q^2 \int \mathrm{d}\mu\, P_0(q) P_0\left(\sqrt{k^2+q^2-2kq\mu}\right) \\ &\quad \times \left[\frac{k^2(7k\mu + q(3-10\mu^2))}{14q(k^2+q^2-2kq\mu)}\right]^2 , \end{aligned} \tag{3.72}$$

where Λ is a cutoff which we discuss in detail in Section 3.6 and we in the second line used rotational invariance to choose a coordinate system with $\mathbf{k} = k(0,0,1)$ and $\mathbf{q} = q(\sqrt{1-\mu^2}, 0, \mu)$. In order to further integrate over q and μ, we need to specify an initial

power spectrum P_0. Similarly, the $P^{(13)}$ contribution is given by

$$\begin{aligned} P_{11}^{(13)}(k,\eta) &= 3\mathrm{e}^{4\Delta\eta}P_0(k)F_1^{(1)}(\mathbf{k})\int_{\mathbf{q}}P_0(q)F_1^{(3)}(\mathbf{k},\mathbf{q},-\mathbf{q}) \\ &= \frac{\pi}{252}\,\mathrm{e}^{4\Delta\eta}P_0(k)\int^{\Lambda}\mathrm{d}q\,q^2P_0(q) \\ &\quad\times\left[\frac{12k^4}{q^4}-\frac{158k^2}{q^2}-\frac{42q^2}{k^2}+100+3\frac{(k^2-q^2)^3(2k^2+7q^2)}{k^3q^5}\ln\left(\frac{k-q}{k+q}\right)\right], \end{aligned} \tag{3.73}$$

where the initial power spectra had no μ-dependence, such that the integral over μ could be done immediately. For the auto-correlations ($a=b$), the last diagram $P^{(31)}$ is equal to $P^{(13)}$, therefore the total one-loop correction is $P_{11}^{1L}=P_{11}^{(22)}+2P_{11}^{(13)}$.

The integrals above are key ingredients in the analysis of galaxy clustering data using the galaxy one-loop power spectrum in redshift space [27–29]. Therefore, lots of effort have been devoted to obtaining methods for fast evaluation [150, 151, 227–229]. In particular, in the *FFTLog*-method, the input power spectrum $P_0(k)$ is written as a sum of self-similar spectra that are (complex) power-laws in k [151]. Then, the $P^{(22)}$ and $P^{(13)}$ integrals are formally equivalent to loop integrals of massless QFTs and can be integrated analytically. Thus the complicated integrals can be evaluated once and for all, and evaluating loop integrals for different cosmologies (input power spectra P_0) reduces to matrix multiplication, yielding a significant speed-up. In this thesis, we will not use these methods, because we will consider generalized kernels beyond EdS-SPT, and we will go to two-loop in perturbation theory, where currently no convenient method for fast loop evaluation exist.

It is useful to consider the behavior of the loop correction diagrams in the IR and UV limits, i.e. when the absolute value of the loop momentum q is much smaller or much larger than the external momentum k. Expanding Eq. (3.72) in the limit $k\gg q$, we obtain

$$P_{11}^{(22)}\xrightarrow[k\gg q]{}4\pi\mathrm{e}^{4\Delta\eta}\left[\frac{569}{735}P_0(k)-\frac{47}{105}k\frac{\mathrm{d}P_0}{\mathrm{d}k}+\frac{1}{10}k^2\frac{\mathrm{d}^2P_0}{\mathrm{d}k^2}\right]\int^{\Lambda}\mathrm{d}q\,q^2P_0(q)+\mathrm{e}^{4\Delta\eta}k^2P_0(k)\sigma_{\mathrm{d}}^2\,, \tag{3.74}$$

where we defined the displacement dispersion of the initial power spectrum,

$$\sigma_{\mathrm{d}}^2\equiv\frac{4\pi}{3}\int^{\Lambda}\mathrm{d}q\,P_0(q)\,. \tag{3.75}$$

Similarly, the IR limit of $P^{(13)}$ reduces to

$$P_{11}^{(13)}\xrightarrow[k\gg q]{}-\frac{2\pi}{3}\mathrm{e}^{4\Delta\eta}k^2P_0(k)\int^{\Lambda}\mathrm{d}q\,P_0(q)\left[1-\frac{116}{105}\frac{q^2}{k^2}+\frac{188}{245}\frac{q^4}{k^4}\cdots\right]=-\frac{1}{2}\mathrm{e}^{4\Delta\eta}k^2P_0(k)\sigma_{\mathrm{d}}^2\,. \tag{3.76}$$

Crucially, after adding all contributions $P_{11}^{(22)}$ and twice $P_{11}^{(13)}$ ($P^{(31)}$ gives an equal contribution), we see that the leading k^2 IR-dependence cancels out. This follows from Galilean invariance [206, 217, 230, 231], in particular the kernel property Eq. (3.51). Therefore we expect this cancellation to occur also for generalized kernels beyond EdS-SPT as long as Galilean invariance is a symmetry.

In the UV-limit, $q \gg k$, we have

$$P_{11}^{(22)} \xrightarrow[q\gg k]{} \frac{18\pi}{49} \mathrm{e}^{4\Delta\eta} k^4 \int^{\Lambda} \mathrm{d}q \, \frac{P_0^2(q)}{q^2} \,, \tag{3.77a}$$

$$P_{11}^{(13)} \xrightarrow[q\gg k]{} -\frac{4\pi}{3} \mathrm{e}^{4\Delta\eta} k^2 P_0(k) \int^{\Lambda} \mathrm{d}q \, P_0(q) \left[\frac{61}{210} - 435 \frac{k^2}{q^2} + \cdots \right] = -\mathrm{e}^{4\Delta\eta} \frac{61}{210} k^2 P_0(k) \sigma_{\mathrm{d}}^2 \,. \tag{3.77b}$$

The k-scaling in this limit could also have been deduced from the general property $F^{(n)}(\mathbf{q}_i, \ldots, \mathbf{q}_n) \propto k^2$ when $\mathbf{k} = \sum_i \mathbf{q}_i$ goes to zero, as a consequence of momentum conservation (see general kernel properties on Page 33)

In the EdS-approximation, the power spectrum has been computed up to three-loop in the literature [138]. The loop corrections are shown in Fig. 3.8 for a ΛCDM cosmology at present time, $z = 0$. Each correction is negative up to a point where they cross zero as can be seen from the spikes in the graphs on the absolute log-log plot ($k \simeq 0.08$, 0.5 and $2h$ Mpc^{-1} at one-, two- and three-loop, respectively). We see that the convergence of the perturbation expansion appears to be poor: the two-loop correction is of the order of the one-loop correction, and the three-loop correction is even larger. In Section 3.6 we discuss how the convergence of SPT can be improved considerably by embedding it in an EFT framework.

Loop integrals for generalized kernels

We now move on to considering generalized kernels as defined in the extension of SPT in Section 3.4. Since we cannot (in general) obtain analytic solutions of the kernel equations of motion (3.57), the one- and two-loop integrals (3.70) and (3.71) cannot be straightforwardly simplified. Our strategy will therefore be to perform the integrals numerically. Since the integrals are multidimensional, Monte Carlo integration is the best option [232], and we employ the `Suave` routine of the `CUBA` library [233].[7] This routine uses global adaptive subdivision as well as importance sampling to optimize the Monte Carlo sampling distribution, and has been successfully applied to power spectrum loop-correction integrals in the past [138].

For efficient evaluation of the loop-correction integrand, we implement and extend the algorithm developed in Refs. [138, 216, 217]. We summarize the main elements here: At L-loop, the integrand contains a summand of kernels at order no higher than $n = 2L+1$. The kernels can be solved numerically and recursively using the equation of motion Eq. (3.57) for each integration point drawn by the Monte Carlo sampler. In the recursive hierarchy, many kernels appear multiple times and hence it is advantageous to use memoization. Moreover, when one of the loop arguments go to zero, individual diagrams exhibit IR-divergences that cancel out in the final result, as we saw explicitly for EdS-SPT kernels in the IR limits of $P^{(22)}$ and $P^{(13)}$ Eqs. (3.74) and (3.76), respectively. The cancellations occur between different integration regions, and therefore numerical uncertainties in the individual large IR contributions lead to sizable errors after the cancellation in the full integral. This numerical

[7] The concurrent update of `CUBA` is described in Ref. [234].

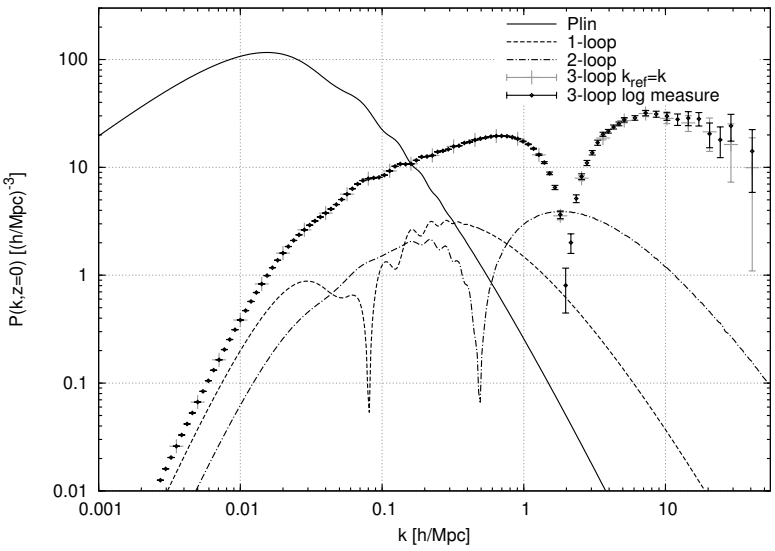

Figure 3.8: One-, two- and three-loop corrections (absolute values) to the power spectrum using EdS-SPT kernels (reprinted from [138]). The results are shown for the density contrast auto-correlation today, i.e. $P_{11}(k, \eta(z = 0))$, and obtained in Ref. [138] using a linear input spectrum from CAMB [92] with WMAP5 parameters [134]. At three-loop, the numerical errorbars are estimated from two times the Monte Carlo uncertainty. Up to $k = 0.55h$ Mpc^{-1}, the relative numerical error is less than 0.002.

instability can be avoided by constructing an *IR safe* integrand, in which the cancellations occur already at the integrand level [138, 217, 235].

3.6 Effective theory of large-scale structure

This is a good point to pause and recap what we did so far. We started with the Vlasov-Poisson system (3.16) and (3.17) and assumed that the cosmic fluid is a perfect, pressureless one on large scales such that the system could be closed via the *single-stream* approximation $\sigma_{ij} = 0$. Subsequently, we expanded the density contrast and velocity divergence in the linear solutions, that ultimately allowed us to compute loop corrections to the power spectrum (or any higher order $\mathcal{N}$-point function) in perturbation theory, both in the EdS-approximation as well as for generalized dynamics. Now, let us examine the validity of this expansion, in particular we will quantify the typical size of the fluctuations. The expectation value of the density fluctuation vanishes (by definition), however we can compute the variance smoothed on a scale $R = 1/\Lambda$, which can be estimated by summing modes up to a cutoff Λ:

$$\sigma_\Lambda^2 = 4\pi \int_0^\Lambda \mathrm{d}q\, q^2 P_0(q) = \int_0^\Lambda \mathrm{d}\ln q\, \Delta_0^2(q)\,, \tag{3.78}$$

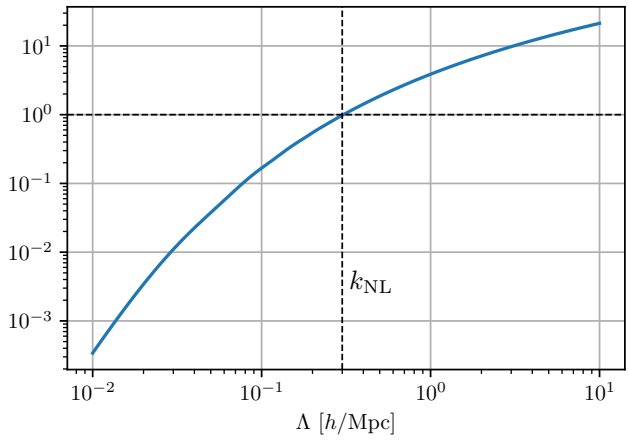

Figure 3.9: Variance of the fluctuation field smoothed on a scale $R = 1/\Lambda$, σ^2_Λ as a function of Λ in the ΛCDM model with $A_s = 2.215 \times 10^9$. The non-linear scale k_{NL} is the wavenumber at which the variance exceeds one.

where we introduced the *dimensionless* power spectrum $\Delta^2(k) = 4\pi k^3 P(k)$. We display the variance σ^2_Λ as a function of the cutoff in Fig. 3.9. A perturbative expansion is warranted when the typical size of fluctuations is less than one. The variance increases for smaller and smaller scales R as we approach the very non-linear dynamics of gravitational collapse, and the wavenumber at which it crosses unity defines the non-linear wavenumber k_{NL}, which in our Universe is around $k_{\mathrm{NL}} \approx 0.3h$ Mpc^{-1}. Beyond this wavenumber structures exhibit shell-crossing where multiple streams cross due to gravitational collapse and eventually form astrophysical objects through virialization [193, 236].

Problems of SPT

In SPT, due to mode-coupling, loop corrections are sensitive to physics at the non-linear scale even when considering scales $k \ll k_{\mathrm{NL}}$. Therefore the perfect, pressureless fluid assumption is inconsistent even on large scales. In particular, at high loop order the SPT predictions are increasingly sensitive to the UV, and therefore including higher order does not improve the accuracy of the prediction [138, 225]. Three-loop calculations in ΛCDM as shown in Fig. 3.8 indicate that there is no convergence even on linear scales. Furthermore, in Eq. (3.77) we found that the UV-sensitivity of one-loop correction is proportional to σ^2_{d},[8] which is divergent for an initial power spectrum $P_0(k) = k^n$ with $n \geq -1$. Hence, for general initial conditions, loop corrections are UV divergent. Therefore, one must impose an arbitrary cutoff, on which predictions will depend. Since the linear power spectrum in the phenomenologically favored ΛCDM universe has $n \simeq -1.5$ for $k \gtrsim 0.1h$ Mpc^{-1} (see Fig. 3.8), the UV-sensitivity of SPT in this case is not too strong, albeit increasing at higher orders. We will see later in this section that EFT corrections of the contributions from the

[8] Even though the result was derived for EdS dynamics, the form of the UV limit follows from momentum conservation and will be analogous in a general cosmology.

UV are of order 1 % on mildly non-linear scales.

The shortcomings of SPT can be summarized as [237]:

- *No well-defined expansion parameter*: The variance of linear fluctuations is not small for all scales and points in time.
- *Deviations from perfect, pressureless fluid*: Departures from the single-stream approximation induced by short-scale non-linearities are not accounted for.
- *Loop corrections are formally UV-divergent*: For general initial conditions, the loop corrections diverge, making predictions cutoff-dependent and unphysical.

In addition, in practice, there is no notion of convergence to the true answer (as obtained from N-body simulations) in SPT, as we can see in Fig. 3.8.

The problems of SPT severely limits its predictive power, and therefore there have been lots of efforts devoted to remedy these shortcomings as well as develop alternative approaches that can extend the wavenumber range for which perturbative methods can reliably be applied. One general direction has been to advance the perturbation theory description by identifying and improving the understanding of the effects that lead to the breakdown of the expansion. There have been attempts to partly resum the expansion, in particular reorganizing it in terms of a non-linear propagator, referred to as *renormalized perturbation theory (RPT)* [225, 238]. Given the slight improvement of these approaches over SPT, other works have performed similar resummations, e.g. Refs. [239–246]. Nevertheless, Ref. [247] considered cosmological perturbation theory in $1+1$-dimensions, where the entire SPT expansion can be resummed, and found that the theory does not accurately model the power spectrum on any mildly non-linear scales.

Another direction to improve the predictive power of cosmological perturbation theory is based on effective equations of motion, often referred to as the effective field theory of large-scale structure (EFTofLSS), proposed in Refs. [144, 145]. The idea is that the true equations of motion are that of an imperfect fluid with various contributions from the effective anisotropic stress tensor σ_{ij}. One way to derive the effective equations of motion is to coarse-grain the fluctuations on some scale beyond which we cannot model the physics. The resulting Vlasov-Poisson system contain contributions to the anisotropic stress tensor from the coarse-graining procedure in addition to the microscopic contributions. Thus, the stress tensor models the unknown UV physics; in the EFT it is not computed from first principles but rather written in terms of operators allowed by symmetries multiplied by a priori unknown coefficients. In this section we will describe the EFT approach in detail, and demonstrate how we can cure the cutoff dependence of the perturbation theory at two-loop order.

Coarse-grained equations of motion

We start by coarse-graining the distribution function, i.e. we *integrate out* the small scales by smoothing it with a window function W_Λ,

$$f_\mathrm{l}(\mathbf{x},\mathbf{p},\tau) = [f]_\Lambda(\mathbf{x},\mathbf{p},\tau) \equiv \int \mathrm{d}^3x'\, W_\Lambda(\mathbf{x}-\mathbf{x}') f(\mathbf{x}',\mathbf{p},\tau)\,, \tag{3.79}$$

with the l subscript indicating long-wavelength fields and where Λ is the smoothing scale which we will take to be the order of the non-linear scale, $\Lambda \sim k_{\rm NL}$. Any observable $\mathcal{O}$ can be coarse-grained in a similar manner: $\mathcal{O}_l = [\mathcal{O}]_\Lambda$, with the corresponding short-wavelength part defined as $\mathcal{O}_{\rm s} = \mathcal{O} - \mathcal{O}_{\rm l}$. In particular, the smoothed energy density ρ_l and velocity flow $\boldsymbol{\pi}$ are in real space given as

$$\rho_{\rm l}(\mathbf{x},\tau) = \frac{m}{a^3}\int \mathrm{d}^3p\, f_{\rm l}(\mathbf{x},\mathbf{p},\tau)\,, \tag{3.80a}$$

$$\boldsymbol{\pi}_{\rm l}(\mathbf{x},\tau) = \rho_{\rm l}(\mathbf{x},\tau)\mathbf{v}_{\rm l}(\mathbf{x},\tau) = \int \mathrm{d}^3p\,\frac{p_i}{am} f_{\rm l}(\mathbf{x},\mathbf{p},\tau)\,. \tag{3.80b}$$

Here, we defined the smooth velocity field as $\mathbf{v}_{\rm l} = \boldsymbol{\pi}_{\rm l}/\rho_{\rm l}$.[9]

The exact form of the window function W_Λ is not important; a top hat filter $W_\Lambda(\mathbf{x}) = \Theta(1/\Lambda - |\mathbf{x}|)$, where Θ is the Heaviside step function, could be used, but it is more convenient to apply a Gaussian filter

$$W_\Lambda(\mathbf{x}) = \left(\frac{\Lambda}{\sqrt{2\pi}}\right)^3 \exp\left(-\frac{1}{2}\Lambda^2|\mathbf{x}|^2\right)\,, \qquad W_\Lambda(\mathbf{k}) = \frac{1}{(2\pi)^3}\exp\left(-\frac{1}{2}\frac{|\mathbf{k}|^2}{\Lambda^2}\right)\,, \tag{3.81}$$

whose integral over real space was normalized to one and has variance

$$\int_{\mathbf{x}'} W_\Lambda(\mathbf{x}-\mathbf{x}')\,(\mathbf{x}-\mathbf{x}')_i(\mathbf{x}-\mathbf{x}')_j = \delta^{(\rm K)}_{ij}/\Lambda^2\,. \tag{3.82}$$

Using this filter, one can derive the following expression for smoothing the products of two fields f and g by Taylor expanding the long-wavelength fields [144],

$$[fg]_\Lambda = f_{\rm l}g_{\rm l} + [f_{\rm s}g_{\rm s}]_\Lambda + \frac{1}{\Lambda^2}\nabla f_{\rm l}\cdot\nabla g_{\rm l} + \cdots\,. \tag{3.83}$$

Hence, in addition to the product of long-wavelength fields, we obtain corrections from short-wavelength modes, as well as higher order corrections in the gradient expansion $k^2/\Lambda^2 \sim k^2/k^2_{\rm NL}$. We will work at leading order in gradients, therefore it turns out that we can neglect the derivative corrections above, because coarse-grained products always enter with additional gradients in the equations of motion.

Applying the groundwork above, the continuity and Euler equations (Eqs. (3.16) and (3.17)) can be coarse-grained yielding

$$\frac{\partial\delta_{\rm l}}{\partial\tau} + \nabla\cdot[(1+\delta_{\rm l})\mathbf{v}_{\rm l}] = 0\,, \tag{3.84a}$$

$$\frac{\partial\mathbf{v}_{\rm l}}{\partial\tau} + \mathcal{H}\mathbf{v}_{\rm l} + (\mathbf{v}_{\rm l}\cdot\nabla)\mathbf{v}_{\rm l} = -\nabla\phi_{\rm l} - \frac{1}{1+\delta_{\rm l}}\mathbf{e}_i\nabla_j\left[\tau^{ij}\right]_\Lambda\,, \tag{3.84b}$$

[9] This definition follows typical conventions of EFTofLSS, even though the velocity is not a purely long-wavelength field when defined as a ratio of coarse-grained fields. There are in principle additional counterterms in the effective theory to absorb short-wavelength contributions from this ratio, but it was shown in Ref. [194] that the finite parts of the counterterms have no physical effect. Therefore, the finite parts can be chosen to exactly cancel the formally infinite parts, which can be taken as a *definition* of what is meant by $\mathbf{v}_{\rm l}$.

where the *effective* stress tensor τ_{ij} contains both the microscopic stress and corrections due to the coarse-graining, in particular from products of short fluctuations in accordance with Eq. (3.83) [144]:

$$\tau^{ij} = (1+\delta_\mathrm{l})\sigma_\mathrm{l}^{ij} + (1+\delta_\mathrm{l})v_\mathrm{s}^i v_\mathrm{s}^j + \frac{\delta^{(\mathrm{K})\,ij}\nabla_k\Phi_\mathrm{s}\nabla^k\Phi_\mathrm{s} - 2\nabla^i\Phi_\mathrm{s}\nabla^j\Phi_\mathrm{s}}{8\pi G\bar{\rho}}\,, \tag{3.85}$$

where Φ is the full gravitational potential sourced by the total energy density, as described by Eq. (3.2). The short-scale physics is therefore contained entirely in the effective stress tensor. Those fluctuations on small scales are large and strongly coupled, and hard to model from first principles. Nevertheless, we are not interested in the specific behavior on small scales, but rather the impact on larger scales. Indeed, the idea of the EFT is to take expectation values of the short wavelength fluctuations, analogously to integrating out UV degrees of freedom in QFT. The expectation value is taken on a background of long wavelength modes, which affect the small scales via tidal effects. Therefore, the effective stress tensor will contain two contributions: a deterministic part which is correlated with the long wavelength modes and a stochastic one which must be modeled statistically. Thus, in the end, one obtains an effective theory where the only degrees of freedom are the long wavelength ones.

Effective stress tensor

Before we discuss the EFT description of the effective stress tensor in more detail, let us formulate the theory in the notation introduced in Section 3.4. We go to Fourier space and neglect vorticity; the additional stress tensor modifies the Euler equation, i.e. the equation for the second component of $\psi_a = (\delta, -\theta/\mathcal{H}f)$ (considering only one species for the moment, $N = 1$). We will only consider coarse-grained fields in the following, unless otherwise specified, and drop the l subscript for brevity. Thus (cf. Eq. (3.57)),

$$\begin{aligned}\frac{\partial}{\partial\eta}\psi_a(\mathbf{k},\eta) + \Omega_{ab}(\eta)\psi_b(\mathbf{k},\eta) = &\int_{\mathbf{k}_1,\mathbf{k}_2}\delta_\mathrm{D}(\mathbf{k}-\mathbf{k}_{12})\gamma_{abc}(\mathbf{k},\mathbf{k}_1,\mathbf{k}_2)\psi_b(\mathbf{k}_1,\eta)\psi_c(\mathbf{k}_2,\eta)\\ &+ \delta_{a2}^{(\mathrm{K})}\tau_\theta(\mathbf{k})\,,\end{aligned} \tag{3.86}$$

where the effective stress term τ_θ is given in real space as

$$\tau_\theta = \frac{1}{\mathcal{H}^2 f^2}\partial_i\frac{1}{1+\delta}\partial_j\tau^{ij}\,. \tag{3.87}$$

The prefactor arose due to the change of time variable to η as well as rescaling the velocity divergence, and is not important for the discussion. Furthermore, the $1/(1+\delta)$ factor which follows from Eq. (3.84b) needs to be present to be consistent with momentum conservation [248].

In the EFT, we will write down the deterministic part of the stress tensor by including all operators of long-wavelength fields allowed by symmetries, multiplied by a priori unknown coefficients, *EFT parameters* or Wilson coefficients, that cannot be determined by the theory itself, but rather has to be calibrated to N-body simulations or marginalized over in data analysis. This expansion is akin to the *bias expansion* that models the response of tracer

fields given the matter density perturbation, see e.g. Ref. [137]. Hence, the deterministic stress tensor can be written schematically as

$$\tau^{ij}_{\text{det}} = \sum_{\mathcal{O}} c_{\mathcal{O}}\, \mathcal{O}^{ij}\,, \tag{3.88}$$

where the time-dependent coefficients $c_{\mathcal{O}}$ are EFT parameters and the operators $\mathcal{O}$ are products of (gradients of) smoothed fields. The possible operators that can appear in the sum (3.88) are constrained by Galilean invariance and the weak equivalence principle, in particular $\mathbf{v}$ cannot appear without derivatives, ϕ without derivatives is unphysical and no terms containing $\nabla\phi$ in addition to the one already in the Euler equation (3.84b) are allowed [194, 248]. Hence, we have the following *building blocks*

$$\partial^i\partial^j\boldsymbol{\phi} \qquad \text{and} \qquad \partial^i u^j\,, \tag{3.89}$$

from which operators preserving the underlying symmetries can be constructed. Here, we defined the rescaled gravitational potential $\boldsymbol{\phi} = 2\phi/(3\Omega_{\text{m}}\mathcal{H}^2)$ that satisfies $\Delta\boldsymbol{\phi} = \delta$ as well as the rescaled velocity field $\mathbf{u} = -\mathbf{v}/\mathcal{H}f = -\,\mathrm{d}\mathbf{x}/\mathrm{d}\eta$ for convenience. Hence, the trace of the operators above yields the density contrast and the (rescaled) velocity divergence. We define the traceless parts as

$$s^{ij} = \left(\partial^i\partial^j - \delta^{(\text{K})ij}\frac{\nabla^2}{3}\right)\boldsymbol{\phi}\,, \tag{3.90a}$$

$$\kappa^{ij} = \partial^i u^j + \partial^j u^i - \frac{2}{3}\delta^{(\text{K})ij}\nabla\cdot\mathbf{u}\,, \tag{3.90b}$$

corresponding to the tidal tensor and velocity shear, respectively. Hence, we can equivalently work with the building blocks $\{\delta, \theta, s^{ij}, \kappa^{ij}\}$.

Both short- and long-wavelength fluctuations evolve on the same time-scale, H^{-1}, which means that the stress-tensor depends on the evolution of the long modes on the entire past Lagrangian trajectory. In other words, the effective theory is non-local in time [249, 250]. Explicitly, for a fluid element at position $\mathbf{x}$ at time η, the stress tensor depends on the past trajectory $\mathbf{x}_{\text{fl}}(\mathbf{x}, \eta; \eta')$ as a function of η',

$$\mathbf{x}_{\text{fl}}(\mathbf{x}, \eta; \eta') = \mathbf{x} + \int_{\eta'}^{\eta} \mathrm{d}\eta''\, \mathbf{u}\left(\mathbf{x}_{\text{fl}}(\mathbf{x}, \eta, \eta''), \eta''\right)\,. \tag{3.91}$$

For operators containing multiple fields, we need to include also products evaluated at different times, i.e. integrate over the past trajectory of each field. Therefore, the most general form of the deterministic stress tensor is given by

$$\tau^{ij}_{\text{det}}(\eta) = \sum_{\mathcal{O}} \int^{\eta} \mathrm{d}\eta_1 \cdots \mathrm{d}\eta_n\, c_{\text{O}}(\eta; \eta_1, \ldots, \eta_n) \prod_{m=1}^{n} \mathcal{O}_m\left(\mathbf{x}_{\text{fl}}(\mathbf{x}, \eta, \eta_m), \eta_m\right)\,, \tag{3.92}$$

where each factor $\mathcal{O}_m$ comprises (gradients of) one of the building blocks $\{\delta, \theta, s^{ij}, \kappa^{ij}\}$ evaluated at time η_m. Each composite operator $\mathcal{O}^{ij}$ in the sum can furthermore be constructed from all compatible index contractions between the factors $\mathcal{O}_m$ (for which we dropped the tensor indices for simplicity).

In the perturbation theory, we will categorize the operators in (3.92) by the number of fields appearing, and include them consistently at each perturbative order. Additionally, operators with increasing number of gradients are suppressed by powers of k/Λ. Hence, one can systematically improve the EFT by going to higher order in perturbation theory or by adding additional terms in the power expansion in gradients (albeit with an increasing number of EFT parameters). At lowest order in fields and gradients, we have

$$\tau^{ij}_{\rm det}|_1 = \int {\rm d}\eta' \left[\delta^{({\rm K})ij}\left(\tilde{c}^2_{\rm s}(\eta')\delta(\mathbf{x}_{\rm fl},\eta') - \tilde{c}^2_{\rm v,b}(\eta')\nabla\cdot\mathbf{u}(\mathbf{x}_{\rm fl},\eta')\right) - \frac{3}{4}\tilde{c}^2_{\rm v,s}(\eta')\kappa^{ij}(\mathbf{x}_{\rm fl},\eta')\right] \tag{3.93}$$

where we introduced the dimensionless EFT parameters $\tilde{c}_{\rm s}$, $\tilde{c}_{\rm v,b}$, $\tilde{c}_{\rm v,s}$ that can be identified as the sound speed, bulk and shear viscosity of the fluid, respectively [194]. Note that we could have in principle included a spatially constant, zeroth-order in fields term above, however it would be killed by a spatial gradient and not contribute to the effective stress term τ_θ.

The non-local in time formulation above is rather cumbersome; if we Taylor expand each operator building block $\mathcal{O}_m(\mathbf{x}_{\rm fl},\eta_m)$ around $\eta_m=\eta$ the time-integral can be performed. We have

$$\begin{aligned}
\mathcal{O}_m(\mathbf{x}_{\rm fl}(\mathbf{x},\eta,\eta_m),\eta_m) &= \sum_n \frac{1}{n!}\left(D^+(\eta_m)-D^+(\eta)\right)^n\left[\frac{{\rm d}^n}{{\rm d}(D^+)^n}\mathcal{O}_m(\mathbf{x}_{\rm fl}(\mathbf{x},\eta,\eta_m),\eta_m)\right]_{\eta_m=\eta}\\
&= \sum_n \frac{1}{n!}\left(\frac{D^+(\eta_m)-D^+(\eta)}{D^+(\eta_m)}\right)^n\left[\frac{{\rm d}^n}{{\rm d}\eta_m^n}\mathcal{O}_m(\mathbf{x}_{\rm fl}(\mathbf{x},\eta,\eta_m),\eta_m)\right]_{\eta_m=\eta}\\
&= \sum_n \frac{1}{n!}\left(\frac{D^+(\eta_m)-D^+(\eta)}{D^+(\eta_m)}\right)^n\left(\frac{\partial}{\partial\eta}-\mathbf{u}(\mathbf{x},\eta)\cdot\nabla\right)^n\mathcal{O}_m(\mathbf{x},\eta)
\end{aligned} \tag{3.94}$$

where we used ${\rm d}\mathbf{x}_{\rm fl}/{\rm d}\eta_m = -\mathbf{u}(\mathbf{x}_{\rm fl}(\eta_m),\eta_m)$. Inserting this into Eq. (3.92), we obtain a local in time formulation, with modified EFT parameters (which we will not calculate in the end, but measure from N-body data or observations). Nevertheless, it comes at the expense of an infinite sum of terms with increasing convective derivatives which in general contribute at the same order in terms of the typical timescale $\mathcal{H}^{-1}$. When working at a finite order in perturbation theory however, the time-dependence of an n-th order field is $(D^+)^n$ if we specialize to SPT and the EdS-approximation. Therefore only a finite number of terms contribute in the sum above, leading to a finite set of local in time operators contributing to the stress tensor. If the stress tensor contributions are only introduced to correct for the spurious UV-sensitivity of SPT, the perturbative fields in the EFT will also satisfy the same time-dependence. Even though the time-dependence of the EFT operators will in general differ from that of EdS in SPT, we expect the dominant EFT terms to be captured this way. In addition, the velocity field in the convective derivative above will be expanded at n-th order in perturbation theory, yielding only a finite number of terms.

All in all, at lowest order, we can perform the integral (3.93) and obtain the following effective stress term:

$$\tau^{\rm det}_\theta|_1 = \frac{1}{\mathcal{H}^2 f^2}\partial_i\frac{1}{1+\delta}\partial_j\tau^{ij}_{\rm det}|_1 = c^2_{\rm s}\nabla^2\delta - c^2_{\rm v,b}\nabla^2\theta - \frac{3}{4}c^2_{\rm v,s}\nabla^2\theta = c^2_{\rm s}\nabla^2\delta - c^2_{\rm v}\nabla^2\theta \tag{3.95}$$

where we expanded $1/(1+\delta)$ and defined new EFT coefficients $c_{\rm s}^2$ and $c_{\rm v}^2$ after integration and rescaling. Notice that there are two spatial gradients acting on the fields in Eq. (3.95). This is required by momentum conservation, in particular the effect of the short-scale physics as described by $\tau_\theta^{\rm det}$ on a long-wavelength density field δ must go to zero faster than k^2 times δ in the limit $k \to 0$ (in Fourier space)[89, 194, 202].

So far, we only discussed the deterministic part of the stress tensor. The second, stochastic contribution does not correlate with the long modes and describes the deviation between the expectation value over the short scales and the actual realization. Including it, we have

$$\tau_\theta = \tau_\theta^{\rm det} + \Delta J \tag{3.96}$$

where $\Delta J = \partial_i \partial_j \Delta\tau^{ij}_{\rm stoch.}$ and $\Delta\tau^{ij}_{\rm stoch.}$ is the stochastic part of the stress tensor. As discussed above, momentum conservation implies that ΔJ vanishes faster than k^2 in the long-wavelength limit. In addition, since ΔJ is uncorrelated with the density field, it will only correct the power spectrum via the auto-correlation $\langle \Delta J \Delta J \rangle$, and hence it is suppressed by k^4.

The importance of different contributions can be studied exactly in an EdS universe with a power-law initial spectrum, $P_0 \propto k^n$. For $n > -3$, the only available scale is where the linear mode variance crosses unity: $k_{\rm NL}$, and the linear, dimensionless power spectrum is given by $\Delta^2_{\rm lin} = (k/k_{\rm NL})^{3+n}$. At L-loop, one finds the following scalings [237]:

$$\Delta^2_{L\text{-loop}} \sim \left(\frac{k}{k_{\rm NL}}\right)^{(n+3)(L+1)}, \qquad \Delta^2_{\rm det} \sim \left(\frac{k}{k_{\rm NL}}\right)^{n+5}, \qquad \Delta^2_{\rm stoch.} \sim \left(\frac{k}{k_{\rm NL}}\right)^{7}. \tag{3.97}$$

In our Universe, we have $n \approx -3/2$ at $k = k_{\rm NL}$. Hence, the stochastic contribution is even less important than the two-loop correction, and we will neglect it in this thesis. Furthermore, the deterministic part contributes similarly to the one-loop correction, hence the EFT corrections start at the lowest non-linear order, effectively counting $c_{\rm s}^2 = \mathcal{O}([\delta^{(0)}]^2)$.

Effective theory in the EdS-approximation

We show explicitly how the EFT corrections can cure the spurious UV sensitivity of SPT in the particular case of EdS dynamics. In Chapter 5, we indeed specialize to EdS when we derive the NNLO bispectrum in an effective theory framework. Moreover, the effective theory in EdS is illustrative for the general case, and serves as a starting point for our application of the effective theory framework to structure formation with massive neutrinos in Chapter 4.

We solve the equations of motion (3.86) in the presence of the effective stress tensor term (3.87). At one-loop, only the lowest-order stress term (3.95) appears, containing linear fields. In EdS, the linear density contrast and velocity divergence are related by $\delta^{(1)} = -\theta^{(1)}/\mathcal{H}f$, hence we can write

$$\tau_\theta|_1 = \tilde{\gamma}_1 \nabla^2 \delta^{(1)}\,, \tag{3.98}$$

at this order (dropping the "det" superscript as we neglect stochastic contributions), with $\tilde{\gamma}_1 = c_{\rm s}^2 + \mathcal{H}f c_{\rm v}^2$. The new source term yields a particular solution in Fourier space

$$\tilde{\delta}^{(1)}(\mathbf{k},\eta) = -k^2 \int {\rm d}\eta'\, G(\eta,\eta')\tilde{\gamma}_1(\eta')\delta^{(1)}(\mathbf{k},\eta') = -{\rm e}^{3\Delta\eta} k^2 \gamma_1 \delta_0(\mathbf{k},\eta) \equiv {\rm e}^{3\Delta\eta}\tilde{F}^{(1)}(\mathbf{k})\delta_0(\mathbf{k})\,, \tag{3.99}$$

where $G(\eta, \eta')$ is the Green's function for the homogeneous system (3.86) and we recall that $\delta^{(1)}(\mathbf{k}, \eta) = \mathrm{e}^{\Delta\eta}\delta_0(\mathbf{k})$ is the linear density contrast increasing with the growth factor. The exact form of the Green function can be found in e.g. Refs. [210, 211], it is not important for this discussion however: in the end we measure the EFT coefficient from simulations, and we could therefore directly perform the time integration above and write the result in terms of a new parameter γ_1. In Eq. (3.99), we extracted a factor $\mathrm{e}^{2\Delta\eta}$ for convenience and defined the *counterterm kernel* $\tilde{F}^{(1)}$. Hence, the density contrast up to third order is given by

$$\delta(\mathbf{k}, \eta) = \delta^{(1)}(\mathbf{k}, \eta) + \delta^{(2)}(\mathbf{k}, \eta) + \delta^{(3)}(\mathbf{k}, \eta) - \mathrm{e}^{3\Delta\eta}\tilde{F}^{(1)}\delta_0(\mathbf{k}, \eta)\,. \tag{3.100}$$

The corresponding correction to the power spectrum at one-loop is the *counterterm*

$$P_{1L}^{\mathrm{ctr}} = -2\mathrm{e}^{4\Delta\eta}\tilde{F}^{(1)}P_0(k) = -2\mathrm{e}^{4\Delta\eta}\gamma_1 k^2 P_0(k)\,. \tag{3.101}$$

Notice that, crucially, the k-dependence of this counterterm matches exactly that of the UV-limit of the one-loop correction to the power spectrum, as seen in Eq. (3.77). This serve as a consistency check: the EFT term indeed precisely correct for the spurious UV contributions to the one-loop corrections. Moreover, the EFT coefficient depends on the smoothing scale Λ, and we can deduce this dependence by demanding that after renormalization, i.e. after adding the counterterm (3.101), the result has no dependence on the artificial smoothing scale Λ. In other words, we have

$$P_{1L}^{\mathrm{ren}}(k) = P_{1L}(k;\Lambda) + P_{1L}^{\mathrm{ctr}}(k;\Lambda) = 2P^{(13)}(k;\Lambda) + P^{(22)}(k;\Lambda) + P_{1L}^{\mathrm{ctr}}(k;\Lambda)\,, \tag{3.102}$$

whose cutoff-dependence is determined by

$$\frac{\mathrm{d}}{\mathrm{d}\Lambda}P_{1L}^{\mathrm{ren}}(k) = \mathrm{e}^{4\Delta\eta}\frac{\mathrm{d}}{\mathrm{d}\Lambda}\left[-\frac{61}{210}k^2P_0(k)\sigma_{\mathrm{d}}^2(\Lambda) - \gamma_1(\Lambda)k^2P_0(k)\right]\,, \tag{3.103}$$

where we in the second equation used the UV-limit from Eq. (3.77). This result is valid at leading power in the expansion in gradients, i.e. up to corrections of $\mathcal{O}(k^4/k_{\mathrm{NL}}^4)$. The cutoff-dependence is exactly zero if we let

$$\gamma_1(\Lambda) = \bar{\gamma}_1 + \frac{4\pi}{3}\frac{61}{210}\int_\Lambda^\infty \mathrm{d}q\, P_0(q)\,. \tag{3.104}$$

where $\bar{\gamma}_1 = \gamma_1(\Lambda = \infty)$ is an initial condition.

Next, we consider the effective stress term at second order in fields, which will be relevant for the two-loop power spectrum and the one-loop bispectrum. For this, we need to include operators at second order to the effective stress tensor:

$$\mathcal{O} \subset \left\{\delta^{(\mathrm{K})ij}\delta_{\eta_1}\delta_{\eta_2},\, s^{ij}_{\eta_1}\delta_{\eta_2},\, s^{ik}_{\eta_1}s^{kj}_{\eta_2},\, \delta^{(\mathrm{K})ij}s^{lk}_{\eta_1}s^{kl}_{\eta_2}\right\} \tag{3.105}$$

where the subscript labels the time along the fluid path, corresponding to η_m in the integral (3.92). There are in addition an equivalent set of operators from the velocity fields θ and κ^{ij}. Rewriting the effective stress tensor contributions in terms of local in time

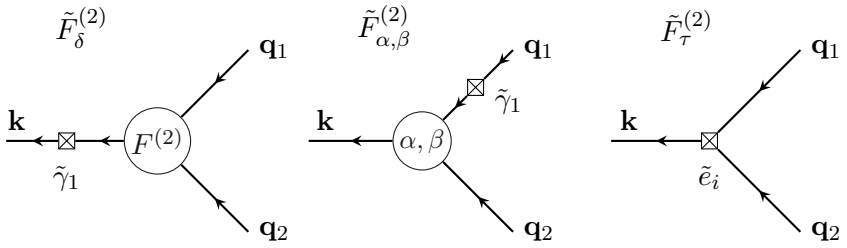

Figure 3.10: Diagrammatic representations of the contributions to $\tilde{F}^{(2)}$. The crossed boxes indicates insertions of EFT operators. Adopted from Ref. [250].

operators via Eq. (3.94), one can obtain the following basis for the second order effective stress term [213, 250][10]

$$\tau_\theta\big|_2 = \tilde{\gamma}_1 \Delta\delta^{(2)} + \tilde{e}_1 \Delta\left[\delta^{(1)}\right]^2 + \tilde{e}_2 \Delta\left[s^{(1)}_{ij} s^{(1)ij}\right] + \tilde{e}_3 \partial_i\left[s^{(1)ij}\partial_j \delta^{(1)}\right] , \tag{3.106}$$

with additional EFT parameters $\tilde{e}_i$ in addition to $\tilde{\gamma}_1$. The particular solution for the density contrast at second order arising from the EFT source term can be written in Fourier space in terms of a new counterterm kernel $\tilde{F}^{(2)}$ [250],

$$\tilde{\delta}^{(2)}(\mathbf{k},\eta) = \int_{\mathbf{q}} \tilde{F}^{(2)}(\mathbf{q}, \mathbf{k}-\mathbf{q})\delta^{(1)}(\mathbf{k},\eta)\delta^{(1)}(\mathbf{k},\eta) \tag{3.107}$$

which can be split into three separate contributions: $\tilde{F}^{(2)} = \tilde{F}^{(2)}_{\delta} + \tilde{F}^{(2)}_{\alpha,\beta} + \tilde{F}^{(2)}_{\tau}$, as depicted in Fig. 3.10. The first term is simply $\tilde{F}^{(2)}_{\delta} = -\gamma_1 k^2 F^{(2)}$, corresponding to the first term in Eq. (3.106). Here, we implicitly integrated the EFT source term over time with an appropriate Green's function (cf. Eq. (3.99)) and incorporated the result in γ_1 (without a tilde). $\tilde{F}^{(2)}_{\alpha,\beta}$ expresses non-linear corrections to the leading order particular solution $\tilde{\delta}^{(1)}$, as given by Eq. (3.99), i.e. coupling $\delta^{(1)}$ or $\theta^{(1)}$ with $\tilde{\delta}^{(1)}$ or $\tilde{\theta}^{(1)}$ by the coupling functions α and β. Finally, the $\tilde{F}^{(2)}_{\tau}$ part captures the three operators in Eq. (3.106) with new coefficients $\tilde{e}_i$. By Fourier transforming those operators, we can write

$$\tilde{F}^{(2)}_{\tau}(\mathbf{q}_1,\mathbf{q}_2) = \sum_{i=1}^{3} e_i E_i(\mathbf{q}_1,\mathbf{q}_2) , \tag{3.108}$$

with

$$E_1(\mathbf{q}_1,\mathbf{q}_2) = (\mathbf{q}_1+\mathbf{q}_2)^2 , \tag{3.109a}$$

$$E_2(\mathbf{q}_1,\mathbf{q}_2) = (\mathbf{q}_1+\mathbf{q}_2)^2\left(\frac{(\mathbf{q}_1\cdot\mathbf{q}_2)^2}{q_1^2 q_2^2} - \frac{1}{3}\right) , \tag{3.109b}$$

[10] This result is obtained from relating $\delta^{(1)} = -\theta^{(1)}/\mathcal{H}f$, as well as noticing that θ_2 is redundant, which can be seen from the relation $(\mathbf{q}_1+\mathbf{q}_2)^2\left[F^{(2)}_1(\mathbf{q}_1,\mathbf{q}_2) - G^{(2)}_1(\mathbf{q}_1,\mathbf{q}_2)\right] = 4E_1/21 - 2E_2/7$, with E_i defined in Eq. (3.109). Furthermore, expanding the denominator $1/(1+\delta)$ in Eq. (3.87) yields no new terms that are not already accounted for in the stress tensor expansion.

$$E_3(\mathbf{q}_1,\mathbf{q}_2) = -\frac{1}{6}(\mathbf{q}_1+\mathbf{q}_2)^2 + \frac{1}{2}\mathbf{q}_1\cdot\mathbf{q}_2\left(\frac{(\mathbf{q}_1+\mathbf{q}_2)\cdot\mathbf{q}_2}{q_2^2} + \frac{(\mathbf{q}_1+\mathbf{q}_2)\cdot\mathbf{q}_1}{q_1^2}\right). \tag{3.109c}$$

The $\tilde{F}^{(2)}_\delta$ and $\tilde{F}^{(2)}_{\alpha,\beta}$ parts contain $F^{(2)}$ and combinations of the mode coupling functions α and β, that can be written as

$$\Gamma(\mathbf{q}_1,\mathbf{q}_2) = (\mathbf{q}_1+\mathbf{q}_2)^2 F_1^{(2)}(\mathbf{q}_1,\mathbf{q}_2) + \frac{2}{11}\left(\frac{10}{21}E_1(\mathbf{q}_1,\mathbf{q}_2) - \frac{5}{7}E_2(\mathbf{q}_1,\mathbf{q}_2) - 3E_3(\mathbf{q}_1,\mathbf{q}_2)\right). \tag{3.110}$$

In total, we can write the counterterm kernel as

$$\tilde{F}^{(2)}(\mathbf{q}_1,\mathbf{q}_2) = \sum_{i=1}^{3} e_i E_i(\mathbf{q}_1,\mathbf{q}_2) + \gamma_1\Gamma(\mathbf{q}_1,\mathbf{q}_2)\,. \tag{3.111}$$

UV sensitivity at two-loop

So far, using EdS-SPT kernels, we showed that $\tilde{F}^{(1)}$ can renormalize the one-loop power spectrum, and we derived $\tilde{F}^{(2)}$ which combined with $\tilde{F}^{(1)}$ can renormalize the one-loop bispectrum, as will be shown in Chapter 5. While one in principle could derive the third[11] and fourth order counterkernels, which is needed for the two-loop power spectrum and bispectrum, respectively, we opt for another approach when renormalizing those corrections, where the explicit expressions of the higher order EFT operators are not needed. The number of operators and corresponding EFT parameters grows rapidly at higher orders, and in practice there is a large degeneracy between them. Therefore, when calibrating the EFT result to N-body simulations, using an ansatz to only fit for the overall amplitude of the counterterms is often sufficient [252, 253]. With a large number of free parameters, there is also the risk of overfitting the data.

We will follow the prescription of Ref. [252], which we explain in the following. The starting point is to examine the UV sensitivity of the two-loop correction. It consists of an integral over two momenta $\mathbf{q}_1$ and $\mathbf{q}_2$ (see Eq. (3.71) for the power spectrum), and we can distinguish between two contributions from the UV: the *double-hard (hh)* and *single-hard (h)* limits. In the double-hard limit, both loop momenta becomes hard compared to the external momentum, schematically $k \ll q_1, q_2$, and in the single-hard limit only one of the momenta become hard, e.g. $k \sim q_2 \ll q_1$. Both in the case of the power- and bispectrum (as well as in the presence of massive neutrinos in Chapter 4), we will show that the double-hard limit can be renormalized by the EFT operators already introduced to renormalize the respective one-loop corrections. Following Ref. [252], the remaining single-hard UV sensitivity can be corrected for by a single additional EFT parameter. We explain this method in detail for the power spectrum in EdS below, and extend it to capture also structure formation with massive neutrinos in Chapter 4 as well as to the bispectrum in Chapter 5.

The different contributions to the two-loop correction to the power spectrum is given in Eq. (3.71) and the corresponding diagrams are shown in Fig. 3.7. Considering first the double-hard limit, it is instructive to consider the parametric scaling of different contributions. We take $q_1 \sim q_2 \sim q$ with $q \to \infty$ and $k \ll q$ fixed. Due to momentum conservation, the

[11] See Ref. [251] for an explicit expression for the $\tilde{F}^{(3)}$ kernel.

kernels entering the different contributions scale as $F^{(n)} \propto k^2/q^2$, hence

$$P^{(15),hh} \sim k^2 P_0(k) \int_{\mathbf{q}} [P_0(q)]^2 / q^2 \,, \qquad P^{(24),hh} \sim k^4 \int_{\mathbf{q}} [P_0(q)]^3 / q^4 \,,$$
$$P^{(33-I),hh} \sim k^4 P_0(k) \int_{\mathbf{q}} [P_0(q)]^2 / q^4 \,, \qquad P^{(33-II),hh} \sim k^4 \int_{\mathbf{q}} [P_0(q)]^3 / q^4 \,. \tag{3.112}$$

The leading UV contribution comes from the propagator correction diagram $P^{(15)}$, which only contains daisy loops. The $P^{(33-I)}$ diagram corresponds to $P^{(13)}$ squared, and is therefore suppressed by an additional factor k^2/q^2. The remaining diagrams represent in the double-hard limit contributions where two short wavelength modes average out to a long wavelength mode, which would be corrected for by stochastic contributions in the effective stress tensor. As we work at leading order in $k^2/k_{\rm NL}^2$, we therefore neglect all double-hard contributions but $P^{(15),hh}$. Its exact dependence on q_1 and q_2 in EdS can be determined [217, 252, 254]:

$$P^{(51),hh}(k) = -\mathrm{e}^{6\Delta\eta} k^2 P_0(k) \frac{11191}{6449625} \int_{\mathbf{q}_1,\mathbf{q}_2} \frac{S_1(q_1/q_2)}{q_1 q_2} P_0(q_1) P_0(q_2) \,, \tag{3.113}$$

where

$$S_1(r) = -\frac{1}{716224 r^6} \Big[4r(1+r^2)(5760 + 13605 r^2 - 128258 r^4 + 13605 r^6 + 5760 r^8) \\ + 30(r^2-1)^4 (384 + 2699 r^2 + 384 r^4) \ln\left(\frac{|1-r|}{1+r}\right) \Big] \,. \tag{3.114}$$

Indeed, we see that the leading double-hard contribution to the two-loop power spectrum correction is proportional to $k^2 P_0(k)$ and can be absorbed by the counterterm that was introduced in Eq. (3.101) to renormalize the one-loop correction.

The leading contributions to the single-hard limit arises from diagrams in which one daisy loop is hard. Hence we neglect the single-hard contribution from $P^{(33-II)}$ and from $P^{(24)}$ where the hard momentum is running in the "connecting" loop between the blobs. Taking $q_1 \to \infty$, the relevant limits are [252]

$$P^{(15),h}(k) = \mathrm{e}^{6\Delta\eta} \sigma_{\rm d}^2 \frac{k^2 P_0(k)}{1412611200} \int_{\mathbf{q}_2} P_0(q_2) \\ \times \Big\{ -2 r_2 (2266005 - 33470730 r_2^2 + 187902172 r_2^4 - 9879110 r_2^6 + 1167375 r_2^8) \\ + 15(-1+r_2^2)^3 (-151067 - 451074 r_2^2 + 77825 r_2^4) \ln\left(\frac{1+r_2}{|1-r_2|}\right) \Big\} \,, \tag{3.115a}$$

$$P^{(24),h}(k) = \mathrm{e}^{6\Delta\eta} \sigma_{\rm d}^2 \frac{k^2}{113190} \int_{\mathbf{q}_2} P_0(|\mathbf{k}-\mathbf{q}_2|) P_0(q_2) F^{(2)}(\mathbf{q}_2, \mathbf{k}-\mathbf{q}_2) \frac{1}{r_2(1+r_2^2-2r_2\mu_2)} \\ \times \Big\{ (-32879\mu_2 + r_2^3(6176 - 48096\mu_2^2) + 32 r_2^2 \mu_2 (1117 + 1503\mu_2^2) +$$

$$r_2(-25933 + 16892\mu_2^2))\Big\}\,, \tag{3.115b}$$

$$P^{(33-I),h}(k) = -2\mathrm{e}^{6\Delta\eta}\frac{61}{210}\sigma_\mathrm{d}^2 k^2 P^{(13)}(k)\,, \tag{3.115c}$$

where $r_2 = q_2/k$ and $\mathbf{k}\cdot\mathbf{q}_2 = kq_2\mu_2$. Noting that all limits contain the displacement dispersion σ_d^2, Ref. [252] makes the assumption that the EFT corrects the UV in a universal manner, by a shift in the displacement dispersion

$$\sigma_\mathrm{d}^2(\Lambda) \mapsto \sigma_\mathrm{d}^2(\Lambda) + \mathcal{N}\gamma_2\,. \tag{3.116}$$

Here, γ_2 is an EFT parameter and $\mathcal{N}$ is a factor introduced for convenience. The replacement thus corresponds to adding a counterterm

$$P_{2L}^\mathrm{ctr}(k;\Lambda) = \mathrm{e}^{6\Delta\eta}p_{2L}^h(k;\Lambda)\mathcal{N}\gamma_2(\Lambda)\,, \tag{3.117}$$

where

$$p_{2L}^h(k;\Lambda) = \frac{1}{\sigma_\mathrm{d}^2}\left[P^{(15),h}(k;\Lambda) + P^{(24),h}(k;\Lambda) + P^{(33-I),h}(k;\Lambda)\right]\,. \tag{3.118}$$

We illustrate the effect of adding EFT corrections to the perturbative prediction of the power spectrum in Fig. 3.11, using the approach described above. The one-loop, or next-to-leading order (NLO) results are displayed in blue and the two-loop, or NNLO results in green, both normalized to the linear power spectrum. For comparison, we plot the power spectrum computed using the Quijote N-body simulations [174]. (Details for this and similar comparisons will be given explicitly in Chapter 4, here we only make a qualitative comparison.) Clearly, the EFT prediction matches the N-body data much better than SPT, in particular also on larger scales $k \simeq 0.1h$ Mpc^{-1}, where the theoretical uncertainty is expected to be small. It is important to note that the relatively good agreement of the SPT prediction on mildly non-linear scales at two-loop is largely due to the cancellation of the one- and two-loop corrections, which on those scales have opposite signs (see Fig. 3.8). If we would add the three-loop correction, the agreement would worsen, an obvious indication of the breakdown of perturbation theory. In the EFT on the other hand, the prediction can be systematically improved by including additional loop corrections and higher derivative operators, however at the expense of additional EFT coefficients.

3.7 Resummation of large bulk flows

We finish this chapter by discussing the resummation of contributions from large wavelength modes, known as IR-resummation. It is well known that Eulerian perturbation theory does not adequately model the effect of large bulk flows on the BAO peak [226, 255]. This can nevertheless be remedied in a relatively straightforward manner by resumming the effect of large displacements in the IR non-perturbatively [146–149]. We will employ IR resummation when modeling massive neutrinos in structure formation in Chapter 4, in order to compare and calibrate to N-body simulations as accurately as possible.

IR resummation in SPT is nicely derived in e.g. Appendix F of Ref. [149], and we repeat the resulting resummation method here. The first step is to split the linear power spectrum

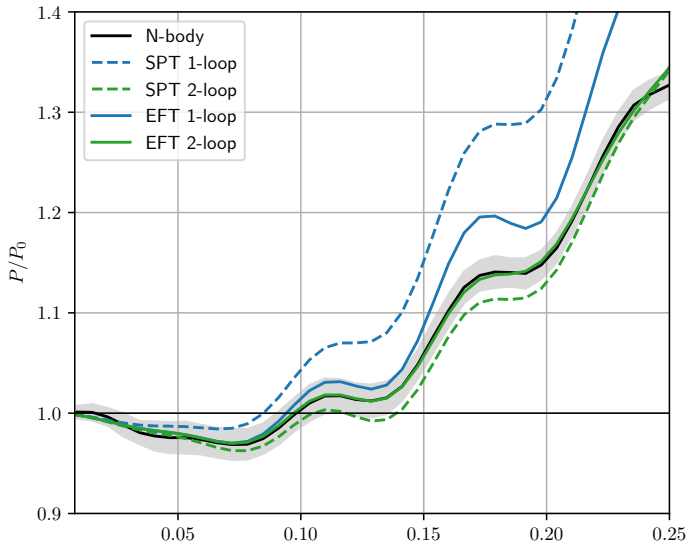

Figure 3.11: Illustration of the convergence of SPT (dashed) and EFT (solid) perturbative predictions of the power spectrum at NLO (blue) and NNLO (green). The thick, black, solid line shows the N-body result with the gray band indicating estimated uncertainty. The perturbative results are obtained with EdS-SPT kernels and the EFT lines are fitted up until a pivot scale $k_{\rm max} = 0.2h$ Mpc^{-1}.

that is input to the loop corrections into a smooth, non-wiggly part and a wiggly part comprising the BAO feature:

$$P_0(k) = P_{\rm nw}(k) + P_{\rm w}(k)\,. \tag{3.119}$$

This separation is useful because the large bulk flows affect only the BAO wiggles [147, 149]. The non-wiggly part of the power spectrum can be obtained by Fourier transforming the spectrum to real space, manually removing the BAO peak, smoothly interpolating the result and back-transforming to Fourier space, as described in Refs. [256, 257]. Alternatively, one can use an analytic formula for the shape of the smooth power spectrum, as described in Ref. [149] using the Eisenstein-Hu formula [258]. We will employ the first method. The next step is to define the damping factor

$$\Sigma^2 = \frac{4\pi}{3}\mathrm{e}^{2\Delta\eta}\int_0^{k_s}\mathrm{d}q\,P_{\rm nw}(q)\left[1 - j_0\left(\frac{q}{k_{\rm osc}}\right) + 2j_2\left(\frac{q}{k_{\rm osc}}\right)\right]\,, \tag{3.120}$$

where k_s is the separation scale between short and long modes, defining two regimes in which the perturbative description is treated differently, $k_{\rm osc} = h/(110{\rm Mpc})$ is the wavenumber corresponding to the BAO period, and j_n are spherical Bessel functions of order n. The IR-resummed power spectrum at N-th order is then given by

$$P^{\rm IR} = \sum_{L=0}^{N} P_{L\text{-loop}}\left[P_{\rm nw} + P_{\rm w}\,\mathrm{e}^{-k^2\Sigma^2}\sum_{n=0}^{N-L}\frac{(k^2\Sigma^2)^n}{n!}\right] \equiv \sum_{L=0}^{N} P_{L\text{-loop}}\left[P_0^{{\rm IR},N-L}\right]\,. \tag{3.121}$$

Here, we defined in the second equality a short-hard notation $P_0^{\mathrm{IR},N-L}$ for the content of the bracket. In addition, the bracket notation $P_{L\text{-loop}}[X]$ indicates that the L-th loop correction should be computed with X as input power spectrum. For example, for the IR-resummed two-loop integral (3.71), P_0 should be replaced by $P_0^{\mathrm{IR},N-2}$ when working at N-th order in perturbation theory. In Eq. (3.121), the exponential factor resums the contributions from the IR. Since the loop integrals themselves also include contributions from the IR, one needs to correct for the overcounting of IR contributions, yielding the additional factor composed of a sum over n. Notice that in the limit $N \to \infty$, $P_0^{\mathrm{IR},N-L} = P_{\mathrm{nw}} + P_{\mathrm{w}} = P_0$, hence the difference due to IR resummation only appears when working at finite order in perturbation theory.

A key ingredient in deriving the result above is the kernel property in Eq. (3.51) when a subset of the arguments is soft [149]. This property follows from Galilean invariance, and therefore also holds for the generalized kernels defined in Section 3.4. Hence, the IR resummation formula (3.121) can be applied also in our extension of SPT.

For convenience, we write down the explicit resummation formulas up to NNLO in perturbation theory, by applying Eq. (3.121):

$$P_{\mathrm{LO}}^{\mathrm{IR}} = P_{\mathrm{tree}}\left[P_{\mathrm{nw}}(k) + \mathrm{e}^{-k^2\Sigma^2}P_{\mathrm{w}}(k)\right], \tag{3.122a}$$

$$\begin{aligned} P_{\mathrm{NLO}}^{\mathrm{IR}} &= P_{\mathrm{tree}}\left[P_{\mathrm{nw}}(k) + \mathrm{e}^{-k^2\Sigma^2}(1+k^2\Sigma^2)P_{\mathrm{w}}(k)\right] \\ &\quad + P_{1L}\left[P_{\mathrm{nw}}(k) + \mathrm{e}^{-k^2\Sigma^2}P_{\mathrm{w}}(k)\right], \end{aligned} \tag{3.122b}$$

$$\begin{aligned} P_{\mathrm{NNLO}}^{\mathrm{IR}} &= P_{\mathrm{tree}}\left[P_{\mathrm{nw}}(k) + \mathrm{e}^{-k^2\Sigma^2}\left(1+k^2\Sigma^2+\frac{1}{2}(k^2\Sigma^2)^2\right)P_w(k)\right] \\ &\quad + P_{1L}\left[P_{\mathrm{nw}}(k) + \mathrm{e}^{-k^2\Sigma^2}(1+k^2\Sigma^2)P_{\mathrm{w}}(k)\right] \\ &\quad + P_{2L}\left[P_{\mathrm{nw}}(k) + \mathrm{e}^{-k^2\Sigma^2}P_{\mathrm{w}}(k)\right]. \end{aligned} \tag{3.122c}$$

Moreover, in practice, it is convenient to simplify the IR resummed expression in the following way,

$$\begin{aligned} &P_{L\text{-loop}}\left[P_{\mathrm{nw}} + P_{\mathrm{w}}\,\mathrm{e}^{-k^2\Sigma^2}\sum_{n=0}^{N-L}\frac{(k^2\Sigma^2)^n}{n!}\right] \\ &\quad \to P_{L\text{-loop}}\left[P_{\mathrm{nw}}\right] + \left(P_{L\text{-loop}}\left[P_{\mathrm{nw}}+P_{\mathrm{w}}\right] - P_{L\text{-loop}}\left[P_{\mathrm{nw}}\right]\right)\times \mathrm{e}^{-k^2\Sigma^2}\sum_{n=0}^{N-L}\frac{(k^2\Sigma^2)^n}{n!}. \end{aligned} \tag{3.123}$$

This replacement is valid up to corrections of $\mathcal{O}(P_{\mathrm{w}}^2)$ and diagrams containing P_{w} inside a hard loop. Such corrections can safely be neglected however, since the wiggly spectrum is very small compared to the non-wiggly spectrum, and its integral vanishes because it oscillates around zero. Eq. (3.123) is useful since it only involves loop integrals with P_{nw} and $P_{\mathrm{nw}} + P_{\mathrm{w}} = P_0$ as input, as opposed to multiple combinations of inputs in Eq. (3.122).

We illustrate the effect of IR resummation in Fig. 3.12. The NLO and NNLO power spectra in the EFT is displayed with and without IR resummation. The results are normalized to the N-body result (the Quijote simulations [174]). There is an initial "bump" in the perturbative results around $k = 0.01$–0.05 which is due to finite box effects in the simulation and unrelated

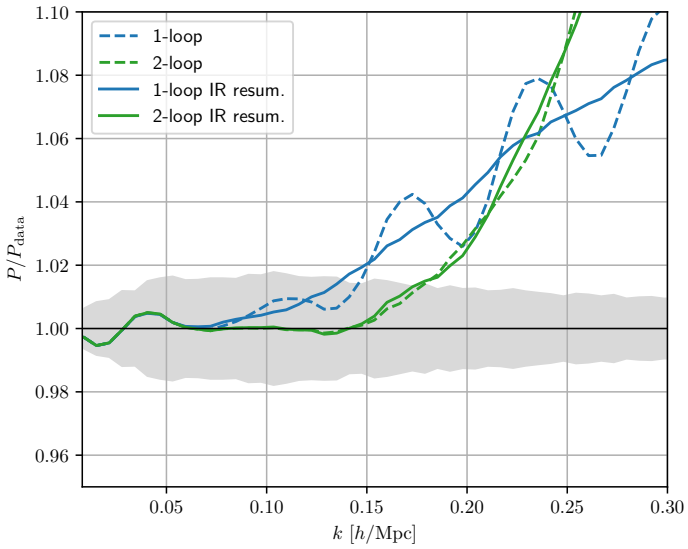

Figure 3.12: Illustration of perturbative results with (solid lines) and without (dashed lines) IR resummation. The NLO (blue) and NNLO (green) predictions are computed in the EdS-approximation, including EFT corrections fitted up to $k_{\rm max} = 0.2h$ Mpc^{-1}. All graphs are normalized to the N-body result (Quijote simulations), with the gray band indicating N-body uncertainty.

to IR resummation. For larger k, it is apparent that the IR resummed predictions better match the BAO wiggles of the N-body results than those without resummation. Note that as higher and higher corrections are added, the perturbative result itself more accurately models the effect of large bulk flows on the BAO wiggles, and there is less need for IR resummation. Indeed, we see in Fig. 3.12 that already at two-loop the effect of IR resummation is modest.

Summary In this chapter, we have introduced cosmological perturbation theory in the Eulerian picture. Starting from the Vlasov-Poisson set of equations, we wrote down perturbative solutions valid in the mildly non-linear regime. In Section 3.4, we introduced an extension of SPT, allowing to capture clustering dynamics with non-trivial scale- and time-dependence. This extention will allow us to treat massive neutrinos in structure formation beyond linear theory in the next chapter. We ended the chapter by describing two ingredients that significantly improve the accuracy of the perturbative prediction: EFT corrections and IR resummation. Both will used when we model the power spectrum in the next chapter, and the EFT formalism will be applied to the bispectrum in Chapter 5.

4 Massive neutrinos in structure formation

Ever since the late 1990s, it has been established that neutrinos oscillate and have non-zero mass [259], providing direct evidence for physics beyond the SM [164, 260]. As neutrinos play a significant role in the history of the Universe, cosmological probes can shed light on various neutrino properties, in particular the absolute mass scale [30].

In this chapter, our focus is on the effect of massive neutrinos on structure formation: we present the results of Papers I [44] and III [46], which computed the power spectrum at NNLO in the presence of neutrinos, going beyond previous studies by including the full scale- and time-dependence of the dynamics induced by the neutrino component, as well as computing perturbations in the neutrino fluid beyond linear theory. We start by a review of the CνB and mention some important cosmological probes for measuring neutrino properties. In Section 4.2, we introduce a two-component fluid model of structure formation with CDM+baryons and neutrinos coupled via gravity, and discuss its performance compared to the full Boltzmann solution at the linear level. This model is perfectly suited to be captured by the extension of SPT introduced in Section 3.4, and we can therefore compute non-linear corrections and compare to simplified treatments in Section 4.3. In Section 4.4, we embed the two-component fluid model in an EFT framework, finding that we can renormalize the loop corrections on scales much smaller than the neutrino freestreaming scale. Finally, we compare and calibrate the model to N-body simulations in Section 4.5.

4.1 Neutrinos in cosmology

The hot Big Bang model predicts the existence of a cosmic neutrino background of relic, non-relativistic (today) neutrinos that were produced thermally in the early Universe. The number density of this background is only slightly less than that of the CMB, but the typical kinetic energy of the cosmic neutrinos today are of order $10^{-4}\,\mathrm{eV}$, which combined with their weakly interacting nature makes them notoriously difficult to detect [261]. We describe in this section the main elements of the evolution of neutrinos throughout the history of the Universe and discuss its impact on cosmological observables as well as current constraints. More comprehensive reviews of neutrinos in cosmology can be found in Refs. [30, 32, 262, 263].

Let us first briefly state the current experimental status of certain neutrino properties. Global fits to neutrino oscillation experiments yield mass splittings $\Delta m^2_{21} \simeq 7.42 \times 10^{-5}\,\mathrm{eV}^2$ and $|\Delta m^2_{31}| \simeq 2.5 \times 10^{-3}\,\mathrm{eV}^2$ [31]. The sign of the last splitting is unknown, leaving two possibilities open for the neutrino mass hierarchy: in *normal ordering* $\Delta m^2_{31} > 0$ and $m_1 < m_2 < m_3$, while for *inverted ordering*, $\Delta m^2_{31} < 0$ and $m_3 < m_1 < m_2$. The measurements imply a lower bound on the sum of neutrino masses $\sum m_\nu \gtrsim 0.06$ eV for normal ordering and $\sum m_\nu \gtrsim 0.1$ eV for inverted ordering. On the other hand, β-decay measurements sets an upper bound $m_\beta < 0.8$ eV at 90 % C.L. on the effective electron

anti-neutrino mass [264]. In addition to particle physics experiments, cosmologial probes offer complementary information. Depending on the combination of data sets used, current cosmological limits constrain $\sum m_\nu < 0.1$–0.2 eV [8, 265] and the limits are expected to tighten significantly in the next years [19, 20]. We discuss the cosmological bounds more in detail below.

The cosmic neutrino background

In the early Universe, neutrinos are strongly coupled to the thermal plasma by frequent weak interactions, keeping the distribution function in an equilibrium Fermi-Dirac form: spatially homogeneous and isotropic and with temperature equal to the plasma $T_\nu = T_\gamma = T$,[1]

$$f(p,z) = \frac{g}{(2\pi)^3}\frac{1}{\mathrm{e}^{p/T}+1}\,. \tag{4.1}$$

For a single neutrino species, $g = 2$, accounting for particle and antiparticle, and we have used $E = p$ in the ultra-relativistic limit. As the Universe cools, weak interactions become less frequent, and when the rate drops below the Hubble rate the neutrinos decouple from the plasma. The weak interaction rate can be approximated by $\Gamma \approx G_\mathrm{F} T_\nu^5$, where G_F is the Fermi constant. Using also $H \approx T^2/M_P$, where $M_P = G^{-1/2}$ is the Planck mass, applicable during radiation domination, one finds a decoupling temperature $T_\mathrm{dec} \approx 1$ MeV. This temperature is much larger than the mass of the neutrinos, hence the neutrinos are still relativistic when decoupling.[2]

After decoupling, neutrinos propagate freely. The distribution function is therefore "frozen" in the *ultra-relativistic* Fermi-Dirac form, even when neutrinos become non-relativistic. Since the particle momentum redshifts as $p \propto (1+z)$, the neutrino temperature[3] also redshifts as $T_\nu \propto (1+z)$. As the plasma temperature also decreases with the scale factor, the neutrino temperature initially follows the plasma temperature after decoupling. However, at $T \sim m_e/3 \sim 0.2$ MeV, when electrons and positrons become non-relativistic, the favored annihilation of e^+e^- into photons transfers their entropy to the photon fluid. Since neutrinos are decoupled from the photon plasma, they do not feel this heating of the photons. Using entropy conservation, one can show that the neutrino and photon temperatures are afterwards related by (see e.g. Refs. [2, 17, 30] for a derivation)

$$T_\nu = \left(\frac{4}{11}\right)^{1/3} T_\gamma \simeq 0.71\, T_\gamma\,. \tag{4.2}$$

This relation remains valid until today, implying that the CνB has a present day temperature $T_\nu(z=0) = 0.71\, T_{\gamma,0} = 1.95\,\mathrm{K}$, where we inserted the measured CMB temperature $T_{\gamma,0}$ [68]. In reality, the neutrino decoupling and e^+e^--annihilation processes are not instantaneous,

[1] We neglect the neutrino chemical potential, which on theoretical grounds is expected to be of the order of the matter-antimatter asymmetry, i.e. $\sim 10^{-10}$ [30, 263].

[2] For neutrinos with $m_\nu = 1$ eV and decoupling temperature $T_\mathrm{dec} = 1$ MeV, only 1 in 10^{19} neutrinos has momentum $p < m_\nu$ at decoupling [263].

[3] After decoupling, the neutrinos are not in thermal equilibrium, and therefore *temperature* is not technically an appropriate term. We use it nonetheless, understanding that it refers to the neutrino distribution in the ultra-relativistic Fermi-Dirac form.

in particular neutrinos on the high-energy tail of the distribution are still coupled to the plasma and heated by the e^+e^- entropy injection. Therefore, the neutrino temperature is slightly larger than that given in Eq. (4.2). We comment on the precise value shortly.

As the Universe expands, the neutrinos redshift and at some point become non-relativistic. We can define the non-relativistic transition as the redshift at which the average neutrino momentum $\langle p \rangle$ equals the neutrino mass. We have

$$\langle p \rangle = \frac{\int \mathrm{d}^3 p \, p \, (\exp[p/T_\nu] + 1)^{-1}}{\int \mathrm{d}^3 p \, (\exp[p/T_\nu] + 1)^{-1}} = \frac{7\pi^4}{180\zeta(3)} T_\nu \simeq 3.15 T_\nu \,, \tag{4.3}$$

and thus the non-relativistic transition occurs at

$$1 + z_{\mathrm{nr}} = 189 \frac{m_\nu}{0.1 \text{ eV}} \,. \tag{4.4}$$

This implies that neutrinos with mass $m_\nu \lesssim 1.8$ eV and $m_\nu \lesssim 0.6$ eV became non-relativistic after matter-radiation equality and recombination, respectively. Given the current experimental upper mass bounds discussed above however, the transition happened at $z_{\mathrm{nr}} = \mathcal{O}(100)$. Furthermore, from the mass splittings from oscillation data quoted previously, we know that at least two neutrinos are non-relativistic today (the lightest neutrino eigenstate in the mass basis could be massless).

By integrating the neutrino distribution function, we obtain the number density for each flavor as a function of neutrino temperature:

$$n_\nu(z) = \frac{3 g \zeta(3)}{4\pi^2} T_\nu^3(z) \,. \tag{4.5}$$

Inserting the temperature today, $g = 2$ and counting three neutrino flavors yields a neutrino particle density today of approximately $340\,\mathrm{cm}^{-3}$. To obtain an expression for the energy density, we need to discriminate before and after the non-relativistic transition. While neutrinos were ultra-relativistic, the energy density of each species was [30],

$$\rho_\nu = \frac{7\pi^2}{120} \left(\frac{4}{11}\right)^{4/3} T_\gamma^4 \qquad (T_\nu \gg m_\nu) \,. \tag{4.6}$$

It is useful to relate this to the photon energy density, $\rho_\gamma = (\pi^2/15) T^4$, so that the total energy density of relativistic species in the early Universe can be expressed as

$$\rho_{\mathrm{r}} = \left[1 + \frac{7}{8} \left(\frac{4}{11}\right)^{4/3} N_{\mathrm{eff}}\right] \rho_\gamma \,. \tag{4.7}$$

Here, the new parameter N_{eff} characterizes the *effective number of relativistic degrees of freedom* in the early Universe. Given that the SM predicts three neutrinos with $g = 2$ degrees of freedom as for the photon, one would expect $N_{\mathrm{eff}} = 3$. However, as we alluded above, the neutrino-photon temperature ratio is not exactly $(4/11)^{1/3}$ due to non-instantaneous neutrino decoupling. Moreover, taking into account finite temperature QED effects and neutrino oscillations, the SM prediction becomes $N_{\mathrm{eff}} = 3.044$ [266]. On the other hand, many extensions of the SM predict the existence of additional (dark) radiation in the early

Universe, and the corresponding additional degrees of freedom are conventionally expressed by $N_{\rm eff}$. The effective number of relativistic degrees of freedom is constrained using CMB measurements by Planck to $N_{\rm eff} = (2.92 \pm 0.37)$ at 95 % C.L. [8].

In the non-relativistic limit, the energy density of the neutrinos is simply $n_\nu \sum m_\nu$, which we can relate to the energy density parameter Ω_ν today by inserting the present day neutrino temperature in Eq.(4.5),

$$\Omega_\nu = \frac{\sum m_\nu n_\nu}{\rho_{\rm crit}} \simeq \frac{\sum m_\nu}{94.14 h^2 \text{ eV}} \simeq 0.0024 \left(\frac{\sum m_\nu}{0.1 \text{ eV}}\right) . \tag{4.8}$$

We also introduce fraction of the neutrino energy density to the total energy density in the late Universe, $f_\nu = \Omega_\nu / \Omega_{\rm m}$. For e.g. a sum of neutrino masses $M_\nu \equiv \sum m_\nu = 0.1$ eV and $\Omega_{\rm m} = 0.3$ today, we have $f_\nu = 0.008$, i.e. a contribution to the present-day total energy budget of less than 1 %.

Freestreaming

An important characteristic of the cosmic neutrinos is that they have a large velocity dispersion, i.e. they *freestream* over large distances. One can define a horizon which corresponds to the typical distance neutrinos can freestream in a Hubble time. The density contrast of the neutrino component can only grow on scales larger than this horizon, because neutrinos cannot remain confined in potential wells with wavelength smaller than the horizon. More quantitatively, we can compute the neutrino velocity dispersion as

$$\left\langle c_\nu^2 \right\rangle = \frac{\int \mathrm{d}^3 p \, p^2/(p^2 + m_\nu^2) \left(\exp[p/T_\nu] + 1\right)^{-1}}{\int \mathrm{d}^3 p \, \left(\exp[p/T_\nu] + 1\right)^{-1}} \xrightarrow[p \ll m_\nu]{} \frac{15\zeta(5)}{\zeta(3)} \left(\frac{4}{11}\right)^{2/3} \frac{T_{\gamma,0}^2 \, (1+z)^2}{m_\nu^2} , \tag{4.9}$$

where we in the second equality evaluated the integral in the non-relativistic limit. In analogy to the Jeans length scale, which generally indicates the scale below which pressure inhibits gravitational collapse, one conventionally defines a *freestreaming length* $\lambda_{\rm FS}$ and the corresponding wavenumber [30, 267]

$$k_{\rm FS} = \sqrt{\frac{3}{2}} \frac{\mathcal{H}}{c_{\rm s}} \simeq \sqrt{\frac{3}{2}} \frac{\mathcal{H}}{\sqrt{\langle c_\nu^2 \rangle}} . \tag{4.10}$$

We approximated the neutrino sound velocity by the velocity dispersion in the last equality; the exact expression will be discussed at length below. We display $k_{\rm FS}$ in Fig. 4.1, computed in Ref. [267] using the full relativistic velocity dispersion (4.9) (thin black line). The figure distinguishes three scales:

(1) A very large scale with $k \ll k_{\rm FS}$ at all times. The neutrino density contrast starts growing after horizon entry, behaving as dark matter.

(2) A small scale for which $k \gg k_{\rm FS}$ at all times. Freestreaming prohibits growth of the neutrino density fluctuation, which oscillates around its small initial value.

(3) An intermediate scale, for which the density contrast is suppressed for a long time, until the freestreaming length decreases to the point where $k = k_{\rm FS}$ and perturbations start to grow.

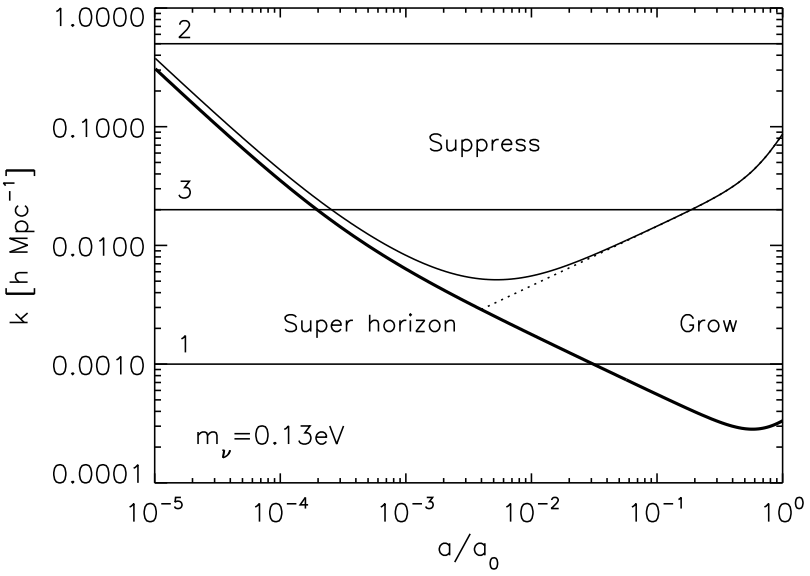

Figure 4.1: Neutrino freestreaming wavenumber $k_{\rm FS}$ as a function of the scale factor a for $m_\nu = 0.13$ eV. The thick solid line shows the comoving horizon, the thinner solid line shows the freestreaming scale computed from the velocity dispersion exactly, while the dotted line corresponds to an approximation in the non-relativistic limit. Three scales (1)-(3) corresponding to different regimes are indicated, see discussion in text. Figure taken from Ref. [267].

In the ultra-relativistic limit, $c_{\rm s} \to 1$ and $k_{\rm FS} \propto (1+z)^{-1/2}$ (during matter domination). In the non-relativistic limit, we can use Eq. (4.9) to conclude that $k_{\rm FS} \propto (1+z)^{1/2}$. The minimal value $k_{\rm FS}$ or the longest freestreaming distance happens at the non-relativistic transition.

In summary, neutrinos are universal throughout the history of the universe. During radiation domination they represent about 40 % of the total energy density, leaving an imprint on the CMB through the gravitational potentials. After decoupling, they freestream over large distances, which prevents growth of the neutrino perturbation, which affects galaxy clustering in the late Universe. We end this section by briefly discussing neutrino impacts on cosmological observables, and current constraints.

Neutrino signatures

Cosmological probes are mainly sensitive to the following neutrino properties: the early Universe energy density and sum of masses. Other properties, such as individual masses, mixing angles and CP violation phase are essentially imperceptible to cosmology, at least with the precision of current and planned surveys [30, 164, 268]. Nevertheless, cosmological experiments can test beyond-SM scenarios with non-standard neutrino interactions, as will be the topic of Chapter 6. We mention here the main signatures of neutrinos on the CMB and galaxy clustering, and refer the reader to more extensive and detailed descriptions in Refs. [8, 30, 32, 164, 262, 263, 269–272].

Neutrino effects on the CMB can be separated into the effect of massless neutrinos, characterized by the parameter N_{eff} and the sum of neutrino masses M_ν. The effects of changing N_{eff} can be mimicked by altering other cosmological parameters, therefore it turns out to be most illuminating to fix matter-radiation equality, matter-vacuum energy equality and ω_{b}, as to isolate the effect of N_{eff} [30]. An increase in N_{eff} leads to increased Silk damping—the washing out of small perturbation modes due to photon diffusion—before decoupling, reducing the damped high-l tail of the angular power spectrum. At the perturbation level, freestreaming neutrinos dampen the gravitational potentials before recombination and decrease the angular peaks. In addition, neutrino perturbations traveling at the speed of light drag along the photons (with a lower speed-of-sound set by the photon-baryon fluid), leading to shifts of the peaks. Similar effects are found for the polarization spectrum, and given that they can hardly be mimicked by other parameters in ΛCDM, CMB measurements yield the constraint $N_{\mathrm{eff}} = (2.92 \pm 0.37)$ at 95 % C.L. [8] as mentioned above, consistent with the standard model prediction [266].

The impact of massive neutrinos is indistinguishable from massless ones in the early Universe, therefore the main signal of the neutrino mass occurs at late times after the non-relativistic transition. Increased neutrino mass raises the total energy density in the late Universe, yielding at the background level a late integrated Sachs-Wolfe (ISW) effect—the impact on the CMB from time-dependent gravitational potentials—and a change of the angular diameter distance to the last scattering surface [30]. Both effects can be mimicked by changing h and Ω_Λ, but not at the same time; since the first peak of the angular power spectrum is very precisely measured, it is most useful to keep the angular diameter distance to the last scattering surface fixed. Then an increase in M_ν is accompanied by a reduced late-ISW effect since matter-vacuum energy equality happens later. A second effect occurs due to the non-relativistic transition, where neutrino perturbations on scales larger than the freestreaming scale, $k < k_{\mathrm{FS}}$, begin acting like a clustering component and reduces the time-variation of the gravitational potentials, yielding an early-ISW effect. Finally, freestreaming neutrinos suppress structure formation on scales smaller than the typical freestreaming distance (we elaborate this directly below), reducing the late-Universe gravitational potential and therefore reducing the lensing of the CMB photons. The Planck experiment constrains the total neutrino mass to be $M_\nu < 0.26$ eV using TT,TE,EE and low-E spectra, and to $M_\nu < 0.24$ eV including CMB lensing, at 95 % C.L. [8].

Next, we consider the effect of neutrinos on the matter power spectrum. If we again consider N_{eff} while keeping z_{eq}, z_Λ and ω_{b} fixed, the amount of dark matter increases with N_{eff}. The altered baryon-to-dark matter ratio has a substantial effect of the power spectrum: CDM experiences gravitational collapse before baryons decouple from photons, while baryons partake in acoustic oscillations and are prevented from clustering until they decouple. Therefore a decreased baryon-to-dark matter ratio leads to increased clustering on small scales, a dampened BAO oscillation feature, and a shift due to the neutrino drag effect as for the CMB.

Due to the large freestreaming scale of the neutrinos, corresponding to a wavenumber $k_{\mathrm{FS}} \sim 0.01h$ Mpc^{-1}, the neutrino density perturbation does not grow on scales $k > k_{\mathrm{FS}}$. Therefore, at late times, neutrinos represent a species that contributes to the background expansion, but only clusters on very large scales. This has important effects on the matter power spectrum, depending on the neutrino mass both from the energy density contribution

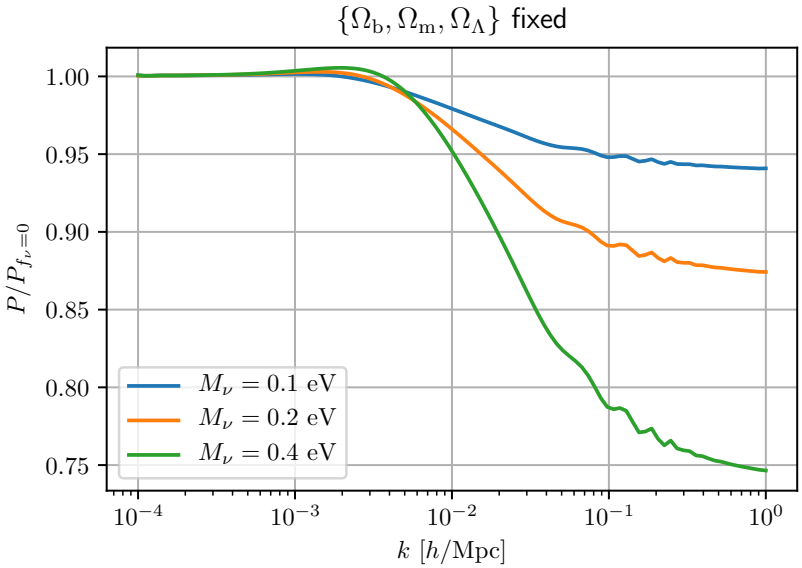

Figure 4.2: Suppression of the matter power for cosmologies with massive neutrinos. We display massive neutrino models with $M_\nu = 0.1$, 0.2, and 0.4 eV, respectively, normalized to a model in which neutrinos have been exchanged for CDM, so that the matter content remains the same.

from the neutrinos as well as the freestreaming scale itself. It is perhaps most illustrative to compare the power spectrum in a massive neutrino model to one in which the CDM density is adjusted so that the total matter energy density is the same in both models (note that $z_{\rm eq}$ would be different between the massive and massless model, and hence the CMB changes significantly). This comparison is shown in Fig. 4.2 for three sums of neutrino masses $M_\nu = 0.1$, 0.2, and 0.4 eV. In the massive models, two effects combine to the suppression of power on scales smaller than the freestreaming scale ($k > k_{\rm FS}$). Firstly, neutrinos do not cluster. Secondly, gravitational wells grow less on these scales since the neutrino perturbation vanishes. The growth of a perturbation in the matter dominated era $\delta \propto a$ that we derived in linear theory in Section 3.2 becomes $\delta \propto a^{1-3f_\nu/5}$ in the presence of neutrinos [30]. In addition, for heavier neutrinos, the non-relativistic transition happened earlier, and matter perturbations were suppressed for a longer time. The effects combine to yield a relative change $\Delta P/P_{f_\nu=0} \simeq -8f_\nu$ at $z = 0$ in linear theory [30]. Numerical simulations find a somewhat larger suppression of $\sim 10 f_\nu$ [273–280]. The full shape galaxy power spectrum obtained from BOSS measurements [85] has been used in combination with Planck CMB data to obtain a neutrino mass bound $M_\nu < 0.16$ eV [265]. As mentioned in Chapter 2, future surveys are expected to detect this characteristic suppression with enhanced accuracy, leading to a forecasted measurement of the neutrino mass sum with $\sigma(M_\nu) \simeq 0.02$–$0.03$ eV [19, 20, 32–41].

It is important to note that cosmology does not directly probe the neutrinos, but measures their properties indirectly. Therefore, the experimental bounds can in principle be evaded if one can construct beyond-SM models that mimick the impact of neutrinos on cosmological observables.

4.2 Two-component fluid: CDM+baryons and neutrinos

Having reviewed the presence of neutrinos in the cosmic evolution, we will in the rest of this chapter focus on making a precise prediction of the matter power spectrum in the presence of neutrinos, in particular quantifying the impact of scale- and time-dependence induced by neutrino perturbations on the clustering dynamics. We will use the extension of SPT described in the previous chapter to compute loop corrections taking neutrinos into account. In order to use that setup, we need a description of structure formation with massive neutrinos, which will be the focus of this section.

Hybrid model

The model we will employ is a hybrid Boltzmann and two-component fluid one, first introduced in Ref. [281] and further developed in Paper I [44]. In the former work, the model was applied using the time-renormalization group (TRG) perturbative approach [282], in which one solves coupled equations for the power- and bispectrum. Scale-dependent dynamics (as we will see occurs for the neutrino perturbations) could not easily be captured fully in TRG, and increasing the accuracy by including NNLO corrections (corresponding to including the trispectrum in that formalism) appeared complicated, therefore in Paper I we opted for solving the two-component fluid equations using the aforementioned extension of SPT. In addition, the fluid description was refined by more accurately modeling the neutrino sound velocity in that work [44].

The idea of the hybrid setup is to describe neutrinos (and other cosmological species) linearly by the full Boltzmann hierarchy up to some intermediate redshift z_{match}, at which the system is mapped onto a fluid model. The fluid has two components: baryons and CDM are treated as one, joint component, which is coupled via gravity to the other component, the neutrinos. Importantly, a fluid description of neutrinos is only valid at late times, sufficiently after the non-relativistic transition. Indeed, Ref. [267] found that a fluid description of neutrinos at *all* times, including times long before the non-relativistic transition, was only accurate at the level of 10–20 %. After the non-relativistic transition however, the coupling between lower and higher moments of the Boltzmann hierarchy becomes suppressed by powers of T_ν/m_ν, allowing us to follow only the lowest moments. In the hybrid model we therefore only employ the fluid model for $z < z_{\mathrm{match}} \ll z_{\mathrm{nr}}$. We will use $z_{\mathrm{match}} = 25$, for which we find sub-permille and percent level differences for the baryons+CDM component and neutrino component, respectively, when comparing the hybrid model to the full Boltzmann hierarchy at $z = 0$. This comparison will be discussed in detail below.

The fluid model is useful at late times since it can be mapped onto a framework for computing non-linear corrections to the power spectrum, which in our case will be the generalization of SPT described in Section 3.4. The full Boltzmann hierarchy is very complex to treat beyond linear order in perturbation theory, and it is moreover not needed to obtain results with sub-percent precision. We will justify this in detail for the neutrino component below, as well as for the baryons+CDM component by including EFT terms accounting for corrections to the single-stream picture. Our interest is wavenumbers in the mildly non-linear regime, $k \simeq 0.1h$ Mpc^{-1}, where non-linearities only become important for

$z < z_{\rm NL} \simeq 10$. In summary, we can use the full Boltzmann hierarchy of linear perturbations until $z_{\rm match} = 25$, with $z_{\rm NL} \ll z_{\rm match} \ll z_{\rm nr}$, and subsequently map the system onto the two-component fluid for which we include non-linear corrections.

We consider three degenerate neutrino species, described by a single fluid component. While it would be possible to extend the formalism to a multi-fluid with each neutrino species having a separate component, we do not expect our results to change significantly in that case. The reason is that cosmological probes are very insensitive to specific neutrino properties beyond the total density and absolute mass scale as discussed above, and moreover errors introduced by treating neutrinos as degenerate appears to be much smaller than the expected sensitivity of future experiments, see e.g. Ref. [268].

Equations of motion

Next, let us construct the equations of motion for the baryon+CDM and neutrino fluid. At first we will only include linear terms. For a general perturbed energy-stress tensor δT^{ij} there are four scalar degrees of freedom: the density contrast δ, velocity divergence θ, pressure perturbation δP and anisotropic stress σ, defined as [30, 283]

$$\bar{\rho}\delta = -\delta T^{0}{}_{0}\,, \tag{4.11a}$$

$$(\bar{\rho} + \bar{P})\theta = \partial^{i}\delta T^{0}{}_{i}\,, \tag{4.11b}$$

$$\delta P = \frac{1}{3}\delta T^{i}{}_{i}\,, \tag{4.11c}$$

$$(\bar{\rho} + \bar{P})\sigma = \left(\partial_i\partial_j - \frac{1}{3}\nabla^2\delta^{(\rm K)}_{ij}\right)\delta T^{ij}\,. \tag{4.11d}$$

For a multi-component universe, the total fluctuation is given by summing the LHS quantities for each component. For the density contrast, this implies that $\delta_{\rm tot} = \sum_i f_i\delta_i$ with $f_i = \Omega_i/\Omega_{\rm m}$ in the late Universe. Thus, we can define the combined baryon+CDM density contrast as

$$\delta_{\rm cb} = \frac{f_{\rm b}\delta_{\rm b} + f_{\rm cdm}\delta_{\rm cdm}}{f_{\rm b} + f_{\rm cdm}}\,. \tag{4.12}$$

On large scales, we can neglect the pressure and anisotropic stress of the baryon+CDM component, treating it as a perfect, pressureless fluid. We will however take corrections to this picture into account by including EFT terms. In any case, the only dynamical quantities for the baryon+CDM component are $\delta_{\rm cb}$ and $\theta_{\rm cb}$, with the latter defined equivalently as Eq. (4.12).

To treat neutrinos accurately we need to account for all the degrees of freedom above for the neutrino fluid. We can however neglect the neutrino equation of state $w_\nu = \bar{P}_\nu/\bar{\rho}_\nu$ in the non-relativistic limit.[4] It follows that the continuity and Euler equations for the coupled

[4] In particular, the neutrino equation of state has negligible impact on the fluid evolution for $z < z_{\rm match} = 25$ and $M_\nu < 0.4$ eV.

fluid follows in Fourier space is given by [283]

$$\partial_\tau \delta_{\rm cb} + \theta_{\rm cb} = 0\,, \tag{4.13a}$$

$$\partial_\tau \theta_{\rm cb} + \mathcal{H}\theta_{\rm cb} + \frac{3}{2}\mathcal{H}^2\Omega_m[f_\nu\delta_\nu + (1-f_\nu)\delta_{\rm cb}] = 0\,, \tag{4.13b}$$

$$\partial_\tau \delta_\nu + \theta_\nu = 0\,, \tag{4.13c}$$

$$\partial_\tau \theta_\nu + \mathcal{H}\theta_\nu + \frac{3}{2}\mathcal{H}^2\Omega_m[f_\nu\delta_\nu + (1-f_\nu)\delta_{\rm cb}] - k^2 c_{\rm s}^2\delta_\nu + k^2\sigma_\nu = 0\,, \tag{4.13d}$$

where we introduced the neutrino sound velocity $c_{\rm s}^2 = \delta P_\nu/\delta\rho_\nu$. Both $c_{\rm s}^2$ and σ_ν need to be provided to close the system of equations above, we return to this point below.

Next, we write the equations above in a form that allows us to employ the generalized framework introduced in Section 3.4. Firstly, we wish to use $\eta = \ln D^+$ as the time variable. However, in the presence of massive neutrinos, there is a subtlety because the scale-dependent suppression of growth due to neutrino freestreaming leads to a growth factor that depends on scale, i.e. $D^+ = D^+(z,k)$. To avoid using a time-variable that also depend on scale, we define another growth factor $D^+_{f_\nu=0}$ for a corresponding cosmology with massless neutrinos where the CDM density is tuned so that the total matter energy density is the same. This growth factor does not have a scale-dependence, and we define $\eta = \ln D^+_{f_\nu=0}$. Note that $D^+_{f_\nu=0}$ is also the $k\to 0$ limit of the scale-dependent growth factor in the massive model.

We collect the density contrast and velocity divergence, suitably rescaled by $-1/\mathcal{H}f$, where $f = f_{f_\nu=0} = {\rm d}\ln D^+_{f_\nu=0}/{\rm d}\ln a$ is the growth rate in the corresponding massless model, into a vector

$$\psi_1 = \delta_{\rm cb}\,, \quad \psi_2 = -\frac{\theta_{\rm cb}}{\mathcal{H}f}\,, \quad \psi_3 = \delta_\nu\,, \quad \psi_4 = -\frac{\theta_\nu}{\mathcal{H}f}\,. \tag{4.14}$$

The set of equations (4.13) becomes

$$\partial_\eta \psi_a + \Omega_{ab}(k,\eta)\,\psi_b = 0\,, \tag{4.15}$$

with

$$\Omega(k,\eta) = \begin{pmatrix} 0 & -1 & 0 & 0 \\ -\frac{3}{2}\frac{\Omega_{\rm m}}{f^2}(1-f_\nu) & \frac{3}{2}\frac{\Omega_{\rm m}}{f^2} - 1 & -\frac{3}{2}\frac{\Omega_{\rm m}}{f^2}f_\nu & 0 \\ 0 & 0 & 0 & -1 \\ -\frac{3}{2}\frac{\Omega_{\rm m}}{f^2}(1-f_\nu) & 0 & -\frac{3}{2}\frac{\Omega_{\rm m}}{f^2}[f_\nu - k^2 c^2_{s,{\rm eff}}(k,\eta)] & \frac{3}{2}\frac{\Omega_{\rm m}}{f^2} - 1 \end{pmatrix}. \tag{4.16}$$

Here, we introduced an effective neutrino sound velocity

$$c^2_{s,{\rm eff}}(k,\eta) \equiv \frac{1}{k^2_{\rm FS}(k,\eta)} = \frac{3}{2\Omega_{\rm m}\mathcal{H}^2}\left[c_{\rm s}^2(k,\eta) - \frac{\sigma_\nu(k,\eta)}{\delta_\nu(k,\eta)}\right]_{\rm lin}\,, \tag{4.17}$$

and its associated freestreaming scale $k_{\rm FS}$. We will compute the bracket in linear theory. Hence we only treat δ_ν and θ_ν non-linearly. In the non-relativistic limit $c_{\rm s}^2 \ll 1$ and $|\sigma_\nu/\delta_\nu| \ll 1$, hence it is a good approximation to treat them linearly, as we see below. In the following we describe in detail how we can compute the bracket above.

Sound velocity and anisotropic stress

We will employ two schemes to evaluate the effective neutrino sound velocity and close the system of equations above: (i) neglecting anisotropic stress and approximating the sound velocity by the adiabatic one, (ii) integrating the Boltzmann neutrino hierarchy numerically to obtain exact sound velocity and anisotropic stress. Before we define them exactly, let us review the relation between the neutrino fluid quantities and the phase-space distribution. As we only discuss the neutrino component below, we drop the ν subscript on fluid quantities for brevity.

The perturbed neutrino distribution function at linear order can be written as

$$f(\mathbf{k}, \hat{\mathbf{n}}, q, \tau) = f_0\,(q/a)\,[1 + \Psi(\mathbf{k}, \hat{\mathbf{n}}, q, \tau)]\,, \tag{4.18}$$

where f_0 is the background, time-independent, ultra-relativistic Fermi-Dirac distribution function as given by Eq. (4.1), we introduced the comoving momentum $q = ap$ and $\mathbf{n} = \mathbf{q}/q$. Its evolution is given by the linearized, collisionless Boltzmann equation [283]

$$\left(\frac{\partial}{\partial\tau} + \frac{\mathrm{i}\,q}{\epsilon(q,\tau)}(\mathbf{k}\cdot\hat{\mathbf{n}})\right)\Psi(\mathbf{k},\hat{\mathbf{n}},q,\tau) + \frac{\mathrm{d}\ln f_0}{\mathrm{d}\ln q}\left(\frac{\partial\phi(k,\tau)}{\partial\tau} - \frac{\mathrm{i}\,\epsilon(q,\tau)}{q}(\mathbf{k}\cdot\hat{\mathbf{n}})\psi(k,\tau)\right) = 0\,, \tag{4.19}$$

with $\epsilon = \sqrt{q^2 + a^2m^2}$ being the comoving energy. The relation above was written in Newtonian gauge, i.e. with the scalar potentials ϕ and ψ characterizing the perturbation around a FLRW metric[5], $\mathrm{d}s^2 = a^2\left(-(1+2\psi)\,\mathrm{d}\tau^2 + (1-2\phi)\,\mathrm{d}x^i\,\mathrm{d}x_i\right)$. The distribution perturbation Ψ can be expanded in Legendre polynomials of $\mu = \mathbf{k}\cdot\hat{\mathbf{n}}/k$,

$$\Psi(\mathbf{k},\mathbf{n},q,\tau) = \sum_{l=0}^{\infty}(-\mathrm{i})^l(2l+1)\Psi_l(k,q,\tau)P_l(\mu)\,. \tag{4.20}$$

Inserting this expansion into the Boltzmann equation (4.19) yields the Boltzmann hierarchy [267, 283]:

$$\frac{\partial\Psi_0}{\partial\tau} = -\frac{qk}{\epsilon}\Psi_1 - \frac{\mathrm{d}\ln f_0}{\mathrm{d}\ln q}\frac{\partial\phi}{\partial\tau}\,, \tag{4.21a}$$

$$\frac{\partial\Psi_1}{\partial\tau} = \frac{qk}{3\epsilon}\left(\Psi_0 - 2\Psi_2\right) - \frac{\epsilon k}{3q}\frac{\mathrm{d}\ln f_0}{\mathrm{d}\ln q}\psi\,, \tag{4.21b}$$

$$\frac{\partial\Psi_l}{\partial\tau} = \frac{qk}{(2l+1)\epsilon}\left[l\Psi_{l-1} - (l+1)\Psi_{l+1}\right]\,, \qquad l \geq 2\,. \tag{4.21c}$$

This is an infinite hierarchy where each multipole is coupled to its predecessor (except for $l = 0$) and successor. To integrate it numerically, one needs to truncate the hierarchy at some maximum multipole $l_{\max}$ with a certain prescription for its evolution. A common choice is to use a truncation scheme [283] $\Psi_{l_{\max}+1} = 2(l_{\max}+1)\epsilon\Psi_{l_{\max}}/qk\tau - \Psi_{l_{\max}-1}$ with $l_{\max} = \mathcal{O}(10)$, this is e.g. adopted by the Boltzmann solver `CLASS` [93]. Notice that in the non-relativistic limit, the coupling between lower and higher multipoles in Eq. (4.21c) is

[5] The metric potential ψ should not be confused with the vector of perturbations ψ_a; the latter is always written with an index subscript.

suppressed by powers of $q/\epsilon \sim T/m$, which is why we are allowed to follow only the lowest ones for neutrinos at late times.

The multipoles can be related to fluid quantities by integrating over particle momentum [267],

$$\bar{\rho}(\tau) = \frac{4\pi}{a^4(\tau)} \int \mathrm{d}q\, q^2 \epsilon(q,\tau) f_0(q)\,, \tag{4.22a}$$

$$\bar{P}(\tau) = \frac{4\pi}{3a^4(\tau)} \int \mathrm{d}q\, q^2 \frac{q^2}{\epsilon(q,\tau)} f_0(q)\,, \tag{4.22b}$$

$$\delta\rho(k,\tau) = \frac{4\pi}{a^4(\tau)} \int \mathrm{d}q\, q^2 \epsilon(q,\tau) f_0(q) \Psi_0(k,q,\tau)\,, \tag{4.22c}$$

$$\delta P(k,\tau) = \frac{4\pi}{3a^4(\tau)} \int \mathrm{d}q\, q^2 \frac{q^2}{\epsilon(q,\tau)} f_0(q) \Psi_0(k,q,\tau)\,, \tag{4.22d}$$

$$(\bar{\rho}+\bar{P})\theta(k,\tau) = \frac{4\pi k}{a^4(\tau)} \int \mathrm{d}q\, q^3 f_0(q) \Psi_1(k,q,\tau)\,, \tag{4.22e}$$

$$(\bar{\rho}+\bar{P})\sigma(k,\tau) = \frac{8\pi}{3a^4(\tau)} \int \mathrm{d}q\, q^2 \frac{q^2}{\epsilon(q,\tau)} f_0(q) \Psi_2(k,q,\tau)\,. \tag{4.22f}$$

Having reviewed these relations, we move on and outline the two schemes we use for computing the effective neutrino sound velocity in linear theory:

Adiabatic approximation (2F-ad) In the non-relativistic limit, the neutrino sound speed approaches the adiabatic sound speed, i.e.

$$c_\mathrm{s}^2 \xrightarrow[z \ll z_\mathrm{nr}]{} c_g^2 = \frac{\partial_\tau \bar{P}}{\partial_\tau \bar{\rho}} = w(\tau) - \frac{\partial_\tau w(\tau)}{3\mathcal{H}(\tau)\,(1+w(\tau))}\,. \tag{4.23}$$

Furthermore, for $q^2 \ll a^2 m^2$, the equation of state is given by (using Eqs. (4.22a) and (4.22b))

$$w(\tau) = \frac{1}{3}\frac{1}{a^2 m^2}\frac{\int \mathrm{d}q\, q^4 f_0(q)}{\int \mathrm{d}q\, q^2 f_0(q)} = \frac{1}{3}\left\langle c_\nu^2 \right\rangle, \tag{4.24}$$

which we in the last equality recognized as the neutrino velocity dispersion (4.9) in the non-relativistic limit. Hence, the adiabatic approximation for the neutrino sound velocity reads

$$c_\mathrm{s}^2 = \frac{1}{3}\left\langle c_\nu^2 \right\rangle + \frac{2}{9}\frac{\langle c_\nu^2 \rangle}{1+\langle c_\nu^2\rangle/3} \simeq \frac{5}{9}\left\langle c_\nu^2 \right\rangle, \tag{4.25}$$

using $\langle c_\nu^2 \rangle \ll 1$ in the last line. This non-relativistic approximation is a significant improvement compared to the naive estimate $c_\mathrm{s} = \langle c_\nu \rangle$ [267]. We neglect the neutrino anisotropic stress, and therefore the effective neutrino sound velocity in this approximation becomes

$$c_\mathrm{s,eff}^2 = \frac{2}{3\Omega_\mathrm{m}\mathcal{H}}\frac{5}{9}\left\langle c_\nu^2 \right\rangle \simeq \frac{1.214}{\Omega_\mathrm{m}(z=0)}\left(\frac{1\ \mathrm{eV}}{m_\nu}\right)^2 (1+z)\frac{\mathrm{Mpc}^2}{h^2}\,. \tag{4.26}$$

This approximation for the neutrino sound velocity was used in Ref. [281]. We use *2F-ad* as a shorthand name for the two-component fluid model using this approximation scheme in the future.

Exact effective sound velocity (2F) We aim for an analytic solution of the full neutrino linear Boltzmann hierarchy, so that we can evaluate the sound velocity and anisotropic stress using Eq. (4.22) in a way that is informed about the complete neutrino distribution in linear theory. The discussion follows Appendix B of Ref. [267].

We collect terms including the perturbation Ψ on the LHS in the collisionless Boltzmann equation,

$$\frac{\partial}{\partial\tau}\Psi(k,q,\mu,\tau) + \mathrm{i}\frac{kq\mu}{\epsilon(q,\tau)}\Psi(k,q,\mu,\tau) = S(k,q,\mu,\tau)\,, \tag{4.27}$$

and define the source term S as

$$S(k,q,\mu,\tau) = \frac{\mathrm{d}\ln f_0}{\mathrm{d}\ln q}\left(\mathrm{i}k\mu\frac{\epsilon(q,\tau)}{q}\psi(k,\tau) - \frac{\partial\phi(k,\tau)}{\partial\tau}\right). \tag{4.28}$$

Given the initial condition $\Psi(k,q,\mu,\tau_{\mathrm{ini}})$, the solution of this first order linear differential equation is given by

$$\Psi(k,q,\mu,\tau) = \Psi(k,q,\mu,\tau_{\mathrm{ini}})\mathrm{e}^{-\mathrm{i}k\mu y(\tau_{\mathrm{ini}},\tau)} + \int_{\tau_{\mathrm{ini}}}^{\tau}\mathrm{d}\tilde{\tau}\,\mathrm{e}^{-\mathrm{i}k\mu y(\tilde{\tau},\tau)}S(k,q,\mu,\tilde{\tau})\,, \tag{4.29}$$

where

$$y(\tau_a,\tau_b) = \int_{\tau_a}^{\tau_b}\mathrm{d}\tau\,\frac{q}{\epsilon(q,\tau)}\,. \tag{4.30}$$

To compute the fluid quantities (4.22), we need the first multipoles of the solution, therefore we project this solution on Legendre polynomials. A useful identity for this purpose is

$$\exp\left(-\mathrm{i}\mu x\right) = \sum_l(-\mathrm{i})^l(2l+1)j_l(x)P_l(\mu)\,, \tag{4.31}$$

where j_l is the spherical Bessel function. The multipole expanded solution therefore reads

$$\begin{aligned}\sum_{l'}(-\mathrm{i})^{l'}(2l'+1)\Psi_{l'}(k,q,\tau)P_{l'}(\mu) = \\ \sum_{l'}\sum_{l''}(-\mathrm{i})^{l'+l''}(2l'+1)(2l''+1)\Psi_{l'}(k,q,\tau_{\mathrm{ini}})j_{l''}\left[ky(\tau_{\mathrm{ini}},\tau)\right]P_{l'}(\mu) \\ +\sum_{l'}(-\mathrm{i})^{l'}(2l'+1)P_{l'}(\mu)\int_{\tau_{\mathrm{ini}}}^{\tau}\mathrm{d}\tilde{\tau}\,\left[\mathrm{i}k\mu\frac{\epsilon(q,\tilde{\tau})}{q}\psi(k,\tilde{\tau}) - \frac{\partial\phi(k,\tilde{\tau})}{\partial\tilde{\tau}}\right]j_{l'}\left[ky(\tilde{\tau},\tau)\right]\,.\end{aligned} \tag{4.32}$$

Finally, we multiply each side by $P_l(\mu)$ and integrate over μ to obtain a solution for each multipole:

$$\begin{aligned}\Psi_l(k,q,\tau) = \frac{\mathrm{d}\ln f_0}{\mathrm{d}\ln q}\times\Bigg(\phi(k,\tau_{\mathrm{ini}})\,j_l[k\,y(\tau_{\mathrm{ini}},\tau)] - \phi(k,\tau)\delta_{l0}^{(\mathrm{K})} \\ -k\int_{\tau_{\mathrm{ini}}}^{\tau}\mathrm{d}\tilde{\tau}\,\left[\frac{\epsilon(q,\tilde{\tau})}{q}\psi(k,\tilde{\tau}) + \frac{q}{\epsilon(q,\tilde{\tau})}\phi(k,\tilde{\tau})\right]\left[\frac{l}{2l+1}\,j_{l-1}[k\,y(\tilde{\tau},\tau)] - \frac{l+1}{2l+1}\,j_{l+1}[k\,y(\tilde{\tau},\tau)]\right]\Bigg) \\ +\sum_{l'}\sum_{l''}(-\mathrm{i})^{l'+l''-l}(2l'+1)(2l''+1)\,\Psi_{l'}(k,q,\tau_{\mathrm{ini}})\,j_{l''}[k\,y(\tau_{\mathrm{ini}},\tau)]\begin{pmatrix}l & l' & l''\\ 0 & 0 & 0\end{pmatrix}^2\,,\end{aligned} \tag{4.33}$$

where $\begin{pmatrix} l & l' & l'' \\ 0 & 0 & 0 \end{pmatrix}$ is the Wigner 3-j symbol. The first two terms in Eq. (4.33) are boundary terms arising from integrating the ϕ-term by parts. Moreover, to obtain the above result we used orthogonality of the Legendre polynomials as well as the recursion relation

$$\frac{\mathrm{d}}{\mathrm{d}x} j_l(x) = \frac{l}{2l+1} j_{l-1}(x) - \frac{l+1}{2l+1} j_{l+1}(x) \,. \tag{4.34}$$

Note that compared to Ref. [267], we fixed a sign typo in the ϕ-term of the second line of Eq. (4.33).

With the analytic result (4.33), we can compute the fluid quantities (4.22) required to obtain the exact neutrino effective sound velocity in linear theory as given by Eq. (4.17). In practice, Eq. (4.33) can be evaluated numerically, taking the metric potentials from a Boltzmann solver as input. Moreover, choosing an early initial time $\tau_{\mathrm{ini}} = 1$ Mpc, the initial perturbations $\Psi(k, q, \tau_{\mathrm{ini}})$ can safely be neglected [44]. Knowing that during matter domination, the metric potentials are constant, one can go back to Eq. (4.32), neglect $\partial_\tau \phi$ and derive a simplified integral solution. Nonetheless, the full integral expression in Eq. (4.33) is needed when integrating $\tilde{\tau}$ during vacuum energy domination.

We give the two-component fluid model in combination with the scheme above to obtain the exact effective neutrino sound speed the shorthand name *2F*.

Comparison to Boltzmann solver

Before we include non-linear terms in the hybrid two-component fluid model, we discuss how its predictions compare to the Boltzmann solver `CLASS`.

First, let us look at the neutrino sound velocity and anisotropic stress computed in the different schemes above and in `CLASS`. Fig. 4.3 makes this comparison for a small neutrino mass $M_\nu = 0.06$ eV and intermediate wavenumber $k = 0.1h$ Mpc^{-1} (right) and a larger $M_\nu = 0.21$ eV and smaller wavenumber $k = 0.01h$ Mpc^{-1}. We show the adiabatic sound speed c_g^2, as given by Eq. (4.26), the sound speed c_{s}^2 and the ratio $|\sigma_\nu/\delta_\nu|$ computed exactly using Eq. (4.33), as well as the same quantities computed by `CLASS`. It is clear that the adiabatic sound speed does not match the exact one; only at late times for the larger neutrino mass do the lines agree, where we are further along in approaching the non-relativistic limit. The anisotropic stress is suppressed by $\sim (T_\nu/m_\nu)^2$ compared to the density contrast in the non-relativistic limit, therefore it decays at late times. We note that the sound speed for $M_\nu = 0.06$ eV is about an order of magnitude larger than for $M_\nu = 0.21$ eV, which is expected since the lighter neutrinos can freestream over longer distances.

The fluid quantities computed using the scheme detailed above have good agreement with those computed in `CLASS`, with the exception of $|\sigma/\delta|$ for large wavenumber and small neutrino mass, as apparent from Fig. 4.3. In that case, the `CLASS` solutions develop oscillatory behavior with only the mean value following our result (Paper I [44]), until the solutions converge at late times. Moreover, the `CLASS` solutions are dependent on the maximum multipole number, indicating that errors from the truncation scheme propagates the Boltzmann hierarchy down to lower multipoles. In this regime the anisotropic stress is small however, and any mistake has negligible impact on the baryon+CDM or neutrino power spectra. We remark that while Eq. (4.33) avoids the problem of truncating the Boltzmann

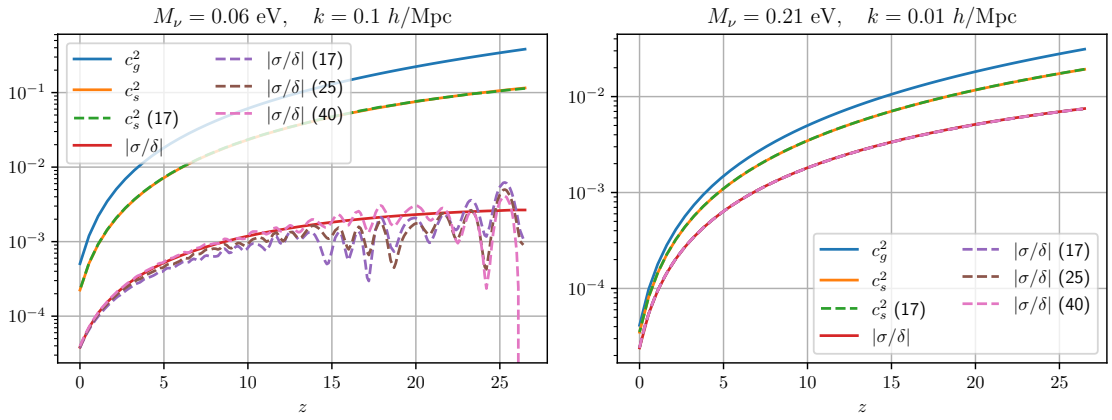

Figure 4.3: Neutrino sound velocity and anisotropic stress for two neutrino masses $M_\nu = 0.06$ eV and $M_\nu = 0.21$ eV, and two wavenumbers $k = 0.1h$ Mpc^{-1} and $k = 0.01h$ Mpc^{-1}. We display the adiabatic sound velocity as well as the exact sound velocity and anisotropic stress computed exactly using Eq. (4.33). Furthermore we show with dashed lines the corresponding quantities computed by `CLASS`, with the maximum multipole number $l_{\max}$ in the parenthesis. Adapted and reprinted from Paper I [44].

hierarchy altogether (having integrated the Boltzmann equation before projecting onto Legendre multipoles), it would be cumbersome to use it in a Boltzmann solver, because the integral has to be performed at every time step to update transfer functions and metric perturbations. In our work, the metric perturbations were taken as external input, and therefore the expression (4.33) was favorable since it bypasses the issues with hierarchy truncation.

Next, we compare the hybrid two-component fluid model to `CLASS` at the level of the power spectrum at $z = 0$. Using $z_{\text{match}} = 25$, we recall that in the hybrid model, the `CLASS` is used up to this point, so that any difference arises due to difference in dynamics at $z < z_{\text{match}}$ or from the matching procedure (we postpone a description of how the matching is done in practice until we include non-linear terms in the next section). The comparison was done in Papers I and III [44, 46], we display the results from Paper I in Fig. 4.4. The left panel reveals that the adiabatic approximation (2F-ad) does not yield an accurate prediction for the neutrino auto spectrum (dotted lines). In fact, the power spectrum is significantly underestimated, because the adiabatic approximation overestimates the sound velocity compared to the true one (see Fig. 4.3), leading to excessive suppression of growth [44]. On scales larger than the freestreaming scale, $k < k_{\text{FS}} \sim 0.01h$ Mpc^{-1}, this mistake is less important however. The adiabatic approximation also works better for larger neutrino masses, where a larger portion of the neutrino distribution has become adequately non-relativistic. On the other hand, larger neutrino masses means that the neutrino fluid influences the baryon+CDM fluid to greater extent, and a mistake in the neutrino transfer function generates a larger error in the baryon+CDM one. In total however, since neutrinos only constitute $f_\nu \sim 1\,\%$ of the matter content, the total matter power spectrum in the 2F-ad model agrees with that from `CLASS` to a few permille.

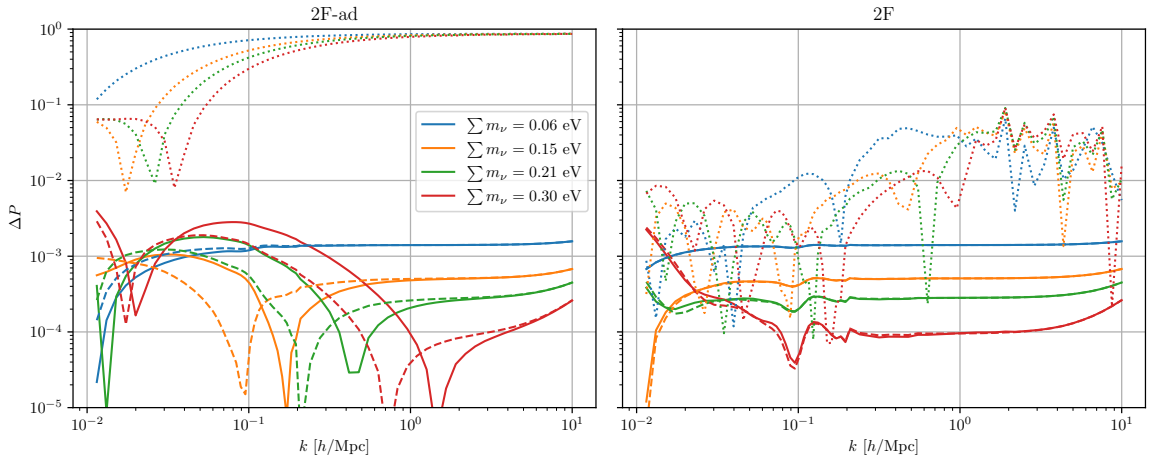

Figure 4.4: Relative difference between power spectra computed in the 2F model and computed by `CLASS`, i.e. $\Delta P = |P^{\mathrm{2F}}/P^{\mathtt{CLASS}} - 1|$ at $z = 0$. Four neutrino masses $M_\nu = 0.06$, 0.15, 0.21 and 0.3 eV are displayed. Moreover, we show the total matter power spectrum $P_{\mathrm{m,m}}$ (solid), the baryon+CDM power spectrum $P_{\mathrm{cb,cb}}$ (dashed) and neutrino power spectrum $P_{\nu,\nu}$ (dotted). *Left*: Two-component fluid model with the adiabatic approximation for the effective neutrino sound velocity (2F-ad). *Right*: The same with exact effective neutrino sound velocity. Figure taken from Paper I [44].

The right panel of Fig. 4.4 performs the same comparison, using the exact neutrino effective sound velocity (2F). There is excellent agreement with the `CLASS` solution, at the level of 10^{-4}–10^{-3} for the total matter power spectrum and better than 1 % for the neutrino auto spectrum for $k \lesssim 0.3h$ Mpc^{-1}. On small scales $k \gtrsim 1h$ Mpc^{-1}, the 2F model cannot be tested beyond an accuracy of a few percent for the neutrino spectrum, because the `CLASS` solution varies at this level depending on the maximum multipole number l_{max}, indicating that the truncation scheme introduces moderate deviations. Note that the outstanding agreement with the Boltzmann solver for 2F is mainly a consistency check: apart from the different means of integrating the Boltzmann hierarchy, the predominant difference between the two is the neglection of the neutrino equation of state in 2F.

We deem the two-component fluid to be sufficiently accurate at the linear level (especially in the 2F case), allowing for a precision calculation at the sub-percent level including non-linear terms, that we discuss next.

4.3 Non-linear power- and velocity spectra

In Chapter 3, we saw that integrating the Vlasov equation generated non-linear terms in the continuity and Euler equations, that were described by coupling functions α and β in Fourier space. The same logic applies for the neutrino component of the two-component fluid, hence we can immediately promote the baryon+CDM and neutrino fluid equations of

motion (4.15) to include non-linear terms:

$$\partial_\eta \psi_a(\mathbf{k},\eta) + \Omega_{ab}(k,\eta)\,\psi_b(\mathbf{k},\eta) = \gamma_{abc}(\mathbf{k},\mathbf{k}_1,\mathbf{k}_2)\psi_b(\mathbf{k}_1,\eta)\psi_c(\mathbf{k}_2,\eta)\,, \tag{4.35}$$

where the only non-zero components of the non-linear vertex are

$$\gamma_{121}(\mathbf{k},\mathbf{k}_1,\mathbf{k}_2) = \gamma_{343}(\mathbf{k},\mathbf{k}_1,\mathbf{k}_2) = \alpha(\mathbf{k}_1,\mathbf{k}_2)\,, \tag{4.36a}$$
$$\gamma_{222}(\mathbf{k},\mathbf{k}_1,\mathbf{k}_2) = \gamma_{444}(\mathbf{k},\mathbf{k}_1,\mathbf{k}_2) = \beta(\mathbf{k}_1,\mathbf{k}_2)\,. \tag{4.36b}$$

Hence, the couplings between the neutrino density contrast (index 3) and the (rescaled) velocity divergence (index 4) is given equivalently as the corresponding baryon+CDM ones.

Eq. (4.35) is precisely on the form (3.57) that can be described by the extended cosmological perturbation theory as defined in Section 3.4. Therefore, we can solve it by the perturbative expansion (3.58), expanding in the initial fluctuation $\delta_0(\mathbf{k}) \equiv \delta_{\mathrm{cb}}(\mathbf{k},\eta_{\mathrm{ini}})$, where $\eta_{\mathrm{ini}} = \eta(z = z_{\mathrm{match}})$. The kernels that furnish the expansion then satisfies the equation of motion (3.59), with the 4×4 evolution matrix $\Omega_{ab}(k,\eta)$ given by Eq. (4.16) (with a certain prescription for the effective neutrino sound velocity) and the non-linear vertex defined in Eq. (4.36). Using this, one can compute loop corrections to the power spectrum with the one- and two-loop expressions (3.70) and (3.71) (or in principle any loop), with $P_0(k) = P^{\mathrm{lin.}}_{\mathrm{cb,cb}}(k, z_{\mathrm{match}})$ as the input, initial power spectrum. In the hybrid model, P_0 is therefore computed by `CLASS` using the Boltzmann hierarchy up to $z = z_{\mathrm{match}}$. Hence, the only final ingredient we need to match the two regimes in the hybrid setup is the initial condition of the kernel hierarchy at z_{match}.

As discussed in Section 3.4, some care needs to be taken when initializing the kernel hierarchy at intermediate redshifts in order to avoid exciting transient modes that do not decay by today (or the time of observation). This is the case also for the two-component fluid model. To this extent, Papers I and III [44, 46] follow the strategy outlined in Section 3.4 to construct a kernel hierarchy residing in the growing mode at η_{ini}: Let $u_a(k)$ and λ_1 be the growing mode eigenvector and corresponding eigenvalue of the evolution matrix at the initial time, $\Omega_{ab}(k,\eta_{\mathrm{ini}})$. Choosing a sufficiently early time $\eta_{\mathrm{asymp}} = -10 \ll \eta_{\mathrm{ini}}$, the kernels can be set using Eq. (3.61). Evolving the kernels up to $\eta = \eta_{\mathrm{ini}}$ using $\Omega_{ab}(k,\eta_{\mathrm{ini}})$ ensures that any decaying modes have vanished, given our choice of η_{asymp} being sufficiently early, and the full perturbative solution comprises the growing mode when dynamics is turned on for $\eta > \eta_{\mathrm{ini}}$.

The total power spectrum is given by the weighted sum of the baryon+CDM and neutrino auto spectra and the cross spectrum:

$$P_{\mathrm{m,m}} = (1-f_\nu)^2 P_{\mathrm{cb,cb}} + 2f_\nu(1-f_\nu)P_{\mathrm{cb},\nu} + f_\nu^2 P_{\nu,\nu}\,. \tag{4.37}$$

The different contributions and corresponding loop corrections as computed in the 2F scheme is shown in Fig. 4.5. As one would expect due to their freestreaming nature, the neutrino power spectra are heavily suppressed compared to the baryon+CDM ones for $k \gg k_{\mathrm{FS}}$. Since the contributions of $P_{\mathrm{cb},\nu}$ and $P_{\nu,\nu}$ to the total power also enters with factors of f_ν, they can safely be neglected in the sum. Crucially however, this does not imply that neutrinos can altogether be neglected: their presence influences the baryon+CDM power spectrum at the level of several percent, as discussed above. For completeness, we include

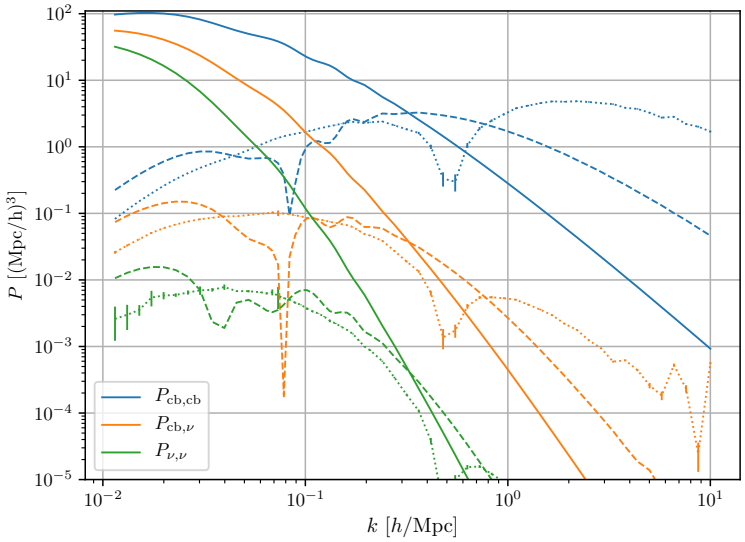

Figure 4.5: Different contributions to the matter power spectrum at $z = 0$ in a cosmology with $M_\nu = 0.15$ eV, computed using the 2F scheme. We show the linear (solid), (unrenormalized) one- (dashed) and two-loop corrections (dotted), for the baryon+CDM auto spectrum (blue), neutrino auto spectrum (green) and the cross spectrum (orange). Note that the graphs correspond to the absolute value; the one-loop corrections are negative until they switch sign at $k \approx 0.08h$ Mpc^{-1} and the two-loop corrections are negative until about $k \approx 0.6h$ Mpc^{-1} (as indicated by the spikes in the graphs). Figure taken from Paper I [44].

also the neutrino spectrum and the cross spectrum when displaying the total matter power spectrum below.

Note that Fig. 4.5 only displays the unrenormalized loop corrections, therefore the loops are large even in the mildly non-linear regime. We discuss an EFT framework to absorb the UV-sensitivity in the 2F scheme in Section 4.4.

Schemes

In addition to the hybrid two-component 2F and 2F-ad models introduced above, we mention a few simplified treatments of neutrinos in structure formation that are used in the literature. The full set of schemes we consider in this work are, in increasing order of complexity:

1. **EdS-SPT scheme (1F)**: Neutrino perturbations are only taken into account on the linear level. Hence, there is only one species: baryons+CDM. Furthermore, the EdS-approximation is utilized (see Section 3.3) so that EdS-SPT kernels can be used. Due to its simplicity and efficiency, this scheme is commonly adopted in the literature, in particular for full-shape analyses of clustering data [28, 29, 265].

2. **One-fluid scheme (1F+)**: Equivalent to 1F, but with the EdS-approximation relaxed. This scheme is only included to gauge in how far any difference between 1F

and 2F arises due to the departure from EdS or due to the treatment of neutrinos.

3. **External source scheme (1F-ext)**: The effect of neutrinos perturbations on the baryon+CDM fluid emanate from the gravitational coupling, which can be approximated by the linear neutrino transfer function [284]. Therefore, only baryons+CDM are treated dynamically, using the evolution matrix

$$\Omega_{ab}(k,\eta) = \begin{pmatrix} 0 & -1 \\ -\frac{3}{2}\frac{\Omega_{\rm m}}{f^2}\xi(k,\eta) & \frac{3}{2}\frac{\Omega_{\rm m}}{f^2} - 1 \end{pmatrix}, \tag{4.38}$$

where

$$\xi(k,\eta) = 1 - f_\nu + f_\nu \left[\frac{\delta_\nu(k,\eta)}{\delta_{\rm cb}(k,\eta)}\right]_{\rm lin.} . \tag{4.39}$$

with the linear transfer function ratio $\delta_\nu/\delta_{\rm cb}$ taken as external input (e.g. from a Boltzmann solver). This scheme can readily be captured by the extension of SPT. As for the two-component fluid models, it can be put in a hybrid setting, using the full, linear Boltzmann hierarchy until $z_{\rm match}$ and the fluid setup afterwards. Then, the initialization of kernels at $z_{\rm match}$ can be done in an equivalent way as described above for 2F and 2F-ad.

4. **Two-component fluid with adiabatic sound speed (2F-ad)**: Baryon+CDM and neutrino perturbations are treated beyond the linear level in the hybrid two-component fluid model. Both the departure from EdS and the effect of non-linear neutrino perturbations on the dynamics are captured by the numerical kernels. The neutrino sound velocity is approximated by the adiabatic one.

5. **Two-component fluid with exact sound speed (2F)**: As 2F-ad, but using the exact, scale-dependent sound velocity and anisotropic stress as described in the previous section. This is the scheme that most accurately models structure formation in the presence of massive neutrinos, and will therefore serve as the benchmark scheme.

In the 1F and 1F+ schemes, the non-linear dynamics is not time-dependent, and one can take the baryon+CDM power spectrum today (or at any other time of interest) as input to loop calculations. Hence, the tree-level power spectrum is simply $P^{\rm tree} = P_0 = P_{\rm cb,cb}(z=0)$. For 1F-ext, 2F-ad and 2F, this is not the case, and the input power spectrum is taken at $z_{\rm match} = 25$.[6] The tree-level spectrum is non-trivial and given by (cf. Eq. (3.68))

$$P^{\rm tree}_{ab}(\mathbf{k},\eta) = {\rm e}^{2\Delta\eta} F^{(1)}_a(\mathbf{k},\eta) F^{(1)}_b(\mathbf{k},\eta) P_{\rm cb,cb}(k,\eta_{\rm ini}) . \tag{4.40}$$

We will now discuss the performance of the various schemes in modeling the power spectrum at NNLO. The most important comparison is 1F vs 2F, since 1F is the scheme commonly used to analyze galaxy clustering data, and it is essential to scrutinize all approximations. Nevertheless, the other schemes are useful in that they give insights into which mechanisms yield the largest effect on observables.

[6] There is more freedom to choose the initial time for the 1F-ext model, since it does not involve a fluid description of neutrinos. Nonetheless, in Paper I [44], the initial time was chosen to agree with 2F-ad and 2F, in order to perform a comparison on equal footing.

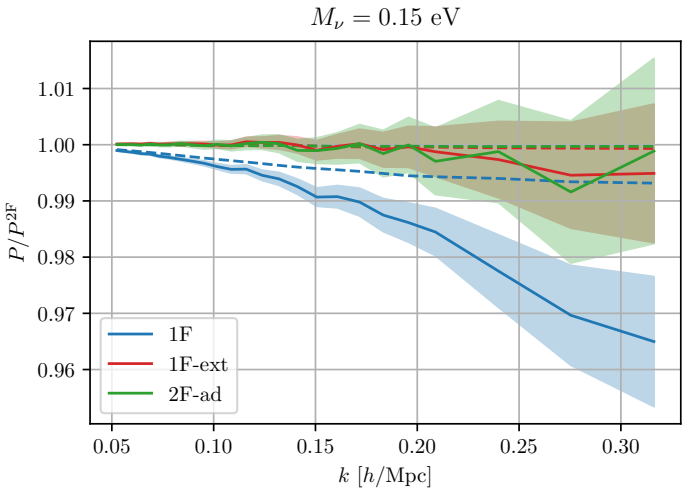

Figure 4.6: Comparison of various schemes that capture neutrinos in structure formation. We show the power spectrum at NLO (dashed) and NNLO (solid), computed in the 1F, 1F-ext and 2F-ad models, normalized to the 2F result. Neutrino mass: $M_\nu = 0.15$ eV. The shaded regions indicate uncertainty from the Monte Carlo integration (invisible at one-loop). Adapted from Paper I [44].

Fig. 4.6 display the total matter power spectrum at NLO (dashed) and NNLO (solid) at $z = 0$ and with $M_\nu = 0.15$ eV, normalized to the 2F result. A similar comparison was shown in Paper I [44]. At large scales, the non-linear contributions are suppressed, and the schemes agree. Around $k \simeq 0.1h$ Mpc^{-1}, the non-linear corrections become important, and we see that the 1F scheme does not accurately capture these. We find a percent deviation at $k = 0.15h$ Mpc^{-1}. On even smaller scales the discrepancy is larger, but there the two-loop contribution becomes of the same order as the linear one, indicating the breakdown of perturbation theory. We return to this point when we perform the same comparison with EFT corrections in Section 4.5. The 1F-ext and 2F-ad schemes agree with 2F within the uncertainty from the numerical integration. This implies that even though the neutrino transfer functions in the adiabatic approximation are miscalculated at the $\mathcal{O}(10\,\%)$-level (see Fig. 4.4), the impact of this mistake on the baryon+CDM sector, which constitutes the predominant part of the total matter power spectrum, is minimal. Nevertheless, for larger neutrino masses, the impact is larger and the 2F-ad scheme deviates up to half a percent from 2F, as is shown in Paper I [44]. It is interesting to see that the 1F-ext scheme is in such good agreement with 2F. Given that the 1F-ext scheme does not capture non-linear neutrino perturbations, this suggests that it is the changed time- and scale-dependent growth in the presence of neutrinos, rather than the non-linear neutrino perturbations themselves, that has the largest effect on the matter power spectrum. On the other hand, as we will shortly see, the departure from EdS has the dominant imprint on the power spectrum, and this is included in 1F-ext. Finally, we remark that the numerical complexity of the 1F-ext and 2F-ad schemes are similar to that of 2F, therefore there is little benefit in using them instead of 2F. In the following, our focus will be on 1F and 2F.

Next, we consider the neutrino mass dependence of the deviation between 1F and 2F.

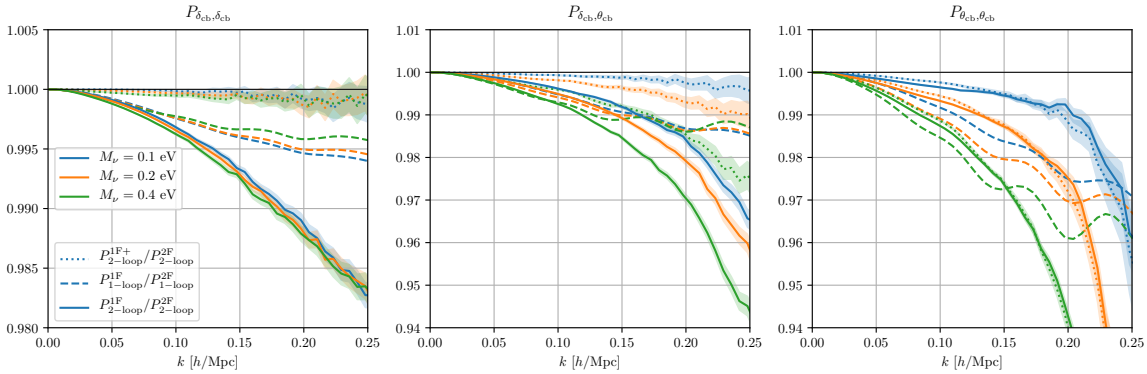

Figure 4.7: Baryon+CDM density-density spectrum $P_{\delta_{\rm cb},\delta_{\rm cb}}$ (left), density-velocity spectrum $P_{\delta_{\rm cb},\theta_{\rm cb}}$ (middle) and velocity-velocity spectrum $P_{\theta_{\rm cb},\theta_{\rm cb}}$ (right) in the 1F and 1F+ schemes, normalized to 2F. The NLO (dashed) and NNLO (solid) prediction in 1F is displayed, as well as the NNLO prediction in 1F+ (dotted). Neutrino masses: $M_\nu = 0.1$ (blue), 0.2 (orange) and 0.4 eV (green). Shaded regions indicate uncertainty from Monte Carlo integration. Figure reprinted from Paper III [46].

This is addressed in the leftmost panel of Fig. 4.7 using three cosmologies with $M_\nu = 0.1$, 0.2 and 0.4 eV, respectively, which shows a similar ratio as Fig. 4.6, but for the baryon+CDM power spectrum $P_{\rm cb,cb}$. The fact that the difference between the schemes are essentially neutrino mass independent suggests that the departure from the EdS-universe at late times is the main source of discrepancy. This hypothesis is also supported by the third set of graphs in Fig. 4.7. It corresponds to the 1F+ scheme, which is equal to 1F but with the EdS-approximation relaxed. We see that the NNLO power spectrum of 1F+ and 2F agree excellently, hence correcting for the departure from EdS rectifies the mistake of 1F to large extent.

The other two panels of Fig. 4.7 show the same comparison for the velocity spectra. This analysis was done in Paper III as a proxy for RSDs: in redshift space, the density contrast is linked to the velocity in real space. A complete RSD analysis is complicated in the 2F model, and is postponed to future work. Nevertheless, we can learn something about the overall effect by considering the velocity spectra.

In contrast to the density-density spectra, the velocity spectra demonstrate a clear dependence on the neutrino mass in the relative difference. Furthermore, in the rightmost plot of $P_{\theta_{\rm cb},\theta_{\rm cb}}$, the 1F and 1F+ curves agree to large extent, implying that the treatment of neutrinos yields the dominant effect. An intricate interpretation of why the impact of neutrinos on velocity loop corrections is larger than that for the density component appears complicated. For $k \gg k_{\rm FS}$, we can do the following qualitative analysis: while the growing mode in the 1F and 1F+ schemes is $(1, 1)$ for baryon+CDM, it is approximately $(1, 1 - 3f_\nu/5)$ in the 2F model.[7] Thus, one could expect the velocity loop corrections to be

[7]The approximate growing eigenmode $(1, 1 - 3f_\nu/5)$ in the 2F model can be found by considering the limit $k \gg k_{\rm FS}$ where $\delta_\nu = 0$. Then the baryon+CDM and neutrino system effectively decouples and the eigenvector can be computed from the upper left 2×2 sub-matrix of Eq. (4.16), assuming $\Omega_{\rm m}/f^2 = 1$ for

larger in absolute magnitude in the 1F/1F+ schemes, which is indeed the case at one-loop. Nonetheless, that naive expectation does not carry to two-loop, where the correction is larger in 2F. This leads to a partial cancellation that yields a better agreement between 1F/1F+ and 2F for the NNLO predictions of $P_{\theta_{\rm cb},\theta_{\rm cb}}$ than for the corresponding NLO ones. On the other hand, the two-loop correction is sensitive to a large range of scales due to mode coupling, and thus not only the limit $k \gg k_{\rm FS}$ where the simple argument above holds. We note that for wavenumbers $k \gtrsim 0.2h$ Mpc^{-1}, the loop corrections are large compared to the linear result, signaling the breakdown of perturbation theory. Finally, we see for the cross spectrum (middle panel) that a combination of the departure from EdS and the neutrino impact leads to deviations that differ both depending on the neutrino mass as well as between the 1F and 1F+ schemes.

4.4 EFT corrections

In this section we describe the EFT setup that we employ to cure the UV-sensitivity in the 2F model. We will show that under the assumption of a large scale separation $k_{\rm FS} \ll k \ll k_{\rm NL}$, the usual $\sim k^2 P_0(k)$ EFT correction can absorb the UV-sensitivity at one-loop. At two-loop we follow the prescription of Ref. [252] as outlined in Section 3.6, however using a numerical evaluation of the single- and double-hard loops. After deriving the renormalized power spectrum at NNLO, we will compare and calibrate both the 1F and 2F models to N-body data, and determine in how far they can reproduce the simulation results in the next section. Note that the quantities defined below can immediately be promoted to IR resummed ones, by performing the replacement $P_0 \to P_0^{{\rm IR},N-L}$ introduced in Section 3.7, where N is the perturbation order and L indicates the loop correction.

Modified equations of motion

The equations of motion in the hybrid two-component fluid model including EFT terms become (cf. Eq. (3.86))

$$\partial_\eta \psi_a(\mathbf{k},\eta) + \Omega_{ab}(\mathbf{k},\eta)\psi_b(\mathbf{k},\eta) = \int_{\mathbf{k}_1,\mathbf{k}_2} \delta_D(\mathbf{k}-\mathbf{k}_{12})\gamma_{abc}(\mathbf{k},\mathbf{k}_1,\mathbf{k}_2)\psi_b(\mathbf{k}_1,\eta)\psi_c(\mathbf{k}_2,\eta) + \delta^{(K)}_{a2}\,\tau_{\theta_{\rm cb}}(\mathbf{k}) + \delta^{(K)}_{a4}\,\tau_{\theta_\nu}(\mathbf{k})\,, \tag{4.41}$$

where the effective stress tensors are defined in real space as

$$\tau_{\theta_{\rm cb}} = \frac{1}{\mathcal{H}^2 f^2}\partial_i \frac{1}{1+\delta_{\rm cb}}\partial_j \tau^{ij}_{\rm cb} \qquad \text{and} \qquad \tau_{\theta_\nu} = \frac{1}{\mathcal{H}^2 f^2}\partial_i \frac{1}{1+\delta_\nu}\partial_j \tau^{ij}_\nu\,. \tag{4.42}$$

We neglect the stochastic contributions to the stress tensors as we only work at leading power in gradients ($k^2/k^2_{\rm NL}$).

In Section 3.6, we derived expressions for the effective stress term τ_θ in the EdS-approximation for a fluid model with two fields: the matter density contrast and (rescaled) velocity divergence. These formulae can be applied in the 1F scheme, in which the dynamical fields are the baryon+CDM density contrast and velocity divergence and the

simplicity.

EdS-approximation is used. In the 2F model however, there are in addition the neutrino density contrast and velocity divergence, and those fields need to be included when writing the stress tensor in terms of all allowed operators. Moreover, at linear order, there is no simple relation between the fields: while in 1F, $\delta^{(1)}_{\rm cb}/\theta^{(1)}_{\rm cb} = -\mathcal{H}f$, we have $\delta^{(1)}_{\rm cb}/\theta^{(1)}_{\rm cb} = -\mathcal{H}f F^{(1)}_1(k)/F^{(1)}_2(k)$ in 2F which is in general k-dependent. Therefore, at leading order in fields, we in principle need to write down

$$\tau_{\theta_{\rm cb}}\big|_1 = \sum_{i=1}^{4} d^2_{{\rm cb},i}\,\Delta\psi^{(1)}_i \qquad \text{and} \qquad \tau_{\theta_\nu}\big|_1 = \sum_{i=1}^{4} d^2_{\nu,i}\,\Delta\psi^{(1)}_i\,, \tag{4.43}$$

in the two-fluid model with EFT coefficients $d_{{\rm cb},i}$, $d_{\nu,i}$. For the baryon+CDM density field, we thus obtain in Fourier space a counterterm

$$\tilde{\psi}^{(1)}_1 \equiv \tilde{\delta}^{(1)}_{\rm cb} = k^2 \sum_{i=1}^{4} \mathsf{d}_i^2\,\Delta^2\psi^{(1)}_i\,. \tag{4.44}$$

Here, each EFT coefficient d_i depends on *both* sets of coefficients $\{d_{{\rm cb},i}\}$ and $\{d_{\nu,i}\}$, because in the time-integration (cf. Eq. (3.99)), the propagator mixes contributions from insertions of both sources $\tau_{\theta_{\rm cb}}$ and τ_{θ_ν}.

In practice, there is a large degeneracy between the EFT-terms corresponding to the d_i's, and we show next that in the limit $k \gg k_{\rm FS}$ Eq. (4.44) can be simplified to only one term. The linear solutions are given by $\psi^{(1)}_a(k,\eta) = {\rm e}^{\Delta\eta}F^{(1)}_a(k,\eta)\delta_{\rm cb}(k)$; we show the linear kernels computed in the 2F model for a cosmology with $M_\nu = 0.1$ eV in Fig. 4.8. For F_1 and F_2 (left panel), we see the reduced growth of the baryon+CDM fluid on small scales, and the step-like behavior around the freestreaming scale $k_{\rm FS} \simeq 0.01h$ Mpc^{-1}. In the right panel the suppressed neutrino perturbations on small scales are apparent. We assume a large scale separation $k_{\rm FS} \ll k \ll k_{\rm NL}$,[8] for a wavenumber in the mildly non-linear regime $k \simeq 0.1h$ Mpc^{-1}. In that limit, the ratio $\psi^{(1)}_2/\psi^{(1)}_1 \approx 1 - 3f_\nu/5$ is k-independent (the exact factor is not important as it will be absorbed in the EFT coefficient), and we can exchange ψ_2 for ψ_1 in the effective stress term above. Furthermore, the neutrino fluctuations ψ_3 and ψ_4 are negligible compared to the baryon+CDM ones in this limit, and based on the expectation that $\mathsf{d}_i^2/k^2_{\rm NL} = \mathcal{O}(1)$, we can disregard the insignificant neutrino contribution to $\tau_{\theta_{\rm cb}}$. In total, the baryon+CDM counterterm at leading order can be written as

$$\tilde{\psi}^{(1)}_1(\eta) = {\rm e}^{3\Delta\eta}\gamma_1(\eta)\,k^2\psi^{(1)}_1(\eta_{\rm ini})\,, \tag{4.45}$$

in complete analogy with Eq. (3.101), with the EFT parameter γ_1. It will in the end be measured by calibration to N-body simulations, and its relation to the coefficients d_i and kernels $F^{(1)}_i$ is therefore not of interest. Note that we extracted an overall growth factor ${\rm e}^{3\Delta\eta}$ in Eq. (4.45) for convenience.

To renormalize the power spectrum at two-loop, we in principle need to consider contributions to the effective stress term at second- and third order in the fields. We gave the

[8] The freestreaming scale (4.10) is not a single scale, but rather a function of scale and time (in the adiabatic approximation only of time). Using the exact neutrino sound speed and anisotropic stress, the effective freestreaming wavenumber increases monotonically with wavenumber and we have approximately $k_{\rm FS}(k,z) \propto (1+z)^{-1/2}$.

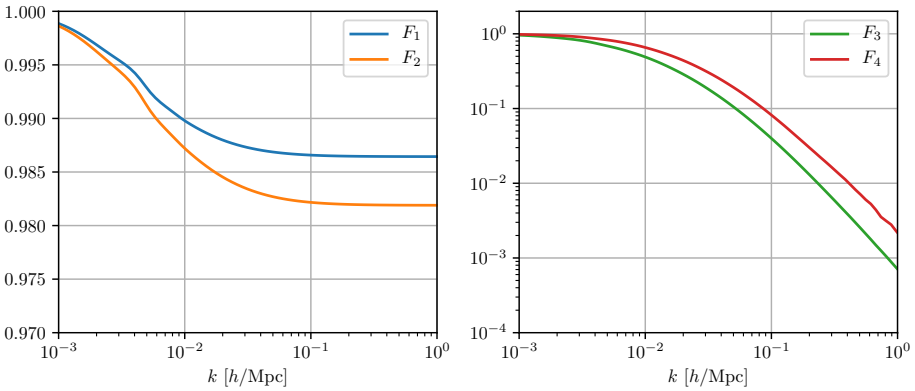

Figure 4.8: Linear kernels $F_a^{(1)}(z = 0)$ for $M_\nu = 0.1$ eV, computed in the 2F scheme. Reprinted from Paper III [46].

expression for the second order effective stress term in the EdS-approximation in Eq.(3.106), which could immediately be used for the modified baryon+CDM Euler equation in the 1F scheme. However, as was the case at leading order, in the 2F scheme there are in general numerous additional operators arising from the neutrino fields and combinations with the baryon+CDM fields. In addition, there are in general no k-independent relations between the fields, e.g. $\Delta\theta^{(2)}$ is not necessarily redundant. Therefore, even if one would argue that neutrino contributions to the effective stress term should be small compared to the baryon+CDM operators, there are still additional terms in comparison to Eq. (3.106) due to the scale-dependence of the dynamics in the presence of freestreaming neutrinos.

With this in mind, we opt for following the prescription introduced in Ref. [252] that we described in Section 3.6 to renormalize the power spectrum at NNLO in the 2F model. As discussed in that section, the benefit of this approach is that we do not need to know the specific form of the effective stress terms at second and third order, introducing only one extra EFT parameter at two-loop.

In the rest of this section, we evaluate the contributions to the one- and two-loop correction from the UV in the 2F model, and show that they can be absorbed by the counterterm (4.45) and the two-loop prescription discussed above, respectively.

Renormalization of the one-loop correction

We start at one-loop. As discussed in Secs. 3.3 and 3.4, the perturbation kernels satisfy the scaling $F^{(n)}(\mathbf{q}_1, \ldots, \mathbf{q}_n) \propto k^2$ in the limit where $\mathbf{k} = \sum_i \mathbf{q}_i$ goes to zero (but the individual $\mathbf{q}_i$ does not). Since this property follows from momentum conservation, it holds also for the generalized kernels, and in particular for the 2F scheme kernels. We calculated the hard limit, i.e. $q \to \infty$, of the one-loop correction using EdS-SPT kernels in Eq. (3.77). In the 2F case, we expect the shape of this limit to be the same due to the kernel property, but the coefficient can change. Hence, we can write the hard limit at leading power in the gradient expansion as

$$P_{1L}^h(k,\eta) = -2\mathrm{e}^{4\Delta\eta} k^2 P_0(k)\, c\, \frac{4\pi}{3} \int^\Lambda \mathrm{d}q\, P_0(q) = -2\mathrm{e}^{4\Delta\eta} k^2 P_0(k)\, c\, \sigma_\mathrm{d}\,. \tag{4.46}$$

The coefficient c depends on the exact dynamics and is in general time-dependent. We will in the rest of this chapter always consider the baryon+CDM power spectrum, and therefore we dropped the cb subscript for brevity. From Eq. (3.77), we obtain $c = 61/210$ in the 1F scheme. In 2F scheme, we are only able to solve for the kernels numerically, and we can therefore not derive c analytically in the limit $q \to \infty$. Nevertheless, we can evaluate it by taking a large value of q in the numerical evaluation of the one-loop correction. The method can be explained as follows: Define the one-loop integrand p_{1L} implicitly by

$$P_{1L}(k,\eta) = \mathrm{e}^{4\Delta\eta} \int^{\Lambda} \mathrm{d}q\, q^2 P_0(q) \int \mathrm{d}\Omega_q\, \mathsf{p}_{1L}(\mathbf{k},\mathbf{q};\eta)\,. \tag{4.47}$$

The integrand comprises the $P^{(31)}$, $P^{(13)}$ (equal to $P^{(31)}$ for the baryon+CDM auto spectrum) and $P^{(22)}$ diagrams contributing to the one-loop correction, with its accompanying kernels (see Fig. 3.5 for the Feynman diagrams). Furthermore, p_{1L} contains one more input power spectrum P_0. In the UV-limit, the leading contribution to the integrand comes from $F^{(3)}(\mathbf{k},\mathbf{q},-\mathbf{q}) \propto k^2/q^2$ (see Eq. (3.70)), and the integral can be factorized

$$P^h_{1L}(k,\eta) = 3\mathrm{e}^{4\Delta\eta} \int \frac{\mathrm{d}\Omega_q}{4\pi} \left(\lim_{q\to\infty} q^2 \mathsf{p}_{1L}(\mathbf{k},\mathbf{q};\eta) \right) \frac{4\pi}{3} \int^{\Lambda} \mathrm{d}q P_0(q) \equiv \mathrm{e}^{4\Delta\eta} p^h_{1L}(k,\eta)\, \sigma_{\mathrm{d}}^2\,. \tag{4.48}$$

Here, we introduced the *q-independent* hard-limit quantity $p^h_{1L}(k,\eta)$ corresponding to the angular integral. It can be evaluated numerically by fixing the loop momentum to a large value, $q \gg \Lambda$. The displacement dispersion σ_{d}^2 was defined in Eq. (3.75). Comparing Eq. (4.48) to Eq. (4.46), we have simply

$$c(\eta) = -\frac{p^h_{1L}(k,\eta)}{2k^2 P_0(k)}\,. \tag{4.49}$$

This coefficient was computed in Paper III [46] for three cosmologies with $M_\nu = 0.1$, 0.2 and 0.4eV, respectively. The result at redshift $z = 0$ is shown in Fig. 4.9, with the constant $c_{\mathrm{EdS}} = 61/210$ in 1F plotted in black for comparison. The cutoff used is $\Lambda = 1h$ Mpc^{-1} and the loop momentum is fixed to $q = 10h$ Mpc^{-1} when evaluating p^h_{1L}. The dashed lines show c with the linear kernel divided out.[9] In the presence of freestreaming neutrinos, c is not scale-independent anymore, but acquires a functional dependence $c = c(k^2/k^2_{\mathrm{FS}})$. Nevertheless, the scale-independence as required by momentum conservation for $k \ll q$ is recovered in both limits $k \ll k_{\mathrm{FS}}$ and $k \gg k_{\mathrm{FS}}$: On scales much larger than the freestreaming scale, $k < k_{\mathrm{FS}}$, neutrinos behave as dark matter, and the two-component fluid behaves as a single-component dark matter fluid, with c constant. This limit can be seen for the largest neutrino mass (which has the largest freestreaming wavenumber k_{FS}) around $k \simeq 10^{-3}h$ Mpc^{-1} in Fig. 4.9. The 1F value of 61/210 is not recovered for $k \ll k_{\mathrm{FS}}$, because the EdS-approximation is relaxed and due to the sensitivity of the $F^{(3)}(\mathbf{k},\mathbf{q},-\mathbf{q})$ to small scales q where the freestreaming neutrinos suppress structure formation.

The other limit $k \gg k_{\mathrm{FS}}$ corresponds to scales where the neutrino density does not grow, $\delta_\nu \simeq 0$, and therefore we have an effective decoupling of the baryon+CDM and neutrino

[9] The diagram $P^{(31)}$ that dominates in the hard limit, encompasses $F^{(3)}$ and $F^{(1)}$, hence the dashed lines isolate the behavior of $F^{(3)}$ in the limit $q \gg k$.

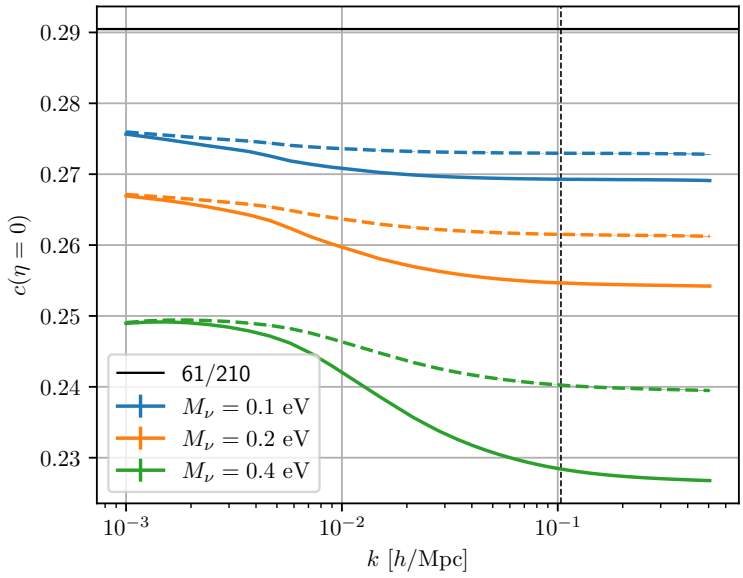

Figure 4.9: The hard limit of the one-loop correction to the power spectrum, as characterized by the coefficient c. We show the 1F result $c = 61/210$, as well as the coefficient evaluated numerically in three models with $M_\nu = 0.1$, 0.2 and 0.4 eV, using Eq. (4.49) and the 2F scheme. In the dashed lines, the linear kernel $F^{(1)}$ is divided out. Taken from Paper III [46].

system. The system is therefore again equivalent to a single-component dark matter fluid, but with slower growth due to the neutrino contribution to the Hubble friction. Accordingly, c approaches a constant for $k \gg k_{\rm FS}$. We see this limit for the two smallest neutrino masses in Fig. 4.9, while the plateau only emerges on even smaller scales for $M_\nu = 0.4$ eV.

Under the assumption $k_{\rm FS} \ll k \ll k_{\rm NL}$, the c-coefficient can thus be measured, and more importantly the hard limit of the one-loop correction has the appropriate scaling that can be corrected for by the EFT counterterms. The values of c that will be used in the following analysis are read off at the vertical dashed line in Fig. 4.9. The above assumption breaks down for $M_\nu = 0.4$ eV, but this model can nevertheless be included for illustrative purposes.

As should be the case in the effective theory, the counterterm (4.45) introduced to model the UV physics can exactly absorb the UV-sensitivity of the (generalized) SPT result (4.46). The EFT prediction for the one-loop correction is therefore

$$P_{1L}^{\rm ren}(k,\eta,\Lambda) = P_{1L}(k,\eta;\Lambda) + P_{1L}^{\rm ctr}(k,\eta;\Lambda)\,, \tag{4.50}$$

where the counterterm is given by

$$P_{1L}^{\rm ctr}(k,\eta;\Lambda) = -2\mathrm{e}^{4\Delta\eta}\,\gamma_1(\Lambda)k^2P_0(k)\,. \tag{4.51}$$

To analyze the cutoff-(in)dependence of this result, we can consider the response to a change of the cutoff:

$$\frac{\mathrm{d}}{\mathrm{d}\Lambda}\left[P_{1L}(k,\eta;\Lambda) + P_{1L}^{\rm ctr}(k,\eta;\Lambda)\right] = -2\mathrm{e}^{4\Delta\eta}k^2P_0(k)\frac{\mathrm{d}}{\mathrm{d}\Lambda}\left[c(\eta)\sigma_{\rm d}(\Lambda) + \gamma_1(\Lambda)\right]\,, \tag{4.52}$$

where we used Eq. (4.46), valid at leading power in gradients. Demanding that the one-loop correction is cutoff-independent thus yields an renormalization group equation (RGE) for $\gamma_1(\Lambda)$ that has solution (cf. Eq. (3.104))

$$\gamma_1(\Lambda) = \bar{\gamma}_1 + \frac{4\pi c}{3}\int_\Lambda^\infty \mathrm{d}q\, P_0(q)\,, \tag{4.53}$$

with $\bar{\gamma}_1$ being an initial condition.

Renormalization of the two-loop correction

At two-loop, there are two loop momenta $\mathbf{q}_1$, $\mathbf{q}_2$ (see the diagrams contributing as well as the full two-loop expression in Fig. 3.7 and Eq. (3.71), respectively). The loop integrals are therefore sensitive to the UV when one or both of the momenta become large. Hence, we distinguish between the single-hard (h) and double-hard (hh) limits as described in Section 3.6.

Double-hard limit As we saw in Section 3.6, the leading contribution of the double-hard region of the two-loop integral comes from the $P^{(51)}$ diagram, and hence the $F^{(5)}$ kernel. In this limit, we have $F^{(5)} \propto k^2$ as required by momentum conservation, and thus the leading double-hard contribution scales as $k^2 P_0(k)$, which can be captured by the counterterm already introduced at one-loop (4.51). At NNLO, we can split the corresponding EFT parameter into a one- and two-loop piece,

$$\gamma_1^{\mathrm{NNLO}} = \gamma_1^{1L} + \gamma_1^{2L}. \tag{4.54}$$

A practical remedy is to choose γ_1^{2L} to precisely cancel the double-hard contribution of the two-loop correction, and let $\gamma_1^{1L} \equiv \gamma_1$ contain the correction of the hard limit of the one-loop as well as the actual impact of short-scale physics (the "finite" part of the counterterm) [252]. In practice, this can be done by subtracting the double-hard limit from the two-loop correction: we define the *subtracted* two-loop correction as

$$\bar{P}_{2L} = P_{2L} - P_{2L}^{hh}\,. \tag{4.55}$$

The double-hard limit is given by $P_{2L}^{hh} = b^{hh} k^2 P_0(k)$, where b^{hh} is a model-dependent constant. In the 2F scheme, we can compute this constant by evaluating $b^{hh} = \lim_{k\to 0} P_{2L}/k^2/P_0$ in the low-k region of the two-loop integral, which has sole support from $q_1, q_2 \gg k$ that precisely corresponds to the double-hard limit.

In the left panel of Fig. 4.10, we show the subtracted two-loop correction $\bar{P}_{2L}$ normalized to $k^2 P_0(k)$ (more precisely, the corresponding IR-resummed quantities, with an overall rescaling growth factor), computed using a cutoff $\Lambda = 1h$ Mpc^{-1}. Both the 1F and the 2F models (with various sums of neutrino masses) attain a plateau around $k \simeq 10^{-3}h$ Mpc^{-1}, indicating that the double-hard $k^2 P_0$-scaling is reached. Due to the presence of the additional freestreaming scale $k_{\mathrm{FS}} \simeq 0.01h$ Mpc^{-1}, the neutrino models recover this scaling for even smaller wavenumbers than in 1F. The limiting values b^{hh} in each model was measured at the subtraction point indicated by the vertical dashed line. It is important to remark that b^{hh} defines the renormalization point, and therefore a change in its value only leads to a shift in γ_1. In Paper III, it was nevertheless checked that changing the subtraction point had negligible impact on observables except for the shift in γ_1 [46].

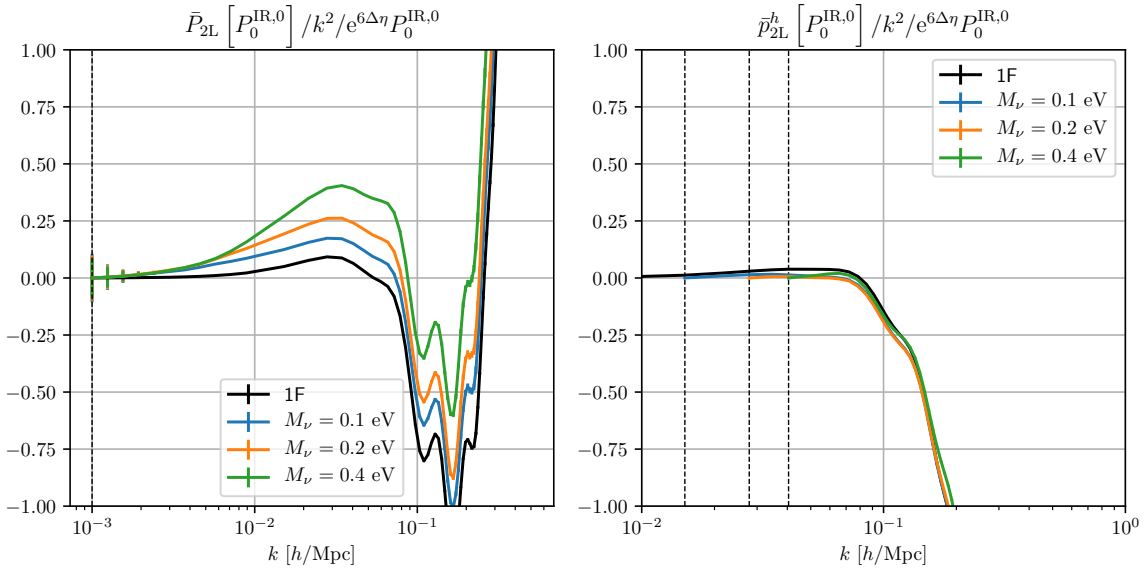

Figure 4.10: Subtracted two-loop correction (left panel) and subtracted single-hard limit of the two-loop (right panel), divided by k^2P_0. We show the corresponding IR-resummed quantities and rescale the result by an appropriate growth factor (see header). In addition to the 1F result, three models with $M_\nu = 0.1$, 0.2 and 0.4 eV computed in the 2F scheme are shown. The vertical dashed lines indicate the subtraction points where the double-hard limits b^{hh} and b^h were evaluated and subtracted. They coincide for all neutrino masses in the left panel, while in the right panel, the subtraction points increase with the neutrino mass. Errorbars indicate uncertainty from the Monte Carlo integration. Reprinted from Paper III [46].

Single-hard limit We proceed to discuss the single-hard region, in which one of the loop momenta becomes large. As alluded above, we will not explicitly write down counterterms that renormalize this region, but correct for the UV-sensitivity in a universal manner using one extra parameter.

To evaluate the single-hard limit, we start by defining the two-loop *integrand* p_{2L}:

$$P_{2L}(k,\eta) = \mathrm{e}^{6\Delta\eta}\int^{\Lambda}\mathrm{d}q_1\, q_1^2 P_0(q_1)\int^{\Lambda}\mathrm{d}q_2\, q_2^2 P_0(q_2)\int \mathrm{d}\Omega_{q_1}\,\mathrm{d}\Omega_{q_2}\,\mathsf{p}_{2L}(\mathbf{k},\mathbf{q}_1,\mathbf{q}_2;\eta)\,. \tag{4.56}$$

In analogy to the one-loop case, we can factorize the integral in the single-hard case. Let q_1 be hard, with $q_2 \sim k$, then the leading contribution to the integral above comes from kernels $F^{(n)}(\ldots,\mathbf{q}_1,-\mathbf{q}_1,\ldots) \propto 1/q_1^2$, and the hard limit is factorized as follows,

$$\begin{aligned} P_{2L}^{q_1\to\infty}(k,\eta) &= 3\mathrm{e}^{6\Delta\eta}\int^{\Lambda}\mathrm{d}q_2\, q_2^2 P_0(q_2)\int\frac{\mathrm{d}\Omega_{q_1}}{4\pi}\left(\lim_{q_1\to\infty} q_1^2\mathsf{p}_{2L}(\mathbf{k},\mathbf{q}_1,\mathbf{q}_2;\eta)\right) \\ &\quad\times\frac{4\pi}{3}\int^{\Lambda}\mathrm{d}q_1\, P_0(q_1) \\ &= \mathrm{e}^{6\Delta\eta}\, p^h_{2L}(k,\eta)\,\sigma_{\mathrm{d}}^2\,, \end{aligned} \tag{4.57}$$

where we defined p^h_{2L} to be the integral in the first line which is q_1-*independent*. We computed the equivalent quantity analytically in EdS in Eq. (3.118). Since the other single-hard contribution with q_2 hard, $q_1 \sim k$, is completely equivalent, the total single-hard limit of the two-loop power spectrum at leading power in gradients is

$$P^h_{2L}(k,\eta) = 2\mathrm{e}^{6\Delta\eta}\, p^h_{2L}(k,\eta)\, \sigma^2_{\mathrm{d}}\,. \tag{4.58}$$

Following Ref. [252], we assume that the unknown UV physics can be captured by a shift in the displacement dispersion, $\sigma^2_{\mathrm{d}}(\Lambda) \mapsto \sigma^2_{\mathrm{d}}(\Lambda) + \mathcal{N}\gamma_2(\Lambda)$, with the EFT parameter γ_2. The factor $\mathcal{N}$ will be defined explicitly below. As we showed in Eq. (3.117), the replacement corresponds to adding a counterterm

$$2\mathrm{e}^{6\Delta\eta}\, p^h_{2L}(k,\eta)\, \mathcal{N}\gamma_2\,, \tag{4.59}$$

to the power spectrum at NNLO. We note however, that the integral p^h_{2L} contains a region in which q_2 is large, corresponding to a double-hard limit if the external wavenumber k is much smaller than the cutoff. Therefore, adding the counterterm (4.59) yields a contribution to the two-loop correction that is degenerate with the $k^2P_0(k)$ counterterm. We choose to remove this contribution, adopting the renormalization scheme where γ_1^{2L} precisely cancels the double-hard region of the two-loop correction, including the contribution from the single-hard counterterm (4.59). In practical terms, the degenerate double-hard part can be removed in an analogous manner as in the definition of the subtracted two-loop correction: we define

$$\bar{p}^h_{2L} = p^h_{2L} - p^{hh}_{2L}\,. \tag{4.60}$$

The quantity p^h_{2L} can be computed numerically by fixing q_1 to a large value, $q_1 \gg \Lambda$, performing the integral over $\mathbf{q}_2$ as well as the angular integral over $\mathbf{q}_1$ as given by the first line of Eq. (4.57). In the results we show below, a cutoff $\Lambda = 1h$ Mpc^{-1} is used and the hard momentum is fixed to $q_1 = 10h$ Mpc^{-1} when evaluating the single-hard limit. Subsequently, the double-hard contribution can be removed by computing the limit $b^h = \lim_{k\to 0} p^h_{2L}/k^2/P_0(k)$. For vanishing k, the integral in the first line of Eq. (4.57) only gets contributions from $q_2 \gg k$, hence we recovered the double-hard limit, where p^h_{2L} scales as k^2P_0. It follows that $p^{hh}_{2L} = b^h k^2 P_0(k)$.

In the right panel of Fig. 4.10, we display the subtracted single-hard contribution $\bar{p}^h_{2L}$, normalized to $k^2P_0(k)$ (as for the subtracted full two-loop correction, the corresponding IR resummed quantities are shown). The 1F scheme (black curve) indeed exhibit the appropriate $k^2P_0(k)$ scaling at low k, and the degenerate double-hard contribution can be subtracted at $k = 10^{-2}h$ Mpc^{-1}. This is also the case for 2F, but on very small wavenumbers there are certain deviations. Due to the large value $q_1 = 10h$ Mpc$^{-1} \gg k$, they could be attributed to large numerical cancellations. In Paper III, it was checked that using a smaller $q_1 = 5h$ Mpc^{-1} extends the range in which the k^2P_0-scaling is manifest in the neutrino models, without changing the result in the region of interest $k \gtrsim 0.05h$ Mpc^{-1} [46]. Hence, the subtraction points can be chosen in the intermediate region where the k^2P_0-scaling is attained, but on wavenumbers larger than the point at which numerical instabilities occur. In particular, for the results that we present, a subtraction point $k = 0.015$, 0.027, $0.04h$ Mpc^{-1} was used for $M_\nu = 0.1$, 0.2 and 0.4 eV, respectively. Note that this is above

the freestreaming scale, and therefore the opposite limit as compared to the subtraction of the full two-loop (right panel in Fig. 4.10). For the largest neutrino mass $M_\nu = 0.4$ eV, the window in which the double-hard scaling is reached is very narrow, and moreover not sufficiently away from the freestreaming scale, i.e. the assumption $k_{\rm FS} \ll k$ breaks down. Finally, we stress again that the subtraction points define the renormalization points, and hence the only impact of changing the subtraction point is a shift in the γ_1 parameter.

In total, we obtain the renormalized two-loop power spectrum as

$$P_{2L}^{\rm ren}(k,\eta;\Lambda) = \bar{P}_{2L}(k,\eta;\Lambda) + P_{2L}^{\rm ctr}(k,\eta;\Lambda)\,, \tag{4.61}$$

where the counterterm is given by

$$P_{2L}^{\rm ctr}(k,\eta;\Lambda) = 2{\rm e}^{6\Delta\eta}\mathcal{N}\gamma_2(\Lambda)\,\bar{p}_{2L}^{h}(k,\eta)\,, \tag{4.62}$$

absorbing the UV-sensitivity in the single-hard region, with the new EFT parameter γ_2. The double-hard region is corrected for by the γ_1 counterterm already introduced at one-loop. The quantities with a bar, $\bar{P}_{2L}$ and p_{2L}^h, have the double-hard contribution subtracted as discussed above, such that they yield no contribution degenerate with the γ_1 counterterm.

Cutoff-independence

We have introduced counterterms at one- and two-loop that can correct for the UV-sensitivity of the baryon+CDM power spectrum in the two-component fluid model. Let us now demonstrate explicitly that adding these counterterms cure the cutoff-dependence of the theory.

The renormalized power spectrum at NNLO is given by

$$P_{\rm NNLO}^{\rm ren}(k,\eta;\Lambda) = P_{\rm tree}(k,\eta) + P_{1L}^{\rm ren}(k,\eta;\Lambda) + P_{2L}^{\rm ren}(k,\eta;\Lambda)\,, \tag{4.63}$$

with the renormalized loop corrections given in Eqs. (4.50) and (4.61). We demand that it should be independent of the cutoff: ${\rm d}P_{\rm NNLO}^{\rm ren}/{\rm d}\Lambda = 0$. In the renormalization scheme we adopted, there are no degenerate UV contributions between the one- and two-loop corrections, which means that the RGE can be solved independently for each correction. Moreover, in this scheme, the one-loop RGE and its solution (4.53) remain the same after adding the two-loop contribution.

After renormalizing the one-loop correction, the only remaining cutoff-dependence of Eq. (4.63) comes from the single-hard region (we removed the double-hard contribution from the two-loop power spectrum, or in other words absorbed it by the one-loop counterterm), hence we require

$$0 = \frac{\rm d}{{\rm d}\Lambda}\left[\bar{P}_{2L}^{h}(k,\eta;\Lambda) + P_{2L}^{\rm ctr}(k,\eta;\Lambda)\right] = 2{\rm e}^{6\Delta\eta}\bar{p}_{2L}^{h}(k,\eta)\frac{\rm d}{{\rm d}\Lambda}\left[\sigma_{\rm d}^2(\Lambda) + \mathcal{N}\gamma_2(\Lambda)\right]\,. \tag{4.64}$$

This result, valid at leading power in gradients, reflect the fact that we assume the UV-sensitivity can be corrected for by a shift in $\sigma_{\rm d}^2$. The solution of the RGE is[10]

$$\gamma_2(\Lambda) = \overline{\gamma}_2 + \frac{4\pi}{3\mathcal{N}}\int_\Lambda^\infty {\rm d}q\, P_0(q)\,, \tag{4.65}$$

[10] For the EFT parameters γ_1 and γ_2, the bar notation is used to denote the initial condition as $\Lambda \to \infty$. This notation is unrelated to the bar labeling the *subtracted* power spectra, e.g. $\bar{P}_{2L}$ as defined in Eq. (4.55).

with $\bar{\gamma}_2$ being an initial condition. The factor $\mathcal{N}$ is purely conventional, and to treat γ_2 on equal footing as γ_1, we use $\mathcal{N} = 1/c$.

In Fig. 4.11, we display the one- and two-loop power spectra before and after renormalization for two cutoffs $\Lambda = 0.8h$ Mpc^{-1} and $\Lambda = 1h$ Mpc^{-1}. The bottom panels display the fractional difference between the renormalized spectra using the two cutoffs, serving as a check that using the EFT framework we have indeed obtained a cutoff-independent result. It is reassuring to see that for the one-loop, the relative difference between the cutoffs is at the permille level up to $k \simeq 0.4h$ Mpc^{-1}. As we increase k, we expect the higher order terms in the gradient power expansion, $\mathcal{O}(k^4/k_{\rm NL}^4)$, which we neglected, to become important. The double-hard limit gives the largest contribution to the bare two-loop correction, as can be seen by comparing the full (blue) and subtracted (yellow) lines in Fig. 4.11. After adding the counterterm (green), we obtain the renormalized two-loop power spectrum (red). It vanishes for small k (corresponding to the double-hard limit, whose contribution is removed), therefore there is a large *relative* difference on these scales in the bottom plot. For $k \simeq 0.08$–$0.25h$ Mpc^{-1}, we find that the renormalized two-loop differs less than 1 % between the two cutoffs.

4.5 Comparison to N-body simulations

We have now obtained a framework for computing loop corrections in the presence of massive neutrinos, using a hybrid fluid model that captures the time- and scale-dependence introduced by neutrino perturbations as well as from the departure from EdS at late times, embedded in an effective theory. To make a precise comparison to the simplified 1F scheme, we calibrate both methods to N-body simulations and measure their performance. We use the EFT approach outlined in the previous section, and promote the theory to include IR resummation by making the replacement $P_0 \to P_0^{\rm IR,N-L}$.

The discussion follows Paper III [46], were the analysis was performed for cosmologies with $\Omega_m = 0.3175$, $\Omega_b = 0.049$, $h = 0.6711$, $n_s = 0.9624$, $\sigma_8 = 0.834$, and three sums of neutrino masses $M_\nu = 0.1$, 0.2 and 0.4 eV. The loop integral cutoff is $\Lambda = 1h$ Mpc^{-1} and hard limits are evaluated by fixing the hard momenta to $q = 10h$ Mpc^{-1}. For the IR resummation, a separation scale $k_s = 0.2h$ Mpc^{-1} was used, as recommended by Ref. [149].

The N-body simulation results is taken from the Quijote suite [174]. In this suite, the simulations including neutrinos have 512^3 CDM and 512^3 neutrino particles, in a box of size 1 $(\text{Gpc}/h)^3$. The simulations use pair fixed initial conditions, which significantly reduce cosmic variance [285–287]. The power spectrum $P_{\rm data}$ and its uncertainty $\Delta P_{\rm data}$ at $z = 0$ can be estimated by computing the mean and variance of the 500 Quijote realizations, respectively.

The calibration and performance measurement of each model is done by computing the following χ^2 at NLO and NNLO:

$$\chi^2_{\rm NLO} = \sum_{k=k_{\rm min}}^{k_{\rm max}} \frac{[P_{\rm data}(k) - P^{\rm ren}_{\rm NLO}(k,\gamma_1)]^2}{[\Delta P_{\rm data}(k)]^2}\,, \tag{4.66}$$

$$\chi^2_{\rm NNLO} = \sum_{k=k_{\rm min}}^{k_{\rm max}} \frac{[P_{\rm data}(k) - P^{\rm ren}_{\rm NNLO}(k,\gamma_1,\gamma_2)]^2}{[\Delta P_{\rm data}(k)]^2}\,. \tag{4.67}$$

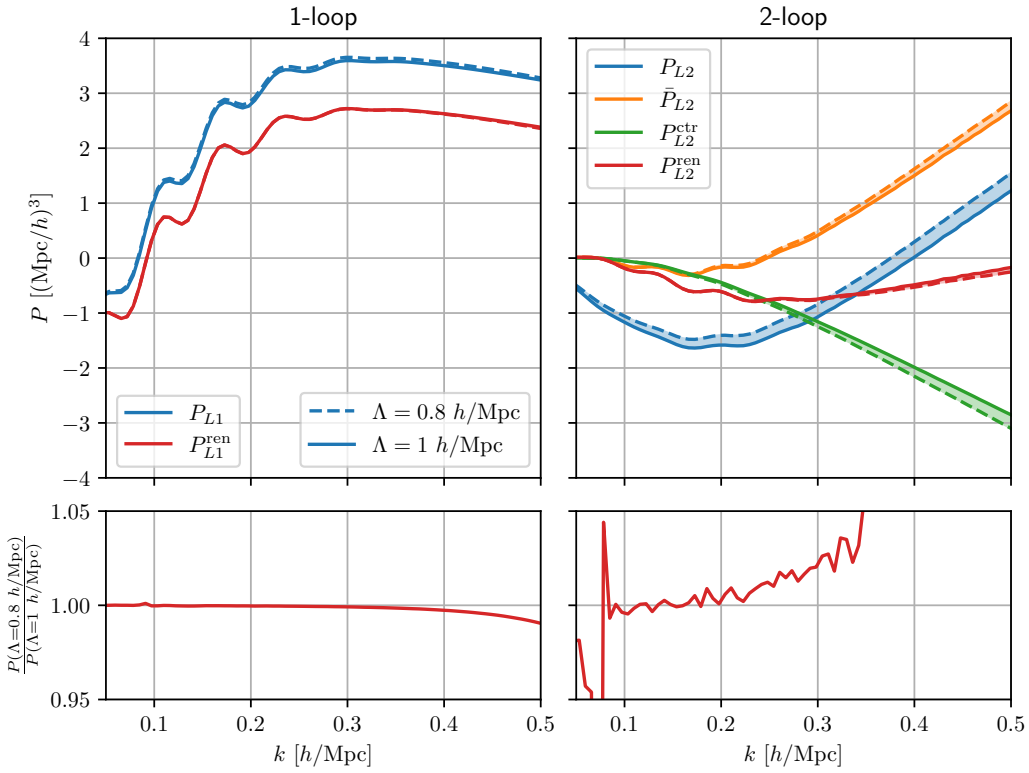

Figure 4.11: Cutoff-dependence of the one- and two-loop corrections, before and after renormalization. *Upper left*: Bare (blue) and renormalized (red) one-loop correction to the power spectrum. *Upper right*: Bare (blue), subtracted (yellow) and renormalized (red) two-loop correction. The single-hard counterterm is shown in green. In both panels the dashed curves use cutoff $\Lambda = 0.8h$ Mpc^{-1} and the solid ones use $\Lambda = 1h$ Mpc^{-1}. The shaded region indicate the difference. *Bottom panels*: Fractional difference between the renormalized results using the two cutoffs, i.e. $P(\Lambda = 0.8h\ \mathrm{Mpc}^{-1})/P(\Lambda = 1h\ \mathrm{Mpc}^{-1})$. Taken from Paper III [46].

The EFT parameters are measured by minimizing the χ^2 above, and their uncertainties estimated by the region $\Delta\chi^2 = \chi^2 - \chi^2_{\rm min} \leq 1$. The analysis uses $k_{\rm min} = 0.0089h$ Mpc^{-1} and utilizes at e.g. $k_{\rm max} = 0.1(0.3)h$ Mpc^{-1} 14(46) wavenumber grid points. Moreover, the following cases are considered in the fits:

NLO	$\{\bar{\gamma}_1\}$	one-loop, 1-parameter,
NLO, $\bar{\gamma}_1 = \bar{\gamma}_1^{\rm [NNLO]}$	$\emptyset$	one-loop, 0-parameter with $\bar{\gamma}_1$ fixed from NNLO fit,
NNLO, $\bar{\gamma}_2 = \bar{\gamma}_1$	$\{\bar{\gamma}_1\}$	two-loop, 1-parameter with $\bar{\gamma}_2 = \bar{\gamma}_1$,
NNLO	$\{\bar{\gamma}_1, \bar{\gamma}_2\}$	two-loop, 2-parameter.

We explain the motivation for the unfitted, 0-parameter NLO scheme (the second case above)

below. The third case, $\bar{\gamma}_1 = \bar{\gamma}_2 \equiv \bar{\gamma}$ is motivated by an assumption that the EFT corrects the displacement dispersion in the same way at one- and two-loop, i.e. $\sigma_{\rm d}^2 \to \sigma_{\rm d}^2 + \gamma/c$.

Finally, we note that on large scales, close to the box size of the simulations, the binning method used to estimate power spectra from particle densities yields significant effects, and needs to be taken into account when comparing simulations results and theory. The same binning procedure can be performed on the (theoretical) linear power spectrum[11] and one can thus "unbin" the simulation power spectra $P_{\rm data}^{\rm binned}(k)$ by multiplying it with the ratio of the linear power spectrum with and without binning effects:

$$P_{\rm data}(k) = \frac{P_0(k, z=0)}{P_0^{\rm binned}(k, z=0)} P_{\rm data}^{\rm binned}(k)\,. \tag{4.68}$$

Results

We present the results of the calibration and comparison to Quijote N-body data, using the most phenomenologically relevant neutrino mass $M_\nu = 0.1$ eV. The power spectrum computed in the 2F scheme normalized to the N-body result is shown in Fig. 4.12, using the four different calibration cases discussed above as well as varying the pivot scale $k_{\rm max}$—up to which maximum wavenumber the fit is performed. We show also the linear power spectrum for comparison. The gray band correspond to N-body uncertainty, $\Delta P_{\rm data}$, and the red shading indicate the expected theoretical uncertainty at one-loop (lighter red) and two-loop (darker red) [288]. In all the perturbative cases, there is a "bumb"-like feature on large scales $k \simeq 0.01$–$0.05h$ Mpc^{-1}, which extends a few permille but well within the uncertainty of the N-body results. It likely arises due to finite box size effects that are not captured by the formula (4.68) correcting for binning effects. We see that in all cases, the perturbative solutions can be fit within the N-body uncertainty up to and beyond the pivot scale.

Inevitably, the results are subject to a degree of overfitting depending on the loop order. We can estimate the extent of overfitting by comparing to the expected theoretical uncertainty: considering e.g. the NLO case, which for all pivot scales deviates much less from the data than expected by the size of the two-loop correction (i.e. the estimated theoretical uncertainty at one-loop, light red shading), suggesting overfitting. An issue in this analysis is that on large scales, there are few grid points and the N-body data is not very precise (even after reducing cosmic variance) due to finite box size effects. Therefore, one cannot accurately constrain the EFT parameters at $k \lesssim 0.05h$ Mpc^{-1}, where the theory is most precise. This issue is most prominent at NLO, because one needs to go beyond $k_{\rm max} \simeq 0.1h$ Mpc^{-1} to get enough data points for a credible calibration, which is beyond the point where the two-loop correction becomes important. At NNLO, the theory is precise up to a larger wavenumber, and one can reliably use a larger pivot scale. This is the motivation for the introduction of the 0-parameter NLO calibration case defined above. It uses the $\bar{\gamma}_1$ parameter measured from the NNLO fit, and should thus be subject to less overfitting (recall that the renormalization scheme was defined in such a way that $\bar{\gamma}_1$ is unchanged after adding the two-loop, up to numerical error and overfitting). We see indeed that the

[11] The Pylians library, github.com/franciscovillaescusa/Pylians, has a routine that bins a power spectrum the same way as is done to estimate non-linear power spectra from the Quijote suite.

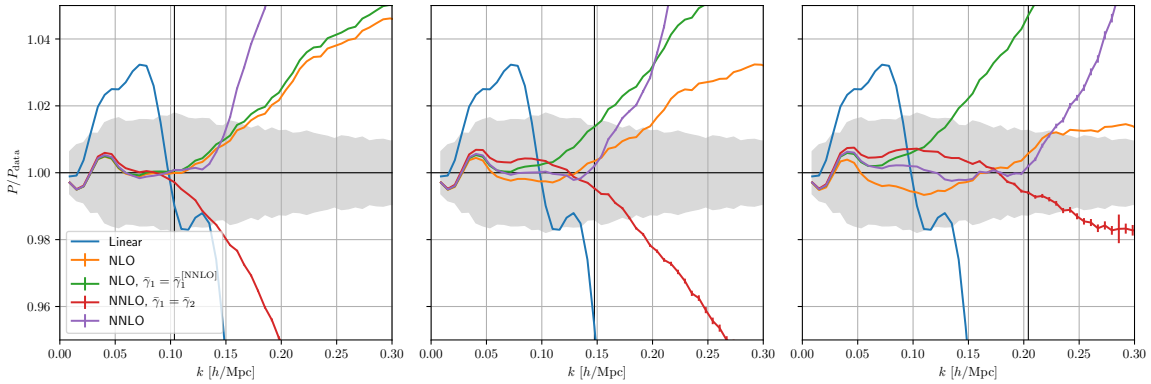

Figure 4.12: The baryon+CDM power spectrum at NLO and NNLO for $M_\nu = 0.1$ eV, using different sets of EFT parameters, computed in the 2F scheme and normalized to the Quijote result. The gray shaded region indicate uncertainty from the N-body simulation, while the light (dark) shaded red region indicate expected theoretical uncertainty at one(two)-loop. The pivot scales are $k_{\rm max} = 0.103$ (left) 0.148 (middle) and $0.204h$ Mpc^{-1} (right), as indicated by vertical black lines. Errorbars display the uncertainty from the numerical loop integration. Reprinted from Paper III [46].

0-parameter case deviates much further than the 1-parameter one at NLO for the two larger pivot scales in Fig. 4.12.

In the left panel of Fig. 4.13, we display the χ^2 per degree of freedom in the different calibration cases. We find $\chi^2/\text{d.o.f} \ll 1$, indicating that the estimator we adopted for the N-body uncertainty is too simple (e.g. neglecting correlations between different bins). Nevertheless, the aim is to compare the performance of the 1F and 2F models, hence the precise value of the χ^2 is not important. Moreover, the results imply that the 1-parameter $\bar{\gamma}_1 = \bar{\gamma}_2$ ansatz proposed by Ref. [252] does not agree too well with the N-body results when including the exact scale- and time-dependence. In particular, this case even performs worse than both NLO cases at $k_{\rm max} \simeq 0.12h$ Mpc^{-1}. We discuss the right panel of this figure shortly.

The measured EFT parameters are showed in Fig. 4.14. We show both schemes 1F and 2F (their difference will be discussed below), where the shaded regions indicate 1σ uncertainty. Consider first the $\bar{\gamma}_1$ parameter at NLO and NNLO (first and third panel). At NLO, the measurement is consistent with a constant until $k \simeq 0.11h$ Mpc^{-1}, after which the parameter begins to run. On the other hand, at NNLO this plateau region is extended to $k \simeq 0.14h$ Mpc^{-1} (and up to $0.2h$ Mpc^{-1} within 1σ uncertainty). The second parameter at NNLO ($\bar{\gamma}_2$) can not be constrained below $k \simeq 0.15h$ Mpc^{-1}, because the counterterm (4.62) (with the double-hard contribution subtracted) vanishes for small k. We note that the measured values of $\bar{\gamma}_1$ and $\bar{\gamma}_2$ differ, yielding another indication that the 1-parameter ansatz at NNLO does not work very well. Moreover, the EFT parameter $\bar{\gamma}$ for this ansatz exhibits a running across all scales, and in particular at low k, as can be seen in the second panel of Fig. 4.14.

Next, let us compare the performance of the 1F scheme and 2F scheme in predicting

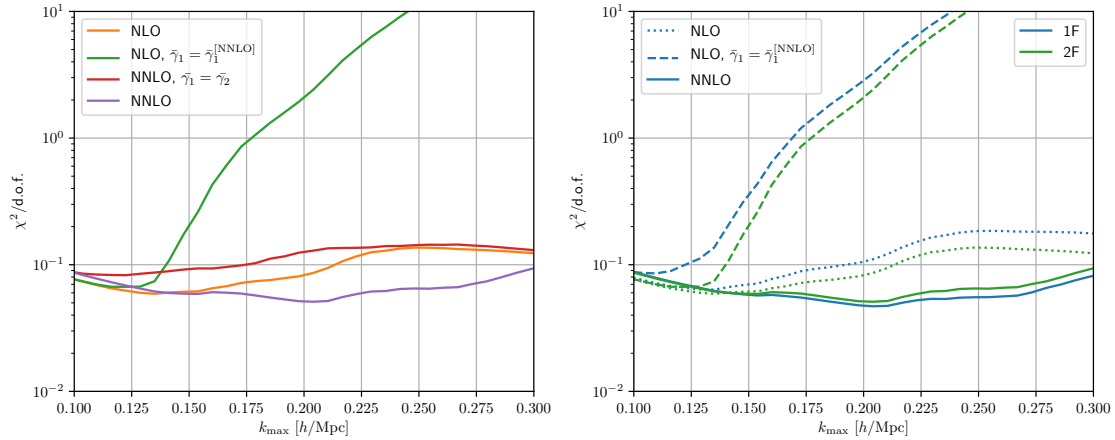

Figure 4.13: Reduced χ^2 as a function of pivot scale k_{max} for the different calibration cases (left) and for different neutrino schemes (right). Taken from Paper III [46].

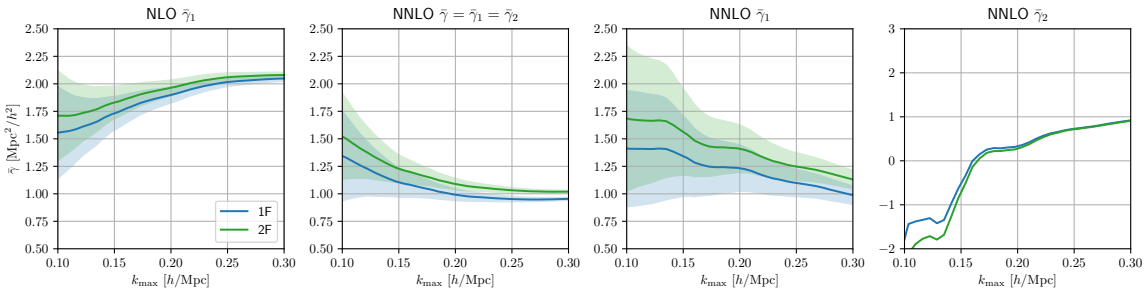

Figure 4.14: Measured EFT parameters γ_1, γ_2 and $\gamma \equiv \gamma_1 = \gamma_2$ as a function of the pivot scale k_{max}. The results are shown from a cosmology with $M_\nu = 0.1$ eV, with the blue and green lines corresponding to the 1F and 2F schemes, respectively. The shaded region indicate 1σ uncertainty. Figure taken from Paper III [46].

the baryon+CDM power spectrum at NLO and NNLO. Their power spectra are shown in Fig. 4.15. It is clear that both schemes can match the N-body power spectrum very well, and the differences between them are minimal. This conclusion is also supported by the right panel of Fig. 4.13, showing only slight differences between the reduced χ^2 in the two schemes. Recalling the percent difference between the bare spectra at $k \simeq 0.17h$ Mpc^{-1} we found in Fig. 4.7, mostly due to the departure from EdS at late times, this result suggests that the discrepancy can be largely absorbed by a shift in the counterterms. Specifically, the difference between the schemes is degenerate with the k^2P_0-counterterm to large extent. This is also apparent from Fig. 4.14, where both in the NLO and NNLO cases there is a shift $\Delta\bar{\gamma}_1 \simeq 0.2$ Mpc$/h^2$ between the 1F and 2F schemes. On the other hand, the $\bar{\gamma}_2$ parameter is not altered between the schemes. The $\Delta\bar{\gamma}_1$ shift is consistent with the findings of Refs. [45, 213] for the bispectrum as we discuss in the next chapter.

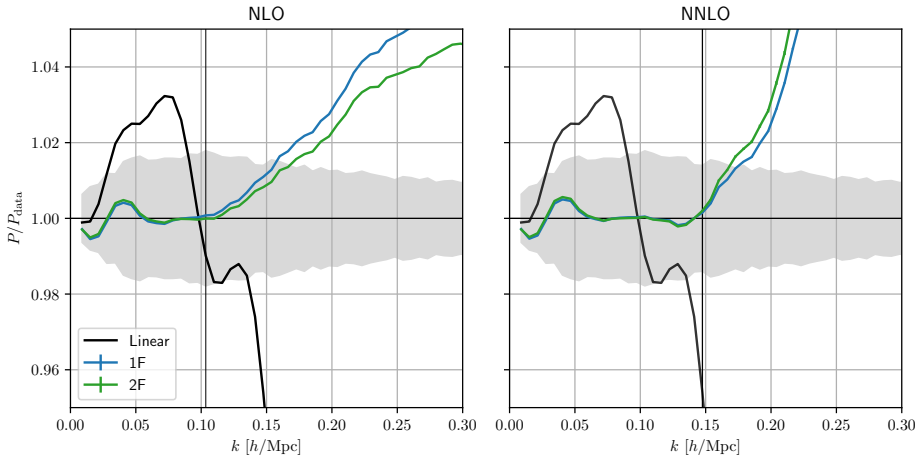

Figure 4.15: The baryon+CDM power spectrum at NLO (left) and NNLO for $M_\nu = 0.1$ eV and using a pivot scale $k_{\rm max} = 0.148h$ Mpc^{-1}. The blue and green lines show the 1F and 2F results, respectively, normalized to the Quijote N-body result. Reprinted from Paper III [46].

Summary In this chapter, we have described structure formation in the presence of massive neutrinos, going beyond linear theory for the neutrino perturbations. Utilizing a hybrid two-component fluid model, with a certain prescription for the neutrino sound velocity, we could compute non-linear corrections to the power spectrum using the extension of SPT introduced in the previous chapter. We find that our results, capturing exact scale- and time-dependence (2F), yield percent differences compared to a commonly simplified treatment (1F) beyond $k \simeq 0.17$ and $0.2h$ Mpc^{-1} for the density and velocity power spectra ($M_\nu = 0.1$ eV), respectively. We constructed an EFT framework for the hybrid model valid on scales much smaller than the freestreaming scale, and we showed that the resulting power spectrum at two-loop is cutoff-independent. Comparing to N-body simulations, we found that the difference of the density power spectrum between 1F and 2F can largely be absorbed into the one-loop counterterm, hence both schemes perform equally well in matching the simulation result.

5 The bispectrum of large-scale structure

Beyond the power spectrum, the leading non-Gaussian LSS statistic is the bispectrum. Containing information complementary to the power spectrum, it allows for breaking degeneracies between cosmological parameters and galaxy bias [223], or even between the cosmological parameters themselves, e.g. between the neutrino mass and amplitude of fluctuations [39, 289]. For instance, recent analyses of the BOSS galaxy clustering data show that including the bispectrum reduces the errorbar for σ_8 (characterizing the amplitude of fluctuations) by $\mathcal{O}(10\,\%)$ [159, 290] (see also Refs. [163, 291]). Moreover, the bispectrum is a natural probe for deviations from Gaussian initial fluctuations, i.e. non-Gaussianity. For example, a detection of a non-zero amplitude in the squeezed limit of the initial bispectrum would rule out single-field inflation [292]. Recent analyses have used the bispectrum in combination with the power spectrum from BOSS data to constrain primordial non-Gaussianity, yielding constraints with similar uncertainties as WMAP [160, 161, 293, 294].[1] Given the expected precision of the DESI [21] and Euclid [19, 20] surveys, these constraints will certainly improve significantly in the future.

The bispectrum was first analyzed in the context of the EFTofLSS at one-loop in Refs. [250, 296], finding percent agreement compared to simulations up to $k_{\rm max} \approx 0.2h$ Mpc^{-1} at $z = 0$. More recent precision investigations show that the range of validity is smaller, concluding that the one-loop prediction is accurate at the percent level for $k_{\rm max} \lesssim 0.1h$ Mpc^{-1} [213, 297]. In this chapter we will indeed see that the two-loop correction becomes important at $k \approx 0.08h$ Mpc^{-1}, which is consistent with expectations based on theoretical uncertainties [288]. Ref. [213] also studied the EdS-approximation in the context of the bispectrum, and found that the error introduced by this approximation on the tree-level bispectrum exceeds the loop corrections for $k \lesssim 0.02h$ Mpc^{-1}.

In this chapter we present the results of Paper II [45]: we derive a renormalized bispectrum at NNLO in an EFT framework. The counterterms that renormalize the one-loop correction are shown to be sufficient to absorb the double-hard region of the two-loop correction, albeit in a different linear combination. To account for the UV-contribution in the single-hard limit, we adopt the prescription described in Section 3.6 (and introduced in Ref. [252]) and extend it to the bispectrum, yielding one additional EFT parameter for the two-loop correction. When comparing to N-body simulations, using a realization based approach to beat cosmic variance, we find that the perturbative description has 1σ agreement up to $k \simeq 0.08h$ Mpc^{-1} and $k \simeq 0.15h$ Mpc^{-1} at one- and two-loop, respectively. In Section 5.2 we also discuss the EdS-approximation and assess its accuracy for the one-loop bispectrum compared to exact time-dependent ΛCDM kernels.

We will work with a single-component, dark matter fluid and adopt the EdS-approximation

[1] Note that galaxy clustering constrain the combination $b_\phi f_{\rm NL}$, where b_ϕ is the primordial non-Gaussianity bias parameter and $f_{\rm NL}$ is the parameter of interest: the amplitude of primordial non-Gaussianity. To constrain the latter, one therefore needs to make assumptions on the former [295].

unless otherwise specified. Specifically, this means that we solve the fluid equations via the expansion (3.55) with the kernels given by the EdS-SPT recursion relations (3.48). We evaluate the bispectrum at present time, and since the time-dependence is in this case factored out, the input linear power spectrum can be taken at $z = 0$ and furthermore $\Delta\eta = 0$. In addition, we will only be concerned with correlations of the matter density field, so only the $a = 1$ components of the kernels $F_a^{(n)}$ are of interest. Therefore, we drop the a subscript for brevity. We do not IR resum the perturbative predictions (at NNLO this is needed to a lesser degree for obtaining accurate results). The results are presented for a cosmology with $\Omega_{\rm m}(z = 0) = 0.272$, $h = 0.724$, $n_s = 0.967$ and $\sigma_8 = 0.81$.

Tree-level bispectrum

The bispectrum was defined in Eq. (3.64). Inserting the perturbative expansion and applying the Wick theorem analogously as for the power spectrum discussed in Section 3.5 yields a "loop" expansion of the bispectrum. We assume Gaussian initial conditions, therefore a non-zero bispectrum can only be generated by non-linear corrections, and indeed the tree-level bispectrum contains the non-linear kernel $F^{(2)}$. Its diagrammatic representation is displayed in Fig. 5.1. Each outgoing line corresponds to one of the fields that are correlated, with the component indicated by the indices a, b and c. (As commented above, we only consider matter density fields in this chapter, $a = b = c = 1$, but keep the indices in the diagrams for generality.) The external wavenumbers for each field are denoted $\mathbf{k}_A$, $\mathbf{k}_B$ and $\mathbf{k}_C$, respectively. We choose their direction as going *out* from diagrams throughout the discussion. Recall that due to statistical homogeneity and isotropy, they sum to zero. Furthermore, the kernels conserve momentum, so for each kernel there is an associated Dirac delta function ensuring that the incoming momentum equals the outgoing one.

As for the power spectrum, the different diagrams contributing to each order in perturbation theory is named after the order of the kernels that appear in them; at tree-level only the $B^{(211)}$-diagram contributes. There are however two additional equivalent diagrams corresponding to permutations of the three fields, i.e. cyclic permutations of $\{\mathbf{k}_A, \mathbf{k}_B, \mathbf{k}_C\}$ (and $\{a, b, c\}$).

In total, the mathematical expression for the tree-level bispectrum is therefore

$$\begin{aligned} B_{\rm tree}(k_A, k_B, k_C) &= 2F^{(2)}(-\mathbf{k}_B, -\mathbf{k}_C)F^{(1)}(\mathbf{k}_B)F^{(1)}(\mathbf{k}_C)P_0(k_B)P_0(k_C) + 2 \text{ perm.} \\ &= 2F^{(2)}(-\mathbf{k}_B, -\mathbf{k}_C)P_0(k_B)P_0(k_C) + 2 \text{ perm.}\,, \end{aligned} \tag{5.1}$$

where we used in the second line $F^{(1)} = 1$ in EdS[2]. The factor 2 is the symmetry factor of the diagram, arising from the sum over parings in the Wick theorem (see Section 3.5).

5.1 One-loop correction

Before we describe the two-loop correction and its renormalization in the EFT, we review the one-loop term and the counterterms correcting its UV-sensitivity. The review serves

[2]The linear kernels are also constant, $F^{(1)} = 1$, when the EdS-approximation is relaxed, because the growing mode is not affected by changes of $\Omega_{\rm m}/f^2$, see Eq. (3.39). As we saw in Chapter 4, this is not the case in general however.

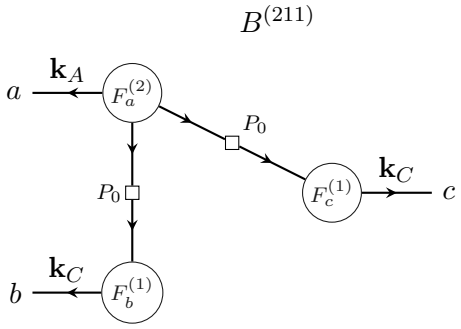

Figure 5.1: The tree-level bispectrum: $B^{(211)}$, containing a second-order and two first-order kernels. On outgoing lines, we indicate the component of the fields a, b and c as well as the external momenta $\mathbf{k}_A$, $\mathbf{k}_B$ and $\mathbf{k}_C$. The square boxes indicate initial, linear power spectra. The corresponding mathematical expression is given in Eq. (5.1), adopting the convention that all external momenta are outgoing.

as a useful way to introduce the method and notation before we tackle the two-loop in Section 5.3. Similar discussions can be found in Refs. [213, 250, 296, 297].

The one-loop correction to the bispectrum is given by

$$B_{1L} = B_{\rm s}^{(411)} + B_{\rm s}^{(321)} + B^{(222)}\,, \tag{5.2}$$

where the s subscript indicates that the term should be symmetrized: $B_{\rm s}^{(411)}$ contains three cyclic permutations while $B_{\rm s}^{(321)}$ contains (all) six permutations of $\{k_A, k_B, k_C\}$. The latter also consists of two distinct topological diagrams, which we label $B^{(321-I)}$ and $B^{(321-II)}$. The diagrammatic representations of each term is shown in Fig. 5.2 (the counterterm diagrams $B^{(\tilde{2}11)}$ and $B^{(2\tilde{1}1)}$ are also displayed, which will be discussed shortly). The corresponding mathematical expressions read [250, 296][3]

$$B^{(411)}(k_A,k_B,k_C) = 12P_0(k_B)P_0(k_C)F^{(1)}(\mathbf{k}_B)F^{(1)}(\mathbf{k}_C)\int_{\mathbf{q}} F^{(4)}(-\mathbf{k}_B,-\mathbf{k}_C,\mathbf{q},-\mathbf{q})P_0(q)\,, \tag{5.3a}$$

$$B^{(321-I)}(k_A,k_B,k_C) = 6P_0(k_C)F^{(1)}(\mathbf{k}_C)\int_{\mathbf{q}} F^{(3)}(-\mathbf{k}_C,-\mathbf{k}_B+\mathbf{q},-\mathbf{q})F^{(2)}(\mathbf{k}_B-\mathbf{q},\mathbf{q}) \times P_0(q)P_0(|\mathbf{k}_B-\mathbf{q}|)\,, \tag{5.3b}$$

$$B^{(321-II)}(k_A,k_B,k_C) = 6P_0(k_A)P_0(k_C)F^{(1)}(\mathbf{k}_C)\int_{\mathbf{q}} F^{(3)}(\mathbf{k}_A,\mathbf{q},-\mathbf{q})F^{(2)}(-\mathbf{k}_A,-\mathbf{k}_C)P_0(q)\,, \tag{5.3c}$$

$$B^{(222)}(k_A,k_B,k_C) = 8\int_{\mathbf{q}} F^{(2)}(\mathbf{k}_A+\mathbf{q},-\mathbf{q})F^{(2)}(\mathbf{q},\mathbf{k}_B-\mathbf{q})F^{(2)}(-\mathbf{k}_B+\mathbf{q},-\mathbf{k}_A-\mathbf{q})$$

[3] Note that the explicit formulas may look different depending on sign conventions and labeling of the different diagram contributions. For the diagram with a loop running around all three "blobs", there are more than one way of evaluating the Dirac delta functions at each blob, yielding slightly different, but equivalent expressions.

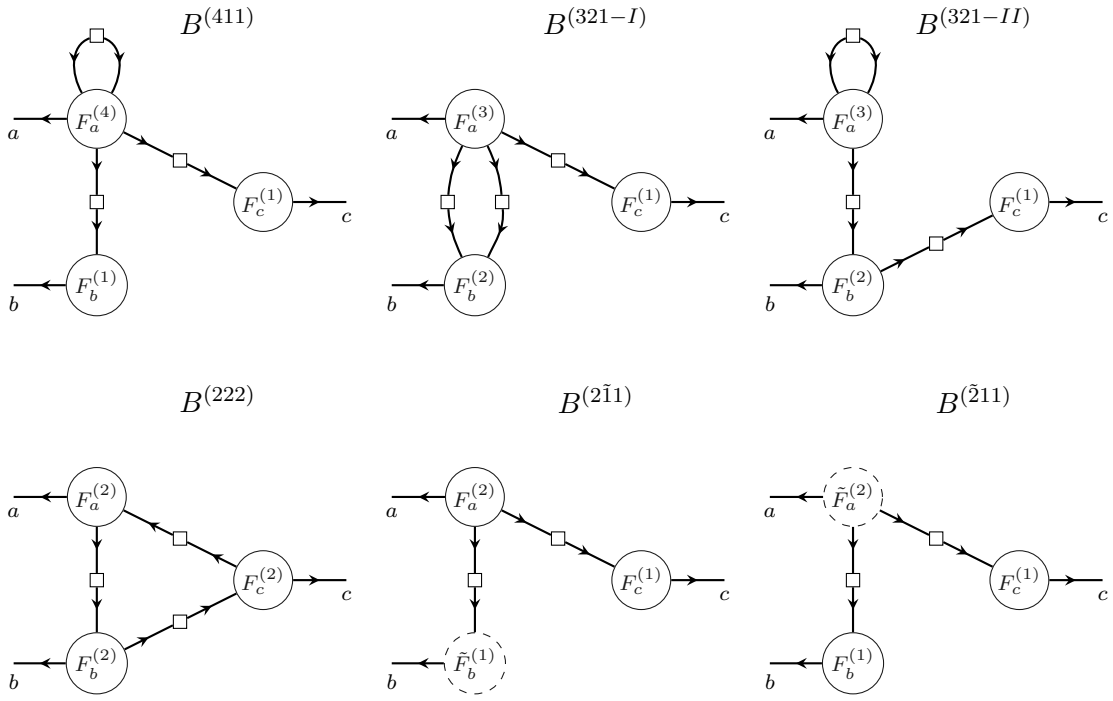

Figure 5.2: Diagrams contributing to the one-loop bispectrum: $B^{(411)}$, $B^{(321-I)}$, $B^{(321-II)}$, $B^{(222)}$, as well as the counterterm diagrams $B^{(\tilde{2}11)}$ and $B^{(2\tilde{1}1)}$. See Eqs. (5.3) and (5.14). We indicate counterterm kernels $\tilde{F}^{(n)}$ by dashed circles.

$$\times P_0(q)P_0(|\mathbf{k}_A+\mathbf{q}|)P_0(|-\mathbf{k}_B+\mathbf{q}|)\,, \tag{5.3d}$$

where we included the trivial $F^{(1)}$ kernels for completeness.

Hard limit

The perturbative expansion is no longer valid when the loop momenta in the integrals above are large, of the order of the non-linear scale. In the EFT, this hard region is corrected for by EFT operators. We will now derive the contribution of the hard limit to the one-loop correction at leading power in gradients ($k^2/k_{\rm NL}^2$), and show that its shape corresponds precisely to that of the EFT operators.

The hard region corresponds to $q \gg k_A, k_B, k_C$. It is instructive to estimate the size of the contributions from different diagrams in this limit, before we derive the explicit expressions. For this purpose, we consider $k_A \sim k_B \sim k_C \sim k$, and $k \ll q$. For all three kernels appearing in each diagram, the sum of arguments are therefore k (absolute value), and any kernel containing the hard loop momentum q thus scales as k^2/q^2 due to momentum conservation (see Section 3.3). Hence, in the hard limit, the different diagrams scales as

$$B^{(411)} \sim k^2 P_0(k_B)P_0(k_C)\int_{\mathbf{q}} P_0(q)/q^2\,, \qquad B^{(321-I)} \sim k^4 P_0(k_C)\int_{\mathbf{q}} [P_0(q)]^2/q^4\,,$$

$$B^{(321-II)} \sim k^2 P_0(k_B) P_0(k_C) \int_{\mathbf{q}} P_0(q)/q^2\,, \qquad B^{(222)} \sim k^6 \int_{\mathbf{q}} [P_0(q)]^3/q^6\,. \tag{5.4}$$

The $B^{(411)}$ and $B^{(321-II)}$ diagrams produce the leading contribution to the hard limit, proportional to k^2/q^2, corresponding to propagator corrections. The $B^{(222)}$ term is proportional to k^6 and corresponds to a pure stochastic contribution, i.e. arising entirely from short wavelength modes that combine into long wavelength modes. Finally, the $B^{(321-I)}$ diagram corresponds to a cross between a propagator correction and a stochastic contribution, suppressed by k^4/q^4. Working at leading power in gradients, we therefore neglect the contributions to the hard limit from the latter two diagrams.

To derive the explicit shape of the hard region, it is useful to define the *integrand* b_{1L} of the loop correction:

$$B_{1L}(k_A, k_B, k_C)) = \int^{\Lambda} \mathrm{d}q\, q^2 P_0(q) \int \mathrm{d}\Omega_q\, \mathsf{b}_{1L}(\mathbf{k}_A, \mathbf{k}_B, \mathbf{k}_C, \mathbf{q})\,. \tag{5.5}$$

In the hard limit, $q \gg k_A, k_B, k_C$, we identified $B^{(411)}$ and $B^{(321-II)}$ as the leading contributions, with $\mathsf{b}_{1L} \propto 1/q^2$. Therefore, the one-loop correction can be factorized for $q \to \infty$:

$$B^h_{1L}(k_A, k_B, k_C)) = 3 \int \frac{\mathrm{d}\Omega_q}{4\pi} \left(\lim_{q\to\infty} q^2 \mathsf{b}_{1L}(\mathbf{k}_A, \mathbf{k}_B, \mathbf{k}_C, \mathbf{q}) \right) \sigma_{\mathrm{d}}^2 \equiv b^h_{1L}(k_A, k_B, k_C)\, \sigma_{\mathrm{d}}^2\,, \tag{5.6}$$

defining the hard limit b^h_{1L} in the last equality, which contain the dependence on external wavenumbers. So far the discussion was analogous to our examination of the UV-limit of the one-loop power spectrum in the presence of massive neutrinos in Section 4.4. In that case however, we did not have analytic expressions for the kernels, and had to evaluate the limit numerically. Here, we consider EdS-SPT kernels, and can therefore obtain the analytic shape dependence. In particular, using the expressions for the kernels appearing in Eqs. (5.3a) and (5.3c), we obtain

$$b^h_{1L}(k_A, k_B, k_C) = 3 \left[12 f^{(4)}(\mathbf{k}_B, \mathbf{k}_C) - 6 \frac{61}{1890} f^{(3)}(\mathbf{k}_B, \mathbf{k}_C) \right] P_0(k_B) P_0(k_C) + 2 \text{ perm.} \tag{5.7}$$

The first term arises from the $B^{(411)}$ diagram, and therefore the hard limit of the $F^{(4)}$ kernel,

$$F^{(4)}(\mathbf{k}, \mathbf{p}, \mathbf{q}, -\mathbf{q}) \xrightarrow[q\gg k,p]{} \frac{1}{q^2} f^{(4)}(\mathbf{k}, \mathbf{p}) + \mathcal{O}\left((\max(k,p)/q)^4 \right)\,, \tag{5.8}$$

with

$$f^{(4)}(\mathbf{k}, \mathbf{p}) = \frac{-1}{4074840} \Bigg[49636 \mu^3 kp + 58812 (k^2 + p^2) + 114624 \mu^2 (k^2 + p^2) + \mu kp \left(32879 \left(\frac{k^2}{p^2} + \frac{p^2}{k^2} \right) + 231478 \right) \Bigg]\,, \tag{5.9}$$

where $\mu = \mathbf{k} \cdot \mathbf{p}/kp$. The second term in Eq. (5.7) comes from the $B^{(321-II)}$ diagram, with the hard limit of the $F^{(3)}$ kernel capturing the daisy loop as well as the other $F^{(2)}$ kernel.

We saw already the hard limit of the $F^{(3)}$ kernel integrated over angles in Eqs. (3.77b) and (4.46), nevertheless we repeat it here for convenience:[4]

$$\int \frac{\mathrm{d}\Omega_q}{4\pi} F^{(3)}(\mathbf{k},\mathbf{q},-\mathbf{q}) \xrightarrow[q\gg k]{} -\frac{1}{3\times 3}\frac{61}{210}\frac{k^2}{q^2} + \mathcal{O}\left((k/q)^4\right) . \tag{5.10}$$

It follows that $f^{(3)}(\mathbf{k},\mathbf{p}) = (k^2+p^2)F^{(2)}(\mathbf{k},\mathbf{p})$, where we included the permutation $\mathbf{k}\leftrightarrow\mathbf{p}$ corresponding to $\mathbf{k}_B\leftrightarrow\mathbf{k}_C$ in Eq. (5.7). Combined with the three permutations included expressly in that equation, we covered all 6 permutations of the $B^{(321-II)}$ diagram.

Only a handful of basis functions appear in the $f^{(3)}$ and $f^{(4)}$ shapes. In particular, we can define

$$\begin{aligned} b_1(\mathbf{k},\mathbf{p}) &= k^2+p^2\,, & b_2(\mathbf{k},\mathbf{p}) &= \mathbf{k}\cdot\mathbf{p}\,, & b_3(\mathbf{k},\mathbf{p}) &= \mathbf{k}\cdot\mathbf{p}\left(\frac{k^2}{p^2}+\frac{p^2}{k^2}\right)\,, \\ b_4(\mathbf{k},\mathbf{p}) &= \mu^2(k^2+p^2)\,, & b_5(\mathbf{k},\mathbf{p}) &= \mu^3 kp\,, \end{aligned} \tag{5.11}$$

from which we can write $f^{(3)}$ and $f^{(4)}$ as linear combinations

$$f^{(i)}(\mathbf{k},\mathbf{p}) = \sum_{j=1}^{5} f_j^{(i)} b_j(\mathbf{k},\mathbf{p})\,. \tag{5.12}$$

The coefficients $f_j^{(i)}$ are given in Tab. A.1. Since the perturbation kernels vanish when the sum of all arguments is zero, we have $f^{(i)}(\mathbf{k},-\mathbf{k})=0$, which yields a condition on the coefficients,

$$2f_1^{(i)} - f_2^{(i)} - 2f_3^{(i)} + 2f_4^{(i)} - f_5^{(i)} = 0\,. \tag{5.13}$$

Hence, one coefficient can be written as a combination of the others, and in the end only four parameters specify the shape dependence of the hard limit of the one-loop correction to the bispectrum.

Counterterms

Next, we compute the EFT corrections to the one-loop bispectrum and show that their shape corresponds exactly to the shape functions defined above, with four independent EFT parameters. Solving the equations of motion in the presence of the first and second order effective stress terms sources (Eqs. (3.98) and (3.106)), yields additional contributions (counterterms):

$$B_{1L}^{\mathrm{ctr}}(k_A,k_B,k_C) = \left(B^{(\tilde{2}11)}(k_A,k_B,k_C) + 2 \text{ perm.}\right) + \left(B^{(2\tilde{1}1)}(k_A,k_B,k_C) + 5 \text{ perm.}\right)\,, \tag{5.14}$$

with

$$B^{(\tilde{2}11)}(k_A,k_B,k_C) = 2\tilde{F}^{(2)}(\mathbf{k}_B,\mathbf{k}_C)P_0(k_B)P_0(k_C)\,, \tag{5.15a}$$

$$B^{(2\tilde{1}1)}(k_A,k_B,k_C) = 2F^{(2)}(\mathbf{k}_B,\mathbf{k}_C)\tilde{F}^{(1)}(\mathbf{k}_B)P_0(k_B)P_0(k_C)\,. \tag{5.15b}$$

[4] In the limit Eq. (3.77b), there is in addition an integration over the absolute value of the momentum q, yielding a factor $3\sigma_{\mathrm{d}}^2$, and the $P^{(31)}$ symmetry factor 3 is included.

The EFT kernels $\tilde{F}^{(1),(2)}$ were given in Eqs. (3.99) and (3.111). Let us first consider the $B^{\tilde{2}11}$ term, which renormalizes $B^{(411)}$. Using also the definitions of the E and Γ shape functions in Eqs. (3.109) and (3.110), respectively, one can readily show that

$$\tilde{F}^{(2)}(\mathbf{k},\mathbf{p}) = \sum_{i=1}^{3} \epsilon_i E_i(\mathbf{k},\mathbf{p}) + \gamma_1 \Gamma(\mathbf{k},\mathbf{p}) = \sum_{j=1}^{5} c_j b_j(\mathbf{k},\mathbf{p}) \tag{5.16}$$

with

$$\begin{aligned} &c_1 = \epsilon_1 - \epsilon_2/3 - \epsilon_3/6 + 72\gamma_1/77\,, \quad && c_2 = 2\epsilon_1 - 2\epsilon_2/3 + 2\epsilon_3/3 + 179\gamma_1/77\,, \quad && c_3 = \gamma_1/2\,, \\ &c_4 = \epsilon_2 + \epsilon_3/2 + 68\gamma_1/77\,, && c_5 = 2\epsilon_2 + 24\gamma_1/77\,. \end{aligned} \tag{5.17}$$

The first order EFT kernel is simply $\tilde{F}^{(1)} = -c_{\rm s}^2 k^2$, where $c_{\rm s}$ is the effective sound speed of the fluid. Thus $B^{(2\tilde{1}1)}$ is proportional to $k_B^2 F^{(2)}(\mathbf{k}_B, \mathbf{k}_C)$. Adding the permutation $\mathbf{k}_B \leftrightarrow \mathbf{k}_C$, we recover the form of $f^{(3)}$, which we found could be written in terms of the basis functions b_j. Therefore, in total, we can write the one-loop counterterm in terms of the basis b_j or equivalently in terms of E_i and Γ,

$$B_{1L}^{\rm ctr}(k_A,k_B,k_C) = -2\left[\sum_{i=1}^{3} \hat{\epsilon}_i E_i(\mathbf{k}_B,\mathbf{k}_C) + \hat{\gamma}_1 \Gamma(\mathbf{k}_B,\mathbf{k}_C)\right] P_0(k_B)P_0(k_C) + 2 \text{ perm.}\,, \tag{5.18}$$

with four EFT parameters $\{\hat{\epsilon}_1, \hat{\epsilon}_2, \hat{\epsilon}_3, \hat{\gamma}_1\}$, related to ϵ_i, γ_1 and $c_{\rm s}^2$ via

$$\hat{\epsilon}_1 = \epsilon_1 - \frac{97}{231} c_{\rm s}\,, \qquad \hat{\epsilon}_2 = \epsilon_2 - \frac{12}{77} c_{\rm s}\,, \qquad \hat{\epsilon}_3 = \epsilon_3 - \frac{68}{77} c_{\rm s}\,, \qquad \hat{\gamma}_1 = \gamma_1 + c_{\rm s}\,. \tag{5.19}$$

Thus, the shape dependence of the EFT correction corresponds exactly to that of the hard region of the one-loop bispectrum, with four independent parameters. This serves as a consistency check: the operators in the EFT precisely correct the spurious UV-dependence of SPT.

We distinguish between two approaches for fitting the EFT parameters to N-body simulations: the *symmetry*-based approach and the *UV-inspired* approach. The same distinction was also made in Ref. [213]. In the symmetry based approach, all four EFT parameters at one-loop are fitted independently (in addition to one extra parameter at two-loop, as we will see below). The parameters could be taken to be $\{\hat{\epsilon}_1, \hat{\epsilon}_2, \hat{\epsilon}_3, \hat{\gamma}_1\}$, however we adopt here the choice of Paper II [45], where instead $\{\epsilon_1, \epsilon_2, \epsilon_3, \gamma_1\}$ were used as free parameters after fixing $c_{\rm s}^2$ from calibrations of the one-loop power spectrum to the N-body simulations utilized in the work.

The other, UV-inspired approach gives a relation between the EFT parameters motivated by the linear combination in which the corresponding shape functions enter in the hard limit of SPT. Hence, only the overall amplitude of the EFT correction is fitted. In particular, we assume that $B^{(\tilde{2}11)}$ can be parametrized by a single EFT coefficient γ_1, multiplied by the shape dependence of the hard limit of $B^{(411)}$, i.e. $\tilde{F}^{(2)}(\mathbf{k},\mathbf{p}) \propto \gamma_1 f^{(4)}(\mathbf{k},\mathbf{p})$. This assumption corresponds to fixing the ϵ_i parameters as

$$\epsilon_1 = \frac{3466}{14091}\gamma_1\,, \qquad \epsilon_2 = \frac{7285}{32879}\gamma_1\,, \qquad \epsilon_3 = \frac{41982}{32879}\gamma_1\,. \tag{5.20}$$

After fixing c_s^2 from fitting the power spectrum to simulations, the bispectrum at NLO is therefore described in this approach by one EFT parameter, γ_1.

This approach can be made even more restrictive by assuming also a relation between c_s^2 and γ_1. The hard region of the one-loop correction is proportional to the displacement dispersion σ_d^2, and one can make an ansatz that the EFT corrects the UV in a universal manner by adjusting its value, i.e. $\sigma_d^2 \mapsto \sigma_d^2 + \Delta\sigma_d^2$. By considering the hard limit of the one-loop power spectrum (3.77b) and the corresponding counterterm $P_{1L}^{\rm ctr} \propto c_s^2 k^2 P_0(k)$, we can identify the shift in σ_d^2 as $\Delta\sigma_d^2 = 61/210 c_s^2$. Moreover, inserting $\tilde{F}^{(2)}(\mathbf{k},\mathbf{p}) \propto \gamma_1 f^{(4)}(\mathbf{k},\mathbf{p})$ into Eq. (5.7) and subsequently Eq. (5.6), the normalization of γ_1 can be chosen such that $\gamma_1 = c_s^2$ (this choice was in fact adopted in Eq. (5.20) above).

In summary, the calibration cases we will consider at one-loop are

$$\begin{aligned}
&\{\epsilon_1, \epsilon_2, \epsilon_3, \gamma_1\} && \text{one-loop, 4-parameter symmetry based}\,,\\
&\{\gamma_1\} && \text{one-loop, 1-parameter UV-inspired with } \epsilon_i/\gamma_1 \text{ fixed}\,,\\
&\emptyset && \text{one-loop, 0-parameter UV-inspired with } \epsilon_i/\gamma_1 \text{ fixed and } \gamma_1 = c_s^2\,. \qquad (5.21)
\end{aligned}$$

5.2 EdS-approximation

Before we embark on the discussion of the two-loop correction to the bispectrum, we make a detour and examine the EdS-approximation at one-loop. As discussed in Section 3.3, this approximation is valid deep in the matter regime, but yields percent deviations at late times when Ω_m/f^2 differs substantially from one.

In Paper II [45], the one-loop bispectrum was computed using exact, time-dependent kernels, where the Ω_m/f^2 ratio that enters the equations were not approximated by 1 but taken from the Boltzmann solver `CLASS`. To perform this calculation, the generalized framework capturing scale- and time-dependence of Section 3.4 was utilized, for a single dark matter fluid. The initial time was taken to be $\eta_{\rm ini} = -2.12$ corresponding to $z \approx 10$ (i.e. long before Ω_m/f^2 differs from 1 in ΛCDM, see Fig. 3.3). To evaluate loop integrals, numerical integration with `CUBA` was used, with analogous methods to accelerate the evaluation of the loop integrands as described in Section 3.5.

Fig. 5.3 displays the relative difference between contributions to the bispectrum computed with EdS-SPT kernels and exact, time-dependent ones. We show the results for three distinct shapes: equilateral ($k_A = k_B = k_C = k$), squeezed ($k_A = k_B = k$, $k_C = 0.02h$ Mpc^{-1}) and isosceles ($k_A = k_B = 2k_C = k$). For all shapes, there is an approximate, k-independent 0.5 % relative difference for the tree-level bispectrum. The $F^{(2)}$ kernel that enters the tree-level bispectrum is not integrated over, therefore this mistake can relatively easily be corrected for by promoting $F^{(2)}$ to the exact kernel. Moreover, in an analysis of galaxy clustering data, this shift would be degenerate with the primordial amplitude of fluctuations as well as linear bias. The departure from EdS is more complicated to capture exactly at one-loop; its effect relative to the tree-level bispectrum exceeds 1 % at $k \simeq 0.1h$ Mpc^{-1} for the equilateral shape and $k \simeq 0.15h$ Mpc^{-1} for the squeezed and isosceles shapes as is apparent from Fig. 5.3. To assess to which extent this discrepancy can be absorbed by the counterterms in the EFT, the green and blue dotted lines show the one-loop bispectrum counterterm fitted to the exact–EdS difference, using the symmetry based (4 parameter)

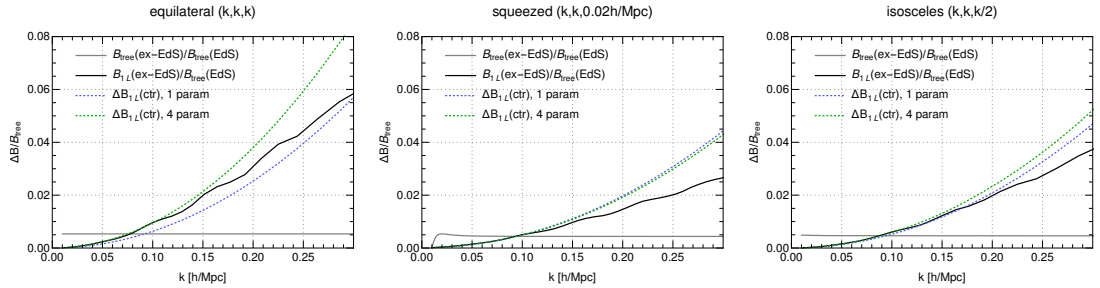

Figure 5.3: Relative difference between the tree (gray) and one-loop (black) bispectrum computed with exact, time-dependent kernels and EdS-SPT kernels for three shapes: equilateral, squeezed and isosceles. The difference is normalized to the tree-level bispectrum in EdS. The dotted lines show the one-loop counterterm fitted to the difference, using the symmetry based ansatz (green) as well as the UV-inspired approach (blue). Reprinted from Paper II [45].

and UV-inspired (1 parameter) approaches, respectively. In the symmetry based case, the difference can be matched to good agreement up to $k \simeq 0.15h$ Mpc^{-1}, independent of shape, while the UV-inspired approach can capture the difference relatively well for the squeezed and isosceles shapes, but not for the equilateral. We note that in latter approach, the measured shift in γ_1 due to the departure from EdS is approximately 0.2 Mpc$^2/h^2$, consistent with the findings of Ref. [213] as well as our conclusion in Section 4.5.

5.3 Two-loop correction

In this section we examine the two-loop correction and how we can cure its UV-sensitivity in the EFT. It is given by

$$B_{2L} = B_{\rm s}^{(611)} + B_{\rm s}^{(521)} + B_{\rm s}^{(422)} + B_{\rm s}^{(431)} + B_{\rm s}^{(332)}\,, \tag{5.22}$$

where each term contains multiple topologically distict contributions which we label with capital roman indices as well as permutations of external wavenumbers:

$$\begin{aligned}
B_{\rm s}^{(611)} &= B^{(611)} + 2 \text{ perm.}\,,\\
B_{\rm s}^{(521)} &= \left(B^{(521-I)} + B^{(521-II)}\right) + 5 \text{ perm.}\,,\\
B_{\rm s}^{(431)} &= \left(B^{(431-I)} + B^{(431-II)} + B^{(431-III)}\right) + 5 \text{ perm.}\,,\\
B_{\rm s}^{(332)} &= \left[\left(B^{(332-I)} + B^{(332-II)}\right) + 2 \text{ perm.}\right] + \left[B^{(332-III)} + 5 \text{ perm.}\right]\,,\\
B_{\rm s}^{(422)} &= \left(B^{(422-I)} + B^{(422-II)}\right) + 2 \text{ perm.}
\end{aligned} \tag{5.23}$$

Hence, there are in total eleven diagrams contributing. We show their diagrammatic representation in Fig. A.1 and the corresponding mathematical expressions in Eq. A.1. Each diagram consists of an integration over both loop momenta $\mathbf{q}_1$ and $\mathbf{q}_2$, with an integrand containing three kernels (whose order sum to 8, e.g. $F^{(6)}F^{(1)}F^{(1)}$), two linear power spectra

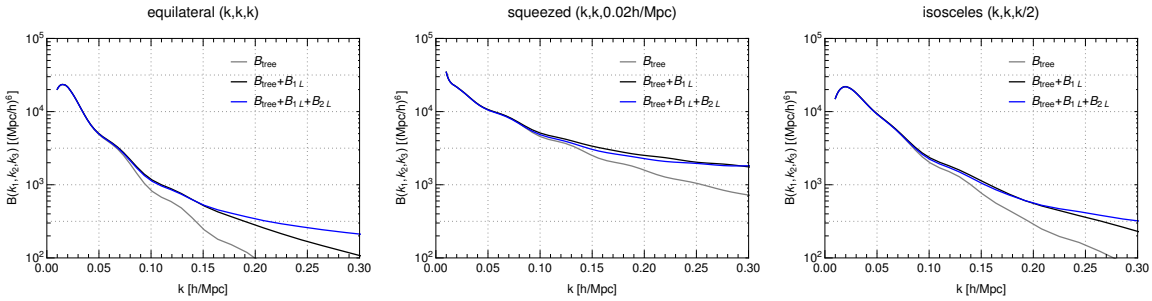

Figure 5.4: The linear (gray), NLO (black) and NNLO (blue) bispectrum in SPT as a function of wavenumber. We show three shapes: equilateral, squeezed and isosceles. Figure taken from Paper II [45].

evaluated at q_1 and q_2 as well as two additional power spectra evaluated at combinations of external and loop momenta depending on the diagram.

The linear, NLO and NNLO bispectrum in SPT, i.e. without EFT corrections, are displayed in Fig. 5.4 for the three shapes. The loop corrections are considerably sensitive to the UV even on large scales, therefore there are sizable deviations from the linear prediction in the log–log plot even at $k \simeq 0.1h$ Mpc^{-1}. These spurious contributions will be corrected for by the EFT.

Let us examine the UV-sensitivity of the two-loop correction. We saw in Section 3.6 and Section 4.4 that it was useful to distinguish two regions comprising the UV limit of the two-loop power spectrum. We make the same distinction here and consider the double-hard limit, $q_1, q_2 \to \infty$, and single-hard limit, $q_1 \sim k$, $q_2 \to \infty$, separately.

Double-hard limit

In a similar manner as for the one-loop correction, we start the discussion by estimating the parametric scaling of the different contributions in the double-hard limit. Consider $k_A \sim k_B \sim k_C \sim k$ and $q_1 \sim q_2 \sim q$ with $q \gg k$. Using the property $F^{(n)} \propto k^2/q^2$ in this limit and the explicit expressions in Eq. (A.1), we have schematically

$$
\begin{aligned}
B^{(611),hh} &\sim k^2 P_0(k_B) P_0(k_C) \int_{\mathbf{q}_1,\mathbf{q}_2} P_0(q_1) P_0(q_2)/q^2 \,, \\
B^{(521-I),hh} &\sim k^4 P_0(k_B) \int_{\mathbf{q}_1,\mathbf{q}_2} P_0(q_1) [P_0(q_2)]^2/q^4 \,, \\
B^{(521-II),hh} &\sim k^2 P_0(k_B) P_0(k_C) \int_{\mathbf{q}_1,\mathbf{q}_2} P_0(q_1) P_0(q_2)/q^2 \,, \\
B^{(431-I),hh} &\sim k^4 P_0(k_B) \int_{\mathbf{q}_1,\mathbf{q}_2} P_0(q_1) [P_0(q_2)]^2/q^4 \,, \\
B^{(431-II),hh} &\sim k^4 P_0(k_B) P_0(k_C) \int_{\mathbf{q}_1} P_0(q_1)/q_1^2 \int_{\mathbf{q}_2} P_0(q_2)/q_2^2 \,, \\
B^{(431-III),hh} &\sim k^4 P_0(k_B) \int_{\mathbf{q}_1,\mathbf{q}_2} P_0(q_1) P_0(q_2) P_0(|\mathbf{q}_1+\mathbf{q}_2|)/q^4 \,,
\end{aligned}
$$

$$
\begin{aligned}
B^{(332-I),hh} &\sim k^6 \int_{\mathbf{q}_1,\mathbf{q}_2} [P_0(q_1)]^2 P_0(q_2) P_0(|\mathbf{q}_1+\mathbf{q}_2|)/q^6\,,\\
B^{(332-II),hh} &\sim k^4 P_0(k_B) P_0(k_C) \int_{\mathbf{q}_1} P_0(q_1)/q_1^2 \int_{\mathbf{q}_2} P_0(q_2)/q_2^2\,,\\
B^{(332-III),hh} &\sim k^6 P_0(k_B) \int_{\mathbf{q}_1} P_0(q_1)/q_1^2 \int_{\mathbf{q}_2} [P_0(q_2)]^2/q_2^4\,,\\
B^{(422-I),hh} &\sim k^6 \int_{\mathbf{q}_1,\mathbf{q}_2} P_0(q_1)[P_0(q_2)]^3/q^6\,,\\
B^{(422-II),hh} &\sim k^6 \int_{\mathbf{q}_1,\mathbf{q}_2} [P_0(q_1)]^2[P_0(q_2)]^2/q^6\,.
\end{aligned}
\tag{5.24}
$$

The leading UV-sensitivity comes from the diagrams $B^{(611)}$ and $B^{(521-II)}$, corresponding to propagator corrections and containing each a factor k^2/q^2. The three diagrams $B^{(332-I)}$, $B^{(422-I)}$ and $B^{(422-II)}$ are pure stochastic contributions in the double-hard limit, suppressed by k^6/q^6. $B^{(322-II)}$ is also proportional to k^6, being a combination of $P^{(31)}(k_B)$ and a stochastic connecting loop, see Fig. A.1. Moreover, the $B^{(431-I)}$ and $B^{(322-II)}$ diagrams are "propagator squared" terms with power k^4/q^4. We discuss their contributions at the end of this section. The remaining diagrams are crosses of stochastic contributions and propagator corrections, proportional to k^4/q^4. These are $B^{(521-I)}$, $B^{(431-I)}$ and $B^{(431-III)}$. Lastly, we note that the leading $B^{(611)}$ and $B^{(521-II)}$ limits are equivalent to that of $P^{(51)}$ (cf. Eq. (3.112)), and in fact $B^{(521-II)}$ is exactly proportional to $P^{(51)}(k_A)$.

In accordance with the gradient power counting so far, we neglect all UV-contributions but the leading $B^{(611)}$ and $B^{(521-II)}$ ones. To obtain the precise shape dependence as well as the dependence on the loop momenta in the double-hard limit, we need the hard limits of the $F^{(5)}$ and $F^{(6)}$ kernels (with the appropriate arguments). The first limit is known from analyses of the power spectrum [217, 252, 254] and the second limit was derived for the first time in Paper II [45]: the results integrated over angles are

$$
\int \frac{\mathrm{d}\Omega_{q_1}}{4\pi}\frac{\mathrm{d}\Omega_{q_2}}{4\pi} F^{(5)}(\mathbf{k},\mathbf{q}_1,-\mathbf{q}_1,\mathbf{q}_2,-\mathbf{q}_2) \xrightarrow[k\ll q_1,q_2]{} -\frac{11191}{6449625}\frac{k^2}{q_1 q_2} S_1\left(\frac{q_1}{q_2}\right)\,, \tag{5.25a}
$$

$$
\begin{aligned}
&\int \frac{\mathrm{d}\Omega_{q_1}}{4\pi}\frac{\mathrm{d}\Omega_{q_2}}{4\pi} F^{(6)}(\mathbf{k}_1,\mathbf{k}_2,\mathbf{q}_1,-\mathbf{q}_1,\mathbf{q}_2,-\mathbf{q}_2)\\
&\qquad\xrightarrow[k\ll q_1,q_2]{} \frac{1}{q_1 q_2}\left[f^{(6,1)}(\mathbf{k}_1,\mathbf{k}_2) S_1\left(\frac{q_1}{q_2}\right) + f^{(6,2)}(\mathbf{k}_1,\mathbf{k}_2) S_2\left(\frac{q_1}{q_2}\right)\right]\,.
\end{aligned}
\tag{5.25b}
$$

The function $S_1(r)$ was defined in Eq. (3.114), and the new S_2 function will be defined shortly. In Eq. (5.25b), the double-hard limit was factorized into shape functions $f^{(6,1)}$ and $f^{(6,2)}$ and the $S_{1,2}$ functions capturing the dependence on the hard loop momenta. The shape functions can be expressed in the b_j basis introduced in Eq. (5.11), or equivalently in terms of the EFT operator shapes E_i and Γ (defined in Eqs. (3.109) and (3.110)). We write down the corresponding coefficients in Tab. A.1. Crucially, neither of $f^{(6,1)}$ and $f^{(6,2)}$ are proportional to $f^{(4)}$, i.e. they comprise a different linear combination of the basis functions. This implies that the UV-inspired approach cannot naively be extended to two-loop, as we argue in detail below.

The second function describing the dependence on the hard loop momenta reads

$$S_2(r) = -\frac{1}{512r^6}\Bigg[4r(1+r^2)(105-340r^2+406r^4-340r^6+105r^8) + 30(r^2-1)^4(7+10r^2+7r^4)\ln\left(\frac{|1-r|}{1+r}\right)\Bigg], \tag{5.26}$$

with $r = q_1/q_2$. Given the limits of $F^{(5)}$ and $F^{(6)}$, we can write down the precise shape-dependence of the leading contributions to the double-hard limit,

$$B^{(611),hh}(k_A,k_B,k_C) = 90\left[f^{(6,1)}(\mathbf{k}_B,\mathbf{k}_C)s_1(\Lambda) + f^{(6,2)}(\mathbf{k}_B,\mathbf{k}_C)s_2(\Lambda)\right]P_0(k_B)P_0(k_C) + 2 \text{ perm.}\,, \tag{5.27a}$$

$$B^{(521-II),hh}(k_A,k_B,k_C) = 30\left[-\frac{11191}{6449625}f^{(3)}(\mathbf{k}_B,\mathbf{k}_C)s_1(\Lambda)\right]P_0(k_B)P_0(k_C) + 2 \text{ perm.}\,, \tag{5.27b}$$

where we included a factor 2 from the trivial permutation $\mathbf{k}_B \leftrightarrow \mathbf{k}_C$ in the second equation, such that the remaining permutations of the $B^{(521-II),hh}$ term are only the three cyclic ones (cf. Eq. (5.23)). The numbers $s_{1,2}(\Lambda)$ denote the integrals over the $S_{1,2}$ functions,

$$s_i(\Lambda) = (4\pi)^2\int^\Lambda \mathrm{d}q_1\, q_1 P_0(q_1)\int^\Lambda \mathrm{d}q_2\, q_2 P_0(q_2)\, S_i(q_1/q_2)\,, \tag{5.28}$$

capturing the cutoff-dependence of the double-hard limit. Evaluating them for the cosmology considered in this chapter with $\Lambda = 0.6h$ Mpc^{-1} yields $s_1 \simeq 52.51$ Mpc$^2/h^2$ and $s_2 \simeq 29.55$ Mpc$^2/h^2$ [45].

In total, the double-hard limit of the bispectrum can be factorized at leading power in gradients as

$$B^{hh}_{2L}(k_A,k_B,k_C)) = b^{hh}_{2L,1}(k_A,k_B,k_C)s_1(\Lambda) + b^{hh}_{2L,2}(k_A,k_B,k_C)s_2(\Lambda)\,, \tag{5.29}$$

in analogy to Eq. (5.6) for the one-loop bispectrum. The hard limits are given by

$$b^{hh}_{2L,1}(k_A,k_B,k_C) = \left[90f^{(6,1)}(\mathbf{k}_B,\mathbf{k}_C) - 30\frac{11191}{6449625}f^{(3)}(\mathbf{k}_B,\mathbf{k}_C)\right]P_0(k_B)P_0(k_C) + 2 \text{ perm.}\,, \tag{5.30a}$$

$$b^{hh}_{2L,2}(k_A,k_B,k_C) = \left[90f^{(6,2)}(\mathbf{k}_B,\mathbf{k}_C)\right]P_0(k_B)P_0(k_C) + 2 \text{ perm.} \tag{5.30b}$$

Hence, given that all three shape functions $f^{(3)}$, $f^{(6,1)}$ and $f^{(6,2)}$ are linear combinations of the basis shapes b_j, the two-loop double-hard limit can be renormalized by the EFT operators E_i and Γ that renormalized the one-loop.

This result is akin to the power spectrum, where the double-hard limit of the two-loop correction could be renormalized by the same k^2P_0 counterterm as the one-loop correction. However, in the bispectrum case, perhaps not too surprisingly, the linear combination of EFT operators needed to absorb the UV-dependence of the one-loop correction is not the

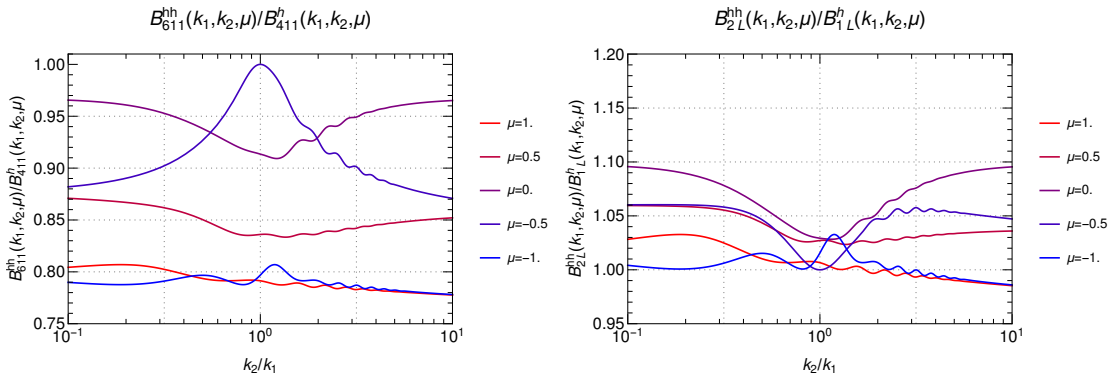

Figure 5.5: Double-hard limit of two-loop correction to the bispectrum divided by the hard-limit of the one-loop correction. *Left*: Ratio of the propagator corrections $B^{(611)}$ and $B^{(411)}$. *Right*: Ratio of the full two-loop and one-loop bispectra. One external wavenumber is fixed to $k_A = k_1 = 0.1h$ Mpc^{-1} and all graphs are normalized to the value in the equilateral configuration with $k_1/k_2 = 1$ and $\mu = 0.5$, where μ is the cosine of the angle between the external wavenumbers. Reprinted from Paper II [45].

same as for the two-loop correction. This is confirmed quantitatively by Fig. 5.5, displaying the ratio of the double-hard limit of the two-loop to the hard limit of the one-loop. Clearly, the shape-dependence of the two limits differ, corresponding to different combinations of the basis shape functions. Therefore, the UV-inspired ansatz introduced in Section 5.1, assuming that the UV-sensitivity can be captured by one overall parameter controlling the amplitude of the counterterm, cannot be naively extended to two loops. In the renormalization scheme we adopt however, it may be applied for the *one-loop part* of the EFT coefficients, with a prescription for the single-hard limit, as we discuss below. The symmetry based approach is on the other hand immediately suited perfectly to correct for both the hard region of the one-loop and simultaneously the double-hard region of the two-loop correction.

We will adopt a similar renormalization scheme for the double-hard limit as we used for the corresponding limit of the power spectrum in Section 4.4. In particular, we can split the e_i and γ_1 EFT parameters into one- and two-loop contributions. The two-loop contributions can be chosen to exactly cancel the double-hard region, while the one-loop part captures the actual effect of small scales on the bispectrum as well as correcting for the spurious hard region of the one-loop integral. In practice, following Ref. [252] and the discussion in Section 4.4, this choice amounts to subtracting the double-hard contribution from the two-loop correction,

$$B^{\rm sub}_{2L}(k_A,k_B,k_C;\Lambda) \equiv B_{2L}(k_A,k_B,k_C;\Lambda) - B^{hh}_{2L}(k_A,k_B,k_C;\Lambda)\,, \tag{5.31}$$

where B^{hh}_{2L} was given in Eq. (5.29).

Finally, we remark that the coefficients of $f^{(6,2)}$ when written in the linear combination of the b_j or the E_i and Γ basis functions are much smaller than the ones for $f^{(6,2)}$, such that in practice $b^{hh}_{2L,2}$ can be neglected to good approximation [45]. It will nevertheless be included here for completeness.

Single-hard limit

To obtain a cutoff-independent prediction for the bispectrum at two-loop, we also need to renormalize the single-hard limit. In principle, this could be done by writing down the effective stress term up to forth order in fields, and solve the equations of motion in its presence, yielding one-loop diagrams with insertions of EFT operators. Even in the EdS case, this is quite complex however, and we opt for correcting the single-hard region in an universal manner with one extra parameter, extending the approach described in Section 3.6. The fact that we find this ansatz to work well suggests that there is in fact a large degeneracy between the effects of the full set of EFT operators allowed by symmetries on the two-loop bispectrum. We will refer to this approach also as *symmetry based*, even though it does not include all EFT operators allowed by symmetries.

Extending the single-hard prescription that has been applied to the power spectrum to the bispectrum is relatively straightforward, and we describe it in detail next. The steps are almost completely analogous to the derivation of the single-hard counterterm in Section 4.4. Given the two-loop *integrand* b_{2L} implicitly defined as

$$B_{2L}(k,\eta) = \int^{\Lambda} \mathrm{d}q_1\, q_1^2 P_0(q_1) \int^{\Lambda} \mathrm{d}q_2\, q_2^2 P_0(q_2) \int \mathrm{d}\Omega_{q_1}\, \mathrm{d}\Omega_{q_2}\, \mathsf{b}_{2L}(\mathbf{k}_A, \mathbf{k}_B, \mathbf{k}_C, \mathbf{q}_1, \mathbf{q}_2; \eta)\,, \tag{5.32}$$

we can factorize the integral in the single-hard limit (assuming q_1 hard and q_2 of the size of the external momenta)

$$\begin{aligned} B_{2L}^{q_1\to\infty}(k_A, k_B, k_C) &= \left[\int^{\Lambda} \mathrm{d}q_2\, q_2^2 P_0(q_2) \int \frac{\mathrm{d}\Omega_{q_1}}{4\pi} \left(\lim_{q_1\to\infty} q_1^2 \mathsf{b}_{2L}(\mathbf{k}_A, \mathbf{k}_B, \mathbf{k}_C, \mathbf{q}_1, \mathbf{q}_2)\right)\right] \sigma_{\mathrm{d}}^2 \\ &= b_{2L}^h(k_A, k_B, k_C)\, \sigma_{\mathrm{d}}^2\,. \end{aligned} \tag{5.33}$$

This factorization was possible because in the single-hard limit, the leading contribution comes from diagrams with a hard daisy loop, containing a kernel $F^{(n)}(\dots, \mathbf{q}_1, -\mathbf{q}_1, \dots)$ and scaling as $1/q_1^2$ in this limit. Assuming that the single-hard region can be renormalized by a change of the displacement dispersion, i.e. $\sigma_{\mathrm{d}}^2(\Lambda) \mapsto \sigma_{\mathrm{d}}^2(\Lambda) + \mathcal{N}\gamma_2(\Lambda)$, we obtain a counterterm

$$2\, b_{2L}^h(k_A, k_B, k_C)\, \mathcal{N}\gamma_2\,, \tag{5.34}$$

where the factor 2 takes into account the equivalent contribution where q_2 is hard. We define the value of $\mathcal{N}$ below. While the expression (5.34) could immediately be added to the bispectrum, it covers a double-hard region ($q_2 \gg k$ in Eq. (5.33)), and since we adopt the renormalization choice where this limit is completely removed from the two-loop correction, we use the *subtracted* single-hard quantity

$$\bar{b}_{2L}^h = b_{2L}^h - b_{2L}^{hh}\,, \tag{5.35}$$

in the counterterm (5.34). Here, the double-hard limit is given by

$$b_{2L}^{hh}(k_A, k_B, k_C)) = b_{2L,1}^{hh}(k_A, k_B, k_C) s_1^h(\Lambda) + b_{2L,2}^{hh}(k_A, k_B, k_C) s_2^h(\Lambda)\,, \tag{5.36}$$

with $b_{2L,1,2}^h$ being the limits derived above in Eq. (5.30). The s_i^h functions are defined as

$$s_i(\Lambda) = 4\pi \lim_{q_1\to\infty} \int^{\Lambda} \mathrm{d}q_2\, \mathrm{d}\Omega_{q_1}\, \frac{q_2}{q_1} S_i(q_1/q_2) P_0(q_2)\,, \tag{5.37}$$

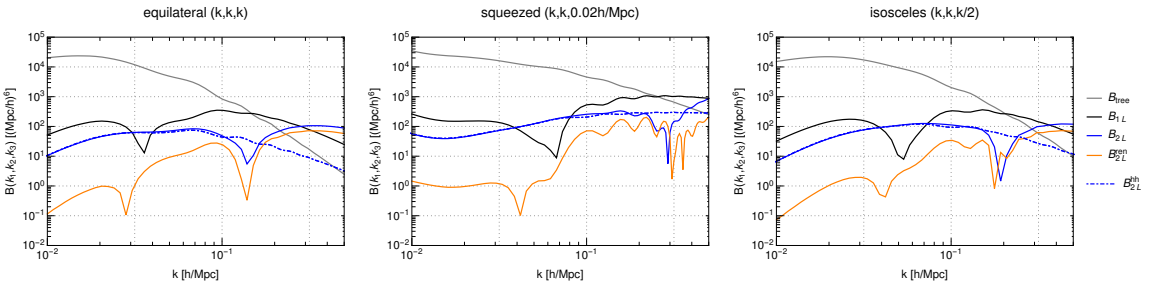

Figure 5.6: The two-loop correction before (blue) and after renormalization (orange). The linear (gray) and unrenormalized one-loop (black) contributions are shown for comparison. We also show the double-hard limit, which on large scales yields the dominant contribution to the two-loop correction. The EFT parameter is set to $\gamma_2 = 1\ \mathrm{Mpc}^2/h^2$ for simplicity. Figure taken from Paper II [45].

and can be evaluated using the expressions for $S_{1,2}$ in Eqs. (3.114) and (5.26):

$$s_1^h(\Lambda) = 4\pi \times \frac{120424}{78337} \int^\Lambda \mathrm{d}q_2\, q_2^2 P_0(q_2)\,, \tag{5.38a}$$

$$s_2^h(\Lambda) = 4\pi \lim_{q_1\to\infty} q_1^2 \int^\Lambda \mathrm{d}q_2\, \frac{64}{21}\frac{q_2^4}{q_1^4} P_0(q_2) = 0\,. \tag{5.38b}$$

In total, the additional counterterm we add at two-loop is

$$B_{2L}^{\mathrm{ctr}}(k_A,k_B,k_C;\Lambda) = 2\mathcal{N}\gamma_2(\Lambda)\,\bar{b}_{2L}^h(k_A,k_B,k_C)\,. \tag{5.39}$$

In practice, the quantities b_{2L} and its double-hard contribution was computed numerically in Paper II [45]: using the same algorithm that computes the two-loop integral, b_{2L} can be obtained by fixing the hard loop momentum to a large value $q_1 \gg \Lambda$. While in the case of massive neutrinos in Chapter 4, some care needed to be taken in fixing q_1 to evaluate the single-hard limit due to the presence of the freestreaming scale as well as numerical instabilities if q_1 was too large, this is to much less a degree an issue for EdS-SPT kernels.

In Fig. 5.6, we display the renormalized two-loop correction for the three shapes. The linear, one-loop and two-loop contributions in SPT are also shown for comparison, as well as the double-hard limit of the two-loop. For wavenumbers $k \lesssim 0.1h\ \mathrm{Mpc}^{-1}$, the double-hard region represent almost the complete two-loop correction, evidencing that the two-loop is dominated by spurious contributions from the UV.

Cutoff-independence

Having seen that the double-hard region of the two-loop can be corrected for by the counterterm appearing already at one-loop, and implemented a prescription for renormalizing the single-hard contribution, we can present the following cutoff-independent prediction for the bispectrum at NNLO

$$B_{\mathrm{NNLO}}^{\mathrm{ren}}(k_A,k_B,k_C) = B_{\mathrm{tree}}(k_A,k_B,k_C) + B_{1L}^{\mathrm{ren}}(k_A,k_B,k_C) + B_{2L}^{\mathrm{ren}}(k_A,k_B,k_C)\,, \tag{5.40}$$

where

$$B_{1L}^{\rm ren}(k_A,k_B,k_C) = B_{1L}(k_A,k_B,k_C;\Lambda) + B_{1L}^{\rm ctr}(k_A,k_B,k_C;\Lambda)\,, \tag{5.41a}$$
$$B_{2L}^{\rm ren}(k_A,k_B,k_C) = \bar{B}_{2L}(k_A,k_B,k_C;\Lambda) + B_{2L}^{\rm ctr}(k_A,k_B,k_C;\Lambda)\,, \tag{5.41b}$$

with the bare one- and subtracted two-loop corrections being given by Eqs. (5.2) and (5.31) and the counterterms defined in Eqs. (5.14) and (5.39). Before we compare and calibrate it to N-body simulations, let us demonstrate the cutoff-independence explicitly.

Given our choice of removing the degenerate double-hard contributions from the renormalized two-loop correction, the RGE $\mathrm{d}B_{\rm NNLO}^{\rm ren}/\mathrm{d}\Lambda = 0$ can be solved independently for the one- and two-loop terms. After subtracting the double-hard limit, the cutoff-dependence comes from the single-hard limit, which we demand is canceled by the counterterm:

$$\begin{aligned} 0 &= \frac{\mathrm{d}}{\mathrm{d}\Lambda}\left[\bar{B}_{2L}^{h}(k_A,k_B,k_C;\Lambda) + B_{2L}^{\rm ctr}(k_A,k_B,k_C;\Lambda)\right] \\ &= 2\bar{b}_{2L}^{h}(k_A,k_B,k_C)\frac{\mathrm{d}}{\mathrm{d}\Lambda}\left[\sigma_{\rm d}^2(\Lambda) + \mathcal{N}\gamma_2(\Lambda)\right]\,, \end{aligned} \tag{5.42}$$

reflecting the renormalization ansatz that the UV is corrected for by a shift in $\sigma_{\rm d}^2$. We choose $\mathcal{N} = 1/c_{\rm EdS} = 210/61$.

Since the we adopt a renormalization scheme in which the double-hard region of the two-loop correction is exactly removed by the *two-loop part* of the EFT coefficients, the UV-inspired approach may still be applied to the *one-loop part* (which in the end are the ones fitted for). One still needs a prescription for the single-hard correction, and following the simplistic spirit of this approach, with 0 or 1 free parameter, one can make the assumption that $\gamma_2 = \gamma_1$, leaving only γ_1 to be fitted for or fixed by measurements of the effective sound speed $c_{\rm s}^2$ from the power spectrum. This assumption is appropriate for $\mathcal{N} = 210/61$ and if γ_1 and γ_2 correct for the displacement dispersion $\sigma_{\rm d}^2$ in an equal manner.

The cutoff-dependence of the two-loop correction before and after renormalization is examined quantitatively in Fig. 5.7. It displays the bare, subtracted and renormalized two-loop for two different cutoffs $\Lambda = 0.6$ and $10h$ Mpc^{-1}, as well as the counterterm with the same cutoffs. The bare correction exhibit a strong cutoff-dependence across a large range of scales, as illustrated by the blue shaded region. After removing the double-hard limit, the cutoff-dependence is significantly reduced. The residual dependence on Λ should be absorbed by the counterterm, and indeed we see that the renormalized two-loop correction (orange) has an insignificant dependence on the cutoff for small k. This result is independent of the free parameter γ_2. For larger k, we see that also the renormalized result exhibit a certain cutoff-dependence, due to the neglected, subleading power corrections $\mathcal{O}(k^4/k_{\rm NL}^4)$ becoming relevant.

Subleading UV contributions

We end the section by discussing the subleading k^4 contributions to the double-hard limit, which was neglected so far. As reviewed above, the k^4 terms $B^{(321-I)}$ and $B^{(222)}$ at one-loop correspond in the hard limit to two short wavelength modes with almost opposite and equal wavenumber that combine to a long wavelength mode. Such a UV-dependence is renormalized

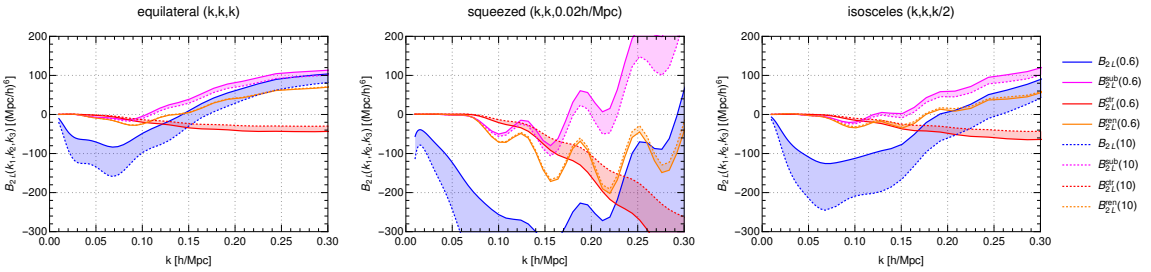

Figure 5.7: Cutoff-dependence of the two-loop correction before and after renormalization for an equilateral, squeezed and isosceles shape. The bare (blue), subtracted (magenta) and renormalized (orange) two-loop corrections as well as the counterterm $B_{2L}^{\rm ctr}$ (red) are shown for two cutoffs $\Lambda = 0.6$ (solid lines) and $10h$ Mpc^{-1} (dashed lines). The shaded regions indicate the difference between the cutoffs, i.e. the cutoff-dependence. For the counterterm and renormalized graph, $\gamma_2 = 1$ Mpc$^2/h^2$ is used. Reprinted from Paper II [45].

by the stochastic contribution to the effective stress tensor (3.96). However, it enters with an integral $\int_{\mathbf{q}} P_0(q)/q^4$ (see Eq. (5.4)) which is very suppressed in a ΛCDM cosmology, and the stochastic EFT can in practice be neglected to good approximation [298, 299].

At two-loop, the only k^4 terms that are not noise-terms, i.e. that do not contain pure stochastic parts, are $B^{(431-II)}$ and $B^{(332-II)}$. They can be written as a products of one-loop bi- and power spectra:

$$B^{(431-II)}(k_A,k_B,k_C) = B^{(411)}(k_A,k_B,k_C) \times \frac{P^{(31)}(k_B)}{P_0(k_B)}\,, \tag{5.43a}$$

$$B^{(332-II)}(k_A,k_B,k_C) = B^{(211)}(k_A,k_B,k_C) \times \frac{P^{(31)}(k_A)}{P_0(k_A)}\frac{P^{(31)}(k_B)}{P_0(k_B)}\,, \tag{5.43b}$$

corresponding to "propagator squared" corrections. The contribution from the double-hard region to these diagrams is simply given by the hard limits of $B^{(411)}$ (Eq. (5.7)) and $P^{(13)}$ (Eq. (3.77b)). We show the double-hard limits in Fig. 5.8. They are very suppressed compared to the one- and two-loop counterterms up to $k \simeq 0.15h$ Mpc^{-1}, and we can safely neglect them in the analysis.

5.4 Numerical results

Finally, having derived a renormalized bispectrum at NNLO, we can calibrate the EFT parameters to N-body simulations and determine how far the wavenumber reach of the perturbative prediction increases when adding the two-loop correction.

The simulations used to compare to are 14 realizations computed with the `Gadget-2` code [300], with 1024^3 particles in a cubic box of size $(1500\text{Mpc}/h)^3$. To beat cosmic variance and avoid features such as seen in Chapter 4 in the comparison of theory and simulation on scales close to the box size, we use the realization based perturbation method gridPT [301–303] to evaluate the theory. This means that the perturbation theory is

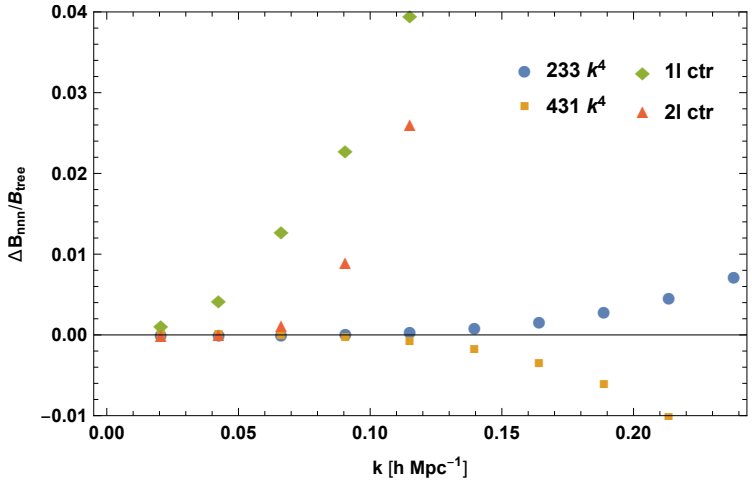

Figure 5.8: Subleading UV-dependence of the two-loop bispectrum: we show the "propagator squared" double-hard contributions $B^{(431-II)}$ and $B^{(332-II)}$, as well as the one- and two-loop counterterms for the equilateral configuration. Reprinted from Paper II [45].

evaluated on the very same modes that were used as seeds of the simulation. The linear, one-loop and subtracted two-loop contributions can be computed with the gridPT method, while the subtracted single-hard limit is more complex to evaluate this way, hence we used Monte Carlo integration (with the linear power spectrum as input, i.e. without specifying to a realization) to obtain it. In Paper II [45], a comparison between the loop corrections computed with Monte Carlo integration and gridPT was done, finding no differences that exceed the uncertainty due to binning effects. We use a cutoff $\Lambda = 0.3h$ Mpc^{-1} unless otherwise specified, although it should be stressed that the EFT predictions are cutoff-independent, up to numerical uncertainty and small, subleading contributions from the UV.

Both the simulation and gridPT work at the field level on particular realizations, hence the wavenumbers must be divided into bins to estimate the bispectrum. We use ten linear bins, and employ an FFT based estimator for the bispectrum measurement [213, 250]. As discussed in Ref. [213] (see also Ref. [176]), there can be small time integration errors in the `Gadget` simulations that yield a slight mistake in the linear growth. While the discrepancy would typically be unimportant compared to cosmic variance, it matters for the realization based approach. To remedy this, we add growth factor corrections ΔD_i at first and second order as free parameters in the fits, thus

$$\delta(\mathbf{x},\tau) = (1+\Delta D_1)\delta^{(1)}(\mathbf{x},\tau) + (1+\Delta D_2)\delta^{(2)}(\mathbf{x},\tau) + \delta^{(3)}(\mathbf{x},\tau) + \cdots . \tag{5.44}$$

The EFT parameters and the growth corrections ΔD_i are determined by minimizing the following χ^2,

$$\chi^2 = \sum_{k=k_{\rm min}}^{k_{\rm max}} \frac{\left[B_{\rm data}(k) - B^{\rm ren}_{\rm NLO/NNLO}(k_A,k_B,k_C;\Delta D_{1,2},\epsilon_i,\gamma_{1,2})\right]^2}{\left[\Delta B_{\rm data}(k)\right]^2}, \tag{5.45}$$

where the renormalized bispectrum at NLO and NNLO were given in Eq. (5.41). At $k_{\rm max} = 0.1(0.2)h$ Mpc^{-1}, we have 65(369) triangles contributing to the sum above. In addition to the cases listed in Eq. (5.21), we consider the following calibration approaches at two-loop,

$$\begin{aligned}
&\{\epsilon_1, \epsilon_2, \epsilon_3, \gamma_1, \gamma_2\} && \text{two-loop, 5-parameter symmetry based}\,, \\
&\{\gamma_1\} && \text{two-loop, 1-parameter UV-inspired with } \epsilon_i/\gamma_1 \text{ fixed and } \gamma_2 = \gamma_1\,, \\
&\emptyset && \text{two-loop, 0-parameter UV-inspired with } \epsilon_i/\gamma_1 \text{ fixed and } \gamma_2 = \gamma_1 = c_{\rm s}^2\,.
\end{aligned} \tag{5.46}$$

It turns out that there is a large degeneracy between the ϵ_i contributions, and we find that fixing $\epsilon_1 = 0$ has insignificant impacts on the results. This simplification is adopted below.

The difference between the perturbative prediction for the bispectrum and the N-body result is shown in Fig. 5.9, using the symmetry based approach with four free parameters at two-loop ($\epsilon_1 = 0$), and pivot scale $k_{\rm max} = 0.115h$ Mpc^{-1}. The unrenormalized SPT results only agree well with N-body for the lowest k-bins, with deviations of a few percent at $k = 0.05h$ Mpc^{-1}, depending on the shape. Nevertheless, the agreement is improved when adding the two-loop correction, especially in the squeezed limit where one of the external wavenumbers are always linear. In the effective theory, the range of wavenumbers with percent agreement is greatly extended. Moreover, the deviations are broadly consistent with theoretical expectations from the missing higher order corrections (gray shaded regions) [288]. As expected, adding the renormalized two-loop bispectrum clearly extends the reach of the perturbation theory, and in addition the agreement is better also on large scales, where the numerical uncertainties are small.

We saw in Section 4.5 that one is easily subject to overfitting when calibrating the EFT prediction to N-body data. In this case however, using the realization based gridPT method, there is essentially no N-body uncertainty on large scales, and thus the fit is strongly penalized for deviations in this region where the theory prediction is most accurate. Therefore, a relatively low pivot scale $k_{\rm max} = 0.115h$ Mpc^{-1} can be used, and one can reasonably assume there is only a limited degree of overfitting, in particular in the two-loop case.

Fig. 5.10 shows the χ^2 over degrees of freedom from the fits. In addition to the symmetry based approach (labeled *EFT* in the legend), the figure also include points corresponding to the UV-inspired approach—we discuss that case shortly. The NLO prediction has $\chi^2/\text{d.o.f} < 1$ up to $k_{\rm max} \simeq 0.08h$ Mpc^{-1}, in agreement with previous analyses [213]. The range of wavenumbers with 1σ agreement is extended to $k_{\rm max}0.15h$ Mpc^{-1} when the two-loop correction is added. As a check, equivalent results were found using a different cutoff $\Lambda = 0.6h$ Mpc^{-1} in Paper II [45].

Next, we investigate the best-fit EFT parameters in the symmetry based approach. They are displayed as a function of the pivot scale $k_{\rm max}$ in Fig. 5.11. The γ_1-parameter exhibit a certain running at one-loop, which is greatly reduced after adding the two-loop. This indicates that the NLO fit is attempting to capture missing higher order pieces, while at NNLO the value is stable over a larger range of wavenumbers, allowing for an accurate calibration. Notice that this parameter is most excellently constrained by the fit, with the smallest error bars.

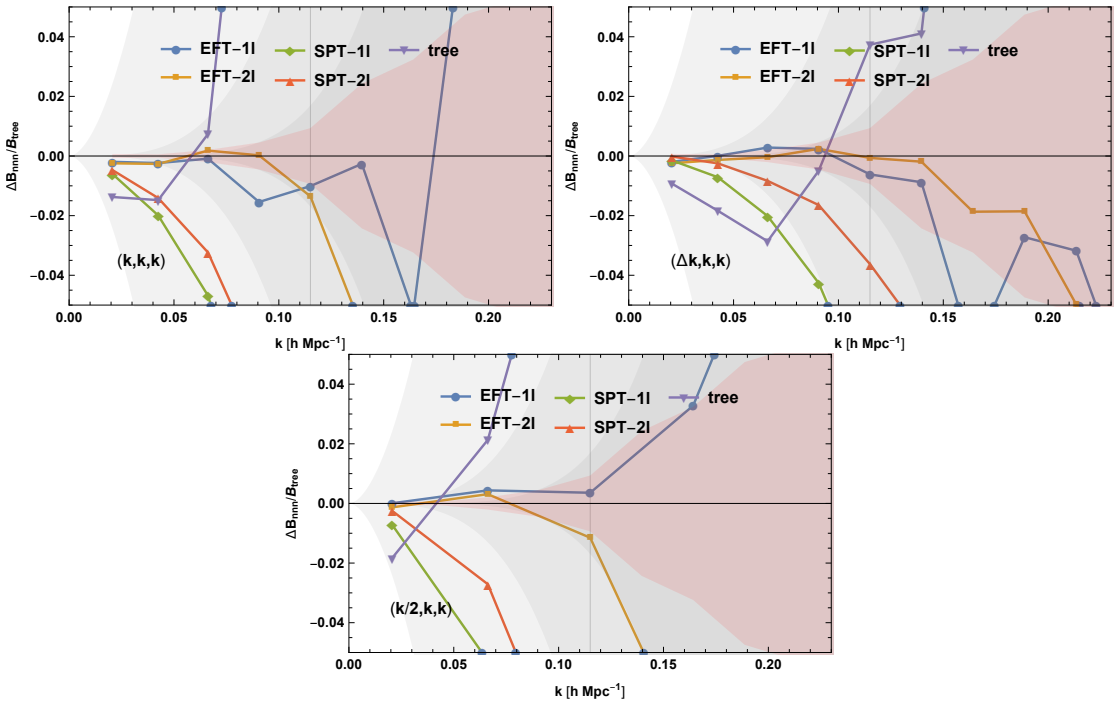

Figure 5.9: Difference between the NLO and NNLO perturbative results and N-body results for the bispectrum, both in the EFT and SPT, normalized to the tree-level bispectrum. The upper left, upper right and lower panel correspond to the equilateral, squeezed ($\Delta k = 0.02h$ Mpc^{-1}) and isosceles shapes, respectively. The N-body uncertainty is displayed with red shading, while the tree-level, one- and two-loop expected theoretical uncertainty is indicated with gray shading, from light to dark, respectively. The pivot scale is $k_{\rm max} = 0.115h$ Mpc^{-1} as indicated by the vertical gray line. Reprinted from Paper II [45].

The EFT parameter correcting for the single-hard limit of the two-loop correction, γ_2, is shown in the uppermost right panel. Since it multiplies the *subtracted* single-hard limit, which by definition vanishes for $k \to 0$ (corresponding to the double-hard limit), it cannot be reliably determined for a low pivot scale. For $k_{\rm max} \gtrsim 0.12h$ Mpc^{-1} however, the subtracted single-hard factor in the counterterm becomes sizable, and we see that the measured value of γ_2 is rather stable beyond this point. This dependence on the pivot scale is analogous to the EFT parameter γ_2 we introduced for the two-loop *power spectrum* with massive neutrinos measured in Section 4.5, which could only be reliably calibrated above $k_{\rm max} \simeq 0.15h$ Mpc^{-1}. Due to the enhanced control over uncertainties on large scales with the gridPT method, the corresponding bispectrum parameter can be accurately constrained for slightly smaller wavenumbers.

The gray horizontal lines in Fig. 5.11 indicate the corresponding value of the coefficient in the UV-inspired approach, in which the EFT is assumed to correct the UV-sensitivity of the perturbative prediction in a universal manner by a shift in the displacement dispersion $\sigma_{\rm d}^2$. For γ_1 and γ_2, the measured value in the two-loop, symmetry based case is not too far from

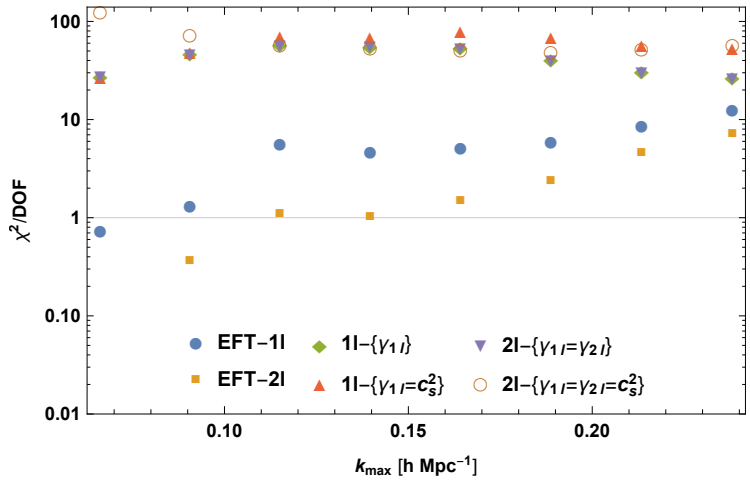

Figure 5.10: Reduced χ^2 for the different calibration approaches as a function of the pivot scale $k_{\rm max}$, see Eqs. (5.21) and (5.46). Figure taken from Paper II [45].

this line, suggesting that the dominant contribution to the EFT correction corresponds to such a universal shift.

The last two parameters in the symmetry based approach are measured in the lower panels of Fig. 5.11. On large scales, the errorbars are large, indicating that the contributions from the corresponding EFT operators are small and the parameters cannot be faithfully determined. On the other hand, for small scales $k_{\rm max} \gtrsim 0.2h$ Mpc^{-1}, we observe a running as a function of the pivot scale, signaling that higher order corrections become important. There are also considerable degeneracies between ϵ_2 and ϵ_3, as well as to some degree with γ_1 and γ_2, such that precise measurements of the ϵ-parameters are challenging. In the intermediate region $k_{\rm max} \approx 0.15h$ Mpc^{-1} however, the error bars are sufficiently small and the values are reasonably stable against changes of the pivot scale, in particular at two-loop, allowing for a fairly precise calibration.

UV-inspired approach

Lastly, we consider the UV-inspired approach and gauge in how far we can match the bispectrum from simulations using only one EFT parameter, controlling the overall amplitude of the counterterms. This method cannot be naively extended to two-loop, because of the different linear combinations of basis functions that comprise the hard limit of the one-loop and double-hard limit of the two-loop corrections. Nevertheless, after the double-hard limit is subtracted, it can be applied to the one-loop part of the EFT coefficients. Furthermore, we can extend it to capture the single-hard correction as well by fixing $\gamma_2 = \gamma_1$, as described above.

The perturbative results for the bispectrum in the equilateral, squeezed and isosceles configurations are displayed in Fig. 5.12. The symmetry based results are shown for comparison, labeled *EFT-1/2l*. Both at NLO and NNLO and using with 0/1 free parameters, the UV-inspired results are not as accurate as the corresponding symmetry based results. Moreover, the deviations start on relatively large scales and exceed the expected theoretical

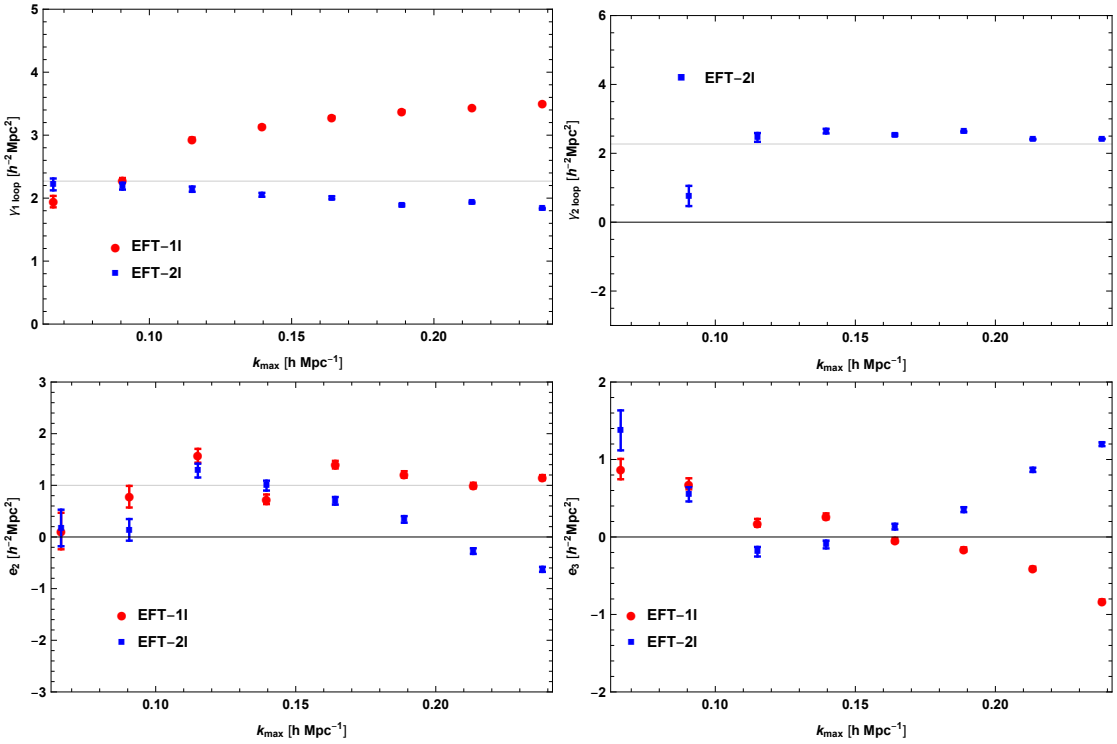

Figure 5.11: EFT parameters measured from calibrating the two-loop prediction in the symmetry based approach to the N-body bispectrum. The panels show γ_1 (upper left), γ_2 (upper right), ϵ_2 (lower left) and ϵ_3 (lower right). (ϵ_1 is fixed to zero as discussed in the text.) The thin gray lines indicate the value the parameters would be fixed to in the UV-inspired approach. Reprinted from Paper II [45].

error based on missing higher order corrections. The decreased accuracy in the UV-inspired approach is also reflected in a much larger χ^2/d.o.f. even at small wavenumbers, as shown in Fig. 5.10. Nevertheless, comparing to Fig. 5.9, the UV-inspired results improve compared to the SPT predictions.

The measured γ_1 parameter is plotted in Fig. 5.12. There is a clear drift, especially in the two-loop case, as compared to the symmetry based approach (cf. upper left panel of Fig. 5.11). For illustration, there green diamonds correspond to a 2-parameter UV-inspired approach where the $\gamma_{1,2}$ parameters are fitted independently. Up to the pivot scale $k_{\rm max} = 0.15h$ Mpc^{-1}, where the NNLO prediction is accurate (in the symmetry based approach), the measured parameter differs little between the 1- and 2-parameter UV-inspired ansatz, implying that the improvement is not too large in the second case and we therefore do not investigate it in more detail.

Summary We have studied the bispectrum at NNLO in an EFT framework. After showing that the double-hard region of the two-loop correction can be renormalized by the same

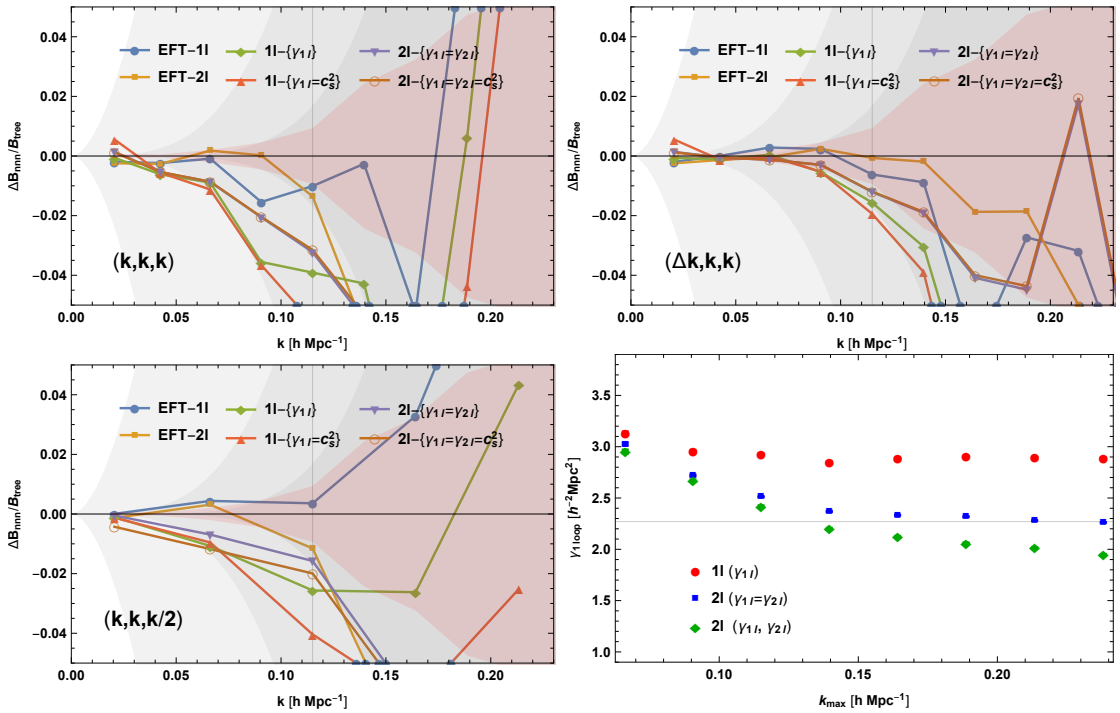

Figure 5.12: Same as Fig. 5.9, however displaying how the various calibration approaches match the N-body data for the three different shapes. The lower right panel shows the measured EFT parameter γ_1 in the UV-inspired 1-parameter approach. In that panel, the gray line indicate the 0-parameter result, $\gamma_1 = c_s^2$, with c_s^2 fitted from the power spectrum. Furthermore, the green diamonds illustrate γ_1 in a 2-parameter extension of the UV-inspired approach where γ_1 and γ_2 are fitted independently. Figure reprinted from Paper II [45].

counterterms that correct the hard region of the one-loop correction, we employed a simplified treatment of the two-loop single-hard limit, introducing one additional EFT parameter. We compared the theory prediction to N-body simulations, using a realization based perturbative approach to beat cosmic variance. In accordance with theoretical expectations based on missing loop-corrections, we found that the one-loop has 1σ agreement with simulations up to $k \simeq 0.08h$ Mpc^{-1}. Adding the two-loop extends the wavenumber range with percent agreement to $k \simeq 0.15h$ Mpc^{-1}. Furthermore, we assessed the impact of exact, time-dependent dynamics on the one-loop bispectrum, finding that the effect is largely degenerate with the counterterm up to $k \simeq 0.15h$ Mpc^{-1}, independent of shape.

6 Non-standard neutrino interactions in cosmology

So far, we assumed that neutrinos have SM interactions. Then, in the standard picture described in Chapter 4, the neutrinos decoupled from the plasma at $T \approx 1$ MeV in the early Universe and have been freestreaming ever since. They are therefore the only species that can acquire a sizable anisotropic stress in the early Universe. Given that neutrinos comprise 40 % of the total energy budget during radiation domination, the neutrino anisotropic stress in turn yield a large effect on the metric potentials via Einstein's equations, leading to observable impacts on cosmological probes. In particular, the metric potentials source the CMB anisotropies, and the freestreaming nature of neutrinos therefore have two effects on the CMB [30, 42, 43]: (i) a dampening of the acoustic peaks due to the neutrinos being distributed more smoothly than the photons and (ii) a shift of the peaks to larger scales due to the photon perturbations—traveling at the speed of sound of the baryon-photon fluid—are dragged along the ultra-relativistic neutrino perturbations. The second effect can not be mimicked by other cosmological parameters given adiabatic perturbations in ΛCDM [42].

Current CMB measurements favor three freestreaming neutrino species in accordance with the prediction of the CνB within the SM [6–8, 304, 305]. Nevertheless, there are many beyond SM models that feature non-standard neutrino interactions that influence the neutrino freestreaming in the early Universe. Thus, CMB measurements are a fruitful way of testing and constraining such models given its indirect sensitivity to neutrino properties. In this chapter, we present the analysis of Paper IV [47]: we take a global perspective and study the redshift range in which neutrinos are allowed to interact given current cosmological data. Using a generic set of interaction rates that model neutrino interactions, we perform a full Planck 2018 CMB analysis and find a window of redshifts, the *freestreaming window*, where neutrino interactions are disfavored. In addition, within this window, we determine the allowed amplitude of the interaction rate. The interaction rates and the methodology are described in Section 6.1 while the results are presented in Section 6.2. Moreover, we investigate to which extent the Planck constraints can be improved in the future by performing a forecast analysis with CMB-S4 in Section 6.3. Altogether, the findings of Paper IV can serve as a guide for particle physics model builders, informing about which models and what regions of parameter space are allowed by cosmological constraints.

As we elaborate below, numerous previous works in the literature have studied cosmological implications in particular scenarios of neutrino interactions. Paper IV goes beyond earlier works by being, to the best of our knowledge, the first to address the freestreaming window in a model-independent manner. Moreover, it investigates the sensitivity of CMB Stage IV experiments as well as the sensitivity of LSS to probe uncharted regions of parameter space in models with interacting neutrinos, for the first time. The latter will not be included in

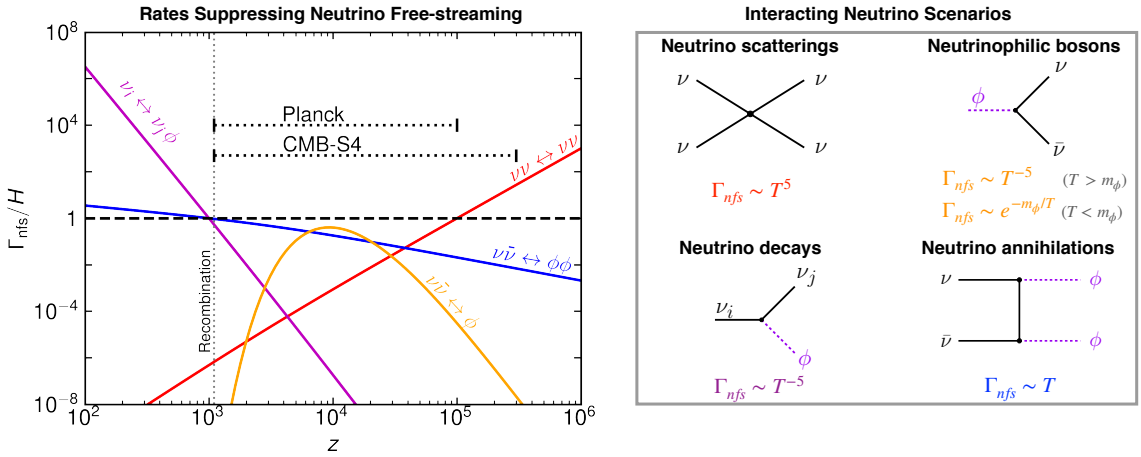

Figure 6.1: Summary of four neutrino interaction scenarios. *Left:* Interaction rate $\Gamma_{\rm nfs}$ dampening neutrino anisotropic stress as a function of redshift normalized to the Hubble rate. The horizontal dotted lines indicate the window of major sensitivity of Planck and CMB-S4. *Right:* Diagrams and overall scaling with temperature in the various scenarios. Reprinted from Paper IV [47].

this thesis and we refer the reader to Paper IV [47]. Furthermore, the paper features an extensive discussion connecting the phenomenological models used in the CMB analysis to particle physics models of interacting neutrinos. We skip also that discussion in this text for conciseness.

Interacting neutrino scenarios

In the last two decades, there have been many studies looking at non-standard neutrino interactions from the cosmological perspective. We give in the following an overview of scenarios containing exotic neutrino interactions that have been extensively studied in the literature, and connect them to the phenomenological set of models we introduce in the next section. For cosmology, the main difference between the models is the temperature dependence of the interaction rate that suppresses neutrino freestreaming, the *non-freestreaming* rate $\Gamma_{\rm nfs}$. The interaction is efficient when this rate is much larger than the Hubble rate; the latter scaling like $H \sim T^2$ and $H \sim T^{3/2}$ in early and late Universe, respectively. The temperature/redshift-dependence of the ratio $\Gamma_{\rm nfs}/H$ is shown in the left panel of Fig. 6.1. The right panel of that figure serves as a visual summary of the primary models, which are

- *Neutrino self-interactions* $\nu\nu \leftrightarrow \nu\nu$: Cosmological consequences of neutrino self-interactions have been studies in e.g. Refs. [306–315]. On dimensional grounds, assuming relativistic neutrinos and a mediator mass $M \gg T_\nu$, the rate at which neutrino freestreaming is dampened scales as $\Gamma_{\rm nfs} \sim G_{\rm eff}^2 T_\nu^5$, where $G_{\rm eff}^2$ is the effective Fermi-constant parametrizing the interaction [306]. Therefore, the interaction is efficient at early times, as can be seen from the red graph in Fig. 6.1. This scenario will correspond to $n_{\rm int} = 5$ in our phenomenological model defined below.

- *Interactions with neutrinophilic bosons* $\phi \leftrightarrow \nu\nu$: A scenario with decays and inverse decays with eV-scale neutrinophilic bosons ϕ was the first interacting model to be considered in the context of signals in the CMB [316]. In recent years, such scenarios have been analyzed in detail [317–319]. The overall temperature dependence of $\Gamma_{\rm nfs}$ can be split into two limits: $\Gamma_{\rm nfs} \sim \Gamma_\phi e^{-m_\phi/T_\nu}$ for $T_\nu \ll m_\phi$ and $\Gamma_{\rm nfs} \sim \Gamma_\phi (m_\phi/T_\nu)^5$ for $T_\nu \gg m_\phi$ [320]. The latter limit has recently been derived by Refs. [321, 322], showing that the actual non-freestreaming rate is suppressed by two additional powers of $(m_\phi/T_\nu)^2$ than what one would expect from the typical energy transport rate $\Gamma \sim \Gamma_{m_\phi}(m_\phi/T_\nu)$. Hence, given $m_\phi \sim$ eV and a sufficiently large decay rate Γ_ϕ, the non-freestreaming interaction rate is efficient around $z \sim 10^4$, see the yellow graph in Fig. 6.1. In the formalism below, this scenario corresponds to the $b = 4$ transient interaction.

- *Neutrino decays* $\nu_i \leftrightarrow \nu_j\phi$: Ref. [323] pointed out that neutrino decays could impact freestreaming almost two decades ago, which has been followed by several works assessing the impact on CMB observations [321, 322, 324–328]. As for the previous item, Refs. [321, 322] have showed that the appropriate rate that suppresses the neutrino anisotropic stress scales with temperature as $\Gamma_{\rm nfs} \sim \Gamma_\tau (m_\nu/T_\nu)^5$. Thus, this type of interaction becomes important at late times, as indicated by the magenta graph in Fig. 6.1. In our analysis below, this model will correspond to $n_{\rm int} = -5$.

- *Neutrino annihilations* $\nu\nu \leftrightarrow \phi\phi$: Neutrinos annihilating into massless species has been considered in the context of CMB observations in Refs. [329–335]. The non-freestreaming rate goes like $\Gamma_{\rm nfs} \sim T$, which means that that its scaling is close to Hubble, nevertheless the interaction is most efficient at late times. This scenario corresponds to $n_{\rm int} = 1$ below, and is shown in blue in Fig. 6.1.

6.1 Dampening of neutrino freestreaming

In this section, we describe the method with which we will describe the effect on neutrino freestreaming due to non-standard interactions, as well as define the phenomenological non-freestreaming rates we will use.

At recombination, fluctuations were of the order of 10^{-5} hence we can use linear theory.[1] Neutrino anisotropic stress sources the metric perturbations via Einsteins equations, which subsequently affects the perturbations in the photon component. Schematically,

$$\sigma_\nu \to \delta G_{\mu\nu} \to \delta T_{\mu\nu}|_\gamma \to \delta T_\gamma \,, \tag{6.1}$$

where the δ prefix indicates a perturbation, $G_{\mu\nu}$ is the Einstein tensor and $T_{\mu\nu}$ is the energy stress tensor of a species. We defined the anisotropic stress in terms of the energy stress tensor in Eq. (4.11). Moreover, T_ν is the CMB temperature. In linear theory, we can model fluctuations around the background, ultra-relativistic Fermi-Dirac neutrino distribution

[1] Features in the angular power spectrum generated after recombination, *secondary anisotropies*, such as lensing of the CMB photons, are subject to non-linear effects in the late Universe [336, 337]. However, as a small secondary effect convoluted with percent changes in metric potentials at late times due to non-linear corrections, it is safe to neglect non-linear effects on the CMB.

function as $\Psi \simeq \delta f$ according to Eq. (4.18). Its linearized Boltzmann hierarchy was given in Eq. (4.21c); to describe interactions suppressing neutrino freestreaming, we add a collision term to all multipoles $l > 2$,[2]

$$\frac{\partial \Psi_0}{\partial \tau} = -\frac{qk}{\epsilon}\Psi_1 - \frac{\mathrm{d}\ln f_0}{\mathrm{d}\ln q}\frac{\partial \phi}{\partial \tau}\,, \tag{6.2a}$$

$$\frac{\partial \Psi_1}{\partial \tau} = \frac{qk}{3\epsilon}\left(\Psi_0 - 2\Psi_2\right) - \frac{\epsilon k}{3q}\frac{\mathrm{d}\ln f_0}{\mathrm{d}\ln q}\psi\,, \tag{6.2b}$$

$$\frac{\partial \Psi_l}{\partial \tau} = \frac{qk}{(2l+1)\epsilon}\left[l\Psi_{l-1} - (l+1)\Psi_{l+1}\right] - a\Gamma_{\mathrm{nfs}}\Psi_l\,, \qquad l \geq 2\,. \tag{6.2c}$$

In order to be able to describe the effect of non-standard neutrino interactions on the neutrino perturbations with the relatively simple addition in the last line above, we made the following assumptions:

i) The non-freestreaming rate is assumed to have no dependence on the momentum $\mathbf{q}$ or the Fourier wavenumber $\mathbf{k}$ (and hence no dependence on multipole number l). It only depends on temperature, and corresponds therefore to an average rate at which neutrino freestreaming is dampened. As we will see, significant impacts on the CMB from neutrino interactions occur for $z \gtrsim 1000$, which means the neutrinos are ultra-relativistic when the interactions were active. (Cosmological bounds imply $\sum m_\nu \lesssim 0.2$ eV as we saw in Section 4.1, and this bound is furthermore consistent with our findings for interacting scenarios below.) For ultra-relativistic species, $\epsilon = q$, and the q-dependence in the Boltzmann equation can be integrated over, with an effective interaction rate. While we keep the q-dependence in the Boltzmann hierarchy to allow for a non-zero neutrino mass in the analysis, the relevant ultra-relativistic limit of that equation is equivalent to the approach in which q is integrated over, as used in e.g. Refs. [306, 325, 334]. See Refs. [307, 322] for discussions on the impact of including the momentum dependence in the interaction rate. Moreover, we assume that the interaction is equally present on all scales (within the horizon) and thus k-independent.

ii) The energy density of the neutrino component in the Universe as a function of time is the same as in the Standard Model. This assumption is generally justified for all the models described above (Fig. 6.1): For neutrino self-interactions, it is trivially satisfied. For neutrino decays and annihilations into lighter species, the total energy density of the system is conserved until $T_\nu < m_\nu$ due to energy conservation. At lower temperatures, only the secondary anisotropies are affected, yielding a much smaller effect than from the suppressed neutrino anisotropic stress. Refs. [321, 330] have studied such scenarios taking into account the change in total energy density. For interactions with neutrinophilic bosons, there can however be a change in total energy density because the bosons are heavier than the neutrinos, and could thus easily become non-relativistic before recombination. Nevertheless, it has been shown that the neutrinophilic boson contribution to the combined energy density with neutrinos is typically only $\mathcal{O}(10\,\%)$ [320], and moreover the altered expansion history

[2] This set of equations is given equivalently in synchronous gauge in Paper IV [47].

influences the CMB much less than the dampened neutrino freestreaming, given that $\Gamma_{\rm nfs}/H \gg 1$ [317].

The benefit of this approach is that it is relatively simple to implement in a Boltzmann solver such as `CLASS`. As discussed in detail in Paper IV [47], our constraints on non-standard neutrino interactions broadly match those in the literature where a subset of the above approximations are relaxed. Therefore, we deem this setup suitable for a global analysis of suppression of neutrino freestreaming as constrained by cosmology.

We are interested in extracting the window of redshifts in which neutrinos cannot interact significantly given Planck measurements in a model-independent manner. Therefore, we will first consider an array of non-freestreaming interaction rates that are power-laws in temperature. Specifically, we define

$$\Gamma_{\rm nfs}(z; z_{\rm int}) = H(z_{\rm int}) \left[\frac{1+z}{1+z_{\rm int}}\right]^{n_{\rm int}} = H(z_{\rm int}) \left[\frac{T(z)}{T(z_{\rm int})}\right]^{n_{\rm int}} , \tag{6.3}$$

corresponding to a family of models with different power-law index $n_{\rm int}$. In Eq. (6.3), the parameter $z_{\rm int}$ effectively describes the overall amplitude of the interaction, but parametrized in a way such that $z_{\rm int}$ corresponds to the redshift at which $\Gamma_{\rm nfs}(z)/H(z) = 1$ ($H(z_{\rm int})$ is the Hubble rate at $z = z_{\rm int}$). In Paper IV [47], we consider two families of power-laws:

$$\text{Low-}z \text{ interactions:} \qquad n_{\rm int} \in \{-5, -3, -1, 1\} \tag{6.4a}$$

$$\text{High-}z \text{ interactions:} \qquad n_{\rm int} \in \{3, 4, 5\}\,. \tag{6.4b}$$

The division is made with respect to the Hubble rate: the low-z interactions have a temperature dependence that decays less than Hubble (or increases) when the neutrino temperature drops, while the high-z interaction rates decay quicker than Hubble as the temperature decreases. While the models are phenomenological, a subset precisely correspond to the physical models discussed in the introduction above. In particular $n_{\rm int} = 5$ corresponds to neutrino self-interactions, $n_{\rm int} = 1$ to neutrino annihilations into massless states and $n_{\rm int} = -5$ to neutrino decays.

The other set of non-freestreaming interaction rates we consider is transient in redshift. We use phenomenological models defined as follows

$$\Gamma_{\rm nfs}(z; z_{\rm int}^{\rm max}, \Gamma/H|_{\rm nfs}^{\rm max}) = \Gamma/H|_{\rm nfs}^{\rm max} \frac{H(z_{\rm int}^{\rm max})}{C} K_2(a\,x)\, x^3 \left[K_1(ax)/K_2(ax)\right]^b , \tag{6.5}$$

where K_i are modified Bessel functions of the second kind, $x = (1 + z_{\rm int}^{\rm max})/(1 + z)$ and $z_{\rm int}^{\rm max}$ corresponds to the redshift at which the interaction rate divided by Hubble is maximal. We tune the constant C such that $\Gamma/H|_{\rm nfs}^{\rm max}$ controls the value of $\Gamma_{\rm nfs}/H$ at this maximum, in particular so that $\Gamma_{\rm nfs}/H|_{z=z_{\rm int}} = \Gamma/H|_{\rm nfs}^{\rm max}$. The parameter b controls the slope in the $z \gg z_{\rm int}^{\rm max}$, where $\Gamma_{\rm nfs} \propto T^{-1+b}$. To make sure that $z_{\rm int}^{\rm max}$ corresponds to the point at which $\Gamma_{\rm nfs}/H$ is maximum, we set $a = 4.7$. The sets of rates we consider are

$$\text{i) } b = 0,\ C = 1/130\,, \qquad \text{ii) } b = 2,\ C = 1/240\,, \qquad \text{iii) } b = 4,\ C = 1/420\,. \tag{6.6}$$

The form of the transient rate (6.5) is motivated by the physical model of neutrino interactions with neutrinophilic bosons. Indeed, $b = 0$ corresponds to the energy transport rate for

such a model, $b = 2$ to the expected non-freestreaming rate by assuming a random walk of angular steps to isotropize the distribution [323] and $b = 4$ to the best motivated rate derived from a complete Boltzmann equation from first principles [321, 322]. The last model is displayed in yellow in Fig. 6.1.

Thus, the transient model entails efficient interactions at some intermediate redshift, controlled by an amplitude and redshift at maximum interactions. Therefore, it can be used both to confirm the existence of a redshift window as established by the power-law cases, but also to determine how large the non-freestreaming interaction is allowed to be in that region, as we see below. Note that $z_{\rm int}$ and $z_{\rm int}^{\rm max}$ control different properties of the interaction rates: $z_{\rm int}$ corresponds to the redshift at which the ratio of the non-freestreaming rate versus Hubble is unity in the power-law cases, while $z_{\rm int}^{\rm max}$ denotes the redshift at which this ratio is maximum in the transient cases.

6.2 Neutrino interactions constrained by Planck

We present the results of the Planck analysis in this section. We implemented the modified Boltzmann hierarchy (6.2c) with the different phenomenological non-freestreaming rates (6.3) and (6.5) in the Boltzmann solver `CLASS`. Then, we performed MCMC analyses using the Metropolis-Hastings algorithm of the `MontePython` sampler [104, 105]. The posterior plots from the MCMC chains were performed with GetDist [338]. Following the Planck legacy analysis, we use these data sets: Planck 2018 TT+TE+EE+lowE [8] and BAO measurements from 6-degree Field Galaxy Redshift Survey (6dFGRS) [115], SDSS DR7 MGS [339] and BOSS DR12 [340]. For the power-law interaction models, we apply the following priors:

$$\log_{10} z_{\rm int} = [2, 4] \quad \text{for } n_{\rm int} \in \{-5, -3, -1, 1\}\,, \tag{6.7}$$

$$\log_{10} z_{\rm int} = [3, 6] \quad \text{for } n_{\rm int} \in \{3, 4, 5\}\,. \tag{6.8}$$

In the transient scenario, there are two parameters $z_{\rm int}^{\rm max}$ and $\Gamma/H|_{\rm nfs}^{\rm max}$. We set the following priors on them:

$$\log_{10} z_{\rm int}^{\rm max} = [1, 7] \qquad \text{and} \qquad \log_{10} \Gamma/H|_{\rm nfs}^{\rm max} = [-4, 7]\,. \tag{6.9}$$

The remaining priors for the cosmological parameters as well as the nuisance parameters in the Planck likelihoods are set to the same as in the Planck analysis [8]. Our chains consist of more than 3×10^6 steps and we check that the Gelman-Rubin convergence diagnostic [341] satisfies $R - 1 < 0.02$ for all cosmological and nuisance parameters in all interaction models.

Freestreaming window

The posterior probabilities for H_0, n_s, $\sum m_\nu$ and $\log_{10} z_{\rm int}$ for our set of seven power-law cases is shown in Fig. 6.2. We do not find any statistically significant preference for neutrino interactions in any of the cases, and can hence derive exclusion limits for $z_{\rm int}$. In the low-z interaction scenarios (Eq. (6.4a)) we find a 95 % C.L. bound on $z_{\rm int}$ to be in the region 1300–2400, depending on the specific scenario (value of $n_{\rm int}$). The precise 95 % and 99.7 % C.L. bounds in all scenarios are listed in Paper IV [47]. We find that those bounds broadly agree with those previously found in the literature for dedicated

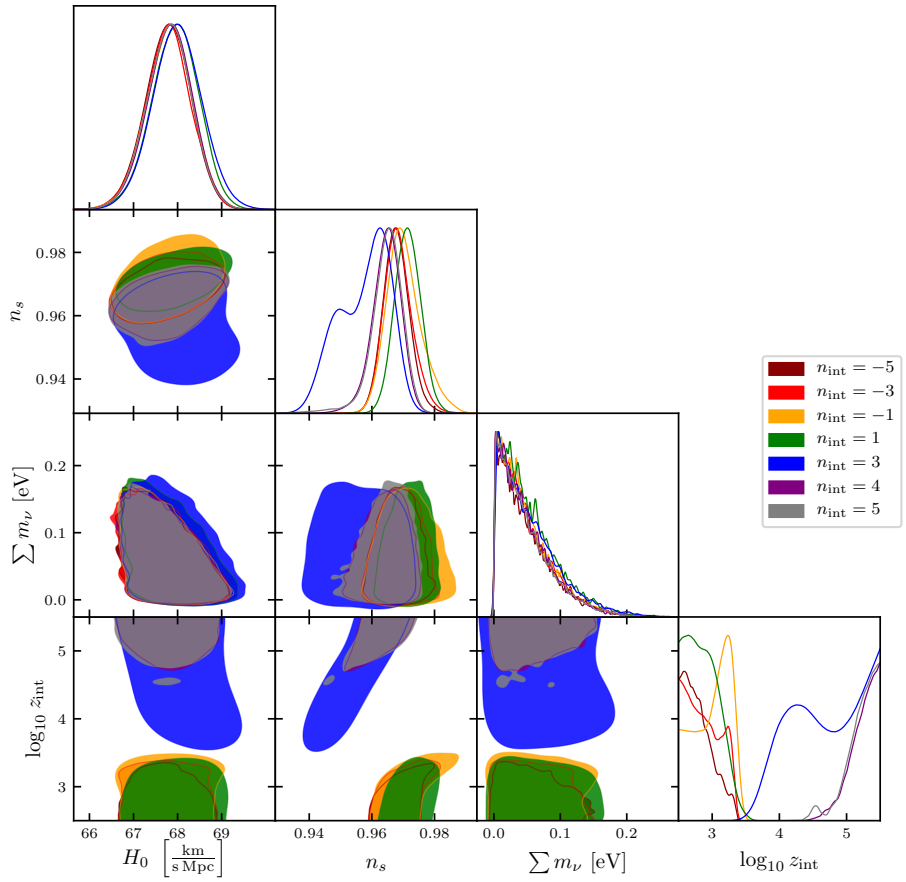

Figure 6.2: The posterior probabilities for H_0, n_s, $\sum m_\nu$ and $\log_{10} z_{\rm int}$ in the power-law interaction cases, $\Gamma_{\rm nfs} \sim T^{n_{\rm int}}$. The contours display 95 % C.L. regions. Reprinted from Paper IV [47].

analyses of specific scenarios, in particular with Ref. [334] for $n_{\rm int} = 1$, Refs. [325, 332] for $n_{\rm int} = -3$ and Ref. [322] for $n_{\rm int} = -5$. Given that we perform a simultaneous analysis, we can compare the bounds in the various scenarios. As can be recognized from the $\log_{10} z_{\rm int}$ posteriors in Fig. 6.2, the $n_{\rm int} = -5$ bound (dark red) is more stringent than the $n_{\rm int} = -3$ bound (red). This is to be expected, as the temperature dependence is stronger in the former case. For the $n_{\rm int} = -1$ (yellow) we see a small $\sim 1\sigma$ preference for interactions, which somewhat weakens the corresponding bound. Similar preferences for non-standard interacting neutrinos at low temperatures have been reported in the literature, e.g. Refs. [317, 319, 322, 325, 332, 334, 335]. In particular, Ref. [325] find the preference to be driven by Planck polarization data at moderately low l.

Similarly, for the high-z cases (Eq. (6.4b)), we find a 95 % C.L. bound $z_{\rm int} > (8\text{–}9) \times 10^4$, with one exception: the $n_{\rm int} = 3$ model, which we discuss in detail below. The $n_{\rm int} = 5$ bound is similar to specific studies in the literature that find $z_{\rm int} > 10^5$ [306, 309, 314]; the insignificant discrepancy can be attributed to small differences in the modeling or the choice

of priors.

With the exception of $n_{\rm int} = 3$, we find no strong correlation between $z_{\rm int}$ and the other cosmological parameters. There is a slight correlation with n_s; high-z interactions prefer a lower value of n_s while low-z interactions prefer a larger value of n_s. From Fig. 6.2, we can appreciate that while the changes are small, there is a clear trend. Similar tendencies have been found in analyses focusing on specific scenarios, see e.g. Refs. [306, 309, 322, 334].

In Fig. 6.2, the $n_{\rm int} = 3$ case stand out from the other as it allows for interactions down to redshifts of a few thousands. Since the temperature dependence of this rate is close to Hubble $H \sim T^2$, the angular power spectrum can be affected across a large range of multipoles, a change that can largely be adjusted for by tuning the amplitude and tilt of the primordial power spectrum. Indeed, the slight preference for interaction at $\log_{10} z_{\rm int} = 4$ is accompanied by a significant decrease in n_s as well as a slight decrease of A_s and increase of H_0. A similar degeneracy with n_s was found in the $n_{\rm int} = 5$ case prior to the Planck legacy data [308, 309]. In Paper IV [47], we check whether this degeneracy can be broken by adding Planck lensing data, finding however no significant difference in the posteriors.

In total, we can conclude that there is a well-defined freestreaming window $2000 \lesssim z \lesssim 10^5$, in which Planck CMB measurements reject efficient neutrino interactions that suppress neutrino freestreaming. The exception is the peculiar $n_{\rm int} = 3$ case, in which the temperature dependence of the interaction is close to Hubble. This scenario can nevertheless be tested by CMB Stage IV experiments, as we see in the next section.

Freestreaming window depth

Having established the freestreaming window for neutrinos as seen by Planck using power-law interaction cases, we wish to investigate how large the interaction rate can be in this window, or in other words, how *deep* the window is. This can be checked with the transient interaction cases (6.5), whose free parameters control the point at which the non-freestreaming interaction is efficient as well as the amplitude.

The 95 % C.L. bounds on the amplitude $\Gamma/H|^{\rm max}_{\rm nfs}$ as a function of the maximum interaction redshift $z^{\rm max}_{\rm int}$ are shown in the left panel of Fig. 6.3 for the three models $b = 0$, 2 and 4. For $z^{\rm max}_{\rm int} \gtrsim 3.5$, all cases agree relatively well, up to fluctuations that can be attributed to uncertainties of the MCMC sampling compared to the true posterior. When the interaction is efficient at late times however, $z^{\rm max}_{\rm int} \ll 3.5$ well after recombination, the CMB probes the high-z tail of the interaction rate controlled by the b parameter and we expect the slope of the curves to differ. This can be discerned in the left panel of Fig. 6.3, however not in a very clear-cut manner due to the uncertainty of the sampled posteriors.

The posterior shows that neutrino interactions cannot be efficient for $10^{3.5} \lesssim z^{\rm max}_{\rm int} \lesssim 10^5$, consistent with our findings for the power-law scenarios. Moreover, we see that the amplitude is constrained to be $\Gamma/H|^{\rm max}_{\rm nfs} \sim 1$–$10$. Hence, even for interaction rates that are only sizable over a finite time interval, Planck CMB measurements constrain them within the freestreaming window.

In the right panel we plot the non-freestreaming interaction rates that saturate the 95 % C.L., combining both the power-law[3] and transient (using the best motivated value $b = 4$)

[3] The $n_{\rm int} = 3$ case is not shown as it is special in allowing for significant interactions due to degeneracies with n_s and A_s.

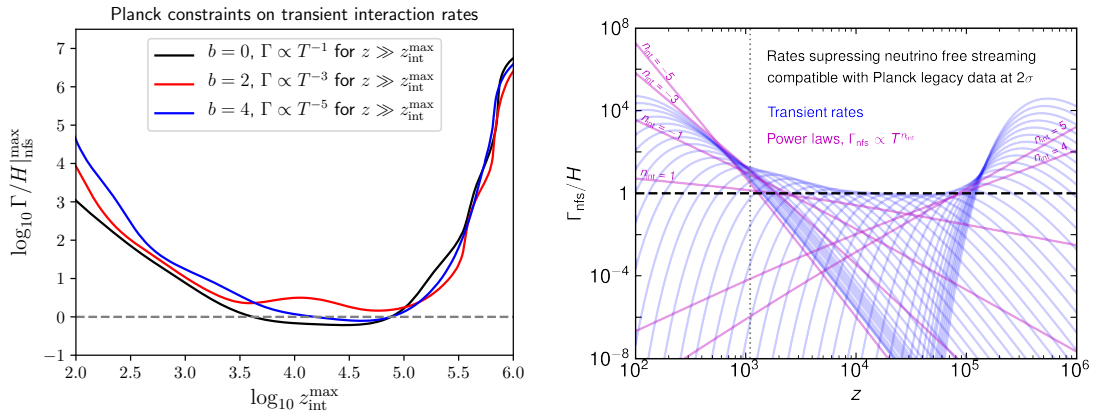

Figure 6.3: Freestreaming window depth. *Left:* 95 % C.L. bounds on $\Gamma/H|_{\rm nfs}^{\rm max}$ as a function of $z_{\rm int}^{\rm max}$ in the three transient models: $b = 0$, 2 and 4. They differ in the high-temperature limit $z \gg z_{\rm int}^{\rm max}$, being proportional to $\Gamma_{\rm nfs} \sim T^{-1}$, T^{-3} and T^{-5}, respectively. *Right:* Plot of the non-freestreaming interaction rates over the expansion rate using the parameters from the Planck+BAO 95 % C.L. bounds. The power-law interaction cases are displayed in magenta, while the transient rates are shown in blue ($b = 4$). The vertical dotted line indicate the redshift of recombination. Figure reprinted from Paper IV [47].

cases. At $z \simeq 10^5$, multiple blue lines (transient interactions) as well as the magenta lines $n_{\rm int} = 4$ and 5 meet, giving another affirmation that this is the upper bound of the freestreaming window. In the other limit of the freestreaming window $z \simeq 2000$, we see that the low-z power-law bounds meet, although $n_{\rm int} = -5$ has a slightly lower $z_{\rm int}$ bound. Curiously, the for the transient cases, the interaction rate is allowed to be somewhat larger, $\Gamma_{\rm nfs}/H \simeq 1$–10, in the range $z_{\rm int}^{\rm max} \simeq 1000$–5000. Nonetheless, slight preferences for neutrinos interactions at low redshift have been found previously in the literature [317, 322, 325, 332, 334, 335].

Hence, in addition to determining the window in which neutrino interactions cannot dampen neutrino anisotropic stress, with the exception of $n_{\rm int} = 3$, we have now seen that the interaction rate at most be at most within an order of magnitude of the Hubble rate in this window, given the Planck CMB measurements.

6.3 CMB Stage IV forecast

Building on the legacy of the Planck CMB measurements, the next generation CMB Stage IV experiments, such as the Simons Observatory [94], LiteBIRD [95] and CMB-S4 [86] are expected to yield noteworthy improvements, in particular by measuring the CMB polarization in greater detail as well as by significantly improving the precision of measurements of small-scale anisotropies. The difference between the precision of e.g. CMB-S4 and Planck can be appreciated for the TT power spectrum in Fig. 6.5, with the expected sensitivity of the former given by the black line and the error bars of the latter

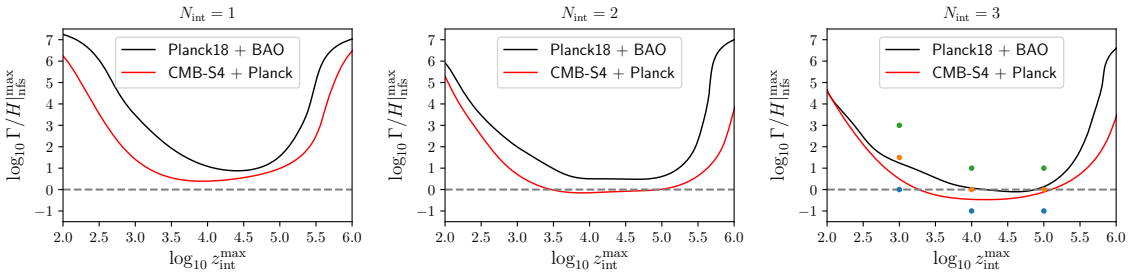

Figure 6.4: Depth of the freestreaming window for $N_{\rm int} = 1$ (left), 2 (middle) and 3 (right) interacting neutrinos. We show the 95 % C.L. bound on $\Gamma/H|^{\rm max}_{\rm nfs}$ as a function of $z^{\rm max}_{\rm int}$, from analysis of Planck+BAO (black) as well as from a forecast of CMB-S4 in combination with Planck. The colored points in the rightmost panel correspond to particular parameter combinations that we show in Fig. 6.5. Taken from Paper IV [47].

shown in gray. We discuss the figure in more detail below.

In light of this, it is appealing to examine in how far CMB Stage IV can further constrain non-standard neutrino interactions. We run again an analysis with `CLASS` and `MontePython`, but using a likelihood with a fiducial ΛCDM cosmology and the expected noise of the CMB-S4 experiment, as described in Ref. [37]. Being ground based, CMB-S4 (and other ground based missions) provide complementary information to space based experiments, in particular by optimizing the measurements for small angular scales. It is therefore useful to combine experiments. In addition to the CMB-S4 likelihood, we add a fake, Planck-like likelihood, assuming for simplicity no overlap between the experiments. Following Ref. [37], we assume that CMB-S4 measures 40 % of the sky for both temperature and polarization multipoles $51 < l < 3000$, and combine this with a fake Planck likelihood with $f_{\rm sky} = 0.57$ for $2 < l < 50$ and $f_{\rm sky} = 0.17$ for $51 < l < 3000$. We use the same priors for the cosmological parameters as in the previous section.

One can imagine scenarios in which only one or two of the neutrino species are interacting. For the transient interaction rates, we therefore analyze models in which only $N_{\rm int} = 1$ or $N_{\rm int} = 2$ neutrinos are interacting (and the remaining neutrino species are SM ones), using both the full Planck+BAO data as well as the forecasted CMB-S4 likelihood.

In Fig. 6.4, we show the 95 % C.L. bound on the non-freestreaming interaction amplitude $\Gamma/H|^{\rm max}_{\rm nfs}$ as a function of the interaction redshift $z^{\rm max}_{\rm int}$ in models in which $N_{\rm int} = 1$, 2, and 3 neutrinos are interacting (transient rate with $b = 4$). The bounds are shown for both Planck+BAO and CMB-S4. We find that CMB-S4 can typically tighten the bound on $\Gamma/H|^{\rm max}_{\rm nfs}$ by an order of magnitude, depending on the redshift of interaction as well as the number of interacting neutrinos. Moreover, not too surprisingly, increasing the number of interacting neutrinos makes the bounds more stringent. For larger $z^{\rm max}_{\rm int}$, the effect of the interaction extends to higher l. Therefore, the increased sensitivity of CMB-S4 on small scales yields significantly improved constraints on high-z interactions. For interactions at low$-z$ the improvement over Planck is on the other hand small for $N_{\rm int} = 3$. Nevertheless, for $N_{\rm int} = 1$ and to some extent for $N_{\rm int} = 2$ the CMB-S4 tightens the bound across all

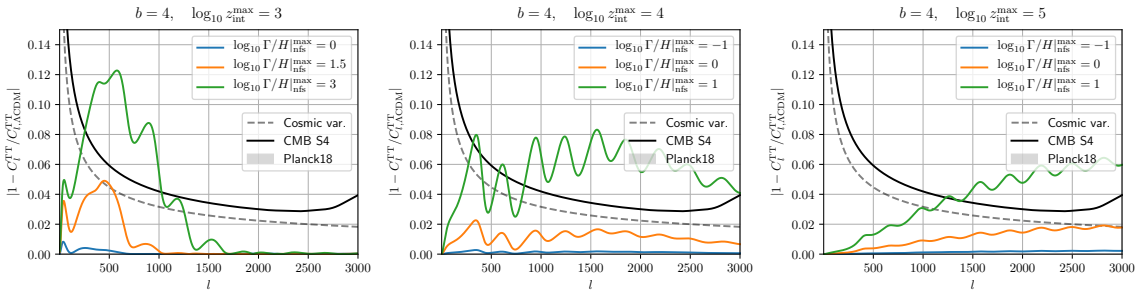

Figure 6.5: Relative difference between the temperature angular power spectra in the neutrino interaction scenarios with transient non-freestreaming rate and the ΛCDM model (fixed fiducial cosmological parameters and $\sum m_\nu = 0.06$ eV). The error bars from Planck 2018 is shown in gray, expected uncertainty for CMB-S4 with $f_{\rm sky} = 0.57$ is indicated by the black line and dashed gray line corresponds to the cosmic variance limit. Reprinted from Paper IV [47].

redshifts. The reason is that when only one species is interacting, the amplitude of the interaction is allowed to be much larger, which in turn means that the interaction is efficient over a longer period in time. Hence, for $N_{\rm int} = 1$, even for small $z_{\rm int}^{\rm max}$, the interaction considerably affects large multipoles, for which CMB-S4 has greater precision, leading to bounds that are more rigid compared to Planck.

To further illustrate the potential of CMB-S4 in constraining non-standard neutrino interactions, we show the relative difference of the temperature angular power spectra between transient interaction models ($b = 4$) and ΛCDM in Fig. 6.5. We recall from the beginning of this chapter that neutrino freestreaming dampens the acoustic peaks and shifts them to larger scales. Hence, non-standard neutrino interactions suppress freestreaming and "undo" these effects: the angular power is larger in the interacting cases (note however that this is not visible in Fig. 6.5 which shows the absolute, relative difference) and the peaks are shifted. Furthermore, for interactions efficient at high redshift, the higher multipoles that entered the horizon at early times are affected, while the low-z interactions influence mainly the lower multipoles. For each interaction redshift $z_{\rm int}^{\rm max}$, we show three amplitudes $\Gamma/H|_{\rm nfs}^{\rm max}$, one rejected by Planck, one which should be ruled out by CMB-S4 and one whose effect is smaller than cosmic variance. The parameter combinations are shown with corresponding colors in the rightmost panel of Fig. 6.4.

Since CMB-S4 has the greatest potential in further constraining neutrino interactions that are efficient at high redshift, we perform also CMB-S4 forecasts for the power-law models $n_{\rm int} = 3$ and $n_{\rm int} = 5$. The forecast yields the following 95 % C.L. bounds on $z_{\rm int}$:

$$n_{\rm int} = 3: \quad z_{\rm int} > 2.4 \times 10^5\,, \qquad\qquad n_{\rm int} = 5: \quad z_{\rm int} > 2.8 \times 10^5\,, \tag{6.10}$$

corresponding to an approximate factor 3 improvement in the latter case. For $n_{\rm int} = 3$, the lower bound is increased by two orders of magnitude, indicating that CMB-S4 can break the degeneracy between the neutrino interaction and n_s and A_s. Indeed, the full posterior including also those parameters reveals that this is the case; this is shown in Fig. 9 in Paper IV [47].

Hence, future Stage IV experiments that measure the CMB have the potential to further constrain scenarios with non-standard neutrino interactions. For transient non-freestreaming rates, we forecast an increased sensitivity of an order of magnitude for the interaction amplitude $\Gamma/H|^{\rm max}_{\rm nfs}$, depending on the interaction redshift and number of neutrinos interacting. Not surprisingly, when only $N_{\rm int} = 1$ or 2 neutrino species are interacting, the bounds are weaker. In these scenarios, CMB-S4 can largely improve the non-freestreaming constraints. Finally, we found that the $n_{\rm int} = 3$ scenario can be fully tested with CMB-S4.

Summary In the standard picture, neutrinos freestream ever since they decouple in the early Universe. While this is in agreement with cosmological data such as from CMB measurements, there are many particle physics models which predict interactions at lower temperatures $T_\nu < 2$ MeV. These models can be tested with CMB experiments, and in this chapter we took a broad, model-independent approach to determine a window in which neutrinos cannot interact given Planck CMB measurements. This *freestreaming window* is found to be $2000 \lesssim z \lesssim 10^5$, in which the non-freestreaming interaction can at most be of the order of the Hubble rate. An exception to this is the peculiar case $n_{\rm int} = 3$, which due to a similar temperature dependence as Hubble yields effects on a large range of multipoles, degenerate with the effect of changing the tilt and amplitude of the primordial power spectrum. Nevertheless, we show that the degeneracy can be broken by Stage IV CMB experiments, such that this scenario can be fully tested.

7 Conclusions and outlook

Cosmology has in the recent decades seen an immense increase in experimental data, allowing us to gain insights about the fundamental composition and evolution of the Universe. In particular, current and near-future surveys of the large-scale structure of the Universe can shed light on the properties of dark matter and dark energy, gravity on large scales, the initial conditions in the early Universe, as well as measure the absolute neutrino mass scale. The increased amount of observational data requires a considerable complementary theoretical effort in order to extract valueable information.

In this thesis, we have performed precision calculations of LSS observables, to assess the validity of common approximations and determine the reach of perturbation theory up to NNLO order. We employed cosmological perturbation theory in the Eulerian picture to model structure formation in the non-linear regime, $k \simeq 0.1$–$0.3h$ Mpc^{-1}. In the standard setup, the clustering dynamics is approximated by that of EdS and neutrinos are neglected beyond the linear level. To scrutinize these simplifications and describe structure formation in models with generic time- and scale-dependent growth, we extended Standard Perturbation Theory by allowing for multiple fields as well as promoting the linear evolution matrix Ω_{ab} to depend on time and scale. This extension is largely versatile and can be applied to a wide range of extended cosmological models. The computational complexity is however extensive, hence the framework is better suited to test and scrutinize approximations as well as extended cosmological models, than to analyze observational data.

We applied our generalized framework to the case of massive neutrinos in cosmological structure formation in Chapter 4. Neutrinos have a large velocity dispersion and can freestream over large distances. The corresponding distance, the freestreaming length, introduces a scale-dependence in the clustering dynamics of baryons and dark matter. We defined a hybrid, two-component fluid model featuring baryons and CDM coupled to neutrinos via gravity, and described two ways of modeling the neutrino sound velocity. This model is readily implemented in our extended framework for non-linear corrections in structure formation, and we computed the matter density and velocity power spectrum at NNLO. To assess the impact of full time- and scale-dependent dynamics, we compared our results to commonly adopted simplified treatments. The difference exceeds one percent at $k \gtrsim 0.17$ and $0.2h$ Mpc^{-1} ($M_\nu = 0.1$ eV) for the density and velocity power spectra, respectively. For the latter the discrepancy is strongly dependent on neutrino mass; for a larger $M_\nu = 0.4$ eV the difference is already 2.7 % at $k = 0.15h$ Mpc^{-1}. Finally, we compared both schemes to N-body simulations. For this purpose, we embedded the baryon+CDM and neutrino fluid model in an EFT framework. We showed that in the limit $k \gg k_{\rm FS}$, where $k_{\rm FS}$ is the neutrino freestreaming wavenumber, we can obtain a renormalized power spectrum at NNLO. Comparing to N-body results, we found that the mistake in the simplified treatment due to not capturing the time- and scale-dependence of the true dynamics could largely be absorbed by the counterterms introduced in the EFT, therefore both schemes could equally

well match the simulation result.

Since we found that the impact of exact time- and scale-dependence due to massive neutrinos to be largest for the velocity spectrum, we conclude that an exact treatment is required to exhaust the information on neutrino mass in redshift space. This motivates an analysis incorporating complete time- and scale-dependence in redshift space, which is left for future work. Moreover, the formalism can relatively straightforwardly be applied to assess the effect of massive neutrinos on the bispectrum beyond linear theory.

As a complementary statistical observable to the power spectrum, the bispectrum of LSS can be instrumental in breaking degeneracies between cosmological parameters and galaxy bias. Moreover, it is a very relevant statistic in probing deviations from Gaussian initial conditions, from which we can gain information about the physics of inflation. We derived the two-loop correction to the bispectrum in an EFT framework in Chapter 5, showing that adding it to the perturbative result extends the wavenumbers with percent accuracy from $k = 0.08$ to $0.15h$ Mpc^{-1}. We showed that the double-hard region of the two-loop correction can be renormalized by the counterterms introduced at one-loop in the EFT. The remaining UV-sensitivity of the two-loop term comes from the single-hard limit. We treated it in a simplified manner, computing the limit numerically and correcting the UV by a shift in the displacement dispersion associated with the hard loops. To assess the perturbative reach of the NLO and NNLO predictions, we compared to N-body simulations using gridPT to beat cosmic variance. Finally, we used the extension of SPT to calculate the one-loop correction to the bispectrum taking into account the exact time-dependence in ΛCDM. We found that the impact of exact kernels is broadly degenerate with the one-loop counterterms up to $k \simeq 0.15h$ Mpc^{-1} independent of shape. Since the range of scales in which we found the two-loop correction to become important is relevant for ongoing and future surveys, an extension to the bispectrum of biased tracers is appealing, and left for future work.

We have seen that neutrinos play a significant role in the evolution of the Universe. Consequently, cosmological probes can be used to investigate the properties of neutrinos. In Chapter 6, we took a global view of non-standard neutrino interactions in cosmology, aiming to establish a window of redshifts in which neutrinos are not allowed to interact significantly given measurements of the CMB by Planck. Freestreaming, non-interacting neutrinos leave a specific imprint on the angular power spectrum, and hence we found a freestreaming window $2000 \lesssim z \lesssim 10^5$ in which the neutrino interaction rate can be at most of the order of the Hubble rate. We made a forecast for the next generation CMB-S4 experiment, assuming a fiducial ΛCDM model with no interactions. Given the expected improved sensitivity on small scales, our results show that CMB-S4 extends the upper bound by an approximate factor of 3, as well as the depth of the freestreaming window by an order of magnitude. Finally, we analyzed a peculiar scenario in which the interaction rate scales as $\Gamma_{\rm nfs} \sim T^3$, i.e. close to the Hubble rate. Since this interaction influences the multipoles over a large range of scales, its impact can be corrected for by adjusting the amplitude and tilt of the primordial power spectrum. Due to this degeneracy, Planck data cannot rule out such an interaction in the redshift window. Nevertheless, when analyzing the model with the expected sensitivity of CMB-S4, the degeneracy is broken so that the model can be fully tested.

The uncovering of the freestreaming window can in particular be useful to guide model builders interested in non-standard neutrinos. Moreover, the modest preferences for interac-

tions in certain models can be explored in more detail with dedicated analyses in the future, for example by investigating which subset(s) of the data drive the preference.

Appendix A

Bispectrum: two-loop contributions and coefficients

The diagrammatical representation of the different contributions to the two-loop bispectrum are shown in Fig. A.1, and the corresponding mathematical expressions are [45] (see also Ref. [140]):

$$B^{611} = 90 P_0(k_B) P_0(k_C) \int_{\mathbf{q}_1,\mathbf{q}_2} F^{(6)}(-\mathbf{k}_B, -\mathbf{k}_C, \mathbf{q}_1, -\mathbf{q}_1, \mathbf{q}_2, -\mathbf{q}_2) P_0(q_1) P_0(q_2)\,, \tag{A.1a}$$

$$B^{(521-I)} = 60 P_0(k_C) \int_{\mathbf{q}_1,\mathbf{q}_2} F^{(5)}(-\mathbf{k}_C, -\mathbf{k}_B + \mathbf{q}_2, -\mathbf{q}_2, \mathbf{q}_1, -\mathbf{q}_1) F^{(2)}(\mathbf{k}_B - \mathbf{q}_2, \mathbf{q}_2) \times P_0(q_1) P_0(q_2) P_0(|\mathbf{k}_B - \mathbf{q}_2|)\,, \tag{A.1b}$$

$$B^{(521-II)} = 30 P_0(k_B) P_0(k_C) \int_{\mathbf{q}_1,\mathbf{q}_2} F^{(5)}(\mathbf{k}_A, \mathbf{q}_1, -\mathbf{q}_1, \mathbf{q}_2, -\mathbf{q}_2) F^{(2)}(-\mathbf{k}_A, -\mathbf{k}_C) \times P_0(q_1) P_0(q_2)\,, \tag{A.1c}$$

$$B^{(431-I)} = 36 P_0(k_C) \int_{\mathbf{q}_1,\mathbf{q}_2} F^{(4)}(\mathbf{k}_A + \mathbf{q}_1, -\mathbf{q}_1, \mathbf{q}_2, -\mathbf{q}_2) F^{(3)}(-\mathbf{k}_C, -\mathbf{k}_A - \mathbf{q}_1, \mathbf{q}_1) \times P_0(q_1) P_0(q_2) P_0(|\mathbf{k}_A + \mathbf{q}_1|)\,, \tag{A.1d}$$

$$B^{(431-II)} = 36 P_0(k_B) P_0(k_C) \int_{\mathbf{q}_1,\mathbf{q}_2} F^{(4)}(-\mathbf{k}_B, -\mathbf{k}_C, \mathbf{q}_1, -\mathbf{q}_1) F^{(3)}(\mathbf{k}_B, \mathbf{q}_2, -\mathbf{q}_2) \times P_0(q_1) P_0(q_2)\,, \tag{A.1e}$$

$$B^{(431-III)} = 24 P_0(k_C) \int_{\mathbf{q}_1,\mathbf{q}_2} F^{(4)}(-\mathbf{k}_C, -\mathbf{k}_B + \mathbf{q}_1 + \mathbf{q}_2, -\mathbf{q}_1, -\mathbf{q}_2) \times F^{(3)}(\mathbf{k}_B - \mathbf{q}_1 - \mathbf{q}_2, \mathbf{q}_1, \mathbf{q}_2) P_0(q_1) P_0(q_2) P_0(|\mathbf{k}_B - \mathbf{q}_1 - \mathbf{q}_2|)\,, \tag{A.1f}$$

$$B^{(332-I)} = 36 \int_{\mathbf{q}_1,\mathbf{q}_2} F^{(3)}(\mathbf{q}_1, \mathbf{k}_A - \mathbf{q}_1 + \mathbf{q}_2, -\mathbf{q}_2) F^{(3)}(-\mathbf{k}_A + \mathbf{q}_1 - \mathbf{q}_2, \mathbf{q}_2, -\mathbf{k}_C - \mathbf{q}_1) \times F^{(2)}(\mathbf{k}_C + \mathbf{q}_1, -\mathbf{q}_1) P_0(q_1) P_0(q_2) P_0(|\mathbf{k}_A - \mathbf{q}_1 + \mathbf{q}_2|) P_0(|\mathbf{k}_C + \mathbf{q}_1|)\,, \tag{A.1g}$$

$$B^{(332-II)} = 18P_0(k_B)P_0(k_C)\int_{\mathbf{q}_1,\mathbf{q}_2} F^{(3)}(\mathbf{k}_A,\mathbf{q}_1,-\mathbf{q}_1)F^{(3)}(\mathbf{k}_B,\mathbf{q}_2,-\mathbf{q}_2)F^{(2)}(-\mathbf{k}_A,-\mathbf{k}_B) \times P_0(q_1)P_0(q_2)\,, \tag{A.1h}$$

$$B^{(332-III)} = 18P_0(k_B)\int_{\mathbf{q}_1,\mathbf{q}_2} F^{(3)}(-\mathbf{k}_B,-\mathbf{k}_C+\mathbf{q}_2,-\mathbf{q}_2)F^{(3)}(\mathbf{k}_B,\mathbf{q}_1,-\mathbf{q}_1) \times F^{(2)}(\mathbf{k}_C-\mathbf{q}_2,\mathbf{q}_2)P_0(q_1)P_0(q_2)P_0(|\mathbf{k}_C-\mathbf{q}_2|)\,, \tag{A.1i}$$

$$B^{(422-I)} = 48\int_{\mathbf{q}_1,\mathbf{q}_2} F^{(4)}(\mathbf{q}_1,\mathbf{k}_A-\mathbf{q}_1,\mathbf{q}_2,-\mathbf{q}_2)F^{(2)}(-\mathbf{k}_A+\mathbf{q}_1,-\mathbf{k}_C-\mathbf{q}_1) \times F^{(2)}(\mathbf{k}_C+\mathbf{q}_1,-\mathbf{q}_1)P_0(q_1)P_0(q_2)P_0(|\mathbf{k}_C+\mathbf{q}_1|)P_0(|\mathbf{k}_A-\mathbf{q}_1|)\,, \tag{A.1j}$$

$$B^{(422-II)} = 48\int_{\mathbf{q}_1,\mathbf{q}_2} F^{(4)}(-\mathbf{k}_B+\mathbf{q}_1,-\mathbf{k}_C+\mathbf{q}_2,-\mathbf{q}_1,-\mathbf{q}_2)F^{(2)}(\mathbf{k}_B-\mathbf{q}_1,\mathbf{q}_1) \times F^{(2)}(\mathbf{k}_C-\mathbf{q}_2,\mathbf{q}_2)P_0(q_1)P_0(q_2)P_0(|\mathbf{k}_B-\mathbf{q}_1|)P_0(|\mathbf{k}_C-\mathbf{q}_2|)\,, \tag{A.1k}$$

where we used $F^{(1)}=1$ in EdS.

Table A.1: Coefficients of the shape functions $f^{(i)}$ when written as a linear combination of the basis shape functions b_j (defined in Eq. (5.11)) or equivalently in terms of E_i and Γ (defined in Eqs. (3.109) and (3.110)).

	$f^{(3)}$	$f^{(4)}$	$f^{(6,1)}$	$f^{(6,2)}$
b_1	$5/7$	$-\frac{4901}{339570}$	$-\frac{1394259753263}{1811404542543750}$	$\frac{104211446312}{11774129526534375}$
b_2	1	$-\frac{115739}{2037420}$	$-\frac{70647110404331}{23548259053068750}$	$-\frac{78591466504}{3924709842178125}$
b_3	$1/2$	$-\frac{61}{7560}$	$-\frac{11191}{38697750}$	0
b_4	$2/7$	$-\frac{1592}{56595}$	$-\frac{9685830431171}{7849419684356250}$	$-\frac{80969969032}{3924709842178125}$
b_5	0	$-\frac{12409}{1018710}$	$-\frac{10098786522983}{23548259053068750}$	$-\frac{41622522056}{11774129526534375}$
E_1	$-\frac{158092425677}{336403700758125}$	$\frac{664042208}{336403700758125}$	$-\frac{97}{231}$	$-\frac{1733}{436590}$
E_2	$-\frac{5853641823383}{47096518106137500}$	$-\frac{20811261028}{11774129526534375}$	$-\frac{12}{77}$	$-\frac{1457}{407484}$
E_3	$-\frac{28205520799243}{23548259053068750}$	$-\frac{34169022472}{905702271271875}$	$-\frac{68}{77}$	$-\frac{6997}{339570}$
Γ	$-\frac{11191}{19348875}$	0	1	$-\frac{61}{3780}$

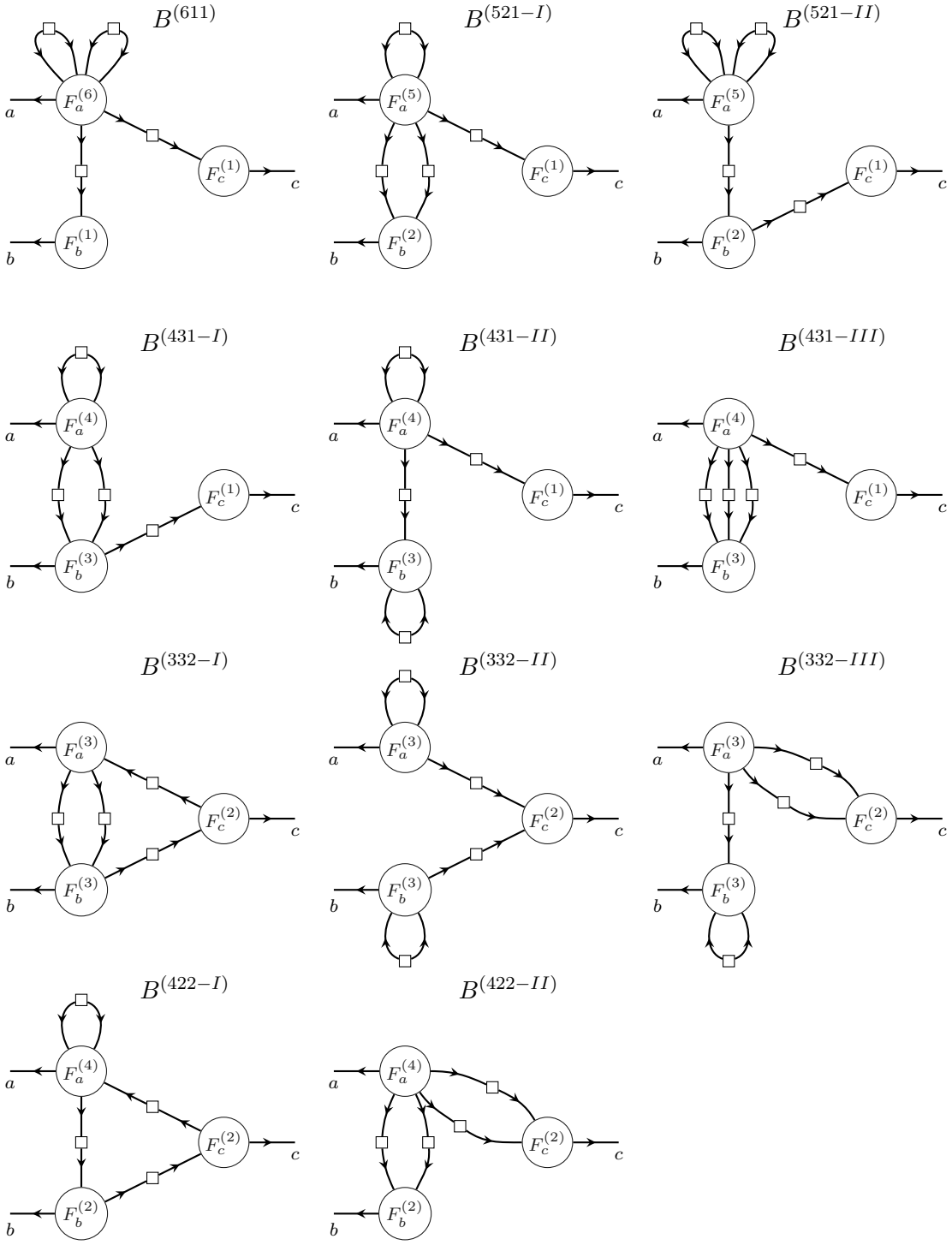

Figure A.1: Diagrams contributing to the two-loop bispectrum correction. The corresponding mathematical expressions are given in Eq. (A.1).

Bibliography

[1] A. Einstein, *The Foundation of the General Theory of Relativity*, *Annalen Phys.* **49** (1916) 769.

[2] S. Dodelson, *Modern Cosmology*. Academic Press, Amsterdam, 2003.

[3] M. S. Turner, *The Road to Precision Cosmology*, 2201.04741.

[4] K. Schmitz, *Modern Cosmology, an Amuse-Gueule*, 2203.04757.

[5] G. F. Smoot, C. L. Bennett, A. Kogut, E. L. Wright, J. Aymon, N. W. Boggess et al., *Structure in the COBE Differential Microwave Radiometer First-Year Maps*, *ApJ* **396** (1992) .

[6] WMAP collaboration, *Nine-Year Wilkinson Microwave Anisotropy Probe (WMAP) Observations: Cosmological Parameter Results*, *Astrophys. J. Suppl.* **208** (2013) 19 [1212.5226].

[7] Planck collaboration, *Planck 2015 results. XIII. Cosmological parameters*, *Astron. Astrophys.* **594** (2016) A13 [1502.01589].

[8] Planck collaboration, *Planck 2018 results. VI. Cosmological parameters*, *Astron. Astrophys.* **641** (2020) A6 [1807.06209].

[9] B. D. Fields, K. A. Olive, T.-H. Yeh and C. Young, *Big-Bang Nucleosynthesis after Planck*, *JCAP* **03** (2020) 010 [1912.01132].

[10] Supernova Search Team collaboration, *Observational evidence from supernovae for an accelerating universe and a cosmological constant*, *Astron. J.* **116** (1998) 1009 [astro-ph/9805201].

[11] Supernova Cosmology Project collaboration, *Measurements of Ω and Λ from 42 high redshift supernovae*, *Astrophys. J.* **517** (1999) 565 [astro-ph/9812133].

[12] SDSS collaboration, *The Sloan Digital Sky Survey: Technical Summary*, *Astron. J.* **120** (2000) 1579 [astro-ph/0006396].

[13] LIGO Scientific, Virgo collaboration, *Observation of Gravitational Waves from a Binary Black Hole Merger*, *Phys. Rev. Lett.* **116** (2016) 061102 [1602.03837].

[14] LISA collaboration, *Laser Interferometer Space Antenna*, 1702.00786.

[15] H. Atek, M. Shuntov, L. J. Furtak, J. Richard, J.-P. Kneib, G. Mahler Adi Zitrin et al., *Revealing Galaxy Candidates out to $z \sim 16$ with JWST Observations of the Lensing Cluster SMACS0723*, *arXiv e-prints* (2022) [2207.12338].

[16] P. J. Peebles, *Principles of physical cosmology*. Princeton University Press, 1994.

[17] V. Mukhanov, *Physical Foundations of Cosmology*. Cambridge University Press, Oxford, 2005, 10.1017/CBO9780511790553.

[18] S. Weinberg, *Cosmology*. 2008.

[19] Euclid Theory Working Group collaboration, *Cosmology and fundamental physics with the Euclid satellite*, *Living Rev. Rel.* **16** (2013) 6 [1206.1225].

[20] L. Amendola et al., *Cosmology and fundamental physics with the Euclid satellite*, *Living Rev. Rel.* **21** (2018) 2 [1606.00180].

[21] DESI collaboration, *The Dark Energy Spectroscopic Instrument (DESI)*, 1907.10688.

[22] LSST collaboration, *LSST: from Science Drivers to Reference Design and Anticipated Data Products*, *Astrophys. J.* **873** (2019) 111 [0805.2366].

[23] PFS Team collaboration, *Extragalactic science, cosmology, and Galactic archaeology with the Subaru Prime Focus Spectrograph*, *Publ. Astron. Soc. Jap.* **66** (2014) R1 [1206.0737].

[24] O. Doré et al., *Cosmology with the SPHEREX All-Sky Spectral Survey*, 1412.4872.

[25] D. Spergel et al., *Wide-Field InfrarRed Survey Telescope-Astrophysics Focused Telescope Assets WFIRST-AFTA 2015 Report*, 1503.03757.

[26] F. Bernardeau, S. Colombi, E. Gaztanaga and R. Scoccimarro, *Large scale structure of the universe and cosmological perturbation theory*, *Phys. Rept.* **367** (2002) 1 [astro-ph/0112551].

[27] M. M. Ivanov, M. Simonović and M. Zaldarriaga, *Cosmological Parameters from the BOSS Galaxy Power Spectrum*, *JCAP* **05** (2020) 042 [1909.05277].

[28] G. D'Amico, J. Gleyzes, N. Kokron, K. Markovic, L. Senatore, P. Zhang et al., *The Cosmological Analysis of the SDSS/BOSS data from the Effective Field Theory of Large-Scale Structure*, *JCAP* **05** (2020) 005 [1909.05271].

[29] T. Tröster et al., *Cosmology from large-scale structure: Constraining ΛCDM with BOSS*, *Astron. Astrophys.* **633** (2020) L10 [1909.11006].

[30] J. Lesgourgues, G. Mangano, G. Miele and S. Pastor, *Neutrino Cosmology*. Cambridge University Press, 2, 2013.

[31] I. Esteban, M. C. Gonzalez-Garcia, M. Maltoni, T. Schwetz and A. Zhou, *The fate of hints: updated global analysis of three-flavor neutrino oscillations*, *JHEP* **09** (2020) 178 [2007.14792].

[32] J. Lesgourgues and S. Pastor, *Massive neutrinos and cosmology*, *Phys. Rept.* **429** (2006) 307 [astro-ph/0603494].

[33] B. Audren, J. Lesgourgues, S. Bird, M. G. Haehnelt and M. Viel, *Neutrino masses and cosmological parameters from a Euclid-like survey: Markov Chain Monte Carlo forecasts including theoretical errors*, *JCAP* **01** (2013) 026 [1210.2194].

[34] A. Boyle and E. Komatsu, *Deconstructing the neutrino mass constraint from galaxy redshift surveys*, *JCAP* **03** (2018) 035 [1712.01857].

[35] S. Mishra-Sharma, D. Alonso and J. Dunkley, *Neutrino masses and beyond- ΛCDM cosmology with LSST and future CMB experiments*, *Phys. Rev. D* **97** (2018) 123544 [1803.07561].

[36] T. Sprenger, M. Archidiacono, T. Brinckmann, S. Clesse and J. Lesgourgues, *Cosmology in the era of Euclid and the Square Kilometre Array*, *JCAP* **02** (2019) 047 [1801.08331].

[37] T. Brinckmann, D. C. Hooper, M. Archidiacono, J. Lesgourgues and T. Sprenger, *The promising future of a robust cosmological neutrino mass measurement*, *JCAP* **01** (2019) 059 [1808.05955].

[38] A. Chudaykin and M. M. Ivanov, *Measuring neutrino masses with large-scale structure: Euclid forecast with controlled theoretical error*, *JCAP* **11** (2019) 034 [1907.06666].

[39] C. Hahn, F. Villaescusa-Navarro, E. Castorina and R. Scoccimarro, *Constraining M_ν with the bispectrum. Part I. Breaking parameter degeneracies*, *JCAP* **03** (2020) 040 [1909.11107].

[40] W. L. Xu, N. DePorzio, J. B. Muñoz and C. Dvorkin, *Accurately Weighing Neutrinos with Cosmological Surveys*, *Phys. Rev. D* **103** (2021) 023503 [2006.09395].

[41] A. Boyle and F. Schmidt, *Neutrino mass constraints beyond linear order: cosmology dependence and systematic biases*, *JCAP* **04** (2021) 022 [2011.10594].

[42] S. Bashinsky and U. Seljak, *Neutrino perturbations in CMB anisotropy and matter clustering*, *Phys. Rev. D* **69** (2004) 083002 [astro-ph/0310198].

[43] B. Follin, L. Knox, M. Millea and Z. Pan, *First Detection of the Acoustic Oscillation Phase Shift Expected from the Cosmic Neutrino Background*, *Phys. Rev. Lett.* **115** (2015) 091301 [1503.07863].

[44] M. Garny and P. Taule, *Loop corrections to the power spectrum for massive neutrino cosmologies with full time- and scale-dependence*, *JCAP* **01** (2021) 020 [2008.00013].

[45] T. Baldauf, M. Garny, P. Taule and T. Steele, *Two-loop bispectrum of large-scale structure*, *Phys. Rev. D* **104** (2021) 123551 [2110.13930].

[46] M. Garny and P. Taule, *Two-loop power spectrum with full time- and scale-dependence and EFT corrections: impact of massive neutrinos and going beyond EdS*, *JCAP* **09** (2022) 054 [2205.11533].

[47] P. Taule, M. Escudero and M. Garny, *Global view of neutrino interactions in cosmology: The freestreaming window as seen by Planck*, *Phys. Rev. D* **106** (2022) 063539 [2207.04062].

[48] E. Hubble, *A relation between distance and radial velocity among extra-galactic nebulae*, *Proc. Nat. Acad. Sci.* **15** (1929) 168.

[49] R. A. Alpher, H. Bethe and G. Gamow, *The origin of chemical elements*, *Phys. Rev.* **73** (1948) 803.

[50] A. A. Penzias and R. W. Wilson, *A Measurement of Excess Antenna Temperature at 4080 Mc/s.*, *ApJ* **142** (1965) 419.

[51] E. W. Kolb and M. S. Turner, *The Early Universe*, vol. 69. 1990, 10.1201/9780429492860.

[52] S. M. Carroll, *Spacetime and Geometry*. Cambridge University Press, 7, 2019.

[53] A. Friedmann, *On the Possibility of a world with constant negative curvature of space*, *Z. Phys.* **21** (1924) 326.

[54] G. Lemaitre, *A Homogeneous Universe of Constant Mass and Growing Radius Accounting for the Radial Velocity of Extragalactic Nebulae*, *Annales Soc. Sci. Bruxelles A* **47** (1927) 49.

[55] H. P. Robertson, *Kinematics and World-Structure*, *Astrophys. J.* **82** (1935) 284.

[56] A. G. Walker, *On milne's theory of world-structure**, *Proceedings of the London Mathematical Society* **s2-42** (1937) 90 [https://londmathsoc.onlinelibrary.wiley.com/doi/pdf/10.1112/plms/s2-42.1.90].

[57] G. Jungman, M. Kamionkowski and K. Griest, *Supersymmetric dark matter*, *Phys. Rept.* **267** (1996) 195 [hep-ph/9506380].

[58] L. Bergström, *Nonbaryonic dark matter: Observational evidence and detection methods*, *Rept. Prog. Phys.* **63** (2000) 793 [hep-ph/0002126].

[59] G. Bertone, D. Hooper and J. Silk, *Particle dark matter: Evidence, candidates and constraints*, *Phys. Rept.* **405** (2005) 279 [hep-ph/0404175].

[60] J. L. Feng, *Dark Matter Candidates from Particle Physics and Methods of Detection*, *Ann. Rev. Astron. Astrophys.* **48** (2010) 495 [1003.0904].

[61] S. Weinberg, *The Cosmological Constant Problem*, *Rev. Mod. Phys.* **61** (1989) 1.

[62] P. J. E. Peebles and B. Ratra, *The Cosmological Constant and Dark Energy*, *Rev. Mod. Phys.* **75** (2003) 559 [astro-ph/0207347].

[63] S. Nojiri and S. D. Odintsov, *Introduction to modified gravity and gravitational alternative for dark energy*, *eConf* **C0602061** (2006) 06 [hep-th/0601213].

[64] T. Clifton, P. G. Ferreira, A. Padilla and C. Skordis, *Modified Gravity and Cosmology*, *Phys. Rept.* **513** (2012) 1 [1106.2476].

[65] A. Joyce, L. Lombriser and F. Schmidt, *Dark Energy Versus Modified Gravity*, *Ann. Rev. Nucl. Part. Sci.* **66** (2016) 95 [1601.06133].

[66] L. Verde, T. Treu and A. G. Riess, *Tensions between the Early and the Late Universe*, *Nature Astron.* **3** (2019) 891 [1907.10625].

[67] E. Di Valentino, O. Mena, S. Pan, L. Visinelli, W. Yang, A. Melchiorri et al., *In the realm of the Hubble tension—a review of solutions*, *Class. Quant. Grav.* **38** (2021) 153001 [2103.01183].

[68] D. J. Fixsen, E. S. Cheng, J. M. Gales, J. C. Mather, R. A. Shafer and E. L. Wright, *The Cosmic Microwave Background spectrum from the full COBE FIRAS data set*, *Astrophys. J.* **473** (1996) 576 [astro-ph/9605054].

[69] R. Barkana and A. Loeb, *In the beginning: The First sources of light and the reionization of the Universe*, *Phys. Rept.* **349** (2001) 125 [astro-ph/0010468].

[70] A. A. Starobinsky, *Spectrum of relict gravitational radiation and the early state of the universe*, *JETP Lett.* **30** (1979) 682.

[71] A. H. Guth, *The Inflationary Universe: A Possible Solution to the Horizon and Flatness Problems*, *Phys. Rev. D* **23** (1981) 347.

[72] V. F. Mukhanov and G. V. Chibisov, *Quantum Fluctuations and a Nonsingular Universe*, *JETP Lett.* **33** (1981) 532.

[73] A. D. Linde, *A New Inflationary Universe Scenario: A Possible Solution of the Horizon, Flatness, Homogeneity, Isotropy and Primordial Monopole Problems*, *Phys. Lett. B* **108** (1982) 389.

[74] A. R. Liddle and D. H. Lyth, *Cosmological Inflation and Large-Scale Structure*. Cambridge University Press, 2000, 10.1017/CBO9781139175180.

[75] D. H. Lyth and A. R. Liddle, *The Primordial Density Perturbation: Cosmology, Inflation and the Origin of Structure*. Cambridge University Press, 2009, 10.1017/CBO9780511819209.

[76] D. Baumann, *Inflation*, in *Theoretical Advanced Study Institute in Elementary Particle Physics: Physics of the Large and the Small*, pp. 523–686, 2011, DOI [0907.5424].

[77] J. Martin, C. Ringeval and V. Vennin, *Encyclopædia Inflationaris*, *Phys. Dark Univ.* **5-6** (2014) 75 [1303.3787].

[78] A. Linde, *Inflationary Cosmology after Planck 2013*, in *100e Ecole d'Ete de Physique: Post-Planck Cosmology*, pp. 231–316, 2015, DOI [1402.0526].

[79] A. G. Cohen, D. B. Kaplan and A. E. Nelson, *Progress in electroweak baryogenesis*, *Ann. Rev. Nucl. Part. Sci.* **43** (1993) 27 [hep-ph/9302210].

[80] V. A. Rubakov and M. E. Shaposhnikov, *Electroweak baryon number nonconservation in the early universe and in high-energy collisions*, *Usp. Fiz. Nauk* **166** (1996) 493 [hep-ph/9603208].

[81] M. Trodden, *Electroweak baryogenesis*, *Rev. Mod. Phys.* **71** (1999) 1463 [hep-ph/9803479].

[82] A. Riotto, *Theories of baryogenesis*, in *ICTP Summer School in High-Energy Physics and Cosmology*, pp. 326–436, 7, 1998, hep-ph/9807454.

[83] J. R. Gott, III, M. Juric, D. Schlegel, F. Hoyle, M. Vogeley, M. Tegmark et al., *A map of the universe*, *Astrophys. J.* **624** (2005) 463 [astro-ph/0310571].

[84] L. G. Balazs, Z. Bagoly, J. E. Hakkila, I. Horvath, J. Kobori, I. Racz et al., *A giant ring-like structure at $0.78 < z < 0.86$ displayed by GRBs*, *Mon. Not. Roy. Astron. Soc.* **452** (2015) 2236 [1507.00675].

[85] BOSS collaboration, *The clustering of galaxies in the completed SDSS-III Baryon Oscillation Spectroscopic Survey: cosmological analysis of the DR12 galaxy sample*, *Mon. Not. Roy. Astron. Soc.* **470** (2017) 2617 [1607.03155].

[86] CMB-S4 collaboration, *CMB-S4 Science Book, First Edition*, 1610.02743.

[87] Planck collaboration, *Planck 2018 results. X. Constraints on inflation*, *Astron. Astrophys.* **641** (2020) A10 [1807.06211].

[88] Planck collaboration, *Planck 2018 results. IX. Constraints on primordial non-Gaussianity*, *Astron. Astrophys.* **641** (2020) A9 [1905.05697].

[89] P. J. Peebles, *The Large-scale Structure of the Universe*, Princeton Series in Physics. Princeton University Press, 1980.

[90] J. Lesgourgues, *The Cosmic Linear Anisotropy Solving System (CLASS) I: Overview*, 1104.2932.

[91] D. Blas, J. Lesgourgues and T. Tram, *The Cosmic Linear Anisotropy Solving System (CLASS) II: Approximation schemes*, *JCAP* **07** (2011) 034 [1104.2933].

[92] A. Lewis, A. Challinor and A. Lasenby, *Efficient computation of CMB anisotropies in closed FRW models*, *Astrophys. J.* **538** (2000) 473 [astro-ph/9911177].

[93] J. Lesgourgues and T. Tram, *The Cosmic Linear Anisotropy Solving System (CLASS) IV: efficient implementation of non-cold relics*, *JCAP* **09** (2011) 032 [1104.2935].

[94] Simons Observatory collaboration, *The Simons Observatory: Science goals and forecasts*, *JCAP* **02** (2019) 056 [1808.07445].

[95] LiteBIRD collaboration, *LiteBIRD: JAXA's new strategic L-class mission for all-sky surveys of cosmic microwave background polarization*, *Proc. SPIE Int. Soc. Opt. Eng.* **11443** (2020) 114432F [2101.12449].

[96] CORE collaboration, *Exploring cosmic origins with CORE: Survey requirements and mission design*, *JCAP* **04** (2018) 014 [1706.04516].

[97] B. M. Sutin et al., *PICO - the probe of inflation and cosmic origins*, *Proc. SPIE Int. Soc. Opt. Eng.* **10698** (2018) 106984F [1808.01368].

[98] B. De Finetti, *Theory of Probability: A Critical Introductory Treatment*, Wiley Series in Probability and Statistics. John Wiley & Sons, Inc., 2017, 10.1002/9781119286387.

[99] G. D'Agostini, *Probability and measurement uncertainty in physics: A Bayesian primer*, hep-ph/9512295.

[100] R. Trotta, *Bayes in the sky: Bayesian inference and model selection in cosmology*, *Contemp. Phys.* **49** (2008) 71 [0803.4089].

[101] L. Verde, *Statistical methods in cosmology*, *Lect. Notes Phys.* **800** (2010) 147 [0911.3105].

[102] G. Efstathiou, *The Statistical significance of the low CMB multipoles*, *Mon. Not. Roy. Astron. Soc.* **346** (2003) L26 [astro-ph/0306431].

[103] A. Lewis and S. Bridle, *Cosmological parameters from CMB and other data: A Monte Carlo approach*, *Phys. Rev. D* **66** (2002) 103511 [astro-ph/0205436].

[104] B. Audren, J. Lesgourgues, K. Benabed and S. Prunet, *Conservative Constraints on Early Cosmology: an illustration of the Monte Python cosmological parameter inference code*, *JCAP* **1302** (2013) 001 [1210.7183].

[105] T. Brinckmann and J. Lesgourgues, *MontePython 3: boosted MCMC sampler and other features*, *Phys. Dark Univ.* **24** (2019) 100260 [1804.07261].

[106] S. Brooks, A. Gelman, G. Jones and X.-L. Meng, *Handbook of Markov Chain Monte Carlo*. Chapman and Hall/CRC, 2011.

[107] N. Metropolis, A. W. Rosenbluth, M. N. Rosenbluth, A. H. Teller and E. Teller, *Equation of state calculations by fast computing machines*, *J. Chem. Phys.* **21** (1953) 1087.

[108] W. K. Hastings, *Monte Carlo sampling methods using Markov chains and their applications*, *Biometrika* **57** (1970) 97 [https://academic.oup.com/biomet/article-pdf/57/1/97/23940249/57-1-97.pdf].

[109] M. A. Amin et al., *Snowmass2021 Theory Frontier White Paper: Data-Driven Cosmology*, in *2022 Snowmass Summer Study*, 3, 2022, 2203.07946.

[110] J. Huchra, M. Davis, D. Latham and J. Tonry, *A survey of galaxy redshifts: 4. The data.*, *Astrophys. J. Suppl.* **52** (1983) L89.

[111] 2dFGRS collaboration, *The 2dF Galaxy Redshift Survey: Power-spectrum analysis of the final dataset and cosmological implications*, *Mon. Not. Roy. Astron. Soc.* **362** (2005) 505 [astro-ph/0501174].

[112] M. Colless et al., *The 2dF Galaxy Redshift Survey: Final data release*, astro-ph/0306581.

[113] V. Springel, C. S. Frenk and S. D. M. White, *The large-scale structure of the Universe*, *Nature* **440** (2006) 1137 [astro-ph/0604561].

[114] D. H. Jones et al., *The 6dF Galaxy Survey: Final Redshift Release (DR3) and Southern Large-Scale Structures*, *Mon. Not. Roy. Astron. Soc.* **399** (2009) 683 [0903.5451].

[115] F. Beutler, C. Blake, M. Colless, D. H. Jones, L. Staveley-Smith, L. Campbell et al., *The 6dF Galaxy Survey: Baryon Acoustic Oscillations and the Local Hubble Constant*, *Mon. Not. Roy. Astron. Soc.* **416** (2011) 3017 [1106.3366].

[116] M. J. Drinkwater et al., *The WiggleZ Dark Energy Survey: Survey Design and First Data Release*, *Mon. Not. Roy. Astron. Soc.* **401** (2010) 1429 [0911.4246].

[117] C. Blake et al., *The WiggleZ Dark Energy Survey: mapping the distance-redshift relation with baryon acoustic oscillations*, *Mon. Not. Roy. Astron. Soc.* **418** (2011) 1707 [1108.2635].

[118] BOSS collaboration, *The Baryon Oscillation Spectroscopic Survey of SDSS-III*, *Astron. J.* **145** (2013) 10 [1208.0022].

[119] SDSS collaboration, *SDSS-III: Massive Spectroscopic Surveys of the Distant Universe, the Milky Way Galaxy, and Extra-Solar Planetary Systems*, *Astron. J.* **142** (2011) 72 [1101.1529].

[120] BOSS collaboration, *The clustering of galaxies in the SDSS-III Baryon Oscillation Spectroscopic Survey: baryon acoustic oscillations in the Data Releases 10 and 11 Galaxy samples*, *Mon. Not. Roy. Astron. Soc.* **441** (2014) 24 [1312.4877].

[121] BOSS collaboration, *The clustering of galaxies in the completed SDSS-III Baryon Oscillation Spectroscopic Survey: Observational systematics and baryon acoustic oscillations in the correlation function*, *Mon. Not. Roy. Astron. Soc.* **464** (2017) 1168 [1607.03145].

[122] K. S. Dawson et al., *The SDSS-IV extended Baryon Oscillation Spectroscopic Survey: Overview and Early Data*, *Astron. J.* **151** (2016) 44 [1508.04473].

[123] eBOSS collaboration, *Completed SDSS-IV extended Baryon Oscillation Spectroscopic Survey: Cosmological implications from two decades of spectroscopic surveys at the Apache Point Observatory*, *Phys. Rev. D* **103** (2021) 083533 [2007.08991].

[124] DESI collaboration, *The DESI Experiment Part I: Science,Targeting, and Survey Design*, 1611.00036.

[125] Astro-WISE, KiDS collaboration, *The Kilo-Degree Survey*, *Exper. Astron.* **35** (2013) 25 [1206.1254].

[126] KiDS collaboration, *KiDS-1000 Cosmology: Cosmic shear constraints and comparison between two point statistics*, *Astron. Astrophys.* **645** (2021) A104 [2007.15633].

[127] DES collaboration, *The dark energy survey*, astro-ph/0510346.

[128] DES collaboration, *Dark Energy Survey year 1 results: Cosmological constraints from galaxy clustering and weak lensing*, *Phys. Rev. D* **98** (2018) 043526 [1708.01530].

[129] H. Aihara et al., *The Hyper Suprime-Cam SSP Survey: Overview and Survey Design*, *Publ. Astron. Soc. Jap.* **70** (2018) S4 [1704.05858].

[130] M. Rauch, *The lyman alpha forest in the spectra of quasistellar objects*, *Ann. Rev. Astron. Astrophys.* **36** (1998) 267 [astro-ph/9806286].

[131] BOSS collaboration, *Quasar-Lyman α Forest Cross-Correlation from BOSS DR11 : Baryon Acoustic Oscillations*, *JCAP* **05** (2014) 027 [1311.1767].

[132] J. E. Bautista et al., *Measurement of baryon acoustic oscillation correlations at $z = 2.3$ with SDSS DR12 Lyα-Forests*, *Astron. Astrophys.* **603** (2017) A12 [1702.00176].

[133] H. du Mas des Bourboux et al., *The Completed SDSS-IV Extended Baryon Oscillation Spectroscopic Survey: Baryon Acoustic Oscillations with Lyα Forests*, *Astrophys. J.* **901** (2020) 153 [2007.08995].

[134] WMAP collaboration, *Five-Year Wilkinson Microwave Anisotropy Probe (WMAP) Observations: Cosmological Interpretation*, *Astrophys. J. Suppl.* **180** (2009) 330 [0803.0547].

[135] F. R. Bouchet, *Introductory overview of Eulerian and Lagrangian perturbation theories*, in *International School of Physics, 'Enrico Fermi', Course 132: Dark Matter in the Universe*, pp. 565–599, 7, 1995, astro-ph/9603013.

[136] F. Bernardeau, *The evolution of the large-scale structure of the universe: beyond the linear regime*, in *100e Ecole d'Ete de Physique: Post-Planck Cosmology*, pp. 17–79, 2015, DOI [1311.2724].

[137] V. Desjacques, D. Jeong and F. Schmidt, *Large-Scale Galaxy Bias*, *Phys. Rept.* **733** (2018) 1 [1611.09787].

[138] D. Blas, M. Garny and T. Konstandin, *Cosmological perturbation theory at three-loop order*, *JCAP* **01** (2014) 010 [1309.3308].

[139] T. Konstandin, R. A. Porto and H. Rubira, *The effective field theory of large scale structure at three loops*, *JCAP* **11** (2019) 027 [1906.00997].

[140] A. Lazanu and M. Liguori, *The two and three-loop matter bispectrum in perturbation theories*, *JCAP* **04** (2018) 055 [1803.03184].

[141] R. Scoccimarro, H. M. P. Couchman and J. A. Frieman, *The Bispectrum as a Signature of Gravitational Instability in Redshift-Space*, *Astrophys. J.* **517** (1999) 531 [astro-ph/9808305].

[142] R. Scoccimarro, *Redshift-space distortions, pairwise velocities and nonlinearities*, *Phys. Rev. D* **70** (2004) 083007 [astro-ph/0407214].

[143] Z. Vlah, U. Seljak, P. McDonald, T. Okumura and T. Baldauf, *Distribution function approach to redshift space distortions. Part IV: perturbation theory applied to dark matter*, *JCAP* **11** (2012) 009 [1207.0839].

[144] D. Baumann, A. Nicolis, L. Senatore and M. Zaldarriaga, *Cosmological Non-Linearities as an Effective Fluid*, *JCAP* **07** (2012) 051 [1004.2488].

[145] J. J. M. Carrasco, M. P. Hertzberg and L. Senatore, *The Effective Field Theory of Cosmological Large Scale Structures*, *JHEP* **09** (2012) 082 [1206.2926].

[146] L. Senatore and M. Zaldarriaga, *The IR-resummed Effective Field Theory of Large Scale Structures*, *JCAP* **02** (2015) 013 [1404.5954].

[147] T. Baldauf, M. Mirbabayi, M. Simonović and M. Zaldarriaga, *Equivalence Principle and the Baryon Acoustic Peak*, *Phys. Rev. D* **92** (2015) 043514 [1504.04366].

[148] Z. Vlah, U. Seljak, M. Y. Chu and Y. Feng, *Perturbation theory, effective field theory, and oscillations in the power spectrum*, *JCAP* **03** (2016) 057 [1509.02120].

[149] D. Blas, M. Garny, M. M. Ivanov and S. Sibiryakov, *Time-Sliced Perturbation Theory II: Baryon Acoustic Oscillations and Infrared Resummation*, *JCAP* **07** (2016) 028 [1605.02149].

[150] J. E. McEwen, X. Fang, C. M. Hirata and J. A. Blazek, *FAST-PT: a novel algorithm to calculate convolution integrals in cosmological perturbation theory*, *JCAP* **09** (2016) 015 [1603.04826].

[151] M. Simonović, T. Baldauf, M. Zaldarriaga, J. J. Carrasco and J. A. Kollmeier, *Cosmological perturbation theory using the FFTLog: formalism and connection to QFT loop integrals*, *JCAP* **04** (2018) 030 [1708.08130].

[152] M. Schmittfull, Z. Vlah and P. McDonald, *Fast large scale structure perturbation theory using one-dimensional fast Fourier transforms*, *Phys. Rev. D* **93** (2016) 103528 [1603.04405].

[153] F. Montesano, A. G. Sanchez and S. Phleps, *Cosmological implications from the full shape of the large-scale power spectrum of the SDSS DR7 luminous red galaxies*, *Mon. Not. Roy. Astron. Soc.* **421** (2012) 2656 [1107.4097].

[154] A. G. Sanchez et al., *The clustering of galaxies in the SDSS-III Baryon Oscillation Spectroscopic Survey: cosmological constraints from the full shape of the clustering wedges*, *Mon. Not. Roy. Astron. Soc.* **433** (2013) 1202 [1303.4396].

[155] A. G. Sanchez et al., *The clustering of galaxies in the SDSS-III Baryon Oscillation Spectroscopic Survey: cosmological implications of the full shape of the clustering wedges in the data release 10 and 11 galaxy samples*, *Mon. Not. Roy. Astron. Soc.* **440** (2014) 2692 [1312.4854].

[156] A. Semenaite et al., *Cosmological implications of the full shape of anisotropic clustering measurements in BOSS and eBOSS*, *Mon. Not. Roy. Astron. Soc.* **512** (2022) 5657 [2111.03156].

[157] S.-F. Chen, Z. Vlah and M. White, *A new analysis of galaxy 2-point functions in the BOSS survey, including full-shape information and post-reconstruction BAO*, *JCAP* **02** (2022) 008 [2110.05530].

[158] H. Gil-Marín, W. J. Percival, L. Verde, J. R. Brownstein, C.-H. Chuang, F.-S. Kitaura et al., *The clustering of galaxies in the SDSS-III Baryon Oscillation Spectroscopic Survey: RSD measurement from the power spectrum and bispectrum of the DR12 BOSS galaxies*, *Mon. Not. Roy. Astron. Soc.* **465** (2017) 1757 [1606.00439].

[159] O. H. E. Philcox and M. M. Ivanov, *BOSS DR12 full-shape cosmology: ΛCDM constraints from the large-scale galaxy power spectrum and bispectrum monopole*, *Phys. Rev. D* **105** (2022) 043517 [2112.04515].

[160] G. D'Amico, M. Lewandowski, L. Senatore and P. Zhang, *Limits on primordial non-Gaussianities from BOSS galaxy-clustering data*, 2201.11518.

[161] G. Cabass, M. M. Ivanov, O. H. E. Philcox, M. Simonović and M. Zaldarriaga, *Constraints on Multi-Field Inflation from the BOSS Galaxy Survey*, 2204.01781.

[162] A. Pezzotta, M. Crocce, A. Eggemeier, A. G. Sánchez and R. Scoccimarro, *Testing one-loop galaxy bias: Cosmological constraints from the power spectrum*, *Phys. Rev. D* **104** (2021) 043531 [2102.08315].

[163] A. Eggemeier, R. Scoccimarro, R. E. Smith, M. Crocce, A. Pezzotta and A. G. Sánchez, *Testing one-loop galaxy bias: Joint analysis of power spectrum and bispectrum*, *Phys. Rev. D* **103** (2021) 123550 [2102.06902].

[164] Particle Data Group collaboration, *Review of Particle Physics*, *PTEP* **2020** (2020) 083C01.

[165] M. Viel, G. D. Becker, J. S. Bolton and M. G. Haehnelt, *Warm dark matter as a solution to the small scale crisis: New constraints from high redshift Lyman-α forest data*, *Phys. Rev. D* **88** (2013) 043502 [1306.2314].

[166] N. Palanque-Delabrouille, C. Yèche, N. Schöneberg, J. Lesgourgues, M. Walther, S. Chabanier et al., *Hints, neutrino bounds and WDM constraints from SDSS DR14 Lyman-α and Planck full-survey data*, *JCAP* **04** (2020) 038 [1911.09073].

[167] A. Garzilli, A. Magalich, O. Ruchayskiy and A. Boyarsky, *How to constrain warm dark matter with the Lyman-α forest*, *Mon. Not. Roy. Astron. Soc.* **502** (2021) 2356 [1912.09397].

[168] S. W. Randall, M. Markevitch, D. Clowe, A. H. Gonzalez and M. Bradac, *Constraints on the Self-Interaction Cross-Section of Dark Matter from Numerical Simulations of the Merging Galaxy Cluster 1E 0657-56*, *Astrophys. J.* **679** (2008) 1173 [0704.0261].

[169] S. Tulin and H.-B. Yu, *Dark Matter Self-interactions and Small Scale Structure*, *Phys. Rept.* **730** (2018) 1 [1705.02358].

[170] J. M. Bardeen, *Gauge Invariant Cosmological Perturbations*, *Phys. Rev. D* **22** (1980) 1882.

[171] V. F. Mukhanov, H. A. Feldman and R. H. Brandenberger, *Theory of cosmological perturbations. Part 1. Classical perturbations. Part 2. Quantum theory of perturbations. Part 3. Extensions*, *Phys. Rept.* **215** (1992) 203.

[172] H. Mo, F. van den Bosch and S. White, *Galaxy Formation and Evolution*. Cambridge University Press, 2010, 10.1017/CBO9780511807244.

[173] V. Springel et al., *Simulating the joint evolution of quasars, galaxies and their large-scale distribution*, *Nature* **435** (2005) 629 [astro-ph/0504097].

[174] F. Villaescusa-Navarro et al., *The Quijote simulations*, *Astrophys. J. Suppl.* **250** (2020) 2 [1909.05273].

[175] V. Springel et al., *First results from the IllustrisTNG simulations: matter and galaxy clustering*, *Mon. Not. Roy. Astron. Soc.* **475** (2018) 676 [1707.03397].

[176] A. Schneider, R. Teyssier, D. Potter, J. Stadel, J. Onions, D. S. Reed et al., *Matter power spectrum and the challenge of percent accuracy*, *JCAP* **04** (2016) 047 [1503.05920].

[177] M. Bartelmann, F. Fabis, D. Berg, E. Kozlikin, R. Lilow and C. Viermann, *A microscopic, non-equilibrium, statistical field theory for cosmic structure formation*, *New J. Phys.* **18** (2016) 043020 [1411.0806].

[178] M. Bartelmann, F. Fabis, E. Kozlikin, R. Lilow, J. Dombrowski and J. Mildenberger, *Kinetic Field Theory: Effects of momentum correlations on the cosmic density-fluctuation power spectrum*, *New J. Phys.* **19** (2017) 083001 [1611.09503].

[179] M. Bartelmann, I. Kostyuk, E. Kozlikin, R. Lilow, C. Littek, F. Fabis et al., *Cosmic Structure Formation with Kinetic Field Theory*, *Annalen Phys.* **531** (2019) 1800446 [1905.01179].

[180] E. Kozlikin, R. Lilow, F. Fabis and M. Bartelmann, *A first comparison of Kinetic Field Theory with Eulerian Standard Perturbation Theory*, *JCAP* **06** (2021) 035 [2012.05812].

[181] L. Heisenberg, S. Hemmatyar and S. Zentarra, *Kinetic Field Theory: Higher-Order Perturbation Theory*, 2207.10504.

[182] L. Hui, J. P. Ostriker, S. Tremaine and E. Witten, *Ultralight scalars as cosmological dark matter*, *Phys. Rev. D* **95** (2017) 043541 [1610.08297].

[183] L. M. Widrow and N. Kaiser, *Using the Schrodinger equation to simulate collisionless matter*, *Astrophys. J. Lett.* **416** (1993) L71.

[184] H.-Y. Schive, T. Chiueh and T. Broadhurst, *Cosmic Structure as the Quantum Interference of a Coherent Dark Wave*, *Nature Phys.* **10** (2014) 496 [1406.6586].

[185] C. Uhlemann, M. Kopp and T. Haugg, *Schrödinger method as N-body double and UV completion of dust*, *Phys. Rev. D* **90** (2014) 023517 [1403.5567].

[186] M. Garny and T. Konstandin, *Gravitational collapse in the Schrödinger-Poisson system*, *JCAP* **01** (2018) 009 [1710.04846].

[187] P. Mocz, L. Lancaster, A. Fialkov, F. Becerra and P.-H. Chavanis, *Schrödinger-Poisson–Vlasov-Poisson correspondence*, *Phys. Rev. D* **97** (2018) 083519 [1801.03507].

[188] J. Veltmaat, J. C. Niemeyer and B. Schwabe, *Formation and structure of ultralight bosonic dark matter halos*, *Phys. Rev. D* **98** (2018) 043509 [1804.09647].

[189] M. Garny, T. Konstandin and H. Rubira, *The Schrödinger-Poisson method for Large-Scale Structure*, *JCAP* **04** (2020) 003 [1911.04505].

[190] R. Galazo García, P. Brax and P. Valageas, *Self-similar solutions for fuzzy dark matter*, *Phys. Rev. D* **105** (2022) 123528 [2203.05995].

[191] L. Landau and E. Lifshitz, *Chapter ii - viscous fluids*, in *Fluid Mechanics (Second Edition)*, L. Landau and E. Lifshitz, eds., pp. 44–94, Pergamon, (1987), DOI.

[192] D. J. Griffiths, *Introduction to Electrodynamics*. Cambridge University Press, 4 ed., 2017, 10.1017/9781108333511.

[193] S. Pueblas and R. Scoccimarro, *Generation of Vorticity and Velocity Dispersion by Orbit Crossing*, *Phys. Rev. D* **80** (2009) 043504 [0809.4606].

[194] L. Mercolli and E. Pajer, *On the velocity in the Effective Field Theory of Large Scale Structures*, *JCAP* **03** (2014) 006 [1307.3220].

[195] O. Hahn, R. E. Angulo and T. Abel, *The Properties of Cosmic Velocity Fields*, *Mon. Not. Roy. Astron. Soc.* **454** (2015) 3920 [1404.2280].

[196] G. Jelic-Cizmek, F. Lepori, J. Adamek and R. Durrer, *The generation of vorticity in cosmological N-body simulations*, *JCAP* **09** (2018) 006 [1806.05146].

[197] D. J. Heath, *The growth of density perturbations in zero pressure Friedmann–Lemaître universes*, *Monthly Notices of the Royal Astronomical Society* **179** (1977) 351.

[198] R. Scoccimarro, *Transients from initial conditions: a perturbative analysis*, *Mon. Not. Roy. Astron. Soc.* **299** (1998) 1097 [astro-ph/9711187].

[199] R. Juszkiewicz, *On the evolution of cosmological adiabatic perturbations in the weakly non-linear regime*, *Monthly Notices of the Royal Astronomical Society* **197** (1981) 931.

[200] E. T. Vishniac, *Why weakly non-linear effects are small in a zero-pressure cosmology*, *Monthly Notices of the Royal Astronomical Society* **203** (1983) 345.

[201] J. N. Fry, *The Galaxy correlation hierarchy in perturbation theory*, *Astrophys. J.* **279** (1984) 499.

[202] M. H. Goroff, B. Grinstein, S. J. Rey and M. B. Wise, *Coupling of Modes of Cosmological Mass Density Fluctuations*, *Astrophys. J.* **311** (1986) 6.

[203] N. Makino, M. Sasaki and Y. Suto, *Analytic approach to the perturbative expansion of nonlinear gravitational fluctuations in cosmological density and velocity fields*, *Phys. Rev. D* **46** (1992) 585.

[204] B. Jain and E. Bertschinger, *Selfsimilar evolution of cosmological density fluctuations*, *Astrophys. J.* **456** (1996) 43 [astro-ph/9503025].

[205] V. Sahni and P. Coles, *Approximation methods for nonlinear gravitational clustering*, *Phys. Rept.* **262** (1995) 1 [astro-ph/9505005].

[206] R. Scoccimarro and J. Frieman, *Loop corrections in nonlinear cosmological perturbation theory*, *Astrophys. J. Suppl.* **105** (1996) 37 [astro-ph/9509047].

[207] R. Scoccimarro and J. Frieman, *Loop corrections in nonlinear cosmological perturbation theory 2. Two point statistics and selfsimilarity*, *Astrophys. J.* **473** (1996) 620 [astro-ph/9602070].

[208] M. B. Wise, *Non-gaussian fluctuations*, in *The Early Universe*, W. G. Unruh and G. W. Semenoff, eds., (Dordrecht), pp. 215–238, Springer Netherlands, (1988), DOI.

[209] N. S. Sugiyama and T. Futamase, *Relation between standard perturbation theory and regularized multi-point propagator method*, *Astrophys. J.* **769** (2013) 106 [1303.2748].

[210] M. Fasiello and Z. Vlah, *Nonlinear fields in generalized cosmologies*, *Phys. Rev. D* **94** (2016) 063516 [1604.04612].

[211] Y. Donath and L. Senatore, *Biased Tracers in Redshift Space in the EFTofLSS with exact time dependence*, *JCAP* **10** (2020) 039 [2005.04805].

[212] M. Fasiello, T. Fujita and Z. Vlah, *Perturbation theory of LSS in the ΛCDM Universe: exact time evolution and the two-loop power spectrum*, 2205.10026.

[213] T. Steele and T. Baldauf, *Precise Calibration of the One-Loop Bispectrum in the Effective Field Theory of Large Scale Structure*, *Phys. Rev. D* **103** (2021) 023520 [2009.01200].

[214] E. Sefusatti and F. Vernizzi, *Cosmological structure formation with clustering quintessence*, *JCAP* **03** (2011) 047 [1101.1026].

[215] P. Zhang and Y. Cai, *BOSS full-shape analysis from the EFTofLSS with exact time dependence*, *JCAP* **01** (2022) 031 [2111.05739].

[216] D. Blas, S. Floerchinger, M. Garny, N. Tetradis and U. A. Wiedemann, *Large scale structure from viscous dark matter*, *JCAP* **11** (2015) 049 [1507.06665].

[217] D. Blas, M. Garny and T. Konstandin, *On the non-linear scale of cosmological perturbation theory*, *JCAP* **09** (2013) 024 [1304.1546].

[218] S. Floerchinger, M. Garny, N. Tetradis and U. A. Wiedemann, *Renormalization-group flow of the effective action of cosmological large-scale structures*, *JCAP* **01** (2017) 048 [1607.03453].

[219] S. Floerchinger, M. Garny, A. Katsis, N. Tetradis and U. A. Wiedemann, *The dark matter bispectrum from effective viscosity and one-particle irreducible vertices*, *JCAP* **09** (2019) 047 [1907.10729].

[220] M. Lewandowski, A. Perko and L. Senatore, *Analytic Prediction of Baryonic Effects from the EFT of Large Scale Structures*, *JCAP* **05** (2015) 019 [1412.5049].

[221] D. P. L. Bragança, M. Lewandowski, D. Sekera, L. Senatore and R. Sgier, *Baryonic effects in the Effective Field Theory of Large-Scale Structure and an analytic recipe for lensing in CMB-S4*, *JCAP* **10** (2021) 074 [2010.02929].

[222] G. Cabass, M. M. Ivanov, M. Lewandowski, M. Mirbabayi and M. Simonović, *Snowmass White Paper: Effective Field Theories in Cosmology*, in *2022 Snowmass Summer Study*, 3, 2022, 2203.08232.

[223] A. Eggemeier, R. Scoccimarro and R. E. Smith, *Bias Loop Corrections to the Galaxy Bispectrum*, *Phys. Rev. D* **99** (2019) 123514 [1812.03208].

[224] G. C. Wick, *The Evaluation of the Collision Matrix*, *Phys. Rev.* **80** (1950) 268.

[225] M. Crocce and R. Scoccimarro, *Renormalized cosmological perturbation theory*, *Phys. Rev. D* **73** (2006) 063519 [astro-ph/0509418].

[226] M. Crocce and R. Scoccimarro, *Nonlinear Evolution of Baryon Acoustic Oscillations*, *Phys. Rev. D* **77** (2008) 023533 [0704.2783].

[227] M. Schmittfull and Z. Vlah, *FFT-PT: Reducing the two-loop large-scale structure power spectrum to low-dimensional radial integrals*, *Phys. Rev. D* **94** (2016) 103530 [1609.00349].

[228] X. Fang, J. A. Blazek, J. E. McEwen and C. M. Hirata, *FAST-PT II: an algorithm to calculate convolution integrals of general tensor quantities in cosmological perturbation theory*, *JCAP* **02** (2017) 030 [1609.05978].

[229] Z. Slepian, *On decoupling the integrals of cosmological perturbation theory*, *Mon. Not. Roy. Astron. Soc.* **507** (2021) 1337 [1812.02728].

[230] A. Kehagias and A. Riotto, *Symmetries and Consistency Relations in the Large Scale Structure of the Universe*, *Nucl. Phys. B* **873** (2013) 514 [1302.0130].

[231] M. Peloso and M. Pietroni, *Galilean invariance and the consistency relation for the nonlinear squeezed bispectrum of large scale structure*, *JCAP* **05** (2013) 031 [1302.0223].

[232] R. Landau, M. Paez and C. Bordeianu, *A survey of computational physics. introductory computational science*, (01, 2008).

[233] T. Hahn, *CUBA: A Library for multidimensional numerical integration*, *Comput. Phys. Commun.* **168** (2005) 78 [hep-ph/0404043].

[234] T. Hahn, *Concurrent Cuba*, *J. Phys. Conf. Ser.* **608** (2015) 012066 [1408.6373].

[235] J. J. M. Carrasco, S. Foreman, D. Green and L. Senatore, *The 2-loop matter power spectrum and the IR-safe integrand*, *JCAP* **07** (2014) 056 [1304.4946].

[236] J. Binney and S. Tremaine, *Galactic dynamics*. Princeton University Press, 1987.

[237] E. Pajer and M. Zaldarriaga, *On the Renormalization of the Effective Field Theory of Large Scale Structures*, *JCAP* **08** (2013) 037 [1301.7182].

[238] M. Crocce and R. Scoccimarro, *Memory of initial conditions in gravitational clustering*, *Phys. Rev. D* **73** (2006) 063520 [astro-ph/0509419].

[239] P. McDonald, *Dark matter clustering: a simple renormalization group approach*, *Phys. Rev. D* **75** (2007) 043514 [astro-ph/0606028].

[240] T. Matsubara, *Resumming Cosmological Perturbations via the Lagrangian Picture: One-loop Results in Real Space and in Redshift Space*, *Phys. Rev. D* **77** (2008) 063530 [0711.2521].

[241] A. Taruya and T. Hiramatsu, *A Closure Theory for Non-linear Evolution of Cosmological Power Spectra*, *Astrophys. J.* **674** (2008) 617 [0708.1367].

[242] S. Matarrese and M. Pietroni, *Resumming Cosmic Perturbations*, *JCAP* **06** (2007) 026 [astro-ph/0703563].

[243] S. Anselmi, S. Matarrese and M. Pietroni, *Next-to-leading resummations in cosmological perturbation theory*, *JCAP* **06** (2011) 015 [1011.4477].

[244] A. Elia, S. Kulkarni, C. Porciani, M. Pietroni and S. Matarrese, *Modeling the clustering of dark-matter haloes in resummed perturbation theories*, *Mon. Not. Roy. Astron. Soc.* **416** (2011) 1703 [1012.4833].

[245] F. Bernardeau, N. Van de Rijt and F. Vernizzi, *Resummed propagators in multi-component cosmic fluids with the eikonal approximation*, *Phys. Rev. D* **85** (2012) 063509 [1109.3400].

[246] A. Taruya, F. Bernardeau, T. Nishimichi and S. Codis, *RegPT: Direct and fast calculation of regularized cosmological power spectrum at two-loop order*, *Phys. Rev. D* **86** (2012) 103528 [1208.1191].

[247] M. McQuinn and M. White, *Cosmological perturbation theory in 1+1 dimensions*, *JCAP* **01** (2016) 043 [1502.07389].

[248] A. A. Abolhasani, M. Mirbabayi and E. Pajer, *Systematic Renormalization of the Effective Theory of Large Scale Structure*, *JCAP* **05** (2016) 063 [1509.07886].

[249] S. M. Carroll, S. Leichenauer and J. Pollack, *Consistent effective theory of long-wavelength cosmological perturbations*, *Phys. Rev. D* **90** (2014) 023518 [1310.2920].

[250] T. Baldauf, L. Mercolli, M. Mirbabayi and E. Pajer, *The Bispectrum in the Effective Field Theory of Large Scale Structure*, *JCAP* **05** (2015) 007 [1406.4135].

[251] D. Bertolini, K. Schutz, M. P. Solon and K. M. Zurek, *The Trispectrum in the Effective Field Theory of Large Scale Structure*, *JCAP* **06** (2016) 052 [1604.01770].

[252] T. Baldauf, L. Mercolli and M. Zaldarriaga, *Effective field theory of large scale structure at two loops: The apparent scale dependence of the speed of sound*, *Phys. Rev. D* **92** (2015) 123007 [1507.02256].

[253] S. Foreman, H. Perrier and L. Senatore, *Precision Comparison of the Power Spectrum in the EFTofLSS with Simulations*, *JCAP* **05** (2016) 027 [1507.05326].

[254] F. Bernardeau, A. Taruya and T. Nishimichi, *Cosmic propagators at two-loop order*, *Phys. Rev. D* **89** (2014) 023502 [1211.1571].

[255] D. J. Eisenstein, H.-j. Seo and M. J. White, *On the Robustness of the Acoustic Scale in the Low-Redshift Clustering of Matter*, *Astrophys. J.* **664** (2007) 660 [astro-ph/0604361].

[256] J. Hamann, S. Hannestad, J. Lesgourgues, C. Rampf and Y. Y. Y. Wong, *Cosmological parameters from large scale structure - geometric versus shape information*, *JCAP* **07** (2010) 022 [1003.3999].

[257] A. Chudaykin, M. M. Ivanov, O. H. E. Philcox and M. Simonović, *Nonlinear perturbation theory extension of the Boltzmann code CLASS*, *Phys. Rev. D* **102** (2020) 063533 [2004.10607].

[258] D. J. Eisenstein and W. Hu, *Power spectra for cold dark matter and its variants*, *Astrophys. J.* **511** (1997) 5 [astro-ph/9710252].

[259] Super-Kamiokande collaboration, *Evidence for oscillation of atmospheric neutrinos*, *Phys. Rev. Lett.* **81** (1998) 1562 [hep-ex/9807003].

[260] M. C. Gonzalez-Garcia and M. Maltoni, *Phenomenology with Massive Neutrinos*, *Phys. Rept.* **460** (2008) 1 [0704.1800].

[261] S. Betts et al., *Development of a Relic Neutrino Detection Experiment at PTOLEMY: Princeton Tritium Observatory for Light, Early-Universe, Massive-Neutrino Yield*, in *Community Summer Study 2013: Snowmass on the Mississippi*, 7, 2013, 1307.4738.

[262] A. D. Dolgov, *Neutrinos in cosmology*, *Phys. Rept.* **370** (2002) 333 [hep-ph/0202122].

[263] Y. Y. Y. Wong, *Neutrino mass in cosmology: status and prospects*, *Ann. Rev. Nucl. Part. Sci.* **61** (2011) 69 [1111.1436].

[264] KATRIN collaboration, *Direct neutrino-mass measurement with sub-electronvolt sensitivity*, *Nature Phys.* **18** (2022) 160 [2105.08533].

[265] M. M. Ivanov, M. Simonović and M. Zaldarriaga, *Cosmological Parameters and Neutrino Masses from the Final Planck and Full-Shape BOSS Data*, *Phys. Rev. D* **101** (2020) 083504 [1912.08208].

[266] J. J. Bennett, G. Buldgen, P. F. De Salas, M. Drewes, S. Gariazzo, S. Pastor et al., *Towards a precision calculation of N_{eff} in the Standard Model II: Neutrino decoupling in the presence of flavour oscillations and finite-temperature QED*, *JCAP* **04** (2021) 073 [2012.02726].

[267] M. Shoji and E. Komatsu, *Massive Neutrinos in Cosmology: Analytic Solutions and Fluid Approximation*, *Phys. Rev. D* **81** (2010) 123516 [1003.0942].

[268] M. Archidiacono, S. Hannestad and J. Lesgourgues, *What will it take to measure individual neutrino mass states using cosmology?*, *JCAP* **09** (2020) 021 [2003.03354].

[269] S. Hannestad, *Neutrinos in cosmology*, *New J. Phys.* **6** (2004) 108 [hep-ph/0404239].

[270] S. Hannestad, *Neutrino physics from precision cosmology*, *Prog. Part. Nucl. Phys.* **65** (2010) 185 [1007.0658].

[271] J. Lesgourgues and S. Pastor, *Neutrino mass from Cosmology*, *Adv. High Energy Phys.* **2012** (2012) 608515 [1212.6154].

[272] J. Lesgourgues and S. Pastor, *Neutrino cosmology and Planck*, *New J. Phys.* **16** (2014) 065002 [1404.1740].

[273] J. Brandbyge, S. Hannestad, T. Haugbølle and B. Thomsen, *The Effect of Thermal Neutrino Motion on the Non-linear Cosmological Matter Power Spectrum*, *JCAP* **08** (2008) 020 [0802.3700].

[274] J. Brandbyge and S. Hannestad, *Grid Based Linear Neutrino Perturbations in Cosmological N-body Simulations*, *JCAP* **05** (2009) 002 [0812.3149].

[275] M. Viel, M. G. Haehnelt and V. Springel, *The effect of neutrinos on the matter distribution as probed by the Intergalactic Medium*, *JCAP* **06** (2010) 015 [1003.2422].

[276] S. Bird, M. Viel and M. G. Haehnelt, *Massive Neutrinos and the Non-linear Matter Power Spectrum*, *Mon. Not. Roy. Astron. Soc.* **420** (2012) 2551 [1109.4416].

[277] Y. Ali-Haimoud and S. Bird, *An efficient implementation of massive neutrinos in non-linear structure formation simulations*, *Mon. Not. Roy. Astron. Soc.* **428** (2012) 3375 [1209.0461].

[278] E. Castorina, C. Carbone, J. Bel, E. Sefusatti and K. Dolag, *DEMNUni: The clustering of large-scale structures in the presence of massive neutrinos*, *JCAP* **07** (2015) 043 [1505.07148].

[279] A. Mead, C. Heymans, L. Lombriser, J. Peacock, O. Steele and H. Winther, *Accurate halo-model matter power spectra with dark energy, massive neutrinos and modified gravitational forces*, *Mon. Not. Roy. Astron. Soc.* **459** (2016) 1468 [1602.02154].

[280] S. Hannestad, A. Upadhye and Y. Y. Y. Wong, *Spoon or slide? The non-linear matter power spectrum in the presence of massive neutrinos*, *JCAP* **11** (2020) 062 [2006.04995].

[281] D. Blas, M. Garny, T. Konstandin and J. Lesgourgues, *Structure formation with massive neutrinos: going beyond linear theory*, *JCAP* **11** (2014) 039 [1408.2995].

[282] M. Pietroni, *Flowing with Time: a New Approach to Nonlinear Cosmological Perturbations*, *JCAP* **10** (2008) 036 [0806.0971].

[283] C.-P. Ma and E. Bertschinger, *Cosmological perturbation theory in the synchronous and conformal Newtonian gauges*, *Astrophys. J.* **455** (1995) 7 [astro-ph/9506072].

[284] J. Lesgourgues, S. Matarrese, M. Pietroni and A. Riotto, *Non-linear Power Spectrum including Massive Neutrinos: the Time-RG Flow Approach*, *JCAP* **06** (2009) 017 [0901.4550].

[285] A. Pontzen, A. Slosar, N. Roth and H. V. Peiris, *Inverted initial conditions: exploring the growth of cosmic structure and voids*, *Phys. Rev. D* **93** (2016) 103519 [1511.04090].

[286] R. E. Angulo and A. Pontzen, *Cosmological N-body simulations with suppressed variance*, *Mon. Not. Roy. Astron. Soc.* **462** (2016) L1 [1603.05253].

[287] F. Villaescusa-Navarro, S. Naess, S. Genel, A. Pontzen, B. Wandelt, L. Anderson et al., *Statistical properties of paired fixed fields*, *Astrophys. J.* **867** (2018) 137 [1806.01871].

[288] T. Baldauf, M. Mirbabayi, M. Simonović and M. Zaldarriaga, *LSS constraints with controlled theoretical uncertainties*, 1602.00674.

[289] C. Hahn and F. Villaescusa-Navarro, *Constraining M_ν with the bispectrum. Part II. The information content of the galaxy bispectrum monopole*, *JCAP* **04** (2021) 029 [2012.02200].

[290] G. D'Amico, Y. Donath, M. Lewandowski, L. Senatore and P. Zhang, *The BOSS bispectrum analysis at one loop from the Effective Field Theory of Large-Scale Structure*, 2206.08327.

[291] O. H. E. Philcox, M. M. Ivanov, G. Cabass, M. Simonović, M. Zaldarriaga and T. Nishimichi, *Cosmology with the Redshift-Space Galaxy Bispectrum Monopole at One-Loop Order*, 2206.02800.

[292] P. Creminelli and M. Zaldarriaga, *Single field consistency relation for the 3-point function*, *JCAP* **10** (2004) 006 [astro-ph/0407059].

[293] WMAP collaboration, *Nine-Year Wilkinson Microwave Anisotropy Probe (WMAP) Observations: Final Maps and Results*, *Astrophys. J. Suppl.* **208** (2013) 20 [1212.5225].

[294] G. Cabass, M. M. Ivanov, O. H. E. Philcox, M. Simonović and M. Zaldarriaga, *Constraints on Single-Field Inflation from the BOSS Galaxy Survey*, *Phys. Rev. Lett.* **129** (2022) 021301 [2201.07238].

[295] A. Barreira, *Can we actually constrain $f_{\rm NL}$ using the scale-dependent bias effect? An illustration of the impact of galaxy bias uncertainties using the BOSS DR12 galaxy power spectrum*, 2205.05673.

[296] R. E. Angulo, S. Foreman, M. Schmittfull and L. Senatore, *The One-Loop Matter Bispectrum in the Effective Field Theory of Large Scale Structures*, *JCAP* **10** (2015) 039 [1406.4143].

[297] D. Alkhanishvili, C. Porciani, E. Sefusatti, M. Biagetti, A. Lazanu, A. Oddo et al., *The reach of next-to-leading-order perturbation theory for the matter bispectrum*, *Mon. Not. Roy. Astron. Soc.* **512** (2022) 4961 [2107.08054].

[298] T. Baldauf, E. Schaan and M. Zaldarriaga, *On the reach of perturbative descriptions for dark matter displacement fields*, *JCAP* **03** (2016) 017 [1505.07098].

[299] T. Baldauf, E. Schaan and M. Zaldarriaga, *On the reach of perturbative methods for dark matter density fields*, *JCAP* **03** (2016) 007 [1507.02255].

[300] V. Springel, *The Cosmological simulation code GADGET-2*, *Mon. Not. Roy. Astron. Soc.* **364** (2005) 1105 [astro-ph/0505010].

[301] N. Roth and C. Porciani, *Testing standard perturbation theory and the Eulerian local biasing scheme against N-body simulations*, *Mon. Not. Roy. Astron. Soc.* **415** (2011) 829 [1101.1520].

[302] A. Taruya, T. Nishimichi and D. Jeong, *Grid-based calculation for perturbation theory of large-scale structure*, *Phys. Rev. D* **98** (2018) 103532 [1807.04215].

[303] A. Taruya, T. Nishimichi and D. Jeong, *Covariance of the matter power spectrum including the survey window function effect: N -body simulations versus fifth-order perturbation theory on grids*, *Phys. Rev. D* **103** (2021) 023501 [2007.05504].

[304] E. Sellentin and R. Durrer, *Detecting the cosmological neutrino background in the CMB*, *Phys. Rev. D* **92** (2015) 063012 [1412.6427].

[305] B. Audren et al., *Robustness of cosmic neutrino background detection in the cosmic microwave background*, *JCAP* **03** (2015) 036 [1412.5948].

[306] F.-Y. Cyr-Racine and K. Sigurdson, *Limits on Neutrino-Neutrino Scattering in the Early Universe*, *Phys. Rev. D* **90** (2014) 123533 [1306.1536].

[307] I. M. Oldengott, C. Rampf and Y. Y. Y. Wong, *Boltzmann hierarchy for interacting neutrinos I: formalism*, *JCAP* **04** (2015) 016 [1409.1577].

[308] L. Lancaster, F.-Y. Cyr-Racine, L. Knox and Z. Pan, *A tale of two modes: Neutrino free-streaming in the early universe*, *JCAP* **07** (2017) 033 [1704.06657].

[309] I. M. Oldengott, T. Tram, C. Rampf and Y. Y. Y. Wong, *Interacting neutrinos in cosmology: exact description and constraints*, *JCAP* **11** (2017) 027 [1706.02123].

[310] C. D. Kreisch, F.-Y. Cyr-Racine and O. Doré, *Neutrino puzzle: Anomalies, interactions, and cosmological tensions*, *Phys. Rev. D* **101** (2020) 123505 [1902.00534].

[311] M. Park, C. D. Kreisch, J. Dunkley, B. Hadzhiyska and F.-Y. Cyr-Racine, *ΛCDM or self-interacting neutrinos: How CMB data can tell the two models apart*, *Phys. Rev. D* **100** (2019) 063524 [1904.02625].

[312] A. Das and S. Ghosh, *Flavor-specific interaction favors strong neutrino self-coupling in the early universe*, *JCAP* **07** (2021) 038 [2011.12315].

[313] S. Roy Choudhury, S. Hannestad and T. Tram, *Updated constraints on massive neutrino self-interactions from cosmology in light of the H_0 tension*, *JCAP* **03** (2021) 084 [2012.07519].

[314] T. Brinckmann, J. H. Chang and M. LoVerde, *Self-interacting neutrinos, the Hubble parameter tension, and the cosmic microwave background*, *Phys. Rev. D* **104** (2021) 063523 [2012.11830].

[315] C. D. Kreisch et al., *The Atacama Cosmology Telescope: The Persistence of Neutrino Self-Interaction in Cosmological Measurements*, 2207.03164.

[316] Z. Chacko, L. J. Hall, T. Okui and S. J. Oliver, *CMB signals of neutrino mass generation*, *Phys. Rev. D* **70** (2004) 085008 [hep-ph/0312267].

[317] M. Escudero and S. J. Witte, *A CMB search for the neutrino mass mechanism and its relation to the Hubble tension*, *Eur. Phys. J. C* **80** (2020) 294 [1909.04044].

[318] M. Escudero and S. J. Witte, *The hubble tension as a hint of leptogenesis and neutrino mass generation*, *Eur. Phys. J. C* **81** (2021) 515 [2103.03249].

[319] M. Escudero Abenza and S. J. Witte, *Could the Hubble Tension be Pointing Towards the Neutrino Mass Mechanism?*, in *Prospects in Neutrino Physics*, 4, 2020, 2004.01470.

[320] M. Escudero Abenza, *Precision early universe thermodynamics made simple: $N_{\rm eff}$ and neutrino decoupling in the Standard Model and beyond*, *JCAP* **05** (2020) 048 [2001.04466].

[321] G. Barenboim, J. Z. Chen, S. Hannestad, I. M. Oldengott, T. Tram and Y. Y. Y. Wong, *Invisible neutrino decay in precision cosmology*, *JCAP* **03** (2021) 087 [2011.01502].

[322] J. Z. Chen, I. M. Oldengott, G. Pierobon and Y. Y. Y. Wong, *Weaker yet again: mass spectrum-consistent cosmological constraints on the neutrino lifetime*, 2203.09075.

[323] S. Hannestad and G. Raffelt, *Constraining invisible neutrino decays with the cosmic microwave background*, *Phys. Rev. D* **72** (2005) 103514 [hep-ph/0509278].

[324] A. Basboll, O. E. Bjaelde, S. Hannestad and G. G. Raffelt, *Are cosmological neutrinos free-streaming?*, *Phys. Rev. D* **79** (2009) 043512 [0806.1735].

[325] M. Escudero and M. Fairbairn, *Cosmological Constraints on Invisible Neutrino Decays Revisited*, *Phys. Rev. D* **100** (2019) 103531 [1907.05425].

[326] Z. Chacko, A. Dev, P. Du, V. Poulin and Y. Tsai, *Cosmological Limits on the Neutrino Mass and Lifetime*, *JHEP* **04** (2020) 020 [1909.05275].

[327] Z. Chacko, A. Dev, P. Du, V. Poulin and Y. Tsai, *Determining the Neutrino Lifetime from Cosmology*, *Phys. Rev. D* **103** (2021) 043519 [2002.08401].

[328] G. F. Abellán, Z. Chacko, A. Dev, P. Du, V. Poulin and Y. Tsai, *Improved cosmological constraints on the neutrino mass and lifetime*, 2112.13862.

[329] J. F. Beacom, N. F. Bell and S. Dodelson, *Neutrinoless universe*, *Phys. Rev. Lett.* **93** (2004) 121302 [astro-ph/0404585].

[330] S. Hannestad, *Structure formation with strongly interacting neutrinos - Implications for the cosmological neutrino mass bound*, *JCAP* **02** (2005) 011 [astro-ph/0411475].

[331] N. F. Bell, E. Pierpaoli and K. Sigurdson, *Cosmological signatures of interacting neutrinos*, *Phys. Rev. D* **73** (2006) 063523 [astro-ph/0511410].

[332] M. Archidiacono and S. Hannestad, *Updated constraints on non-standard neutrino interactions from Planck*, *JCAP* **07** (2014) 046 [1311.3873].

[333] F. Forastieri, M. Lattanzi and P. Natoli, *Constraints on secret neutrino interactions after Planck*, *JCAP* **07** (2015) 014 [1504.04999].

[334] F. Forastieri, M. Lattanzi and P. Natoli, *Cosmological constraints on neutrino self-interactions with a light mediator*, *Phys. Rev. D* **100** (2019) 103526 [1904.07810].

[335] J. Venzor, G. Garcia-Arroyo, A. Pérez-Lorenzana and J. De-Santiago, *Massive neutrino self-interactions with a light mediator in cosmology*, *Phys. Rev. D* **105** (2022) 123539 [2202.09310].

[336] N. Aghanim, S. Majumdar and J. Silk, *Secondary anisotropies of the CMB*, *Rept. Prog. Phys.* **71** (2008) 066902 [0711.0518].

[337] M. Bartelmann and P. Schneider, *Weak gravitational lensing*, *Phys. Rept.* **340** (2001) 291 [astro-ph/9912508].

[338] A. Lewis, *GetDist: a Python package for analysing Monte Carlo samples*, 1910.13970.

[339] A. J. Ross, L. Samushia, C. Howlett, W. J. Percival, A. Burden and M. Manera, *The clustering of the SDSS DR7 main Galaxy sample ? I. A 4 per cent distance measure at $z = 0.15$*, *Mon. Not. Roy. Astron. Soc.* **449** (2015) 835 [1409.3242].

[340] BOSS collaboration, *The clustering of galaxies in the completed SDSS-III Baryon Oscillation Spectroscopic Survey: cosmological analysis of the DR12 galaxy sample*, *Mon. Not. Roy. Astron. Soc.* **470** (2017) 2617 [1607.03155].

[341] A. Gelman and D. B. Rubin, *Inference from iterative simulation using multiple sequences*, *Statistical Science* **7** (1992) 457.